
Chemical analysis of globular star clusters: theory and observation

Karin Lind



München 2010

Chemical analysis of globular star clusters: theory and observation

Karin Lind

Dissertation
an der Ludwig-Maximilians-Universität
München

vorgelegt von
Karin Lind
aus Motala, Schweden

München, den 28.09.2010

Erstgutachter: Priv. Doz. Dr. Achim Weiß

Zweitgutachter: Priv. Doz. Dr. Joachim Puls

Tag der mündlichen Prüfung: 13.12.2010

Contents

Zusammenfassung	xiii
Summary	xv
Preface	xvii
1 Abundance analysis of late-type stars	1
1.1 The chemical composition of stars	1
1.2 Model atmospheres	2
1.3 LTE analysis	3
1.4 Non-LTE analysis	5
1.4.1 Atomic data	6
1.4.2 Motivation for new calculations	7
1.4.3 Non-LTE effects	7
2 Non-LTE calculations for neutral Na using improved atomic data	11
2.1 Astrophysical motivation	11
2.2 Non-LTE modelling procedure	12
2.2.1 Structure of the model atom	13
2.2.2 Radiative transitions	14
2.2.3 Electron collisions	14
2.2.4 Hydrogen collisions	17
2.2.5 Line broadening	18
2.3 Discussion	18
2.3.1 Departures from LTE	18
2.3.2 The influence of collisions	23
2.3.3 Consequences for stellar abundance analysis	26
2.4 Conclusions	28
3 Departures from LTE for neutral Li	31
3.1 Astrophysical motivation	31
3.2 Non-LTE modelling procedure	31
3.3 Results	34

3.4	Discussion	35
4	3D, non-LTE line formation of Na I in the Sun	41
4.1	Introduction	41
4.2	Modelling procedure	42
4.3	Line formation in 3D	45
4.4	Centre-to-limb variation	46
4.5	The solar Na abundance	51
5	Globular clusters	53
5.1	Definition and basic properties	53
5.2	Evolution of low-mass stars	56
5.3	Observational applications	57
5.4	High-resolution spectroscopy with FLAMES	59
5.4.1	The observational setup	59
5.4.2	Data reduction and processing	60
5.5	Determination of stellar parameters	61
5.5.1	Effective temperature	61
5.5.2	Surface gravity	64
6	Signatures of intrinsic Li depletion and Li-Na anti-correlation in the metal-poor globular cluster NGC 6397	65
6.1	Introduction	65
6.2	Observations	68
6.2.1	High and medium-high resolution spectroscopy	68
6.2.2	Strömngren photometry	69
6.3	Analysis	74
6.3.1	Effective temperatures and surface gravities	75
6.3.2	Metallicity	76
6.3.3	Lithium	79
6.3.4	Sodium	79
6.3.5	Calcium	80
6.4	Results	80
6.4.1	Li abundances	80
6.4.2	Lithium data from the ESO archive	83
6.4.3	The Li-Na anti-correlation	83
6.5	Discussion	86
6.5.1	Signatures of intrinsic lithium depletion	86
6.5.2	Effects of stellar parameters and non-LTE	91
6.5.3	Comparison to other studies	91
6.5.4	Comparison to diffusion-turbulence models	92
6.6	Conclusions	95

7	Tracing the evolution of NGC 6397 through the chemical composition of its stellar populations	97
7.1	Introduction	97
7.2	Observations and analysis	99
7.3	Abundance analysis	101
7.3.1	O, Na, Mg, and Al	105
7.3.2	Nitrogen	109
7.3.3	α and iron-peak elements	110
7.3.4	Neutron capture elements	112
7.3.5	Helium	113
7.4	Consequences for the evolutionary scenario	116
7.4.1	Method	116
7.4.2	Amount of dilution between massive star ejecta and pristine gas . .	117
7.4.3	Expected anti-correlations	119
7.4.4	He content	122
7.4.5	Initial cluster mass	122
7.5	Conclusions	123
8	Conclusions and outlook	129
8.1	The cosmological Li problem	129
8.2	Multiple populations in globular clusters	130
8.3	The future of high-precision abundance analysis	131
	Bibliography	146
	Acknowledgments	149
	Curriculum Vitae	154

List of Figures

1.1	The optical depth dependence of the mean radiation field J_ν and the Planck function B_ν for a solar atmospheric model.	8
1.2	Solar LTE and non-LTE curves-of-growth for one of the Na D lines ($\lambda 589.5$ nm).	9
2.1	Schematic term diagram of the 23-level Na I model atom.	13
2.2	Three sample excitation cross-sections for collisions between Na I and electrons.	16
2.3	Comparison between rate coefficients at $T = 6000$ K for collisional excitation of Na I by neutral hydrogen atoms.	19
2.4	Non-LTE abundance corrections as functions of equivalent widths of selected Na I lines.	20
2.5	Contour diagrams illustrating non-LTE abundance corrections.	24
2.6	The sensitivity of Na I departure coefficients to hydrogen collisions.	25
2.7	Comparison with the non-LTE Na abundance corrections determined in earlier studies.	27
2.8	Comparison between temperature stratifications and curves-of-growth of Na lines for different 1D model atmosphere codes.	29
3.1	The sensitivity of Li non-LTE abundance corrections to hydrogen collisions for different stellar parameters.	36
3.2	The sensitivity of Li non-LTE abundance corrections to choice of 1D model atmosphere code.	37
3.3	Comparison of the derived Li non-LTE abundance corrections to earlier studies.	38
4.1	Temperature and electron density structures of solar model atmospheres in 1D and 3D.	44
4.2	Solar disk centre intensity profiles of the Na I 615.4 nm line.	45
4.3	Departure coefficients for Na I 3s and 3p with optical depth	47
4.4	Surface images of atmospheric variables for a solar 3D radiation-hydrodynamic simulation	48
4.5	Centre-to-limb variation of the equivalent widths of Na I lines.	49
4.6	Centre-to-limb variation of solar Na I line profiles.	50
5.1	A schematic view of the positions of all known globular clusters in the Galaxy.	54

5.2	A zoomed in view of Fig. 5.1.	55
5.3	The observed HR-diagram of NGC 6397.	58
5.4	Cross-section along the order direction of the GIRAFFE CCD deector. . .	62
6.1	$(b - y) - T_{\text{eff}}$ and $(v - y) - T_{\text{eff}}$ relations derived for NGC6397.	70
6.2	The $(b - y)_0 - M_V$ fiducial sequence.	71
6.3	Histograms of the FeI and FeII excitation and ionisation equilibria of the targets.	77
6.4	Example fits to the Li I 670.7 nm line and the Na I 819.4 nm line.	78
6.5	Li abundances plotted next to the observed HR diagram of NGC 6397. . .	82
6.6	Comparison between our observed Li data and archival data.	84
6.7	Li and Na abundances for dwarfs and subgiants.	87
6.8	Bin-averaged Li abundances against absolute visual magnitude.	88
6.9	Bin-averaged Li abundances against effective temperature.	89
6.10	Comparison of Li abundance trends with luminosity to stellar structure models with atomic diffusion and mixing.	93
6.11	Same as in in Fig 6.10 but with effective temperature as the reference axis.	94
7.1	The targeted red giant branch stars are marked with black bullets in the $V - (v - y)$ diagram of NGC 6397.	100
7.2	Sample UVES spectra and best-fit synthetic model.	102
7.3	Elemental abundances of all targets.	103
7.4	Non-LTE Na abundance variation with effective temperature in NGC 6397.	105
7.5	Na abundance histograms.	106
7.6	Na, Mg, Al, and O abundances.	108
7.7	Comparison between abundances of RGB stars in NGC 6397 and halo field stars.	109
7.8	Correlation between Na-abundance and colour index c_y on the red giant branch.	111
7.9	Model predictions for the Li and Na abundances for unevolved stars in NGC 6397.	118
7.10	Model predictions for the O–Na and O–Al anti-correlations for red giant stars.	120
7.11	Expected anti-correlation between helium mass fraction and $[O/Na]$	121

List of Tables

2.1	Line data for the ten Na I lines considered in the detailed spectrum synthesis.	15
3.1	Wavelengths, oscillator strengths, and broadening data for the two considered Li I lines.	33
3.2	Non-LTE abundance corrections and equivalent widths for the Li I $\lambda = 670.7$ nm line.	35
3.3	Non-LTE abundance corrections and equivalent widths for the Li I $\lambda = 610.3$ nm line.	37
4.1	The solar Na abundance derived from five Na I lines with different modelling assumptions.	52
6.1	FLAMES observations.	71
6.2	Photometry and effective temperatures.	72
6.3	Iron lines measured in the UVES spectrum of one red giant branch star. . .	73
6.3	Continued.	74
6.4	Adopted stellar parameters, equivalent widths, and Li, Na, and Ca abundances. The full table can be retrieved from CDS/Vizier.	81
7.1	Mean abundances and abundance dispersions compared to literature values for NGC 6397.	104
7.2	Stellar parameters for #5644 and #14565 derived assuming a normal-star hydrogen and helium composition.	114
7.3	Iron mass fractions derived for #5644 and #14565, assuming different mass fractions of helium	115
7.4	Line list with reference to the adopted oscillator strength.	124
7.4	Continued.	125
7.4	Continued.	126
7.5	Individual star abundances and stellar parameters.	127
7.6	Continued.	128

Zusammenfassung

Einige Minuten nach der Geburt des Universums im Urknall wurden durch Kernreaktionen leichtere Isotope wie ${}^7\text{Li}$ gebildet. Seither finden solche Reaktionen im heißen Inneren der Sterne statt; dabei versorgen sie die Sterne mit Energie und bilden die chemischen Elemente. In dieser Dissertation beschreibe ich, wie wir die chemische Zusammensetzung von Sternen in einem Kugelsternhaufen finden, der eine der ältesten Populationen unserer Galaxie enthält. Damit behandle ich zwei grundlegende astrophysikalische Probleme.

Das erste Problem betrifft Lithium und seine ursprüngliche Häufigkeit, wie sie aktuelle kosmologische Theorien über den Ursprung des Universums vorhersagen. Die Lithiumhäufigkeiten, die wir in Sternen in Kugelsternhaufen messen, sind geringer als diese Schätzung. Daher untersuchen wir die Möglichkeit, daß Lithium von der Sternoberfläche in weiter innen liegende Schichten transportiert wurde. Die vorliegende Arbeit untermauert diese Hypothese mit Evidenz aus Beobachtungsdaten, dass Sterne geringer Masse in der Spätphase ihrer Entwicklung eine kleine Zunahme der Lithiumhäufigkeiten an ihrer Oberfläche erfahren.

Die zweite Frage betrifft die Entstehung und Entwicklung von Kugelsternhaufen. Diese dichten Sternpopulationen erlebten früh eine einzigartige Form von Anreicherung indem sie den Gasabfluss langsamer Sternwinde zurückhielten. Dieses Material wurde dann zur Produktion einer zweiten Generation von Sternen verwendet. Mit Ausnahme leichterer Elemente wie Natrium zeigen die beide Generationen dieselben chemischen Signaturen. In dieser Arbeit möchte ich verschiedene Aspekte dieser Anreicherungsprozesse besprechen.

Nur mit einer korrekten physikalischen Beschreibung des Energietransports durch Konvektion und Strahlung durch die Sternatmosphäre und des Gleichgewichtszustands der Atome, Ionen und Moleküle in dem dünnen Gas können wir solide Vorhersagen für das produzierte Spektrum treffen und daraus genaue Häufigkeiten ableiten. Im Besonderen werde ich darlegen, wie die vereinfachende Annahme eines lokalen thermischen Gleichgewichts zu systematischen Fehlern bei der Spektrallinienanalyse von Li und Na führt. Die verursachten Fehler in den Elementhäufigkeiten der Sterne werden auf 10–50% geschätzt, in Einzelfällen sogar um eine Größenordnung mehr. Erstmals haben wir außerdem eine Untersuchung des kombinierten Einflusses der Abweichungen vom lokalen thermischen und hydrostatischen Gleichgewicht bei der Bestimmung der solaren Natriumhäufigkeit durchgeführt.

Summary

A few minutes after the Big Bang that created our Universe, nucleosynthesis reactions forged some lighter isotopes, including ${}^7\text{Li}$. Ever since then, such reactions have taken place in the hot stellar interiors, providing the stars with the energy to shine and forming all chemical elements necessary for life as we know it. In this thesis I describe how we have inferred the chemical composition of stars in a globular cluster, hosting one of the oldest stellar populations in our Galaxy, in order to address two fundamental astrophysical problems.

The first problem is related to lithium, and the prediction of its primordial abundance from present cosmological theories of how the Universe was born. The Li abundances that we measure in the envelopes of globular cluster stars are lower than this estimate and we investigate the possibility that Li has been drained from the stellar surfaces. This thesis presents observational evidence that low-mass stars experience a small increase in their surface Li abundances during the course of their late phases of evolution, supporting this hypothesis.

The second question is related to the formation and evolution of globular clusters. It appears that these dense stellar environments early underwent a unique form of self-enrichment, by retaining the gas outflow from slow stellar winds. The material was then incorporated into a second stellar generation with identical chemical signatures to the first, except for a handful of lighter elements, including sodium. I here discuss several aspects of this stellar pollution process.

Only with a correct physical description of the radiative and convective energy transport through the stellar atmosphere, and the equilibrium state of the atoms, ions and molecules that form the tenuous gas, can we make solid predictions of the emergent spectrum and derive accurate abundances. In particular, I discuss how the simplifying assumption of local thermal equilibrium give rise to systematic errors in the analysis of Li and Na spectral lines, commonly mis-estimating the elemental abundances in stars by 10–50%, and in certain cases considerably more. Moreover, we have for the first time investigated the combined influence from departures from local thermal equilibrium and hydro-static equilibrium in the determination of the solar Na abundance.

Preface

The dissertation consists of eight chapters of which two are introductory, five contain journal articles that have been published or are being prepared for publication, and one (Chapter 8) summarises the main conclusions and discusses future prospects.

Chapter 1 introduces the basic concepts and physical assumptions behind modelling of stellar atmospheres and abundance analysis of late-type stars. This is followed by three chapters that present theoretical investigations of lithium (3) and sodium abundance determination (2 and 4). I conducted essentially all the practical work presented in these chapters myself, with minor assistance by the listed co-authors. This included e.g. the assembly of new improved model atoms for Na and Li, setting up and executing an efficient numerical procedure for comprehensive 1D, non-LTE calculations, and conducting several tests on my own and my co-authors' initiatives, in order to interpret the results. To perform the 3D, non-LTE investigation presented in Chapter 4, I also took significant part in adapting the presented code to accurate abundance analysis and testing its performance to that end. The field of combined 3D, non-LTE analyses of elemental abundances is indeed in its infancy and my work has significantly contributed to its development.

Chapter 5 describes fundamental properties of globular clusters and outlines the steps involved in processing of high-resolution spectroscopic data and the basic concepts of stellar parameter determination. Chapters 6 and 7 contain observational investigations of globular cluster stars and extensive discussions on the astrophysical gain of the presented analyses. The work has been based on data collected during two observing runs at the ESO Very Large Telescope at Paranal Observatory, Chile. I was the Principal Investigator of one of the observing programmes and thus had the main responsibility for the application for observing time and preparation of the observational procedure for this run. Further, I was responsible for the data reduction and processing of all observational data, the determination of stellar parameters, the assembly of the adopted line lists, and the development of techniques to efficiently perform large-scale abundance analysis through spectrum synthesis and equivalent width measurements. I also took the leading part in interpreting the results and placing them in a larger context. With the exception of Sect. 4.1, 6.1, and 7.4 I am the main author of all sections presented in this work.

Chapter 1

Abundance analysis of late-type stars

The chemical composition of a star's outermost layer is imprinted onto its electromagnetic spectrum, in particular through the strengths of spectral lines. By constructing a model of the temperature and density stratification of the atmosphere and use radiative transfer to predict the spectrum of emitted radiation, we may constrain the chemical abundances of different elements in the atmosphere. Depending on the level of sophistication of the modelling procedure and the desired accuracy of the result, this can be anything from a relatively straightforward to a highly complex process.

The following chapter introduces the reader to some of the basic assumptions and terminology involved in traditional abundance analysis of so called late-type stars. This collective term refers to stars that have masses similar to the Sun and thus share several other characteristics as well, such as size, luminosity, surface temperature and gravity, at a given evolutionary phase. Here we are mainly concerned with late-type stars of spectral classes F, G, and K (see e.g. Gray, 2005), and luminosity classes III (giants), IV (subgiants) and V (dwarfs). These stars have masses $M = 0.5 - 1.6 M_{\odot}$ and main sequence (MS) luminosities $L = 0.1 - 6.5 L_{\odot}$ ¹.

1.1 The chemical composition of stars

A 'normal' star consists of roughly 90% hydrogen and 10% helium particles. All other species are referred to as 'metals' and their total number density is typically $\lesssim 0.1\%$. Even though they are insignificant in numbers, the metals have a profound importance for many aspects of the evolution of individual stars and galaxies, not to mention planet formation. The vast majority of all heavier elements that exist in the Universe today have indeed been synthesised inside stars and partly returned to the interstellar gas during the late phases of stellar evolution. By studying the chemical composition of stars in different environments and ages, we can trace this cosmic recycling process.

The abundance of metals in a star is usually specified on a logarithmic scale relative to hydrogen, such that $A(X) = \log(\epsilon(X)) + 12 = \log(N(X)/N(H)) + 12$, where $N(X)$ is the

¹The quoted values are adopted from "A dictionary of Astronomy" (www.encyclopedia.com)

number density of element X. This notation will be used throughout the text. Further, it is common to use the iron abundance relative to the Sun as a measure of the total 'metallicity' of the star, using a bracket notation: $[\text{Fe}/\text{H}] = \log(N(\text{Fe})/N(\text{H})) - \log(N(\text{Fe})/N(\text{H}))_{\odot}$. A star with $[\text{Fe}/\text{H}] = -2$ thus has 100 times less iron compared to the Sun, and the same (or similar) scaling factor is usually applied to all other elements.

Individual elemental abundances in stars are specified either in absolute numbers, $A(X)$, or using the bracket notation $[\text{X}/\text{Fe}]$. The latter notation indicates how much an element is deficient or in excess with respect to the solar composition, again with iron as the reference element. As an example, inter-mediate mass elements with even atomic number (O, Ne, Mg, Si, S, Ar, Ca, Ti) are usually assumed to be enhanced in metal-poor stars, such that $[\text{X}/\text{Fe}] > 0$. This is referred to as α -enhancement.

1.2 Model atmospheres

The most common physical assumptions behind atmospheric modelling of late-type stars are (see e.g. Kurucz, 1970; Gray, 2005; Gustafsson et al., 2008):

- hydro-static equilibrium, where gravity is balanced by the thermal and turbulent pressure of the gas and by radiation pressure.
- a one-dimensional, plane-parallel or spherically symmetric, geometry.
- energy transport via radiation and convection, with the efficiency of convective flux parametrised with so called 'mixing length theory'.
- local thermodynamic equilibrium (LTE).

These assumptions are all more or less realistic approximations of the actual physical state of the atmosphere. During recent decades it has been possible to relax the three first assumptions, and 3D, hydro-dynamical models (e.g. Stein & Nordlund, 1998; Nordlund et al., 2009; Vögler et al., 2005; Freytag et al., 2010), simulating the convective motions in the atmospheres from first principles, are becoming increasingly realistic and suitable for abundance analysis (see further Chapter 4). Still, much work remains to be done in this direction before 3D models can be used for quantitative spectroscopy of a large number of stars, and the observational applications that are described in Chapters 2 and 3 are based on traditional 1D models (Gustafsson et al., 2008). Section 4 explores 3D line formation for the specific case of the Sun.

A traditional 1D model is characterised by a set of stellar parameters:

- the effective temperature, T_{eff} , which gives an indication of the typical temperatures in the photospheric layers from which the bulk of the radiation is emitted. It is related to the total flux, F , emitted by the star via Stefan-Boltzmann's law of black-body radiation, $F = \sigma T_{\text{eff}}^4$.

- the (logarithmic) surface gravity, $\log(g)$, where $g = GM/R^2$, M is the mass of the star, R is the stellar radius, and G is Newton's constant of gravity.
- the chemical composition, usually indicated by $[\text{Fe}/\text{H}]$.
- the stellar mass (only for spherically symmetric models).
- the 'microturbulence' ξ_t , which is a parametrised way of accounting for the pressure and thus additional line broadening caused by (small-scale) turbulent gas motions. This velocity parameter is an artifact of the approximate treatment of convection in static 1D models and becomes obsolete with 3D hydro-dynamical simulations.
- a set of additional parameters describing the convective flux, of which the most important is $\alpha = l/H_p$, where l is a characteristic length scale mixed by convection and H_p is the pressure scale height.

In the theoretical investigations of LTE departures for Li and Na that are described in following two chapters we use an extensive grid of 1D models. The effective temperature of the grid ranges from 4000 K to 8000 K, the logarithmic surface gravity from 1.0 to 5.0 (cgs units, g given in $[\text{cm s}^{-2}]$), the metallicity from solar to $[\text{Fe}/\text{H}] = -3.0$, and the microturbulence from 1 to 5 km/s. This parameter space covers metal-rich and metal-poor dwarf and giant stars, mainly of spectral type FGK, and the calculations are thus applicable to stars in all types of Galactic populations (see further Chapter 5).

Note that when discussing different depths in the photosphere, it is common to use the optical depth, τ , at 500 nm as the reference scale, rather than the geometrical distance. The continuum radiation emitted at this reference wavelength has its largest contribution from a depth where $\tau_{500} = 1$. In solar-type stars, continuum regions at shorter wavelengths typically probe slightly deeper layers and vice versa for longer wavelengths. The flux emitted at wavelengths where spectral lines are located receives part or most contribution (depending on line strength) from shallower depths, i.e. $\tau_{500} < 1$. Also note that all models that are discussed here neglect magnetic fields, and are not reproducing the chromospheric temperature rise.

1.3 LTE analysis

The assumption of LTE in the computation of model atmospheres simplifies the problem dramatically, as all excitation and ionisation fractions of atoms and molecules depend only on the local electron temperature and density in LTE. The task of finding the number densities of different excitation and ionisation stages for a given chemical composition, and thus obtain the monochromatic opacity at each point in the atmosphere, becomes computationally manageable. Further, model atmospheres computed in LTE successfully predict the absolute fluxes of solar-type stars (with the possible exception of the far ultraviolet regime, e.g. Allende Prieto et al. 2003) and the centre-to-limb variation of the continuum intensity (using 3D models, see Pereira et al. 2009b).

In LTE, the relative number populations of different excitation levels of a given species follow the Boltzmann distribution:

$$\frac{N_j}{N_i} = \frac{g_j}{g_i} e^{-\Delta E/kT}, \quad \Delta E = E_j - E_i \quad (1.1)$$

In this expression, g_i , is the statistical weight and E_i the excitation energy of level i . The only atmospheric variable in this equation is thus temperature. Similarly, the relative ionisation fractions are given by the Saha equation:

$$\frac{N_{n+1}}{N_n} = \frac{(2\pi m_e kT)^{3/2}}{N_e h^3} \frac{2u_{n+1}}{u_n} e^{-I/kT} \quad (1.2)$$

Here, N_n is the total number density of a given atom or ion, N_{n+1} is the number density of the next ionisation stage and N_e the electron density. I is the ionisation potential, and $u_n = \sum_i g_i e^{-E_i/kT}$ is the partition function of species n . The other variables have their usual meaning. The ionisation fraction at different depths of the atmosphere is thus dependent both on the surface gravity and the chemical composition through N_e , as well as on the temperature.

Once the level populations of all elements are specified, the radiation transport can be solved for at any given wavelength and a model of the emitted flux from the star can be produced (spectrum synthesis) and compared to the observed spectrum. A simplified approach is to compare the integrated spectral line strengths, the so called equivalent width, defined as:

$$W_\lambda = \int_{line} (1 - F_\lambda/F_c) d\lambda \quad (1.3)$$

F_λ is the wavelength-dependent flux and F_c the continuum flux (the equivalent width can also be defined from the intensity, as in Chapter 4). W_λ is thus measured in units of distance, commonly in pm ($= 10^{-12}$ m) or mÅ ($= 10^{-13}$ m). It is not always appropriate or even possible to compare the equivalent widths of model and observations, especially not in cases where lines are blended (overlapping) with lines from other species.

Weak, single lines have approximate Gaussian shapes and are in general the most suitable for abundance analysis purposes (not considering observational challenges). One of the main reasons is that in this regime, the line strength has the strongest dependence (linear) on the number density of atoms residing in the lower level involved in the bound-bound transition (Fig. 1.2). Depending on the temperature and density structure of the atmosphere, the excitation and ionisation equilibrium changes, and different spectral lines may thus be suitable as abundance indicators for different stars (Sect. 2.3.3).

To compute a synthetic spectrum of a line, given the LTE assumption and the continuous background opacity, one must know the transition probability (oscillator strength f) for the bound-bound radiative transition that is producing the spectral line. In addition, atomic data for line broadening are necessary to determine its width and shape. Broadening of spectral lines is caused by the finite life time of atomic states (natural or radiative broadening) and by perturbations of the energy levels by surrounding neutral particles

(van der Waals-broadening, mainly due to HI) and charged particles (Stark broadening, mainly due to electrons).

1.4 Non-LTE analysis

Modelling that relaxes the assumption of LTE is usually referred to simply as 'non-LTE' or statistical equilibrium (SE), which in practise means that the level populations of all possible excitation and ionisation states for a given element are assumed not to change with time. To obtain the correct level populations, one must know the rates of radiative and collisional transitions between the different states. The main complexity of the problem arises because the rates of radiative excitation and ionisation depend on the radiation field, while the radiative transport through the atmosphere cannot be solved for without explicit knowledge of the level populations. This calls for an iterative procedure, solving simultaneously for the equations of statistical equilibrium (Eq. 1.4) and radiative transfer (Eq. 1.5). Numerical solutions to this problem for multi-level atoms are described in e.g. Mihalas (1978); Rybicki & Hummer (1991); Scharmer & Carlsson (1985).

$$\frac{dN_i}{dt} = \sum_{j \neq i} N_j P_{ji} - N_i \sum_{j \neq i} P_{ij} = 0 \quad (1.4)$$

Here $P_{ij} = R_{ij} + C_{ij}$ is the total transition rate from level i to j , including radiative rates and collisional rates. C_{ij} is simply determined by the collisional cross-section and the frequency of collisions, whereas R_{ij} is dependent on the transition probabilities for photon absorption and emission, as well as on the profile-averaged mean intensity $\bar{J}_{\nu_0}^{\phi} = 1/2 \int_0^{\infty} \int_{-1}^{+1} I_{\nu} \phi(\nu - \nu_0) d\mu d\nu$. In this expression, $\mu = \cos\theta$, where θ is the angle between the ray and the normal direction and ϕ is the normalised line profile. The specific intensity is found through the transport equation in plane-parallel geometry (see e.g. Rutten 2003 for a derivation of this equation):

$$\mu \frac{dI_{\nu}}{d\tau_{\nu}} = S_{\nu} - I_{\nu} \quad (1.5)$$

S_{ν} is the monochromatic source function, which represent the local addition of radiation, as defined from the opacity and emissivity of the gas. In LTE, $S_{\nu} = B_{\nu}$, where B_{ν} is the Planck function, simplifying the problem tremendously. In non-LTE, the source function depends on the relevant level populations of all species contributing opacity at the specific wavelength.

It is beyond the power of current supercomputers to produce full non-LTE model atmospheres for late-type stars, with a self-consistent treatment of the vast number of possible atomic and molecular transitions. Still, efforts have been made in the direction of implementing a non-LTE treatment including at least tens of thousands lines for the most important opacity sources in atmospheric modelling of late-type stars (Hauschildt et al., 1999; Short & Hauschildt, 2003, 2005). Such non-LTE atmospheric modelling has found

that the ultra-violet fluxes as well as the temperatures in the outermost layers may be significantly affected by non-LTE, especially for giant stars.

However, even if a full non-LTE treatment is not yet possible, hybrid techniques can be extremely useful. In abundance analysis of late-type stars, a common assumption is that the element of interest is a 'trace element', i.e. the LTE departures of the level population of the element do not significantly change the atmospheric structure. It is thus possible to establish the statistical equilibrium of this element for a given atmospheric structure and background LTE opacity, and then use the non-LTE level populations in the computation of the synthetic spectrum. Indeed, it is inconsistent to only allow for LTE departures of one element at the time, and it hinges critically on the assumption that the model structure is accurately established with the LTE assumption. The success of such hybrid non-LTE approaches for hydrogen and helium in the computation of model atmospheres for hotter dwarfs of spectral type O and B, may give some confidence of the method (Nieva & Przybilla, 2007). In Chapters 2 and 3 we adopt the trace-element modelling technique for Li I and Na I and show the impact on abundance analysis of these two elements.

In a general simplification, it is true that LTE is a good approximation in dense plasmas, when the collisional rates dominate the radiative rates. In stellar atmospheres, this means that the LTE assumption is most likely to break down in shallow layers, where the density is low. This is another reason why weak spectral lines, formed deep in the photosphere, are to be preferred as abundance indicators. Also note that the level populations of minority atoms or ions can be severely affected by a small perturbation in the overall ionisation equilibrium. Therefore, LTE is usually appropriate for majority species like Li II and Na II (which cannot be used for abundance work, due to the lack of visible spectral lines), but may be a poor approximation for the neutral atoms.

1.4.1 Atomic data

To set up the statistical equilibrium equations for an element requires immensely more atomic data than in the LTE case. To compute the radiative rates, R_{ij} , between all levels i and j of the system, the corresponding oscillator strengths and photo-ionisation cross-sections are needed. In addition, the cross-sections for collisional excitation and ionisation must be known for all relevant colliding species, to obtain C_{ij} . In late-type stars, collisions with free electrons are the most frequent, due to their high thermal speed. However, collisions with neutral hydrogen, which is the most abundant particle, may also be important. Collisions with all other species are in all likelihood too rare to be of any significance.

Experimental data of radiative and collisional transition probabilities do exist, but usually only for strong, key transitions. Theoretical calculations are thus necessary to provide data in sufficient quantities. As discussed in detail for Na in Sect. 2.2, such theoretical methods may be of varying quality. Generally, the largest uncertainties affecting the non-LTE calculations in stellar atmospheres are collisional cross-sections, especially for collisions with hydrogen atoms (e.g. Asplund, 2005). As described in Barklem et al. (2003) and Sect. 2.2.4, recent quantum mechanical calculations of cross-sections for collisions with

hydrogen have significantly improved the situation for Li and Na and reliable model atoms can now be constructed. In our non-LTE study of Na, we have put extra emphasis on assessing how much the remaining uncertainties in collisional rates influence the statistical equilibrium, considering also improved calculations for collisional cross-sections with electrons.

1.4.2 Motivation for new calculations

The non-LTE analyses presented in Chapters 2 and 3 were triggered by our studies of the detailed chemical composition of globular cluster stars (see Chapters 6 and 7). Only by investing time to establish a reliable modelling procedure could we obtain high-precision abundances for Li and Na, with important implications for the formation and evolution of these stellar populations, the physics of stellar interiors, and the primordial nucleosynthesis of Li. Literature searches convinced us for the need of new non-LTE analyses for several reasons.

For Li, existing studies (Carlsson et al., 1994; Pavlenko & Magazzu, 1996; Takeda & Kawanamoto, 2005) did not cover the needed stellar parameter ranges with a dense enough model grid, to ensure reliable interpolation. Second, new quantum mechanical data for collisional cross-sections with neutral hydrogen had previously been implemented only for a handful of stars (Barklem et al., 2003; Asplund et al., 2003). These studies had shown that the level populations of Li I are significantly affected by charge transfer reactions, specifically mutual neutralisation and ion-pair production ($\text{Li}^* + \text{H} \rightleftharpoons \text{Li}^+ + \text{H}^-$), which therefore were implemented in our Li I model atom. Third, the LTE departures are sensitive to the atmospheric structure, and we thus found it important to implement the most up-to-date models in our calculations. For Na, the calculations of new quantum mechanical rates for collisions with both electrons and hydrogen atoms were the main triggers, as their influence on the statistical equilibrium of Na had never been investigated.

We thus computed 1D, non-LTE calculations for neutral Li and Na for a large stellar grid. The given non-LTE abundance corrections can be interpolated to arbitrary stellar-parameter combinations within the covered grid and will thus serve useful for Li and Na abundance analyses with a variety of applications, such as those mentioned in Sect. 2.1 and Sect. 3.1 and described in detail in Chapters 6 and 7. Chapter 4 is of a more exploratory nature, describing a combined 3D, non-LTE investigation of Na I line formation and thereby addressing the shortcomings of 1D modelling. These results that are not directly applicable to globular cluster stars, but are specific to the Sun. We plan to extend our 3D, non-LTE work to cover a larger stellar parameter space in the future.

1.4.3 Non-LTE effects

When calculating the level populations through statistical equilibrium equations, the spectral lines can become stronger or weaker compared to the LTE approximation. As described in Sect. 2.3.1 this depends critically on the departure coefficients, $\beta_x = N_x/N_x^*$, of the upper level (u) and lower (l) level of the transition, where N_x^* is the population found in LTE.

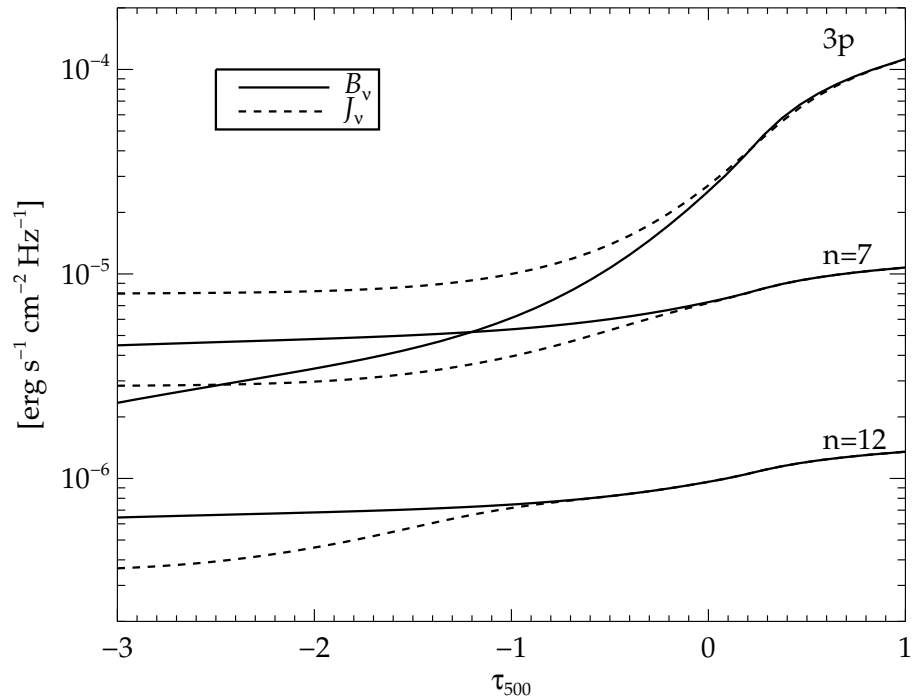


Figure 1.1: The optical depth dependence of the mean radiation field J_ν and the Planck function B_ν for a solar atmospheric model, at wavelengths corresponding to photoionisation thresholds of NaI. These are ~ 408 nm for the first excited state 3p, ~ 4336 nm for the super-level $n = 7$, and ~ 13053 nm for $n = 12$. The ultraviolet wavelengths show strong excess of $J_\nu - B_\nu$, whereas the situation is reversed for the near infra-red regime.

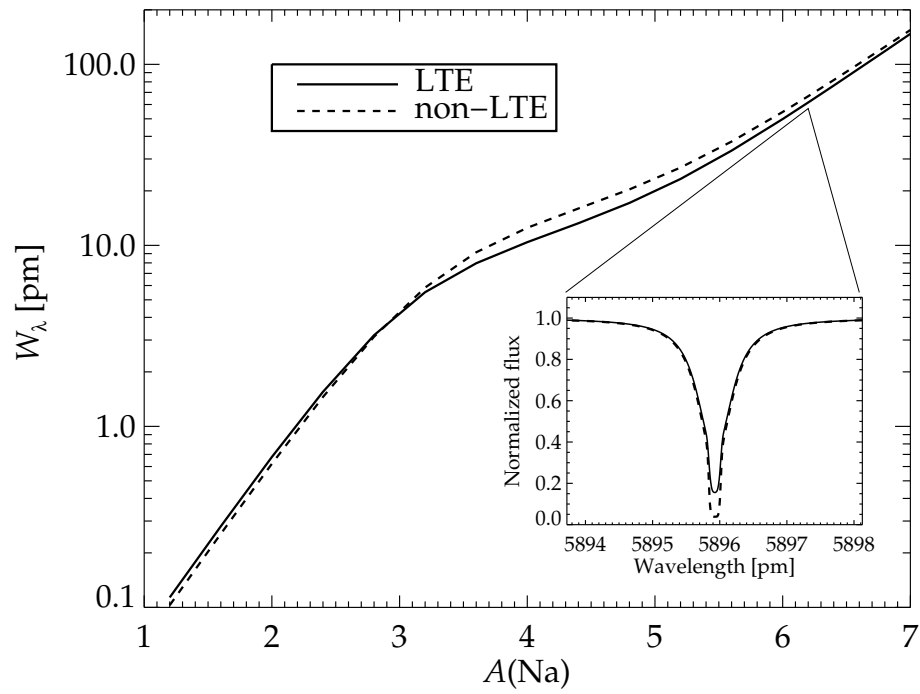


Figure 1.2: The LTE and non-LTE curves-of-growth for one of the Na D lines (589.5 nm) for a solar model. The the corresponding lines profiles at the approximate solar abundance ($A(\text{Na}) = 6.2$) are shown in the inserted graph.

β_l determines the change of line opacity, whereas β_u/β_l determines the change in the line source function compared to LTE. If the departures are such that $\beta_l > 0$ and $\beta_u/\beta_l < 0$, both effects tend to strengthen the spectral line in non-LTE, and vice versa.

In LTE, the ionisation fractions of different ions fulfil the Saha equation (Eq. 1.2), whereas in non-LTE, the ionisation balance is determined by the strength of the radiation field at influential photo-ionisation continua. In general, J_ν is in excess of B_ν in the ultra-violet and part of the optical wavelength regime, whereas the roles are reversed in the near-infra red. As will be described in more detail in the following chapters, the ionisation equilibria of Li and Na are set by the competing effects of over-ionisation (i.e. the photo-ionisation rates are higher than in LTE, due to the $J_\nu - B_\nu$ excess) from the first excited states, whose photo-ionisation thresholds lie in the ultra-violet, and over-recombination to higher excited states. This is illustrated in Fig. 1.1. The strength of J_ν is model dependent, especially on the atmospheric temperature gradient, such that the ionisation equilibrium is somewhat shifted over the grid.

In addition to the perturbed ionisation balance, the radiation fields in the spectral lines themselves influence the statistical equilibrium in non-LTE. This connection is especially clear for the resonance line transitions of Li I (2s-2p) and Na I (3s-3p), whose source functions behave similarly to a two-level atom (this is also a good approximation for the strongest subordinate transitions, Li I 2p-3d and Na I 3p-3d). In particular, the line source functions are set directly by the profile-averaged mean intensity $\bar{J}_{\nu_0}^\phi$ (see further Sect. 2.3.1). As a result, the size of the LTE departures are very much dependent on the strengths of the lines themselves.

Clearly, the non-LTE modelling procedure has a much greater complexity and the results depend on the accuracy of atomic data for a large number of transitions. However, one must bear in mind that the LTE result is recovered in the strong-collision limit and is thus only an extreme version of non-LTE. The LTE assumption inevitably leads to a systematic bias, be it small or large, that we should strive to investigate for all species. As an example, Fig. 1.2 illustrates the different curves-of-growth, i.e. line strength as a function of total elemental abundance, established with LTE and non-LTE modelling of the Na I line at 589.5 nm in the Sun.

Chapter 2

Non-LTE calculations for neutral Na using improved atomic data

The following chapter contains a slightly modified version of an article that was submitted to *Astronomy & Astrophysics* in September 2010 (Lind, Asplund, Barklem, & Belyaev).

2.1 Astrophysical motivation

Sodium has established itself as an important tracer of Galactic chemical evolution and numerous investigations of the Na abundances of late-type stars, residing in different regions of the Galaxy, have been conducted (see e.g. Takeda et al., 2003; Gehren et al., 2006; Andrievsky et al., 2007, and Chapter 7). Na is mainly synthesised during hydrostatic carbon burning in massive stars, in the reaction $^{12}\text{C}(^{12}\text{C},\text{p})^{23}\text{Na}$. As pointed out by Woosley & Weaver (1995), the production is dependent on the available neutron excess through secondary reactions, which implies metal-dependent yields. In addition, there is a production channel via proton capture reactions, $^{22}\text{Ne}(\text{p},\gamma)^{23}\text{Na}$ (Denisenkov & Denisenkova, 1990). The latter, so called NeNa-cycle, occurs when temperatures are high enough for H-burning through the CNO-cycle, e.g. in the cores or H-burning shells of inter-mediate mass and massive stars.

Abundance studies of late-type stars in the thin disk show an increase from solar to positive [Na/Fe] ratios at super-solar metallicities, while thin and thick disk stars slightly below solar metallicities rather form a decreasing trend (Edvardsson et al., 1993; Reddy et al., 2003; Bensby et al., 2003; Shi et al., 2004). Relying exclusively on weak lines for the analysis, LTE has been proved a reasonable approximation in this metallicity regime. For metal-poor stars the situation is different, especially in cases where the strong Na I D resonance lines at 588.9/589.5 nm are the only available abundance indicators. As shown by Takeda et al. (2003) and Gehren et al. (2006), [Na/Fe] ratios are slightly sub-solar ($-0.1\dots -0.5$) in metal-poor stars in the thick disk and the halo, in the metallicity range $[\text{Fe}/\text{H}] = -3.0\dots -1.0$. This deficiency is only recovered through non-LTE analysis, since

LTE investigations tend to overestimate the abundances, sometimes by more than 0.5 dex (see Sect. 2.3.1). Further, almost solar values result from non-LTE analysis of extremely metal-poor stars below $[\text{Fe}/\text{H}] < -3.0$, where LTE analysis at least of giants rather results in positive ratios (Cayrel et al., 2004; Andrievsky et al., 2007). Finally, Nissen & Schuster (2010) found evidence for systematic Na abundance differences of order 0.2 dex between α -poor and α -rich halo stars, with important implications for the presumably separate origin of these two Galactic components. To place all Galactic stellar populations on an absolute Na abundance scale to the same and better precision, non-LTE is clearly required.

In globular clusters, Na is of particular interest, since the large over-abundances of this element, compared to field stars of similar metallicities, imply a chemical evolution scenario that is specific to these dense stellar systems (see further Chapter 7). By detailed mapping of the Na abundance and its correlating behaviour with similar-mass and lighter elements we may distinguish between stars formed in different formation episodes in globular clusters and eventually identify the elusive self-enrichment process that so efficiently polluted the star-forming gas with the nucleosynthesis products of hot H-burning through the CNO-cycle and the related NeNa- and MgAl-chains (i.e. enhancement of N, Na, and Al, and depletion of C, O, and Mg, see e.g. Carretta et al. 2009a and Chapter 7).

2.2 Non-LTE modelling procedure

We use the code MULTI, version 2.3 (Carlsson, 1986, 1992) to solve simultaneously the statistical equilibrium and radiative transfer problems in a plane-parallel stellar atmosphere. Na is considered a trace element, neglecting feedback effects from changes in its level populations on the atmospheric structure. The LTE assumption is used for all other species in the computation of background continuum and line opacity. A simultaneously computed line-blanketed radiation field is thus used in the calculation of photo-ionisation rates.

The modelling procedure and model atmosphere grid are the same as described in Lind et al. (2009a). A grid of ~ 400 1D, LTE, opacity-sampling, MARCS model atmospheres (Gustafsson et al., 2008) is used in the analysis. The models span $T_{\text{eff}} = 4000\text{--}8000$ K, $\log g = 1.0\text{--}5.0$, $[\text{Fe}/\text{H}] = 0.0\text{--}-3.0$. Sodium abundances vary from $[\text{Na}/\text{Fe}] = -2\text{--}2$, in steps of 0.2 dex. The highest effective temperature is 5500 K for models with $\log g = 1.0$, 6500 K for $\log g = 2.0$, 7500 K for $\log g = 3.0$, and 8000 K for $\log g \geq 4.0$. For models with $\log g \geq 3.0$, we adopted a microturbulence parameter $\xi_t = 1.0 \text{ km s}^{-1}$ and $\xi_t = 2.0 \text{ km s}^{-1}$, and for models with $\log g \leq 3.0$, we adopted $\xi_t = 2.0 \text{ km s}^{-1}$ and $\xi_t = 5.0 \text{ km s}^{-1}$. All models have standard composition, i.e. with scaled solar abundances according to Grevesse et al. (2007), plus 0.4 dex enhancement of alpha-elements in all metal-poor models ($[\text{Fe}/\text{H}] \leq -1.0$).

We define a non-LTE correction for each abundance point as the difference between the LTE sodium abundance and the non-LTE abundance that corresponds to the same equivalent width. Corrections are given for equivalent widths in the range 0.01 – 100 pm. The equivalent width is obtained by numerical integration over the line profile, considering

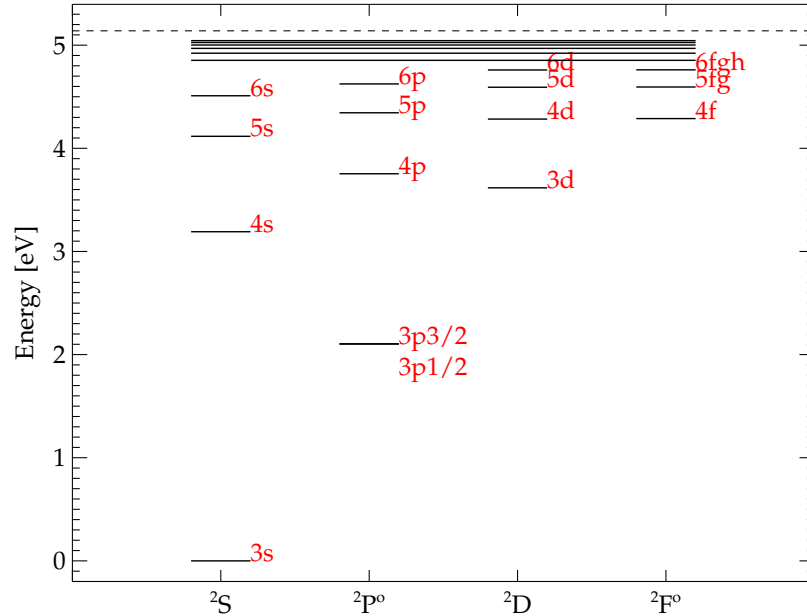


Figure 2.1: Schematic term diagram of the 23-level Na I model atom. The dashed line marks the ground state of Na II. The highest level considered in Na I is $n = 12$.

a spectral region that extends $\pm(0.3 - 3)$ nm from the line centre, depending on the typical line strength.

2.2.1 Structure of the model atom

The model atom we have constructed for Na consists of 22 energy levels of Na I, plus the Na II continuum (see Fig. 2.1). The energy levels are coupled via radiative transitions and via collisional transitions with electrons and neutral hydrogen. Experimentally measured energies are taken from the recent compilation by Sansonetti (2008) (for highly excited states isoelectronic fitting is used). Since we are not concerned with modelling the detailed structure of highly excited levels, we have collapsed all sub-levels for $n = 7 - 12$ into super-levels. The fine-structure components of the 3p level are accounted for in the statistical equilibrium calculations, by treating 3p_{1/2} and 3p_{3/2} as separate, collisionally coupled levels¹. In addition, the fine-structure components of the 3p–3d and 3p–4d transitions, as well as the hyper-fine structure components of the 3s–3p_{1/2} and 3s–3p_{3/2} transitions, are accounted for by computing the line profile as a linear combination of the sub-components

¹Accounting for the fine-structure of the 3p level simplifies the numerical procedure, while also predicting correct line formation depths for the individual lines Mashonkina et al. (e.g. 2000).

(see Table 2.1).

The collisional transition probabilities have been computed for the 3p level, not for its fine-structure components. To calculate these we assume that the ionisation and excitation rates of the sub-levels are equal to that of the collapsed level. We further assume that the de-excitation rates to 3s scale with the statistical weights, i.e. the de-excitation rate from 3p3/2 is twice as large as from 3p1/2, and the sum of the rates is equal to that of the collapsed level. The collisional cross-section for electron impact excitation between the two fine-structure levels has been estimated with Seaton's impact parameter method (Seaton, 1962). We note that the detailed rates are not important for the non-LTE problem.

2.2.2 Radiative transitions

In total, 166 allowed bound-bound radiative transitions are included, adopting where possible oscillator strengths from the *ab initio* calculations of C. Froese Fischer². For most remaining transitions, we use the calculated transition probabilities by K.T. Taylor, as part of the Opacity Project³. The two sets of f -values are typically within 3% agreement, for the strongest, most important transitions. For the Na I D lines, accurate experimental data exist, and we adopt the values listed in the NIST data base⁴ (see Table 2.1).

Photo-ionisation cross-sections for levels with $l \leq 4$ are drawn from the TOP base (computations by K. T. Taylor). For the highly excited collapsed levels we adopt hydrogenic cross-sections.

2.2.3 Electron collisions

Cross-sections for collisional excitation by electrons can be estimated using general semi-classical recipes such as the Born approximation, which is, however, known to overestimate the cross-sections at low impact energies Park (e.g. 1971). Those near-threshold energies are most relevant for stellar atmospheres, hosting electrons with typical kinetic energies of order 1 eV. Seaton (1962) tried to rectify the Born cross-sections by modifying the transition probability for low impact parameters, thus accounting for strong coupling between states, which was previously neglected (the so called impact parameter approximation). Another approach is to empirically adjust the Born rates, to reach better agreement with experimental data, which has been done by van Regemorter (1962) and Park (1971). In the absence of alternatives, non-LTE applications have long had to rely almost exclusively on such simple semi-empirical formulae.

Nowadays, much more rigorous quantum mechanical calculations can be performed for simple atoms like Na. Igenbergs et al. (2008) presented new convergent close-coupling (CCC) calculations for excitation and ionisation of neutral Na by electron impact, giving good agreement with experimental data when available (e.g. with the measurements by

²Multi-configuration Hartree-Fock computations (MCHF). http://www.vuse.vanderbilt.edu/~cff/mchf_collection/

³TOP base, <http://legacy.gsfc.nasa.gov/topbase>

⁴<http://physics.nist.gov/PhysRefData/ASD/index.html>

Table 2.1: Line data for the ten Na I lines considered in the detailed spectrum synthesis.

nl-n'l'	λ [nm]	$^{(a)}\Delta E$ [cm $^{-1}$]	J	J'	F	F'	f	$^{(b)}\Gamma$ [rad s $^{-1}$]	$^{(c)}\sigma$ [a.u.]	$^{(d)}\alpha$	$\log C_4$
3s-3p	589.6	-0.033	1/2	1/2	1	1	2.67×10^{-2}	6.14×10^7	407	0.237	-15.11
		-0.039	1/2	1/2	1	2	1.33×10^{-1}				
		0.026	1/2	1/2	2	1	8.00×10^{-2}				
		0.020	1/2	1/2	2	2	8.00×10^{-2}				
3s-3p	589.0	-0.036	1/2	3/2	1	0,1,2	3.21×10^{-1}	6.16×10^7	407	0.237	-15.11
		0.022	1/2	3/2	2	1,2,3	3.21×10^{-1}				
3p-3d	818.3		1/2	3/2			8.63×10^{-1}	1.13×10^8	804	0.270	-13.76
3p-3d	819.5	-0.020	3/2	3/2			8.63×10^{-2}	1.13×10^8	804	0.270	-13.76
		0.030	3/2	5/2			7.77×10^{-1}				
3p-4d	568.3		1/2	3/2			9.82×10^{-2}	8.05×10^7	1955	0.327	-12.18
3p-4d	568.8	-0.014	3/2	3/2			9.82×10^{-3}	8.07×10^7	1955	0.327	-12.18
		0.021	3/2	5/2			8.84×10^{-2}				
3p-5s	615.4		1/2	1/2			1.42×10^{-2}	7.43×10^7	-	-	-13.20
3p-5s	616.1		3/2	1/2			1.42×10^{-2}	7.45×10^7	-	-	-13.20
3p-6s	514.8		1/2	1/2			4.52×10^{-3}	6.81×10^7	-	-	-12.55
4s-5p	1074.6		1/2	3/2			2.54×10^{-2}	2.91×10^7	-	-	-12.64

^(a) ΔE is the difference in energy between the given sub-component and the average energy gap bridged by the transition. The energy separations of the hyperfine components of 3s-3p are taken from Sydoryk et al. (2008)

^(b) Γ is the natural broadening width (FWHM).

^(c) σ is the broadening cross-section for collisions with neutral hydrogen at relative velocity $v = 10^4 \text{ m s}^{-1}$.

^(d) α is the velocity dependence of σ .

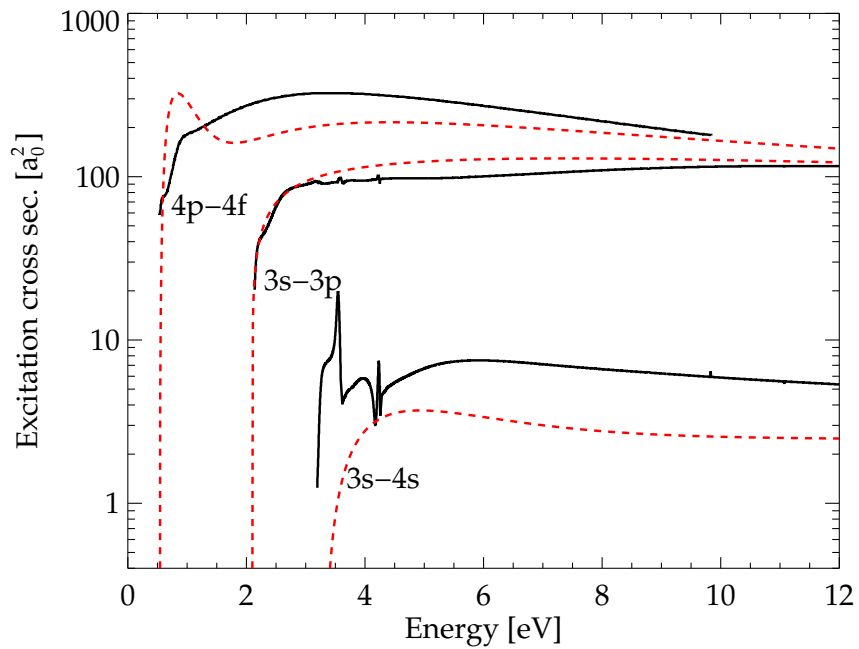


Figure 2.2: Three sample excitation cross-sections for collisions between Na I and electrons. The black solid lines represent R-matrix calculations (Gao et al., 2010; Feautrier et al., in preparation) and the red dashed lines represent the analytical fitting functions derived by Igenbergs et al. (2008). The transitions are marked with labels next to the energy thresholds.

Phelps & Lin 1981). Even more rigorous are the R-matrix calculations by Gao et al. (2010), which are able to recover the detailed resonant structures of the cross-sections at threshold impact energies (< 5 eV). Here, we have adopted cross-sections calculated with the R-matrix method, in a manner identical to that described in Gao et al. but extended to include seven real spectroscopic states of Na I (3s, 3p, 4s, 3d, 4p, 4d, and 4f) and four polarized pseudo-orbitals to take into account the polarization effects between the scattered electron and the target electrons (see Feautrier et al., in preparation). The calculations were performed for impact energies in the range 0–14 eV. Fig. 2.2 compares the cross-sections obtained for some sample transitions with the R-matrix method and the analytical fitting functions by Igenbergs et al. (2008). The two methods agree very well; the typical difference between calculated rate coefficients in the temperature regime 2000 – 20000 K is only a factor of two, although individual rates could differ by up to a factor of ten.

For more highly excited states of Na I, quantum mechanical data are lacking and we are still dependent on the semi-classical formulae. However, the empirically adjusted rates by Park (1971) perform surprisingly well in comparison with the newer data, with half of the transitions at 6000 K agreeing within a factor of three and 90% of the transitions agreeing to within a factor of ten. We adopt these for transitions involving levels above 5s.

Cross-sections for ionisation by electron impact have also been calculated with the CCC method up to 5s by Igenbergs et al. (2008), and compare well with existing experimental data for the ground and first excited state. For ionisation from more highly excited levels, we rely on the general recipe given in Allen (2000). Also, to bridge the small energy gap between the ionisation edge and the minimum energy for which the analytical fits to the ionisation cross-sections are valid (see Table 2 in Igenbergs et al. 2008), we assume that the cross-sections for all levels are given by the general recipe (Allen, 2000) at the edge.

In Sect. 2.3.2 we evaluate the influence from uncertainties in collisional rates on the statistical equilibrium of Na I by multiplying and dividing all electron collisional rates by a factor of two, which given the present data may be indicative of the true uncertainty.

2.2.4 Hydrogen collisions

Neutral hydrogen atoms are the most abundant atomic species in late-type stellar atmospheres. Still, collisional cross-sections between hydrogen and other atoms are notorious sources of uncertainty for non-LTE applications, and some empirical calibration of the classical recipe by Drawin (1968) is usually the only option, using a general rate scaling factor S_H . Again, the situation for Na is today much better in this respect.

Barklem et al. (2010) presented for the first time quantum mechanical rates for a large number of bound-bound transitions in Na I, due to collisions with neutral hydrogen, as well as charge transfer reactions between sodium and hydrogen ($\text{Na}^* + \text{H} \rightleftharpoons \text{Na}^+ + \text{H}^-$). We use the rates given in Barklem et al. (2010) involving all levels and all possible transitions below the ionic limit, i.e. up to 5p (for levels above the ionic limit, there is no possibility for charge exchange to take place). The bound-bound rates for allowed transitions are smaller than what is found with the commonly used classical recipe by Drawin by one to

six orders of magnitude, depending on the transition (see Fig. 2.3). The Drawin recipe cannot be applied to forbidden bound-bound transitions, ionisation or charge exchange, unless an arbitrary radiative transition probability is applied.

We estimate the bound-bound collisional rates for transitions between highly excited levels with the free electron model described by Kaulakys (1991), applicable for Rydberg atoms (Eq. 18 in Kaulakys, using non-hydrogenic wave-functions in momentum space calculated using the methods of Hoang Binh & Van Regemorter 1997). Fig. 2.3 compares the rate coefficients found by Barklem et al. (2010) to those given by the Drawin recipe for transitions between low excited states, and also compares the rates by Kaulakys and Drawin for transitions between highly excited states. It is easily appreciated from these figures that no single scaling factor can be applied to the Drawin recipe to reproduce either the quantum mechanical rates or the Kaulakys rates.

Barklem et al. (2010) also provide estimates of the rate uncertainty, so called fluctuation factors, from different sources of input chemical data (potentials and couplings). In Sect. 2.3.2 the effect on the non-LTE calculations when multiplying all quantum mechanical rates by the maximum fluctuation factors or by the suggested minimum value (0.5), is discussed.

2.2.5 Line broadening

For line broadening due to collisions with neutral hydrogen, we use the ABO theory by Anstee & O’Mara (1995); Barklem & O’Mara (1997) whenever applicable, and otherwise adopt the C_6 constant for van der Waals-broadening by Unsöld (1955). The latter are enhanced by a factor of 2 ($\Delta \log C_6 \approx 0.8$), which is typically required to match the observed line profiles in the Sun (e.g. Mashonkina et al. 2000). Stark broadening constants (C_4) are estimated from the tables of Dimitrijević & Sahal-Bréchet (1985, 1990). The line data are summarised in Table 2.1 for the ten principally considered transitions.

2.3 Discussion

2.3.1 Departures from LTE

There is a great regularity in the statistical equilibrium of Na over the whole stellar grid covered by our analysis. As we will describe below, the non-LTE abundance corrections are much dependent on the line strength and much of the model dependence can thus be easily understood through the variation of the excitation and ionisation equilibrium with temperature and density.

To describe the non-LTE line formation of Na lines, we define the departure coefficient $\beta_x = N_x/N_x^*$, representing the population of a certain level x in non-LTE, divided by the corresponding population in LTE. Given a specific background continuum opacity, the strength and shape of a spectral line are determined by the line opacity, proportional to the population of the lower level of the transition, and the source function S_ν , proportional

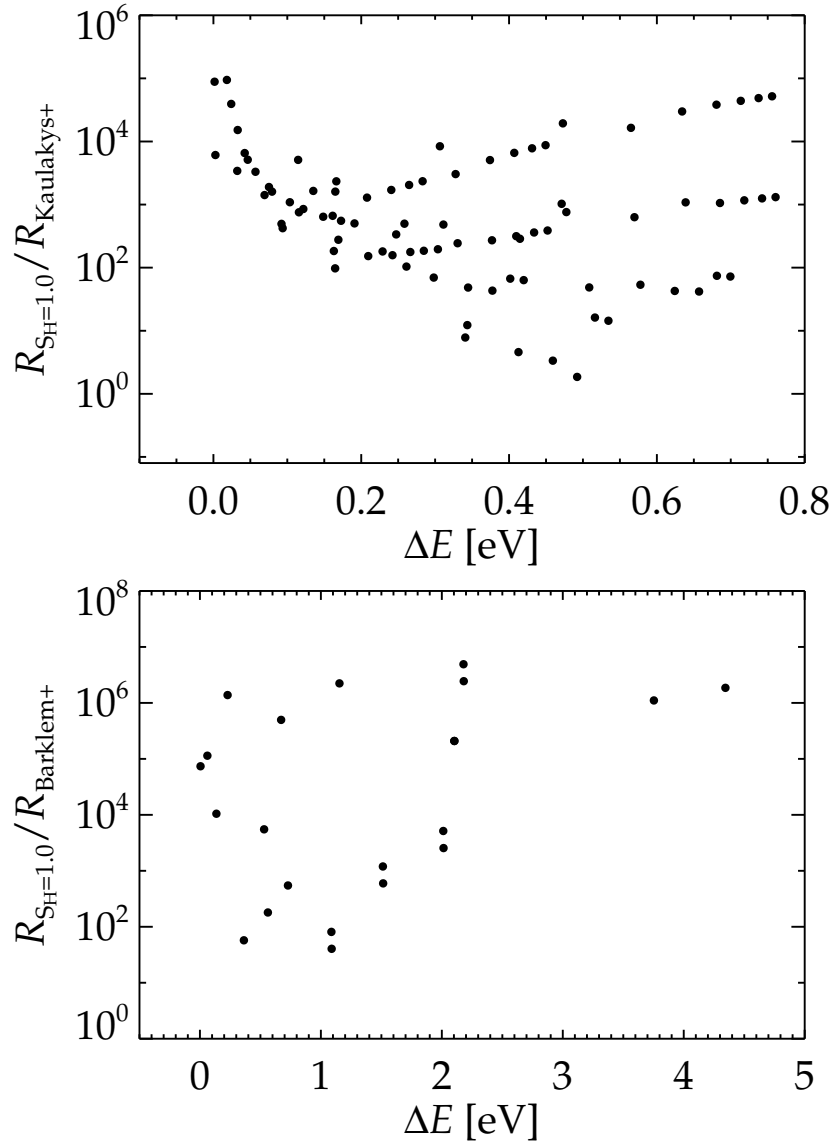


Figure 2.3: Comparison between rate coefficients at $T = 6000$ K for collisional excitation of Na I by neutral hydrogen atoms. Only optically allowed transitions are shown with the x-axis representing the energy of the transition. *Top*: The ratio between the unscaled Drawin formula and the free electron model of Kaulakys (1991) for transitions between highly excited states. *Bottom*: The ratio between the unscaled Drawin formula and the quantum mechanical calculations by Barklem et al. (2010) for transitions between levels up to 5s.

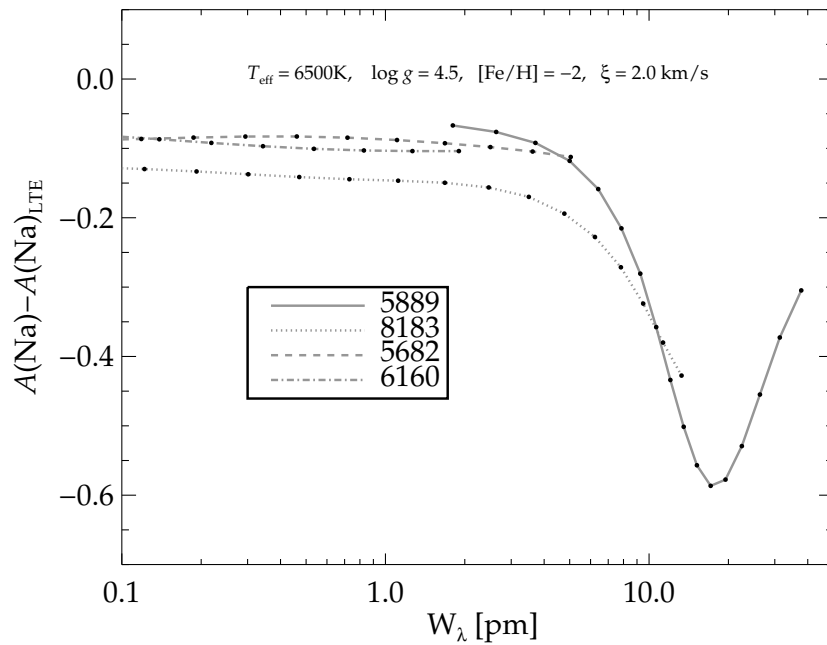


Figure 2.4: Non-LTE abundance corrections as functions of equivalent widths of selected Na I lines for a model with $T_{\text{eff}} = 6500 \text{ K}$, $\log g = 4.5$, $[\text{Fe}/\text{H}] = -2$, and $\xi_t = 2.0 \text{ km/s}$. The leftmost value of each line (this point falls outside of the plot for all lines except the solid) corresponds to $[\text{Na}/\text{Fe}] = -1.6$, and the rightmost to $[\text{Na}/\text{Fe}] = +1.6$.

to the population ratio between the upper and lower level⁵. Lifting the assumption of LTE, both the line formation depth and source function may change and thus alter the strength and shape of the spectral line.

The strong Na I D doublet lines at 588.9/589.5 nm are commonly used in abundance studies of metal-poor stars. In fact, in certain cases (warm, metal-poor dwarfs) they are the only lines that are sufficiently strong. The doublet originates from the resonance line transition between the ground state (3s) and the two fine structure components of the first excited state (3p_{1/2} and 3p_{3/2}). As a general rule, the line source function resembles perfectly that of a pure scattering line in a two-level atom, i.e. to a very good approximation $S_l = \bar{J}_\phi$ at all depths, where \bar{J}_ϕ is the profile-averaged mean intensity. This merely reflects the fact that for these lines, the photon absorption and emission rates strongly dominate the collisional rates and all interactions with other levels, including the continuum. Although in principle, for a two-level atom, $S_l = (1 - \epsilon_\nu)\bar{J}_\phi + \epsilon_\nu B_\nu$, the probability for true absorption, ϵ_ν , is very close to zero at shallow depths where \bar{J}_ϕ departs from B_ν , so the approximation of a pure scattering line holds at all depths.

The ratio between the population of the upper and lower level is therefore always set by the mean intensity, and, for a specific line strength, this is correctly established with a simple two-level atom. However, the actual population of the ground level, which governs the line opacity and typical formation depth of the line, is underestimated when more highly excited levels of Na I are neglected. As described by Bruls et al. (1992), a number of high excitation levels and a ladder of high-probability transitions connecting these with lower excitation levels, must be established to obtain the correct populations. This is needed because the first and second excited state have photo-ionisation thresholds in the ultra-violet, where the radiation field exceeds the Planck function ($J_\nu > B_\nu$), pushing the ionisation balance to over-ionisation of Na I. The situation is reversed for more highly excited levels since their photo-ionisation thresholds lie in the near infra-red regime, where the radiation field rather is sub-thermal (see Fig. 1.1). This ionisation/recombination picture has been described previously by Takeda et al. (2003) and Mashonkina et al. (2000).

We can now qualitatively understand the non-LTE formation, starting with the Na I resonance lines. When either line is weak, it will obviously have small influence on its own radiation field. Therefore, $J_\nu - B_\nu > 0$, as is the case for neighbouring continuum regions. This is governed by the temperature gradient, which determines how rapidly B_ν decreases with optical depth. At these wavelengths, the gradient is steep enough to produce a $J_\nu - B_\nu$ excess and, consequently, a line source function that is stronger than in LTE ($\beta_u/\beta_l > 1$). This tends to weaken the resonance lines compared to LTE. On the other hand, the ionisation balance of Na I is always shifted to over-recombination in the line-forming regions. The ground state of Na I is thus over-populated compared to LTE ($\beta_l > 1$) and the combined effect is a moderate line strengthening. The resulting abundance corrections for the resonance lines are always minor, $|\Delta A| < 0.1$ dex at line strengths below 5 pm. However, the lines are only this weak in extremely metal-poor stars.

As the line strength increases towards saturation in any given model, J_ν drops, and

⁵Neglecting stimulated emission, the line source function S_l is directly given by $S_l/B_\nu = \beta_u/\beta_l$

the line source function becomes weaker than in LTE. This is naturally accompanied by a decrease in the excitation rate. Also the ionisation rates drop with increasing abundance as the photo-ionising radiation field weakens. This allows recombination from the Na II reservoir, and all levels of Na I are increasingly over-populated. The combination of larger line opacity and a weaker source function produce significant line strengthening in non-LTE, with negative abundance corrections as a result. This behaviour is illustrated in Fig. 2.4 for a metal-poor dwarf. We note that even if the statistical equilibrium is not necessarily pushed further from LTE, the abundance corrections become larger and larger as the line saturates, simply because the abundance sensitivity to equivalent width is small in this regime. With further strengthening, the line enters onto the damping part of the curve-of-growth with the development of broad wings. Since photons from a wider frequency range then are able to excite the atoms, the excitation rate actually increases again, lessening the over-population in deep layers. The abundance sensitivity to line strength also starts to increase again, so the abundance corrections, as we define them here, reach a minimum value when the line is fully saturated (see Fig. 2.4) and then become less negative with higher abundance, although such strong lines are hardly suitable for accurate abundance analysis through equivalent width measurements. Line profile analysis especially of the wings is more appropriate, but that is not addressed here.

Even if the two-level approximation holds true only for the resonance lines, the subordinate transitions (with 3p as lower level), show a very similar behaviour. At low line strength each line has a 'plateau' of close-to-constant, small abundance corrections, becoming increasingly negative as the line saturates around 20 pm. This general behaviour with line strength has been discovered previously e.g. by Takeda et al. 2003. The strongest subordinate transitions, 3p–3d at 818.3/819.4 nm, follow an almost identical behaviour as the resonance lines, but are offset to more negative corrections. The latter is due to the shallower temperature gradient with continuum optical depth in the near infra-red wavelengths, producing a $J_\nu - B_\nu$ deficiency in the line, and a source function that is weaker than in LTE also when the lines are very weak.

Naturally, the abundance corrections at a given line strength are still somewhat model dependent. For saturated lines, the corrections are more negative for hotter models, and models with lower surface gravity, whereas the metallicity dependence seems almost negligible. Fully un-saturated lines (below 5 pm) almost always have corrections in the range $-0.1... - 0.2$ dex.

As a curiosity, we note the very close resemblance in the non-LTE line formation of sodium and the lighter alkali atom lithium, whose departures from LTE have been described e.g by Lind et al. (2009a) and Carlsson et al. (1994). There are many striking similarities between the two elements, especially in the shape of the abundance correction curves. Differences mainly arise from the higher degree of over-ionisation of Li, which in turn is a direct result of the larger photo-ionisation rate from the first excited state of Li I (2p), compared to Na I (3p). The abundance corrections at low line strengths thus tend to be somewhat higher, even positive, for Li (over-ionisation causes under-population of Li I, thus weakening the spectral lines).

2.3.2 The influence of collisions

As described in Sect. 2.2.3 and 2.2.4, the statistical equilibrium of NaI is calculated by accounting for collisional excitation and ionisation by electrons and hydrogen atoms. We now discuss the impact on the derived abundance corrections by varying the strength of collisional rates.

When multiplying/dividing all rates for collisional excitation and ionisation by electrons by a factor of two, the solar equivalent widths of NaI lines change systematically by typically 1%. This propagates to less than ~ 0.01 dex in terms of non-LTE abundance corrections and is thus not much of concern. Somewhat larger impact is seen for hotter, higher surface gravity models, where electrons are more abundant. Still, the non-LTE equivalent widths calculated for a $T_{\text{eff}} = 8000$ K, $\log(g) = 5.0$, solar metallicity model are affected by only 2–4%, corresponding to approximately 0.02 dex for relevant lines. Giants and cooler dwarfs are less sensitive, having lower densities of the colliding free electrons. The non-LTE calculations thus seem robust with respect to input atomic data for collisions with electrons.

The quantum mechanical calculations by Barklem et al. (2010) result in rate coefficients for collisional excitation by hydrogen atoms that are lower than the commonly used classical Drawin recipe, by one to six orders of magnitude. The new rates thus have very small influence on the statistical equilibrium of NaI, in the stellar parameter range that we consider here. However, again analogously to Li, charge exchange reactions turn out to be much more influential. Fig. 2.6 illustrates how the departure coefficients of low excited levels change for a solar model, when including and neglecting collisions with neutral hydrogen.

It is conceptually correct to say that higher collisional rates have a thermalising effect, i.e. tend to drive the level population towards LTE. However, as seen for the Sun in Fig. 2.6, this is not generally true for all levels. The populations of the ground state and first excited states are rather pushed further from LTE in shallow atmospheric layers, when charge exchange is included. This seemingly contradictory behaviour can be understood by realising that the collisional cross-sections of 3s and 3p are very small, and the changes in their level population are rather a secondary effect, stemming from the thermalisation of higher excited levels. Especially, 4s, whose departure coefficients are also displayed in Fig. 2.6, has a large cross-section for charge exchange and the level becomes almost thermalised with the inclusion of this process. In deep layers, where $\beta_{4s} > 1$, the over-recombination of NaI is lessened, decreasing the over-population of the level itself, but also lower excited levels. In shallow layers, where $\beta_{4s} < 1$, recombination is enhanced, lessening the under-population of 4s, but increasing further the over-population of lower levels. In practise, also excited levels higher than 4s influence the outcome, but to a smaller extent.

Even if the statistical equilibrium is indeed influenced by hydrogen collisions, the strengths of the emergent spectral lines need not necessarily be so. This is due to the fact that the source functions remain unchanged, and as discussed above, the effect on the level populations of 3s and 3p is opposite in different regimes of the atmosphere, so that the net effect on the line strength is small. The situation is a bit different from that

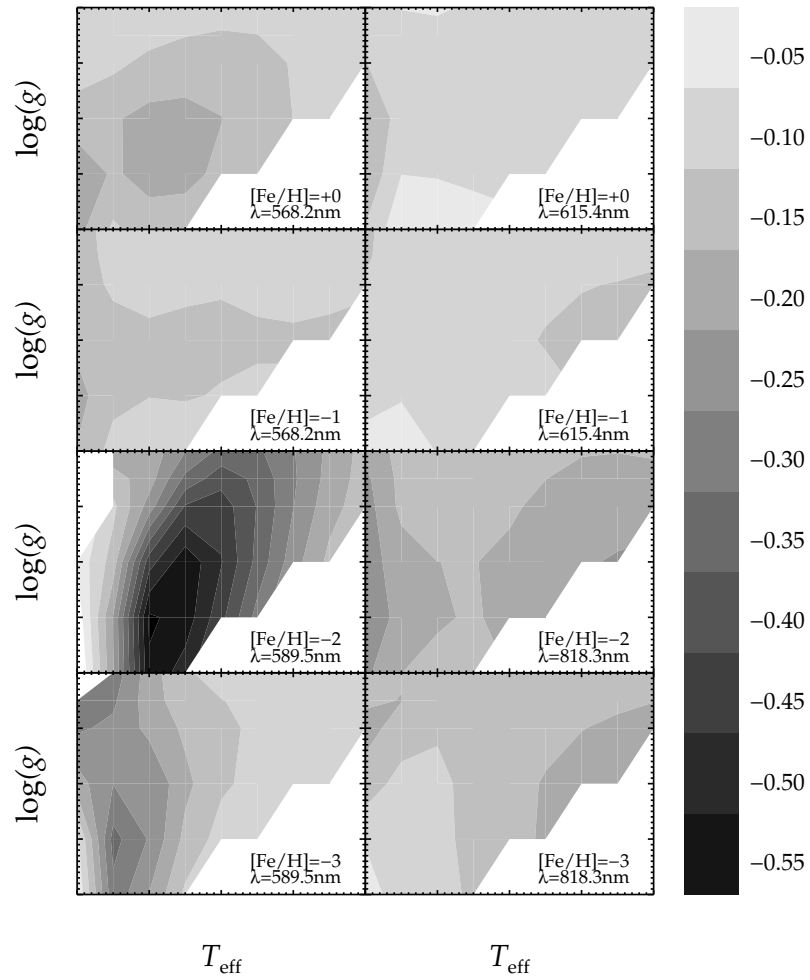


Figure 2.5: Contour diagrams illustrating how the abundance corrections vary with effective temperature and surface gravity, for four lines commonly analysed lines of Na I. Only the results for $\xi = 2$ km/s and $[\text{Na}/\text{Fe}] = 0$ are shown.

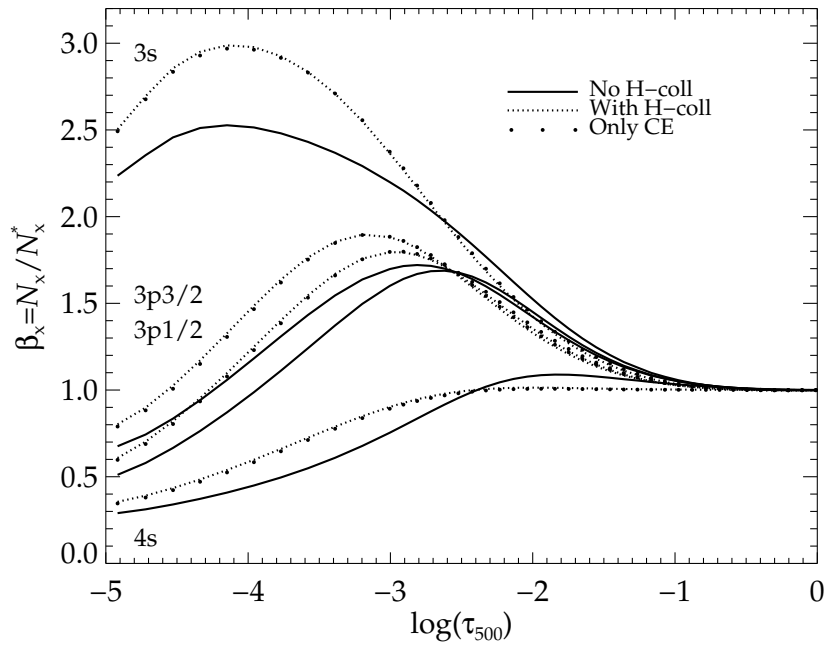


Figure 2.6: Departure coefficients for a solar model, for the Na I levels indicated with labels in the plot. *Solid*: neglecting collisions with neutral hydrogen. *Dotted*: including charge exchange reactions and bound-bound collisional excitation by neutral hydrogen. *Bullets*: including only charge transfer reactions.

of Li, for which charge exchange reactions always lead to more recombination throughout the atmosphere, with significant line strengthening as a result (Barklem et al., 2003; Lind et al., 2009a).

Charge exchange is most important in cool, high surface gravity models, for which abundance corrections are affected by up to ~ 0.2 dex, whereas the effect in solar-type stars is only ~ 0.01 dex. This is a direct reflection of the ionisation equilibrium of hydrogen, as H^- is abundant in cool, dense atmospheres. We have therefore tested how the uncertainty in collisional rates affects the abundance corrections for the extreme case of a $T_{\text{eff}} = 4000$ K, $\log g = 5.0$ model. When multiplying all rates with their maximum fluctuation factors (see Sect. 2.2.4), the abundance corrections vary with typically 0.04 dex for such a model. For the Sun, the corresponding variation is < 0.01 dex, i.e. essentially irrelevant for practical purposes.

2.3.3 Consequences for stellar abundance analysis

Obviously, it is always preferable to base the abundance analysis through equivalent width measurements on un-saturated spectral lines, not least since non-LTE abundance corrections for fully saturated lines may reach -1 dex in extreme cases. This means that the resonance lines should be used only as a last resort for metal-poor stars ($[\text{Fe}/\text{H}] < -3.0$), when the near infra-red doublet lines are not detectable or too severely blended with telluric lines. At metallicities in the range $[\text{Fe}/\text{H}] = -2.0 \dots -1.0$, the 568.2/568.8 nm doublet lines are usually to be preferred, whereas the 615.4/616.0 are good indicators for solar metallicity stars. Given the estimated uncertainties in collisional data, the non-LTE modelling give abundances for weak lines that normally can be trusted to high precision.

Fig. 2.7 compares our inferred corrections to those of Andrievsky et al. (2007), Shi et al. (2004), Takeda et al. (2003) and Mashonkina et al. (2000) for selected models within the grid. Overall, the agreement between the studies are never worse than 0.2 dex and usually they agree to within 0.1 dex. Considering that all studies have (to various degree) differences in input atomic data, atmospheric models, and the numerical methods this is not surprising. Still, all statistical equilibrium calculations in 1D are conceptually similar and a larger consensus is clearly desired for accurate analysis.

While our model atom is superior to previous studies, in that it contains more reliable atomic data for collisions, we do not expect that this is the primary reason behind some of the larger offsets with previous studies. As discussed in Sect. 2.3.2, the sensitivity to the detailed collisional rates is rather low for the specific case of Na in the stellar parameter range and we suspect that differences in model atmospheric structure have a larger impact. Takeda et al. (2003), Mashonkina et al. (2000) and Andrievsky et al. (2007) all use Kurucz ATLAS9 models, while Shi et al. (2004) use the grid by Fuhrmann et al. (1997). The atmospheric temperature gradient is inevitably different for models of identical stellar parameters for example because of differences in the treatment of convection, equation of state, and opacity. This is illustrated in Fig. 2.8, showing the difference in temperature stratification for different versions of ATLAS9 models relative to a MARCS model for a

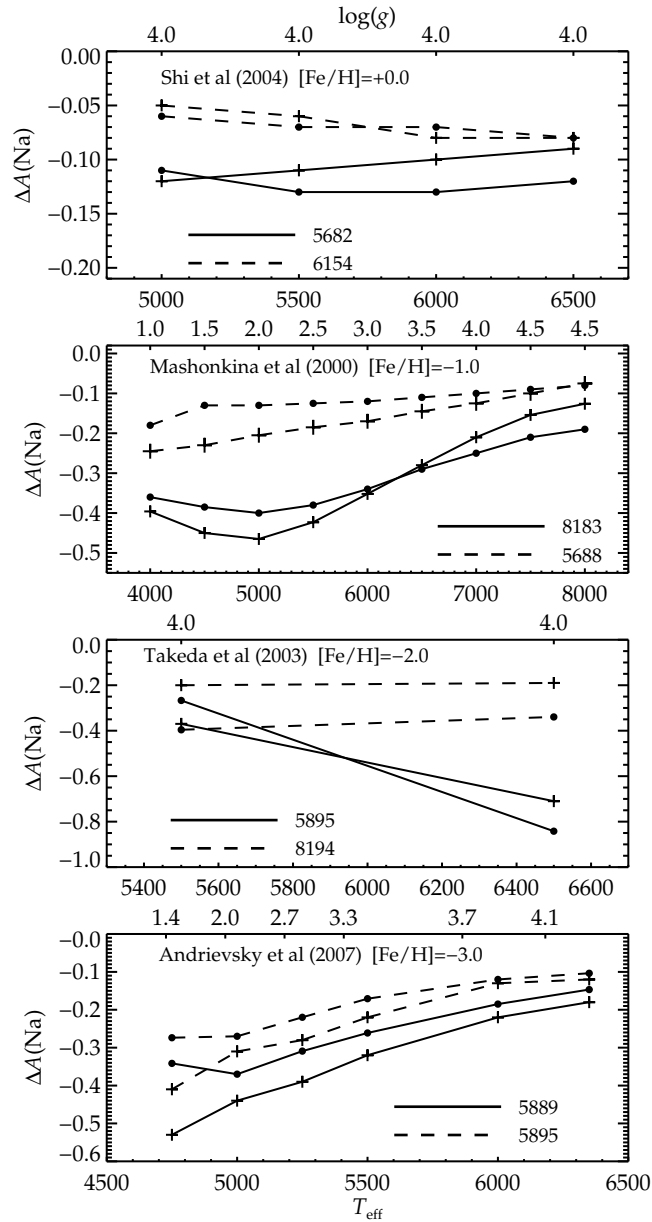


Figure 2.7: Comparison between the abundance corrections determined in this study (lines connected with bullets) and earlier studies, as indicated in each panel (lines connected with plus signs). The literature studies shown are, from the top to the bottom; Shi et al. (2004); Mashonkina et al. (2000); Takeda et al. (2003); Andrievsky et al. (2007). Effective temperature is used as reference axis, with surface gravity values for each model indicated along the top axis of each panel. All calculations used the assumption of $[\text{Na}/\text{Fe}] = 0.0$.

metal-poor giant⁶. As can be seen in this figure, the stratification is critically dependent on the inclusion of convective over-shooting in the 1993 grid by Kurucz. The most up-to-date versions of ATLAS9 (Castelli & Kurucz, 2004) and MARCS (Gustafsson et al., 2008) both neglect over-shoot, and the models shown have similar, but not identical, parameters for the mixing length, but nevertheless show differences on the 100 K level.

The lower panel of Fig. 2.8 illustrates the effect on derived non-LTE abundance corrections for the 819.4 nm line, when using different atmospheric models. At low line strength, the height of the plateau appears, as expected, to be connected to the temperature gradient around $\log(\tau_{500}) = 0$. The ATLAS9 model without over-shoot has the steepest gradient, producing a larger $J_\nu - B_\nu$ -excess in the ultra-violet which counteracts over-recombination. The ATLAS9 model with over-shoot has the flattest gradient, and thus the most negative corrections. Still, the differences between the models are not large, $\lesssim 0.05$ dex, for unsaturated lines. As seen in the plot, saturated lines show a larger sensitivity, and it is easily appreciated that different model atmospheres can produce results that are discrepant by more than 0.1 dex for such a metal-poor giant. We also note that the largest discrepancies between the non-LTE studies are indeed present for strong lines (the line strength increases from right to left, with decreasing effective temperature in Fig. 2.7).

2.4 Conclusions

Using our calculated abundance corrections and/or non-LTE curves-of-growth for ten important neutral Na I lines, Na abundances that are superior to those inferred with the LTE assumption can easily be obtained for late-type dwarf and giant stars. The results show a small sensitivity to uncertainties in input atomic data for collisional cross-sections, but are sensitive to the detailed structure of the atmosphere. To minimise the influence from possible systematic errors in the model, un-saturated lines are definitely to be preferred as abundance indicators based on integrated line strengths. As always, a good test of the soundness of the modelling procedure is to compare Na abundances from lines of different strengths.

In a forthcoming paper we will explore the impact of the model atmosphere on the abundance determination more closely, and extend our work to include 3D, hydrodynamical model atmospheres, superseding the crude mixing length recipes used for convection in static 1D models. The model atom presented here will then be applied to specific cases of solar-metallicity and metal-poor dwarfs and giants, and we will discuss the prospects for accurate analysis of the Galactic chemical evolution of Na.

⁶The ATLAS9 models were downloaded from <http://kurucz.harvard.edu/grids/>, with convective over-shoot (gridm20), without over-shoot (gridm20NOVER), and using more updated opacity and abundances (gridm20a2ODFNEW).

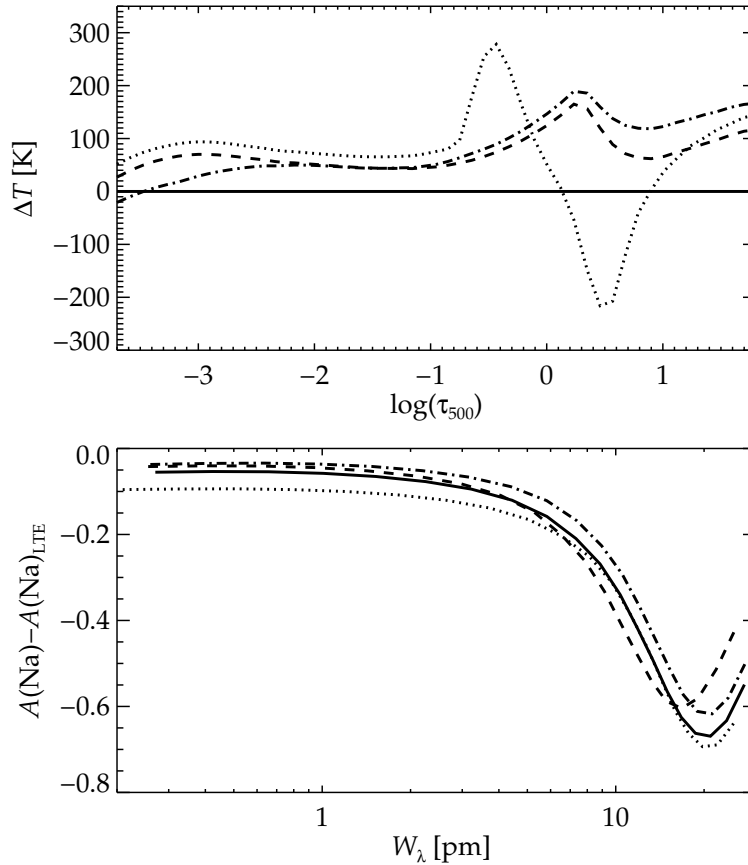


Figure 2.8: *Top*: Temperature difference between ATLAS9 models relative to a MARCS model (Gustafsson et al., 2008), for a metal-poor giant ($T_{\text{eff}} = 5000$ K, $\log g = 2.0$, $[\text{Fe}/\text{H}] = -2.0$, $\xi_t = 2.0$ km/s). The dotted line represents an ATLAS9 model with scaled solar composition and convective over-shoot from the Kurucz 1993-grid. The dashed line has the same composition but without over-shoot. The dashed-dotted line represents a 0.4 dex alpha-enhanced ATLAS9 model without over-shoot from the grid by Castelli & Kurucz (2004). *Bottom*: Non-LTE abundance corrections as function of equivalent width for the 819.4 nm Na I line, derived using the models shown in top plot. The solid line represents our study, using MARCS models. The Na abundance varies from left to right between $[\text{Na}/\text{Fe}] = -2.0 \dots +2.0$.

Chapter 3

Departures from LTE for neutral Li

The following chapter contains a modified version of an article that was published in *Astronomy & Astrophysics* in August 2009 (Lind, Asplund, & Barklem).

3.1 Astrophysical motivation

Stellar lithium abundances are continuing to attract strong interest among the astronomical community. In particular, many studies are devoted to constraining and finding explanations for the famous “Spite plateau” of warm metal-poor halo stars, first discovered by Spite & Spite (1982). For recent studies of lithium in halo field stars see e.g. Ryan et al. (2001), Charbonnel & Primas (2005), Asplund et al. (2006), Bonifacio et al. (2007a), and Hosford et al. (2009). To put constraints on the primordial lithium abundance in the Universe, it is of fundamental importance to determine if and by how much the Li abundances increase with increasing metallicity on the Spite plateau. The behaviour of Li abundance with effective temperature is of equal importance, as it could lend support to the notion that atomic diffusion is acting in metal-poor stellar atmospheres. Lithium depletion through atomic diffusion has been suggested as a solution to the discrepancy between the Spite plateau abundance and the predicted value of the primordial lithium abundance (Korn et al., 2007; Lind et al., 2009b). To accurately infer both the mean lithium abundance in the halo and the abundance behaviour with metallicity and effective temperature, it is crucial to have a realistic description of the lithium line formation. Previous non-LTE analyses spanning a large stellar-parameter space (Carlsson et al., 1994; Pavlenko & Magazzu, 1996; Takeda & Kawanomoto, 2005) have shown that departures from LTE are generally small but significant at the required accuracy.

3.2 Non-LTE modelling procedure

We use the radiative-transfer code MULTI, version 2.3 (Carlsson, 1986, 1992) to perform non-LTE calculations. The model atom used includes the same 20 energy levels for

neutral lithium as described in Carlsson et al. (1994), plus the LiII ground state. The highest considered level in LiI has principle quantum number $n = 9$. We have used TOP-base data (Peach et al., 1988) for energy levels, oscillator strengths, and photo-ionisation cross-sections for levels with orbital quantum number $l \leq 3$. For the remaining levels, hydrogenic values are used. For the resonance line at 670.7 nm, we adopt the oscillator strength $f = 0.7468$, as calculated by Yan et al. (1998), and consider six hyperfine components in ${}^7\text{Li}$ (neglecting ${}^6\text{Li}$), with measured wavelengths given by Sansonetti et al. (1995). For the subordinate line at 610.3 nm, we adopt $f = 0.6386$, also determined by Yan et al. (1998), and account for the three fine-structure components with wavelengths determined by Lindgård & Nielson (1977). For both lines, van-der-Waals-broadening parameters follow Anstee & O'Mara (1995) and Barklem & O'Mara (1997). Stark broadening is unimportant in the late-type atmospheres of interest here and is therefore neglected. Table 3.1 lists wavelengths, oscillator strengths, and broadening data adopted for the 670.7 nm and 610.3 nm lines.

Cross-sections for collisional excitation by electrons are taken from Park (1971) and collisional ionisation by electrons from Seaton (1962) as given by Allen (1976). We add rate coefficients for excitation and de-excitation from collisions with neutral hydrogen atoms according to Belyaev & Barklem (2003) and Barklem et al. (2003), as well as charge transfer reactions with neutral hydrogen and the negative hydrogen ion according to Croft et al. (1999). The number abundance of the negative hydrogen ion is calculated by assuming LTE. Ionisation by hydrogen atom impact is not included. For low-lying states at low collision energies, it is expected to be negligible compared to charge transfer reactions and excitation (Krstić & Schultz, 2009).

A grid of 1D, LTE, opacity-sampling, MARCS model atmospheres (Gustafsson et al., 2008) is used in the analysis. Non-LTE computations for lithium as a trace element are performed in the plane-parallel approximation, for models with $T_{\text{eff}} = 4000\text{--}8000$ K, $\log g = 1.0\text{--}5.0$, $[\text{Fe}/\text{H}] = 0.0\text{--}-3.0$, for lithium abundances in the range $A(\text{Li}) = -0.30\text{--}-4.20$. The highest effective temperature is 5500 K for models with $\log g = 1.0$, 6500 K for $\log g = 2.0$, 7500 K for $\log g = 3.0$, and 8000 K for $\log g \geq 4.0$. For models with $\log g \geq 3.0$, we adopted a microturbulence parameter $\xi_t = 1.0 \text{ km s}^{-1}$ and $\xi_t = 2.0 \text{ km s}^{-1}$, and for models with $\log g \leq 3.0$, we adopted $\xi_t = 2.0 \text{ km s}^{-1}$ and $\xi_t = 5.0 \text{ km s}^{-1}$. In total, 392 atmospheric models are included in the computations.

In the statistical equilibrium calculations, the background opacity include continuum and line opacity provided by the MARCS model atmospheres. MULTI thus calculates a line-blanketed photo-ionising radiation field while solving for the statistical equilibrium of lithium. Based on the LTE and non-LTE equivalent widths obtained for the stellar-parameter grid, we subsequently define a non-LTE correction for each abundance point as the difference between its LTE lithium abundance and the non-LTE abundance that corresponds to the same equivalent width. The limiting equivalent widths for which corrections are given are set to 0.01 pm and 100 pm. The equivalent width is obtained by numerical integration over the line profile, considering a spectral region that extends ± 9 nm from the line centre. For lines weaker than 50 pm the numerical precision is better than 0.01 pm whereas the equivalent widths of the strongest lines are determined to within 0.1 pm.

Table 3.1: Wavelengths, oscillator strengths, and broadening data for the two considered lines.

$2s^2S - 2p^2P^o$					
$(a)\Gamma = 3.690 \times 10^7$		$(b)\sigma = 346$		$(c)\alpha = 0.236$	
$\lambda[\text{nm}]$	J_l	J_u	f	F_l	F_u
670.79080	1/2	1/2	1.037×10^{-2}	1	1
670.79066	1/2	1/2	5.186×10^{-2}	1	2
670.79200	1/2	1/2	3.112×10^{-2}	2	1
670.79187	1/2	1/2	3.112×10^{-2}	2	2
670.77561	1/2	3/2	1.245×10^{-1}	1	0,1,2
670.77682	1/2	3/2	1.245×10^{-1}	2	1,2,3

$2p^2P^o - 3d^2D$					
$(a)\Gamma = 1.055 \times 10^8$		$(b)\sigma = 837$		$(c)\alpha = 0.274$	
$\lambda[\text{nm}]$	J_l	J_u	f		
610.3538	1/2	3/2	6.386×10^{-1}		
610.3664	3/2	3/2	6.386×10^{-2}		
610.3649	3/2	5/2	5.747×10^{-1}		

(a) Γ [rad s^{-1}] is the natural broadening parameter.

(b) σ [a.u.] is the broadening cross-section for collisions with neutral hydrogen at relative velocity $v = 10^4 \text{m s}^{-1}$ (Anstee & O'Mara, 1995).

(c) α is the velocity dependence of σ .

3.3 Results

The abundance corrections and LTE and non-LTE equivalent widths for each grid point are given in Table 3.2 for the 670.7 nm line, and in Table 3.3 for the 610.3 nm line. In the following we summarise the most important non-LTE effects and describe the size of the corrections over the cool-star grid. Because our results are in qualitative agreement with Carlsson et al. (1994), we refer the reader to this paper for a detailed explanation of the non-LTE line formation of lithium.

At $A(\text{Li}) < 2$ for the coolest giants and $A(\text{Li}) < 3$ for the hottest giants (i.e. at unsaturated line strengths), the dominant non-LTE effect is over-ionisation of neutral lithium, driven mainly by the super-thermal radiation field at $\lambda \lesssim 349.5$ nm ($J_\nu > B_\nu$, where J_ν is the mean intensity and B_ν the Planck function), corresponding to the photo-ionisation threshold of the first excited level. This leads to smaller number populations of all states of neutral Li, including the ground (2s) and first excited (2p) states, compared to LTE. The line source functions are in excess at such small line strengths, following the $J_\nu - B_\nu$ excess at line frequencies. Both the effect on the source functions and the loss of line-opacity weaken the lines in non-LTE, making the abundance corrections positive. The corrections range from being close to zero for the hottest giants to a maximum +0.45 dex for cool, metal-rich giants for the 670.7 nm line. For the 610.3 nm line, the corrections are slightly smaller, $\leq +0.3$ dex.

In dwarfs, the $J_\nu - B_\nu$ excess is smaller in the 2p photo-ionisation continuum and the radiation field is sub-thermal, $J_\nu < B_\nu$, in other influential continua, e.g. those corresponding to photo-ionisation from 3p and 3d. In layers close to continuum optical depth unity, hot dwarfs have over-populations in the ground state, which in combination with a decrease in the resonance-line source function strengthens the 670.7 nm line. Abundance corrections are therefore negative or approximately zero for this line for dwarfs hotter than 6000 K.

At $A(\text{Li}) > 2$ for the coolest stars and $A(\text{Li}) > 3$ for the hottest stars, photon losses in the resonance line become apparent, driving recombination from Li II in both dwarfs and giants. This mainly affects the population of the ground state and to a lesser degree higher excited states. The resonance-line source function drops accordingly and the non-LTE corrections become less positive or more negative with increasing abundance over the whole grid. For metal-poor, extremely lithium-rich giants, the corrections can reach almost -1.0 dex.

The 610.3 nm abundance corrections for $A(\text{Li}) < 4.0$ are approximately constant for fixed stellar parameters, since this line does not saturate in the abundance range considered here.

As described in Barklem et al. (2003), including hydrogen collisions strengthens the collisional coupling between singly ionised lithium and neutral lithium, especially through the charge transfer reaction involving H and Li I in the 3s state and its inverse reaction. The number populations of low excited states increase when charge transfer is included, while the line source functions are barely affected. In turn, the abundance corrections become generally lower, i.e. less positive or more negative. Notice that the added collisions

Table 3.2: Non-LTE abundance corrections and equivalent widths for the Li I $\lambda = 670.7$ nm line. The whole table can be retrieved in machine-readable format from the CDS: <http://vizier.u-strasbg.fr/viz-bin/VizieR?-source=J/A+A/503/541>.

T_{eff} [K]	$\log g$	[Fe/H]	ξ_t [km/s]	$A(\text{Li})_{\text{LTE}}$	$\Delta^{(a)}$	$W_{\lambda,\text{LTE}}$ [pm]	$W_{\lambda,\text{NLTE}}$ [pm]
4000	1.0	-3.0	2.0	-0.3	0.25	2.24	1.29
4000	1.0	-3.0	2.0	0.0	0.25	4.20	2.49
4000	1.0	-3.0	2.0	0.3	0.25	7.48	4.65
4000	1.0	-3.0	2.0	0.6	0.24	12.28	8.28
4000	1.0	-3.0	2.0	0.9	0.21	18.05	13.66
4000	1.0	-3.0	2.0	1.2	0.14	23.71	20.40
...

^(a) $\Delta = A(\text{Li})_{\text{non-LTE}} - A(\text{Li})_{\text{LTE}}$

do not always have a thermalising effect, but can contribute to over-population of levels compared to LTE. The effect is illustrated in Fig.3.1, for a selected metal-poor and solar-metallicity dwarf and giant. As seen in Fig.3.1, the change in $A(\text{Li})_{\text{non-LTE}} - A(\text{Li})_{\text{LTE}}$ when including charge transfer is -0.12 dex for the metal-poor giant and -0.06 dex for the metal-poor dwarf.

While the charge transfer reaction has a significant influence on the statistical equilibrium of lithium, including bound-bound (and bound-free) transitions due to collisions with neutral hydrogen has no influence at all. However, this is not true if one relies on the classical Drawin recipe for estimates of the cross-section for those collisions. For comparison, Fig.3.1 also shows the results obtained when neglecting charge transfer reactions but including excitation and ionisation by neutral hydrogen according to Drawin’s recipe, with the rate formula given by Lambert (1993) and with the scaling factor $S_{\text{H}} = 1.0$. Generally, the Drawin cross-sections are much higher than the quantum mechanical calculations by Belyaev & Barklem (2003). When adopting the higher classical rates, the ground state is more populated and the abundance corrections become lower, by ~ -0.05 dex, compared to the results obtained with quantum mechanical rates.

3.4 Discussion

We have compared our results for the lithium resonance line to Carlsson et al. (1994) abundance corrections for dwarfs and giants with $[\text{Fe}/\text{H}] = -3.0 \dots 0.0$ to Pavlenko & Magazzu (1996) results for dwarfs and subgiants with solar metallicity and to Takeda & Kawanomoto (2005) corrections for dwarfs and subgiants with $[\text{Fe}/\text{H}] = -1.0 \dots 0.0$ (see Fig. 3.3). To aid in the comparison we converted the LTE and non-LTE equivalent widths listed in Table 1 in Pavlenko & Magazzu (1996) to abundance corrections. The largest difference is 0.12 dex between our results and those of Pavlenko & Magazzu (1996) and 0.15 dex between our

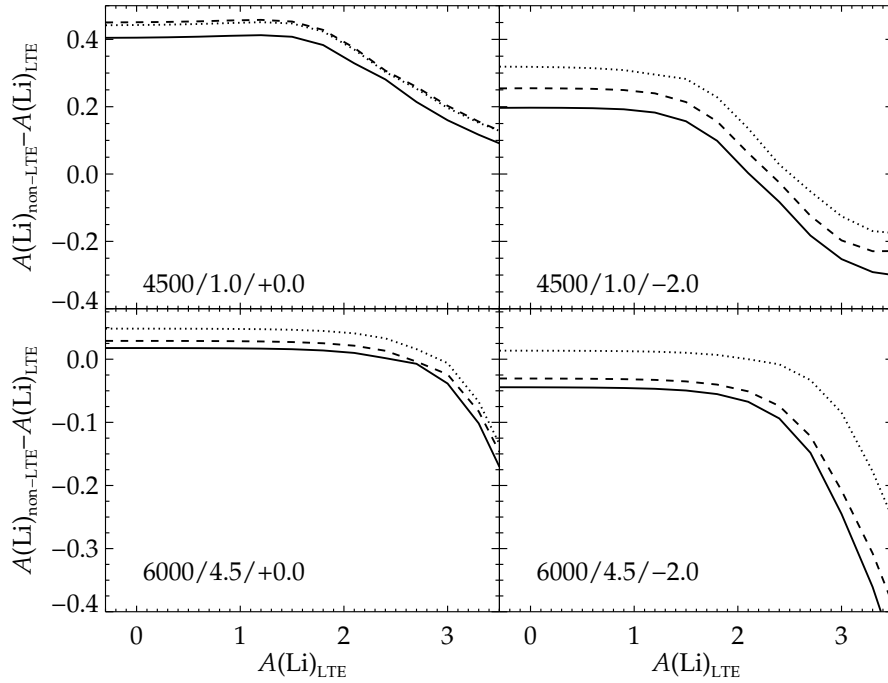


Figure 3.1: Non-LTE abundance corrections for 670.7 nm as functions of LTE lithium abundance for the indicated stellar parameters in the lower left corner of each plot, to be read as $T_{\text{eff}}/\log g/[\text{Fe}/\text{H}]$. *Solid*: Including charge transfer reactions with hydrogen as well as bound-bound transitions due to collisions with neutral hydrogen. The cross-sections are calculated with quantum mechanics (Belyaev & Barklem, 2003; Croft et al., 1999). *Dotted*: Neglecting charge transfer reactions, but including bound-bound transitions, calculated with quantum mechanics. *Dashed*: Neglecting charge transfer reactions, but including hydrogen collisions for bound-bound and bound-free transitions. The cross-sections are calculated with the classical Drawin recipe (Lambert, 1993).

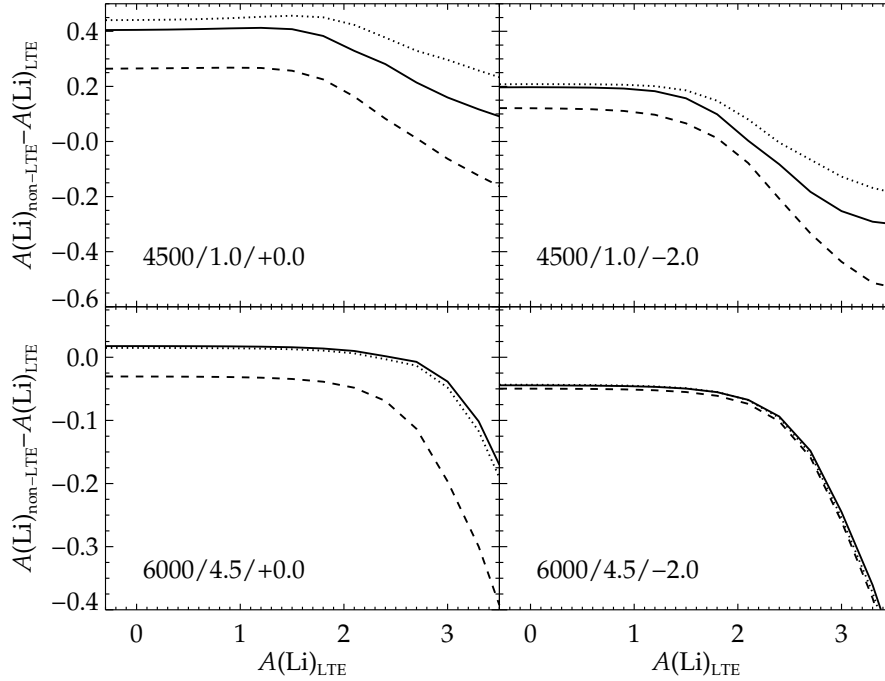


Figure 3.2: Panels as in Fig. 3.1. *Solid*: Same as in Fig. 3.1. MARCS model atmospheres from Gustafsson et al. (2008) are used, with $\xi_t = 2 \text{ km s}^{-1}$. *Dashed*: MARCS model atmospheres from Gustafsson et al. (1975) are used, with $\xi_t = 2 \text{ km s}^{-1}$. *Dotted*: MARCS model atmospheres from Gustafsson et al. (2008) are used, with microturbulence parameter set to $\xi_t = 5 \text{ km s}^{-1}$ in the two upper panels and $\xi_t = 1 \text{ km s}^{-1}$ in the lower panels.

Table 3.3: Non-LTE abundance corrections and equivalent widths for the Li I $\lambda = 610.3 \text{ nm}$ line. The whole table can be retrieved in machine-readable format from the CDS: <http://vizier.u-strasbg.fr/viz-bin/VizieR?-source=J/A+A/503/541>

T_{eff} [K]	$\log g$	[Fe/H]	ξ_t [km/s]	$A(\text{Li})_{\text{LTE}}$	$\Delta^{(a)}$	$W_{\lambda, \text{LTE}}$ [pm]	$W_{\lambda, \text{NLTE}}$ [pm]
4000	1.0	-3.0	2.0	0.0	0.17	0.02	0.02
4000	1.0	-3.0	2.0	0.3	0.17	0.05	0.03
4000	1.0	-3.0	2.0	0.6	0.17	0.09	0.06
4000	1.0	-3.0	2.0	0.9	0.17	0.19	0.13
4000	1.0	-3.0	2.0	1.2	0.17	0.37	0.25
4000	1.0	-3.0	2.0	1.5	0.17	0.73	0.49
...

^(a) $\Delta = A(\text{Li})_{\text{non-LTE}} - A(\text{Li})_{\text{LTE}}$

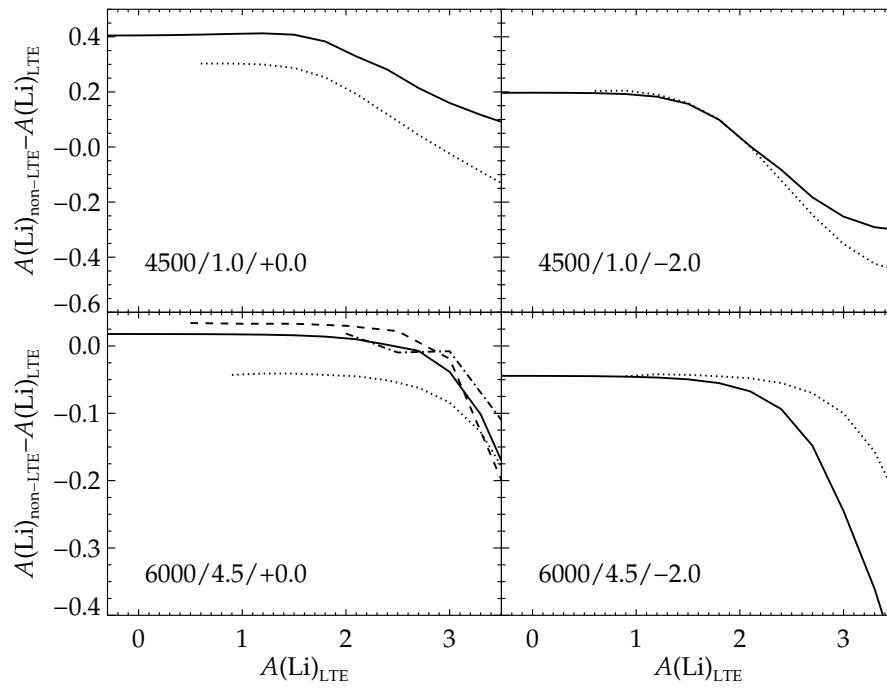


Figure 3.3: Panels as in Fig. 3.1. *Solid*: Same as in Figs.3.1 and 3.2. *Dotted*: Corrections by Carlsson et al. (1994). *Dashed*: Corrections by Takeda & Kawanomoto (2005). *Dash-dotted*: Corrections by Pavlenko & Magazzu (1996).

results and those of Takeda & Kawanomoto (2005), but generally the values agree quite well. The Carlsson et al. (1994) values agree with ours to within 0.15 dex for dwarfs and 0.20 dex for giants. Such differences are reasonable considering differences in the model atom and in the atmospheric models. Carlsson et al. (1994) use Gustafsson et al. (1975) MARCS models and Takeda & Kawanomoto (2005) and Pavlenko & Magazzu (1996) use Kurucz (1993) ATLAS9 models. The effects on the non-LTE abundance corrections when using MARCS models from Gustafsson et al. (1975) and Gustafsson et al. (2008) are illustrated in Fig. 3.2. Especially for the two giants, the choice of model atmosphere is important for the corrections. The newer models include more line opacity, causing a steeper temperature gradient in the upper part of the photosphere, which increases the ultraviolet $J_\nu - B_\nu$ excess and leads to more over-ionisation. The use of newer model atmospheres thus leads to more positive or less negative abundance corrections and partly cancels with the effect of including hydrogen collisions (see Sect. 3.3)

Varying the microturbulence between 1 km s^{-1} and 2 km s^{-1} barely affects the abundance corrections (lower panels in Fig. 3.2), especially for low lithium abundances. In a giant star, the non-LTE abundance corrections become systematically higher when adopting a microturbulence of 5 km s^{-1} instead of 2 km s^{-1} , the differences being especially significant when the line is strong (upper panels Fig. 3.2). However, the parameter still has some significance at low lithium abundances, when the formation of the line itself is unaffected by the microturbulence. This is because the choice of microturbulence influences the amount of line opacity included in the computations of the model atmosphere and consequently also the atmospheric temperature gradient, which in turn partly drives the departures from LTE.

Our results are valid within the assumptions of 1D model atmospheres in LTE and hydrostatic equilibrium. Non-LTE calculations for lithium in 3D, hydrodynamical model atmospheres have to this date been performed only for a few types of stars (Asplund et al., 2003), and we plan to extend our work to 3D in the future.

Chapter 4

3D, non-LTE line formation of Na I in the Sun

In this chapter we explore departures from LTE for Na I in a realistic 3D hydrodynamical model of the solar atmosphere. The results will be described in a forthcoming article in *Astronomy & Astrophysics* (Lind, Asplund, Barklem, Leenaarts, & Pereira). The introductory section (Sect. 4.1) has been adopted from Asplund & Lind (2010).

4.1 Introduction

Traditionally, abundance analyses of late-type stars have been carried out relying on 1D, time-independent, hydrostatic model atmospheres, which treat convection with the rudimentary mixing length theory. All of these are dubious approximations as even a casual glance at the solar atmosphere will immediately reveal. The solar atmosphere, as for other late-type stars, is dominated by granulation, which is the observational manifestation of convection: an evolving pattern of broad, warm up-flows in the midst of narrow cool downdrafts. Because of the great temperature sensitivity of the opacity, the temperature drops precipitously as the ascending gas nears the optical surface before it overturns and is accelerated downwards. The temperature contrast is therefore very pronounced in the photospheric layers, amounting to $> 1000\text{K}$ at the optical surface for the Sun (even when averaged over surfaces of equal optical depths these rms-differences amount to 400K). In addition to ignoring such atmospheric inhomogeneities, 1D model atmospheres can not be expected to have the correct mean temperature stratification because of the simplified convection treatment and the neglect of convective overshoot. Even small temperature differences can propagate to very large changes in the emergent stellar spectrum because of the non-linearities in the radiative transfer and the extreme opacity variations.

Over the past decade or so, 3D, time-dependent, hydrodynamical model atmospheres for a range of stellar parameters have started to be developed and applied to stellar abundance work (e.g. Asplund 2005, and references therein). Such 3D models solve the standard hydrodynamical conservation equations coupled with a simultaneous solution of the

3D radiative transfer equation and therefore self-consistently predict the convective and radiative energy transport (see e.g. Nordlund et al. 2009, for further details). To make the 3D modelling computationally tractable, the radiative transfer is not solved for the many thousands of wavelength points as routinely done in 1D model atmosphere codes. Instead the frequencies are sorted in opacity and more recently also in wavelength space for 4 – 20 bins for which the radiative transfer is solved. The resulting total radiative heating/cooling as a function of atmospheric depth is surprisingly well reproduced. The 3D models are based on similarly realistic microphysics (equation-of-state and continuous/line opacity) as employed in standard 1D model atmospheres. Currently there are mainly four different codes being used to develop 3D models; STAGGER (e.g. Nordlund et al. 2009), CO5BOLD (e.g. Ludwig et al. 2009), MURAM (e.g. Vögler et al. 2005) and ANTARES (e.g. Muthsam et al. 2010), although essentially all abundance related work to date has been performed within the first two collaborations.

Being more sophisticated in the modelling does not automatically translate to being more realistic. Over the past few years, substantial effort has therefore been dedicated to verify the suitability of the 3D models for quantitative stellar spectroscopy using an arsenal of observational diagnostics. Some of the striking successes are that the 3D models accurately predict the detailed solar granulation properties (e.g. Nordlund et al. 2009) as well as spectral line profiles, including their asymmetries and shifts (e.g. Asplund et al. 2000), which strongly suggests that the 3D modelling captures the essence of the real atmospheric structure and macroscopic gas motions. Another crucial test is the continuum centre-to-limb variation, which is an excellent probe of the mean temperature stratification in the solar atmosphere. The latest generation of 3D models computed with the STAGGER code reproduces the observations extremely well (Pereira et al., submitted); the CO5BOLD solar model does a similarly good job (H.-G. Ludwig, private communication). This is a remarkable achievement. The 3D solar model not only outperforms all tested theoretical 1D model atmospheres like the ATLAS, MARCS and PHOENIX flavours in this respect, it also does noticeably better than the semi-empirical model by Holweger & Mueller (1974), which was constructed largely to fulfil this observational constraint. The 3D solar model also performs very well when confronted with other tests, such as the spectral energy distribution, H lines (Pereira et al., submitted) and spatially resolved line profiles (Pereira et al., 2009b,a). In all aspects the most recent 3D solar models are clearly highly realistic and can therefore safely be trusted for abundance analysis purposes (Asplund et al., 2009).

4.2 Modelling procedure

To compute Na lines in LTE and non-LTE in 3D, we solve for the radiative transfer on multiple snapshots from a realistic 3D, time-dependent, hydro-dynamical simulation. The 3D model atmosphere was computed with an updated version of the STAGGER code, using 12 opacity bins (see Asplund et al. 2009). The 3D, LTE lines profiles have been calculated by performing detailed radiative transfer on 90 snapshots, with $400 \times 400 \times 250$ grid-points. The selected time series has a total flux corresponding to $\langle T_{\text{eff}} \rangle =$

5777 ± 10 K. Each snapshot corresponds to a Cartesian box of $6 \times 6 \times 1$ Mm, with a horizontal extension that spans over a handful of granules (see Fig. 4.4). To improve the accuracy of the line formation calculations, the original simulation (extending down to 3 Mm below the optical surface) has been interpolated to a finer vertical resolution. These calculations were performed with the newly developed code SCATE (Hayek et al., submitted), which is an MPI code for 3D, LTE line formation with continuum scattering treated properly. The line profile is then spatially and temporally averaged, using all 90 snapshots. Fig. 4.1 illustrates the temperature and electron density stratifications of one such 3D model snapshot compared to a standard 1D model (Gustafsson et al., 2008).

With the added complexity of non-LTE, even if limited to a single species, computer power becomes essential to meet the precision demand of abundance work. To thus save computing time, we calculated the detailed non-LTE line profiles for only three representative snapshots ($\sim 100 \times 100 \times 80$) using the code MULTI3D. For the same snapshots, we also computed the LTE profiles with the same code and multiplied the averaged non-LTE to LTE ratio with the 3D, LTE profiles from the more rigorous calculations with SCATE. This profile ratio is fairly invariant from snapshot to snapshot, and can thus be reliably established with this technique. MULTI3D is a domain-decomposed and MPI-parallelised code for statistical equilibrium and radiative transfer calculations in 3D, based on the original codes by (Botnen, 1997; Carlsson et al., 1994), with extensive further development (see e.g. Leenaarts & Carlsson 2009 for more details).

MULTI3D uses a short-characteristic radiative transfer scheme to compute the radiation field that is needed to establish the statistical equilibrium. The essence of this technique lies in that it solves the radiative transfer equation through multiple short rays, crossing through each grid point and extending to the cell face boundaries. We use the A4-quadrature by Carlson (1963), i.e. 24 rays in total intersect each point. To obtain the values of the source function at the boundaries, second-order Bezier interpolation is used. Once the iterative procedure has converged to a solution for the level populations of each grid point ($\Delta N_x/N_x < 10^{-3}$), a long-characteristic Feautrier solver is used to predict the emergent intensity for different viewing angles.

The 1D results shown here for comparison have been obtained as described in Chapter 2, using a MARCS model atmosphere (Gustafsson et al., 2008) or the semi-empirical model by Holweger & Mueller (1974, H-M model). The non-LTE calculations uses the code MULTI2.3. MULTI3D and MULTI2.3 can be supplied with identical atomic data and background opacity and they give consistent results for 1D models.

The atomic model is the same as was described in detail in Chapter 2, with some minor modifications. Here, we include 20 levels of Na I, coupled via 122 bound-bound radiative transition and 186 collisional transitions. All levels are radiationally and collisionally coupled to the ground state of Na II. Except for the separate treatment of the fine structure levels of Na I 3p, we neglect line asymmetry due to fine- and hyperfine structure.

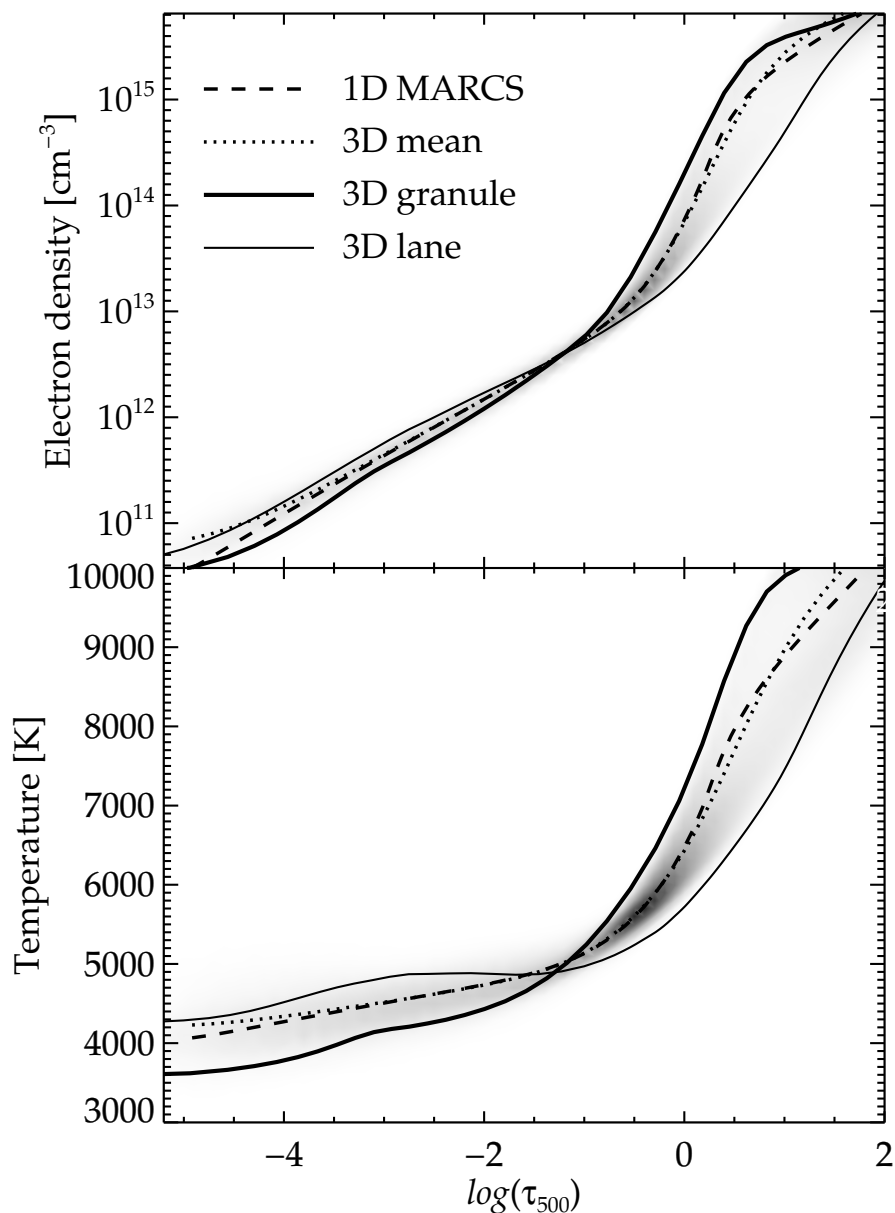


Figure 4.1: Temperature and electron density structures of solar model atmospheres. The shaded areas represent probability maps of the 3D hydrodynamical simulation, with dark regions corresponding to high probability. The dotted line marks the average structure of the three snapshots that were used for the non-LTE analysis. The solid lines illustrate the extreme stratifications in the middle of a typical bright granule (thick) and a dark intergranular lane (thin). The dashed line represents a 1D MARCS solar model (Gustafsson et al., 2008). Note the temperature reversal above $\log \tau_{500} = -1$, i.e. granules become cooler and thus darker than inter-granular lanes.

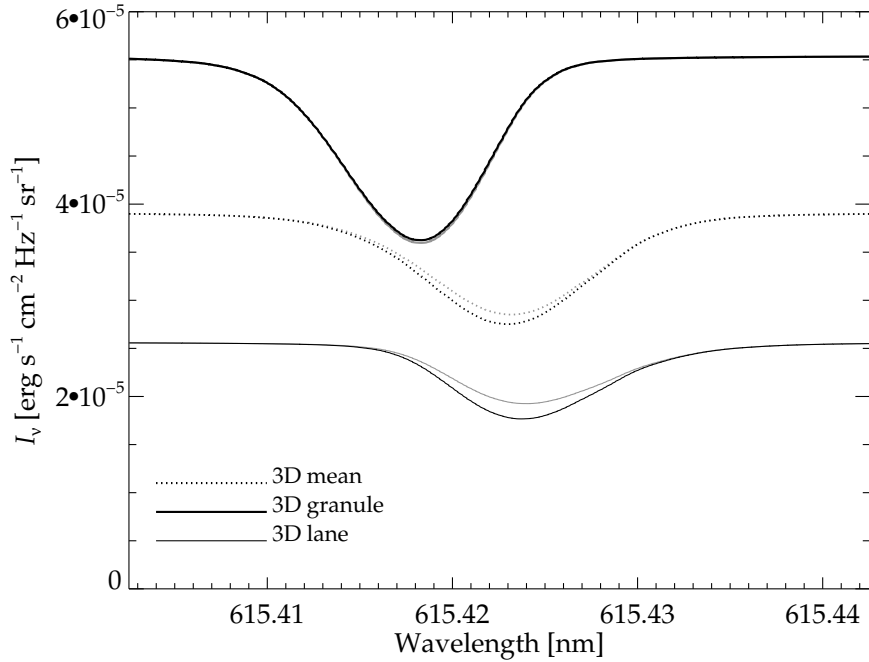


Figure 4.2: Solar disk centre intensity profiles of the Na I 615.4 nm line, computed in LTE (grey lines) and non-LTE (black lines). The lines have the same meaning as in Fig. 4.1

4.3 Line formation in 3D

In 3D radiative transfer it becomes apparent that the spectrum emitted from different regions of the (quiet) solar surface actually look very different. Fig. 4.2 illustrates how the Na I line at 615.4 nm line has a completely different appearance in a granule of bright up-flowing gas and a dark, inter-granular lane. Not only the continuum brightness is very different between the two, but also the strength and shape of the line, due to the different temperature and velocity structures. The bright granule Doppler-shifts the line toward the blue, and the cool temperatures in the line-forming regions strengthens it. In the lanes, the situation is reversed. The mean profile is therefore inherently asymmetric (see e.g. Asplund et al. 2000).

The temperature and density inhomogeneities present in a realistic 3D atmosphere, naturally cause also LTE departures to vary between different regions (Kiselman, 1997; Asplund et al., 2003). As shown in Fig. 4.3 the departure coefficients for the ground and first excited state of neutral Na differ dramatically between the granules and the lanes. As described in detail in Chapter 2, the overall ionisation balance is governed by over-ionisation from the first excited state, and the opposite effect, over-recombination, to higher excited levels. The steeper temperature gradient of the granules give rise to a larger $J_\nu - B_\nu$ -excess in the ultra-violet, boosting the over-ionisation. Na I is therefore slightly under-populated

in the brightest regions, whereas the dark lanes rather show pronounced over-population and lines that are stronger compared to LTE. Fig 4.4 illustrates clearly how both the LTE line strength and departures from LTE of the Na I 615.4 nm line correlates well with the pattern shaped by the convective motions.

4.4 Centre-to-limb variation

The close proximity of the Sun makes it possible to study its spectrum in much greater detail than other stars. In particular, observations that separates the light from different regions of the stellar surface can provide invaluable information about the atmospheric conditions. In accordance with the Eddington-Barbier approximation (for the case of a linearly varying source function, $I_\nu^+ = S_\nu(\tau_\nu = \mu)$, Rutten 2003), light emitted closer to the limb of the solar disk, i.e. having $\mu < 1$, probe shallower layers, i.e. greater heights. The centre-to-limb variation of the solar intensity spectrum can thus serve as an excellent test of the modelling of the atmospheric structure and line formation.

We have compared our synthetic spectra against spatially resolved solar observations, collected with the TRIPPEL spectrograph on the Swedish 1-m solar telescope on La Palma (Scharmer et al., 2003). A detailed description of the observations and data processing is presented in Pereira et al. (2009b). The observational data have extremely high quality, with a signal-to-noise ratio of ~ 1500 , for the spatially averaged spectra, and a resolution $\lambda/\delta\lambda = 200000$. The wavelength range covers the Na I 615.4 nm and 616.1 nm doublet, commonly used for abundance analyses of solar-metallicity stars. The centre-to-limb variation of the Na I line strength was studied by forming the spatial and temporal mean of five sets of viewing angles ($\mu \approx 0.2, 0.4, 0.6, 0.8, 1.0$). The 1D and 3D results are shown in Figs. 4.5, comparing integrated line strengths, and 4.6, comparing the line profiles directly.

In 1D, two fudge factors must be adopted to reproduce observed line profiles, namely microturbulence, accounting for the effect that turbulent small-scale gas motions widen the core of spectral lines, and macroturbulence, accounting for the Doppler shifts and thereby additional line broadening induced by the large scale convective motions of rising and sinking gas. For the Sun we adopt a microturbulence $\xi_t = 1$ km/s, and a radial-tangential macroturbulence $\zeta_{RT} = 2$ km/s (Gray, 2005). The 3D spectrum synthesis incorporates the velocity field resulting from hydro-dynamical simulations, and therefore do not require these parameters. Both 1D and 3D synthetic spectra are convolved with the instrumental profile and rotationally broadened, adopting $v \sin i = 2$ km/s. The equivalent widths of model and observations have been computed by direct integration over a wavelength region extending ± 0.012 nm from the line centre, to exclude nearby lines from other metals. In all comparisons, the Na abundance is adjusted to match the line strength at disk centre.

As is apparent from Fig. 4.5, traditional 1D, LTE modelling fails miserably to describe the centre-to-limb variation of the Na doublet, underestimating the line strengths at $\mu = 0.2$ by as much as 30%. 3D, LTE modelling performs better in comparison, although still underestimating the equivalent width. Non-LTE modelling in 1D does a much better job in reproducing the observed equivalent widths, which gives confidence to the ability of the

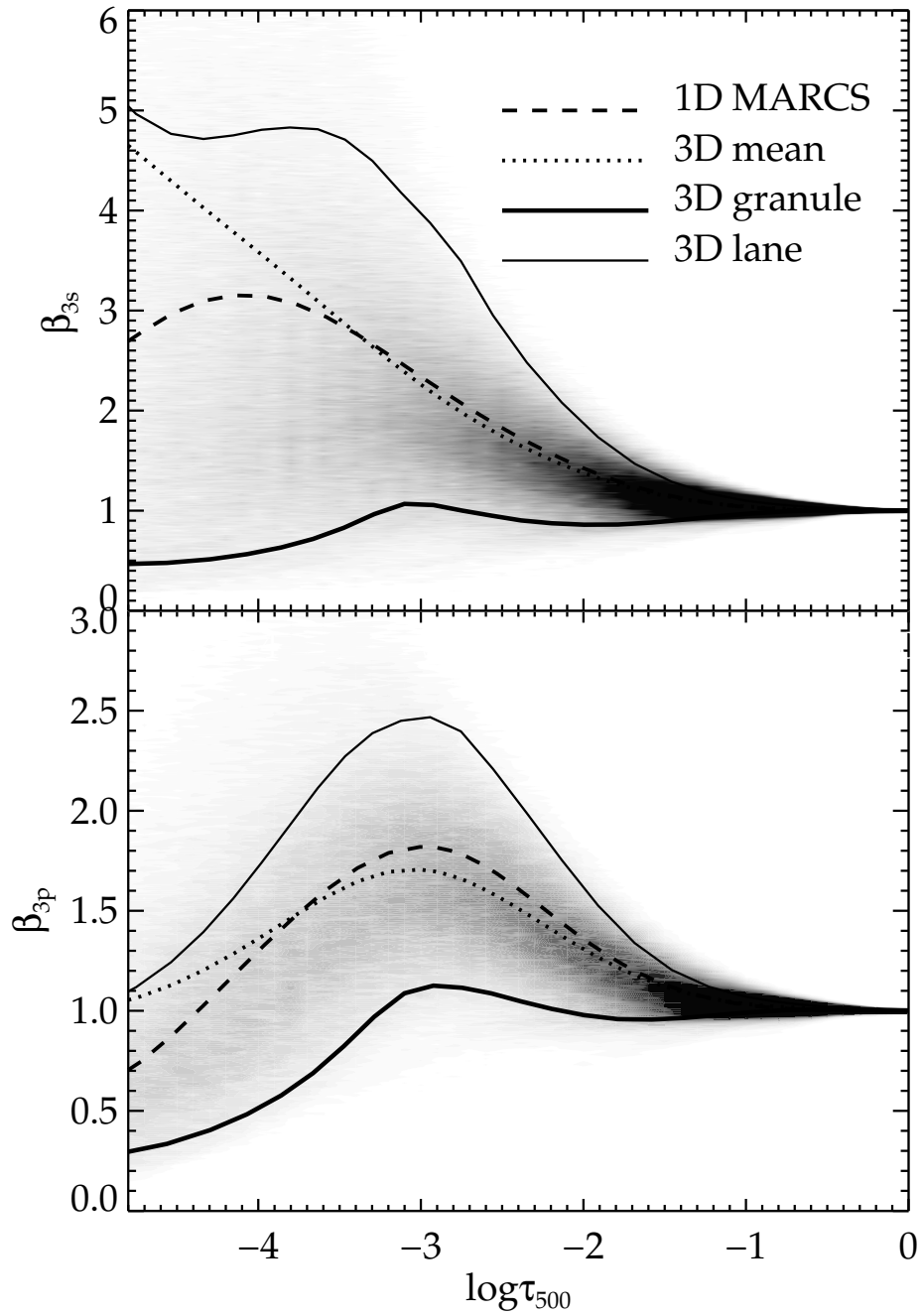


Figure 4.3: Departure coefficients for NaI 3s and 3p with optical depth. The lines and shaded areas have the same meaning as in Fig. 4.1.

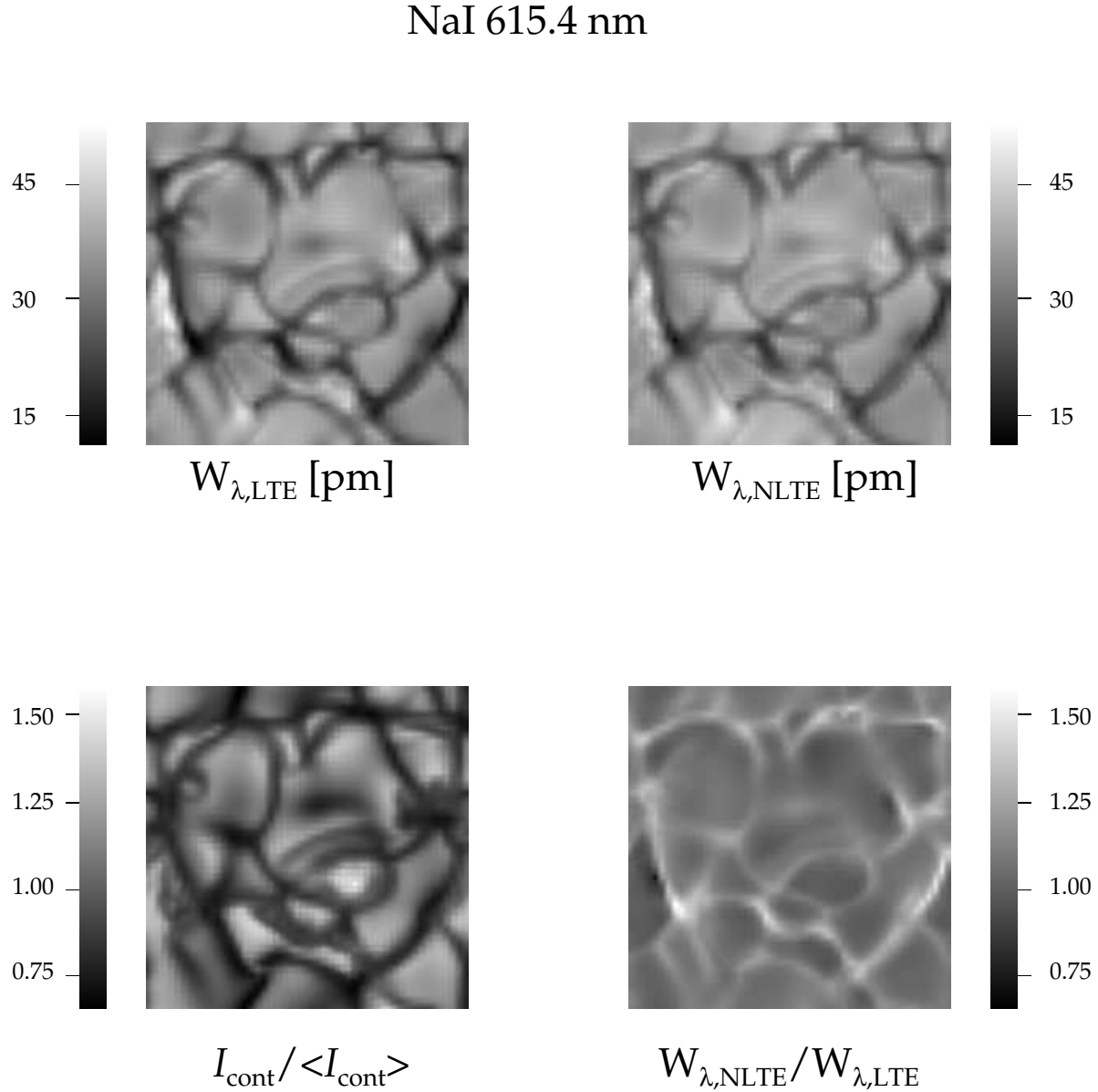


Figure 4.4: Surface images of atmospheric variables for a solar simulation. The equivalent widths have been computed from disk centre intensity profiles. *Bottom left*: The disk centre continuum intensity at 615.4 nm relative to the spatial average. *Bottom right*: The non-LTE to LTE ratio of equivalent widths. *Top left*: Equivalent widths computed in LTE. *Top right*: Equivalent widths computed in non-LTE. The images have been linearly interpolated to the twice the resolution used in the 3D, non-LTE calculations.

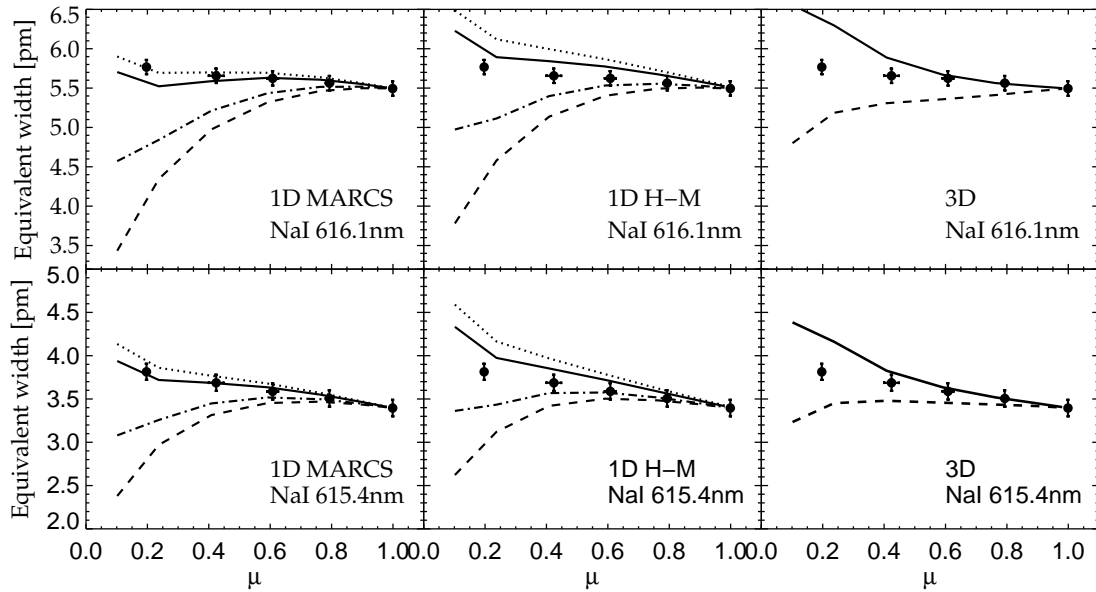


Figure 4.5: Centre-to-limb variation of the equivalent widths of the NaI 615.4 nm and 616.0 nm lines. The black bullets correspond to measurements of observed solar spectra and the lines represent different models. In each panel, the dashed line correspond to LTE and the solid line to non-LTE modelling including hydrogen collisions calculated by quantum mechanics. The left-hand and middle panels also shows the results obtained when neglecting hydrogen collisions completely (dotted lines) and including hydrogen collisions calculated with the classical Drawin recipe (dashed-dotted lines).

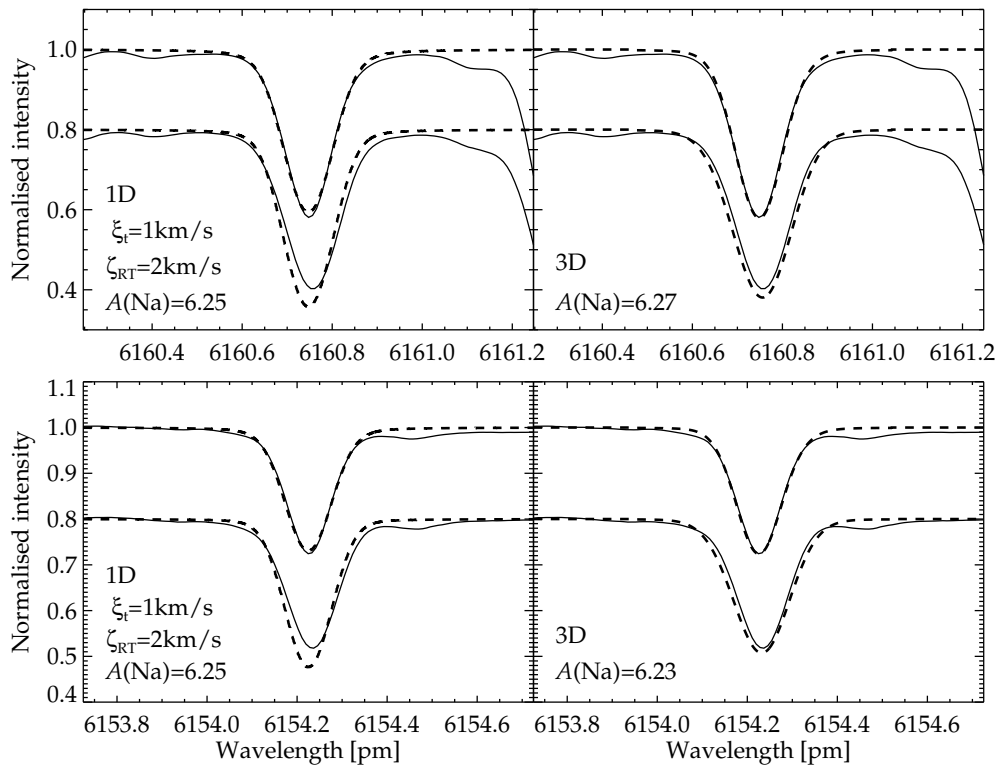


Figure 4.6: The solid lines represent the observed, normalised solar spectra at disk centre ($\mu = 1$, top spectrum in each panel) and limb ($\mu = 0.2$, normalised spectrum displaced by -0.2 for clarity). The dashed lines correspond to non-LTE modelling in 1D and 3D, as described in the text. The 1D synthetic spectrum has been computed with a MARCS model, adopting a microturbulence parameter of 1 km/s and a radial-tangential macroturbulence of 2 km/s. The solar value of $v \sin i$ is assumed to be 2 km/s.

1D model to establish a realistic mean radiation field in the upper atmosphere of the Sun. Apparently, the NaI over-population predicted by non-LTE analysis is a robust feature, critical for the accurate modelling of spectral lines.

Even though 1D, non-LTE modelling of the Sun may predict the centre-to-limb variation of equivalent widths very well, the same is not true for line profiles. As seen in Fig. 4.6 the value of ζ_{RT} that is needed to reproduce the line profile at disk centre, is insufficient to model the limb profile. The 3D modelling is clearly superior in this respect, consistently reproducing the observed line profiles of both limb and disk centre.

As can be perceived from Figs. 4.5 and 4.6, 3D, non-LTE modelling over-estimates the line strengths at the limb. The reason behind the offset is not fully clear and its origin will be further investigated. Finally, we note that the influence of hydrogen collisions on the centre-to-limb variation is very small, when quantum mechanical data are used, whereas the non-scaled Drawin recipe performs almost reproduces the LTE results. This is consistent with the findings of Allende Prieto et al. (2004), who concluded that the complete absence of hydrogen collisions is a better approximation than any scaling of the Drawin formula when modelling solar NaI lines in 1D.

4.5 The solar Na abundance

The solar chemical composition is essential for our understanding of the structure and evolution of the Sun and solar system. Furthermore, it serves as an important reference standard against which the elemental abundances of stars, planets and galaxies are compared. Recently, Asplund et al. (2009) have undertaken a reanalysis of the solar chemical composition with a 3D model of the solar atmosphere, with important downward revisions of e.g. C, N and O.

The solar Na abundance were determined by Asplund et al. (2009) with a 3D, LTE analysis of five weak lines of NaI (see Table 4.1). Corrections for departures from LTE were estimated with the 1D calculations of Shi et al. (2004) and Takeda et al. (2003) and applied to the 3D, LTE results. Here, we can for the first time present a consistent 3D, non-LTE determination of the solar Na abundance, adopting the equivalent width measurements of Asplund et al. (2009). Table 4.1 lists the resulting line-by-line abundances, derived with different modelling techniques. As mentioned previously, the non-LTE effects of such weak lines are minor in solar-type stars, although somewhat increased with a 3D analysis. Also the differences between 1D and 3D models are small for the specific case of the Sun, as expected (see Chapter 8). With 3D, non-LTE modelling the solar Na abundance is thus $A(\text{Na}) = 6.25$, with a gratifyingly small line-by-line abundance dispersion of 0.02 dex. This is in excellent agreement with the $A(\text{Na}) = 6.24 \pm 0.03$ derived by Asplund et al. (2009). We also note a good consistency with the 1D, non-LTE analysis by Mashonkina et al. (2000) who found $A(\text{Na}) = 6.20 \pm 0.02$ with an ATLAS model and 6.28 ± 0.03 with a H-M model.

Table 4.1: The solar Na abundance as determined from disk centre equivalent width measurements of five Na I lines, taken from Asplund et al. (2009). The columns correspond to different atmospheric models, assuming Na I level populations in LTE and non-LTE.

λ [nm]	W_λ [pm]	$A(\text{Na})$					
		MARCS 1D		H-M 1D		3D	
		LTE	non-LTE	LTE	non-LTE	LTE	non-LTE
475.1822	1.11	6.25	6.24	6.32	6.28	6.26	6.23
518.8838	1.27	6.22	6.20	6.30	6.26	6.27	6.24
615.4225	3.73	6.25	6.21	6.33	6.27	6.31	6.27
616.0747	5.70	6.22	6.17	6.31	6.23	6.33	6.28
1074.644	1.33	6.21	6.22	6.29	6.28	6.24	6.24
$\langle A(\text{Na}) \rangle$		6.23	6.21	6.31	6.26	6.28	6.25
σ		0.02	0.03	0.02	0.02	0.04	0.02

Chapter 5

Globular clusters

The following chapter introduces the reader to the basic properties of globular star clusters and gives examples of what we may learn from chemical analysis of stars in these unique environments. Also, a short summary is given of multi-object, high-resolution spectroscopy and the necessary steps involved in observation, data processing, and abundance determination.

5.1 Definition and basic properties

All stars in our Galaxy reside in either of its four main components; i.e. in the compact bulge in the centre, in the surrounding thin and thick disk holding the famous spiral arms, or in the extended spheroidal-shaped halo. Commonly, stars in the disk, with similar metallicities to our Sun, are referred to as Pop I stars, whereas metal-poor halo stars are referred to as Pop II. Halo stars are very rare compared to disk stars; the local number density ratio between the halo and the thin disk is only $\sim 0.5\%$ (Jurić et al., 2008).

The dense stellar conglomerates called globular clusters are found in the halo and the bulge, and all stars in the halo that do not belong to a globular cluster are simply called field stars. There is no one-parameter definition of a globular cluster, although it is generally accepted that they are very old (age $\gtrsim 10$ Gyr). The most complete catalogue (Harris, 1996)¹ contains 150 known clusters on elongated orbits of seemingly random orientation around the Galactic centre. The majority of clusters are located within 20 kpc of the centre, but they can be found out to distances of 120 kpc (AM 1). Fig. 5.1 shows a schematic view of the distribution of the known globular clusters in the Milky-Way.

Even among the Galactic globular clusters, there is large diversity in fundamental properties, such as mass, $M = 10^3 \dots 10^7 M_\odot$ (Meylan & Heggie, 1997), metallicity, $[\text{Fe}/\text{H}] = -2.4 \dots +0.07$ (Gratton et al., 2004), and luminosity $M_V = -1.5 \dots -10.2$ (Harris, 1996)².

¹with subsequent updates found at <http://physwww.mcmaster.ca/~harris/mwgc.dat>

² M_V is the absolute visual magnitude. It is related to the bolometric magnitude, M_{bol} , via the bolometric correction, BC , according to $M_V = M_{\text{bol}} - BC$. The bolometric magnitude is defined from the stellar luminosity: $M_{\text{bol}} - M_{\text{bol},\odot} = -2.5 \log(L/L_\odot)$

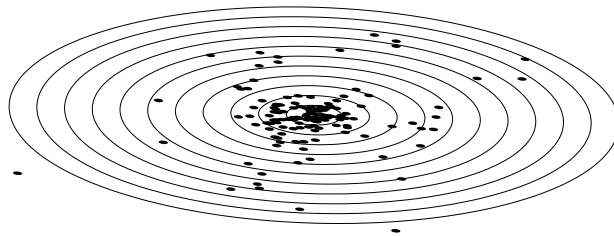


Figure 5.1: A schematic view of the positions of all known globular clusters in the Galaxy (black bullets). The concentric circles, whose radii are multiples of 3kpc, represent the approximate extension of the Galactic disk.

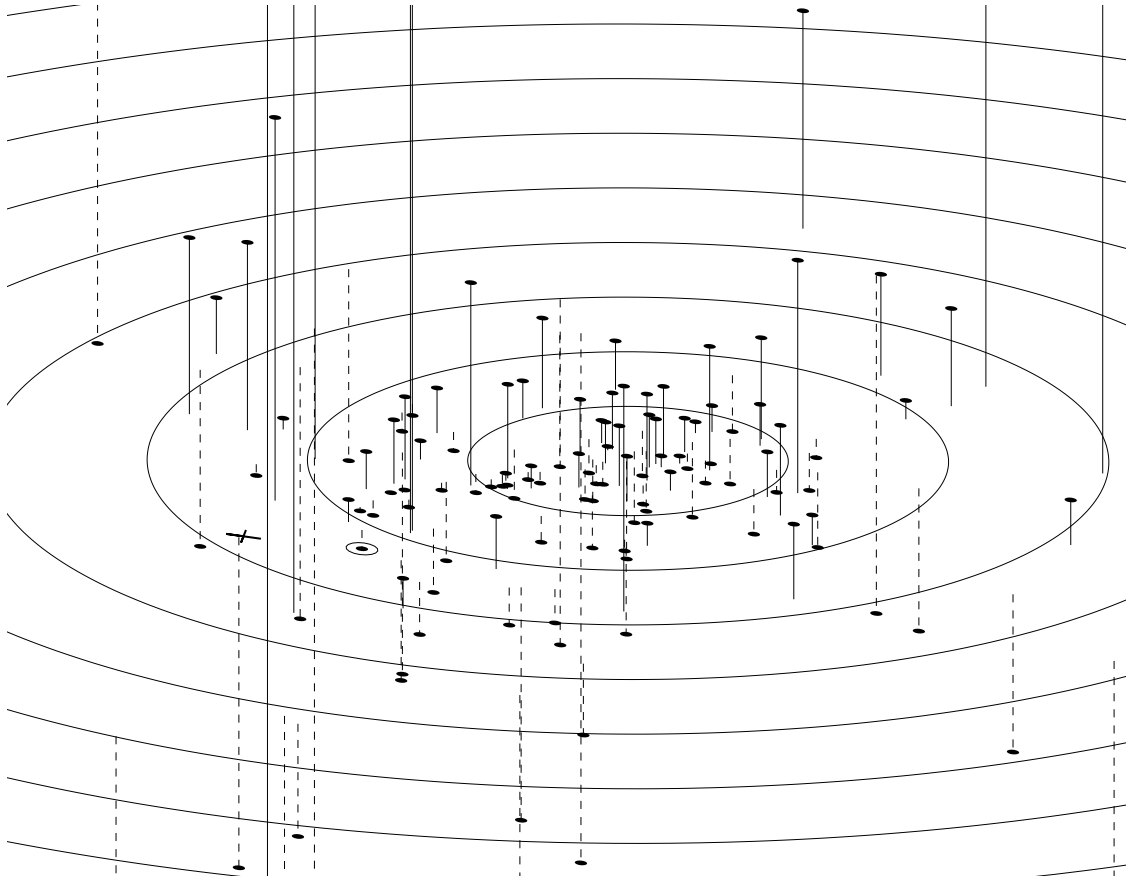


Figure 5.2: A zoomed in view of Fig. 5.1. The distance to the Galactic plane is indicated for each globular cluster with a solid line (object above plane) or dashed line (object below plane). The location of the Sun is marked with a cross, and the globular cluster NGC 6397 is highlighted with a circle.

In fact, there is much evidence for the existence of two separate sub-populations of globular clusters, one metal-rich, more centrally concentrated and rapidly rotating, bulge system and one metal-poor, more dispersed and slowly rotating, halo system (e.g. Brodie & Strader 2006). Our observational target in the following chapters is a nearby metal-poor (Pop II) globular cluster, NGC 6397, which is part of the halo population. The location of this cluster is indicated with a circle in Fig. 5.2.

Concerning the distinction between globular clusters and open clusters, which generally contain fewer stars and are much younger, one may base it on the presence or not of a O–Na anti-correlation (Carretta et al. 2010, see below), or on the different shapes of the luminosity functions of the two cluster types (van den Bergh, 1993). Dwarf spheroidal galaxies, on the other hand, are generally bigger, more luminous and complex systems, and can be distinguished through their mass-to-light ratio, abundance spread in heavier elements or simply by shape (see e.g. discussion by van den Bergh 2008).

Globular clusters were long thought to be simple systems, both in terms of chemical and dynamical evolution. The idealistic view of a single stellar population of unique age and chemical composition, suffering only from slow evaporation due to dynamical relaxation, has been overturned by numerous observational evidence for multiple stellar populations (Sect. 6.1), the discovery of peculiar objects (blue stragglers, millisecond pulsars, ...), and the realisation that a hypothetical central intermediate-mass black hole and processes like mass segregation, stellar mergers, and core collapse may affect the evolution. See Gratton et al. (2004) and Meylan & Heggie (1997) for extensive reviews of the chemical and dynamical properties of Galactic globular clusters.

5.2 Evolution of low-mass stars

To a first approximation, globular clusters are still considered to be rather simple, and they can be extremely useful as laboratories for improving our knowledge of stellar physics and evolution. Under the hypothesis of uniform ages and chemical composition, the individual evolution of single stars in the cluster is almost uniquely determined by the stellar mass (neglecting e.g. rotational velocity). The HR-diagram of the cluster, i.e. a diagram with magnitude (alias stellar luminosity) indicated on the y-axis and colour (alias effective temperature) on the x-axis, can then reveal the mass and evolutionary status of each object (see Figs. 5.3, 6.5, and 7.1).

Globular clusters are thought to be genuinely old, having experienced no further star formation since shortly after their formation in the very early universe. Therefore, they host (with few exceptions) only low-mass, long-lived stars. As an example, the expected life-time of a star like the Sun is roughly 10 Gyr and more massive stars are thus extinct in a cluster of this age. The reader is referred to any textbook on the topic of stellar structure and evolution (e.g. Prialnik 2000) for a detailed description of the life and death of stars in different mass ranges.

Again, in the idealistic view of a globular cluster, the main sequence (MS) is a thin, tilted line in the HR-diagram, along which stars (alias dwarfs) of different masses are

distributed during the long-lasting quiescent H-burning phase. The MS ends on the high-mass, left-hand side, with the cluster turn-off (TO) point, which indicates the age of the cluster. Stars that are more massive have exhausted their fuel of hydrogen in the core, and started to move to the left in the HR diagram along the subgiant branch (SGB). In this evolutionary phase, the envelope of the star cools and expands and the convective zone extends inward, whilst hydrogen is burnt in a shell surrounding the contracting core. The shell-burning continues as the star ascends the almost vertical red giant branch (RGB), and the core grows in size, while the convective envelope recedes. As will be discussed in Sect. 6.4.1, an important event in the stellar evolution occurs when hydrogen-burning shell crosses the boundary that marks the deepest penetration of the convective envelope, at the so called RGB bump. The red giant phase ends at the uppermost tip, when the star ignites helium in its core (if it is massive enough). These giant phases of evolution are very rapid compared to the MS life time and, as may be appreciated from Fig. 5.3, the vast majority of stars are thus MS stars, although the total light is dominated by the much brighter giants.

5.3 Observational applications

By spectroscopic analysis of stars, we can only infer the chemical composition of the very outermost layers, from which the light is emitted. Any chemical gradients or discontinuities in the stellar interior (i.e. below the outer convection zone, which is continuously mixed and thus chemically homogeneous) is beyond our reach to probe directly. Nevertheless, by comparing stars of different masses and evolutionary phases, which presumably share the same initial composition, we may trace such phenomena indirectly. Globular cluster stars are the obvious targets for such investigations. This methodology is discussed in detail in the following chapter, where we analyse the post-MS evolution of the surface abundance of lithium as well as the MS mass dependence (or, equivalently, the effective-temperature dependence).

The main trigger of the observational project presented in Chapter 6 was the discrepancy between the Li abundances commonly observed in Pop II dwarfs and subgiant stars and the prediction of the primordial abundance, i.e. the small amounts of Li created in the nucleosynthesis reactions that took place only minutes after the Big Bang. To alleviate this factor of 2–5 discrepancy, it has been suggested that the stars observable today have undergone photospheric depletion of lithium during their life times. The hypothesis is that some Li, and also other metals, has settled below the outer convection zone during the time the star has spent on the MS. The photospheric composition of a MS star therefore does not correspond exactly to that it was born with. However, during the giant phases of evolution the convective zone grows dramatically and erases any chemical differences in the affected region, and we may once again see the initial elemental abundances at the surface. For Li, the situation is complicated by the fact that this light nuclei is destroyed in the hot stellar interiors and the surface abundance of giants therefore becomes severely diluted at a certain point in their evolution. By comparing Li abundances of dwarfs and giants, we

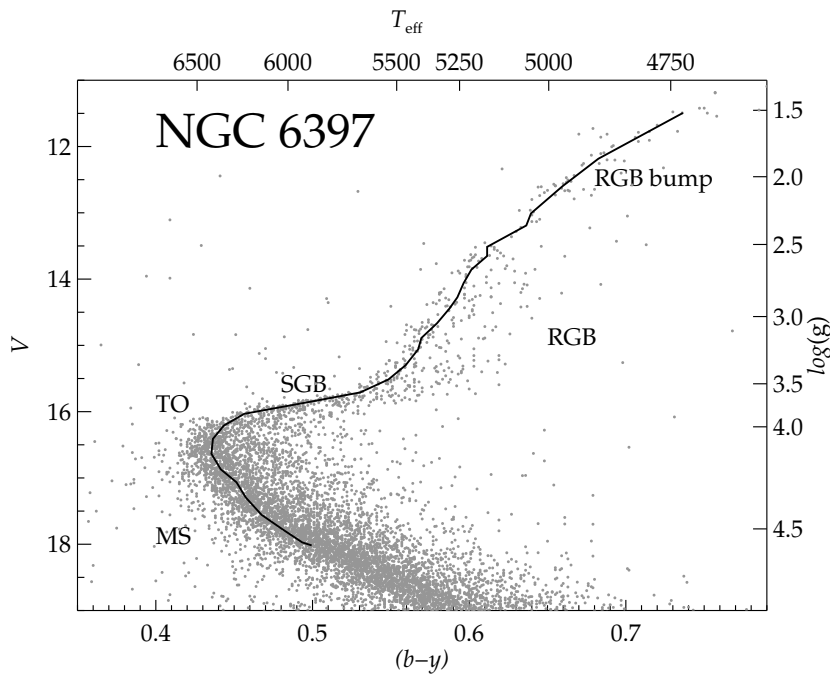


Figure 5.3: The observed HR-diagram of NGC 6397, with apparent visual magnitude (V) vs. Strömgen colour index $b - y$. The grey bullet represent individual stars, and the black solid line marks the average cluster sequence. The main sequence (MS), the turn-off point (TO), the subgiant branch (SGB), red giant branch (RGB), and RGB bump are marked in the figure. On the opposite axes, stellar parameters T_{eff} and $\log g$ that we have inferred for the stars are marked (Sect. 6.3.1).

can study the internal processes in detail and thereby constrain the physics of stars both on microscopic, atomic, scales and the convective and turbulent motions on macroscopic scales.

Obviously, studies that trace the surface evolution of elements through globular cluster stars in different evolutionary phases, would be biased, or maybe even rendered useless, if the basic assumption of a common initial abundance of all stars is falsified. It is thus important to carefully investigate this aspect. Especially, the abundance spread among stars with similar stellar parameters can lend support to, or refute the hypothesis of a common initial abundance. Such investigations of globular cluster stars have shown a rather complex picture: On the one hand, the star-to-star abundance scatter is always very small in commonly analysed elements like Ca, Ti, and Fe (a notable exception to the rule is ω cen), seemingly consistent with the simplistic view. On the other hand, light species like N, O and Na show large star-to-star scatter, incompatible with observational errors, and thus clearly disfavour a common initial abundance (see Sect. 7.1 and references therein). Rather, it is believed that present-day globular clusters host more than one stellar generation, with slightly different initial chemical composition of light elements.

In our investigation of signatures of in-situ depletion of Li in dwarfs, subgiants and giants (Chapter 6), we use Na abundances to distinguish between the different generations and assess possible bias in the interpretations. In Chapter 7 we focus instead on the detailed chemical compositions of a large number of elements in a sample of giant stars, in order to investigate closer the origin of multiple population and constrain chemical evolution of the cluster as a whole.

5.4 High-resolution spectroscopy with FLAMES

To perform our spectroscopic investigations of the globular cluster NGC 6397, we have used the fibre-fed, multi-object instrument FLAMES (Pasquini et al., 2002), mounted on VLT-UT2, at ESO Paranal, Chile. This instrument is ideal for medium-to-high resolution studies of dense stellar environments, since it is capable of collecting data for > 100 targets simultaneously, located within a total field-of-view of $25'$. This section will describe the most important steps in the observational procedure.

5.4.1 The observational setup

We use the UVES+MEDUSA combined mode of FLAMES. In this mode, eight optical fibres with $1''$ aperture are fed to the red arm of the high-resolution ultra-violet and visual echelle spectrograph (UVES, Dekker et al. 2000). The standard settings of UVES cover a large wavelength region (470–700 nm or 700–1000 nm) with a resolving power of $R = 47\,000$. At the same time, 135 individual fibres of $1.2''$ aperture are fed to the GIRAFFE instrument, with a typical wavelength coverage of 30 nm and a resolving power of $R = 20\,000$, in the settings that we used. The fibres are all either allocated to individual stars or placed at random, empty positions around the field-of-view. The latter are so called sky-

fibres and intended to sample the light only from background sources, mainly the reflected moonlight.

The targeted stars are selected from a photometric catalogue of the cluster. The photometry should be as precise and well calibrated as possible, to allow the fibres to be placed centrally on the target, thus maximising the number of photons collected by the CCD detector (CCD stands for charged coupled device). The GIRAFFE CCD consists of roughly 2000×4000 pixels, with longer of the two being the dispersion direction. The echelle orders, one for each fibre and target, lie barely separated from each other along the other direction.

5.4.2 Data reduction and processing

The purpose of the data reduction procedure is to collapse the data from the two-dimensional CCD format, to a one-dimensional, calibrated spectra for each target. The calibration steps involve transforming the data from pixel to wavelength space, correcting for the varying sensitivity over the detector, and subtracting background contribution from the instrument itself (see Fig. 5.4). The manipulation of the science exposure and a number of calibration frames are performed in the following order:

- Subtraction of bias, which is a background signal dependent on electronics of the system. This signal is determined by performing a number of read-outs from zero-time exposures.
- Subtraction of dark current, which is a time-dependent signal stemming from the non-zero temperature of the detector. This is measured by performing pseudo-observations without exposing the CCD to a light source.
- Determining the order architecture for the given setup, i.e. a model of how the light is distributed on the detector. This is achieved by exposing the CCD to a bright, continuous, light source with known properties (i.e. a lamp or a white wall) and create so called flat fields. The order pattern is masked with fitted polynomials, whose parameters are saved for later use.
- Determining the dispersion solution, i.e. the correlation between pixel and wavelength scale. This is achieved by exposing the CCD with the light from a lamp containing excited noble gas particles (thorium and argon). The detected signal shows narrow emission lines with known wavelengths, and can thus be used for calibration.
- The science frame is divided by a normalised flat field frame, which corrects the data for various instrumental artifacts such as the inhomogeneous illumination, dust on the optical system, varying sensitivity over the detector etc.
- The order architecture is used to extract the two-dimensional data from the science frame, and convert them to one dimension, simply by summing up the signal across each individual order.

Fig 5.4 shows a cross-section along the order direction of the GIRAFFE CCD plate, and illustrates the detected signal of science and calibration frames at a specific wavelength.

Once the observed data are in the format of one-dimensional spectra of stars and sky positions, some further processing is needed before the abundance analysis can start. First, the sky-spectra are averaged and the mean signal is subtracted from the stellar spectra. Second, the Doppler shift caused by the movement of the star relative to the telescope at the time of observation, is corrected for by identifying absorption lines in the spectrum. Usually we collected multiple exposures of each star,³ and once they are all brought to the same local rest frame, they are coadded to improve the quality. At the same time, outlying pixel values are removed, such as pixels affected by cosmic ray hits. Figs. 6.4 and 7.2 show examples of the final product.

5.5 Determination of stellar parameters

As discussed in Sect. 1.2, it is necessary to determine a number of fundamental stellar parameters to infer elemental abundances. In particular, we need to estimate the effective temperature T_{eff} and the surface gravity $\log(g)$ of all our stars. In the following we introduce the methods used to determine these parameters, and discuss some advantages and disadvantages.

5.5.1 Effective temperature

Especially for the determination of the Li abundance, an accurate estimate of T_{eff} is very important. We adopt three different methods to this end, based on different photometric and spectroscopic observables.

Photometry

Given that the continuous flux spectrum emitted by a star has the approximate shape of a black-body, it is easily realised that colours, i.e. differences between the flux sampled in different wavelength regions, can be used as temperature indicators. Analogously to Wien's displacement law for black-body radiation ($\lambda_{\text{max}} \propto T^{-1}$), the flux peak is located at shorter wavelength, the higher the effective temperature of the star (the solar spectrum peaks at ~ 450 nm).

To translate between colour and effective temperature, we use calibrated scaling relations obtained by empirical or theoretical means. The relations derived by (Alonso et al., 1996, 1999; Ramírez & Meléndez, 2005; Casagrande et al., 2010) are calibrated on the so called infra-red flux method (IRFM). The essence of this technique lies in obtaining the apparent bolometric flux for a large calibration sample, and use the ratio between the

³This is simply done for practical purposes. If the CCD is exposed for too long without interruption, it is more badly affected by cosmic rays. Also, external conditions may change rapidly, and thus decrease the quality of the collected signal or even render it useless.

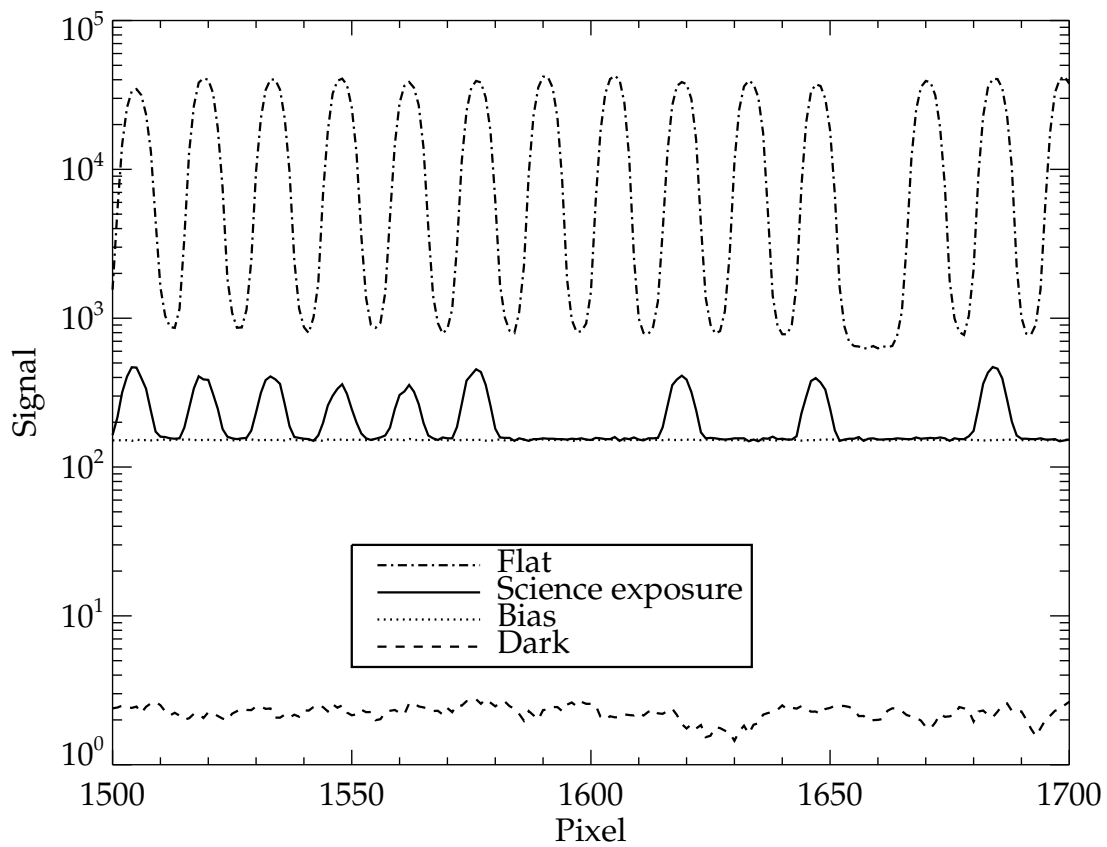


Figure 5.4: Cross-section along the order direction of the GIRAFFE CCD. The exposure type is indicated with labels. Only the stellar spectra can be clearly identified in the science exposure. Some of the orders that appear to be without signal are pointed to sky positions.

bolometric flux ($\propto T_{\text{eff}}^4$) and the flux measured at a specific reference wavelength in the near infra-red ($\propto T_{\text{eff}}$). This ratio remains highly sensitive to T_{eff} , while independent of e.g. the distance to the star. Having derived the effective temperatures of the calibration sample through the IRFM, the mentioned studies present polynomial fits between T_{eff} and a variety of different colour indices. A great advantage with this method is that it is fairly model independent, and we have only to ensure that the calibration is appropriate for the colour ranges, metallicities, and surface gravities spanned by our targets. In addition to the IRFM calibrations, we have used the colour- T_{eff} relations derived by Önehag et al. (2009). These rely solely on synthetic colours, computed using atmospheric models (Gustafsson et al., 2008). The good agreement between the two is indeed reassuring (Sect. 6.3.1).

Spectroscopy

Effective temperatures can also be estimated directly from the stellar spectrum, which contrary to photometric methods, is independent on the assumed value of the 'reddening'. The absolute flux needed to compute colours may be significantly affected by light-absorbing dust particles residing in gas clouds in the line-of-sight towards the star. This is called reddening, since the bluer wavelengths are more efficiently scattered by dust thereby making the star appear more red. Spectroscopic techniques, on the other hand, rely on the relative flux of spectral lines and continuum, and are therefore not affected by reddening.

As described in Sect. 6.3.1, we derive T_{eff} by fitting a LTE synthetic spectrum to the observed $\text{H}\alpha$ line profile. This spectral line originates from the bound-bound transition between the first and second excited state of neutral hydrogen ($n = 2 - 3$). The population of the first excited state of H I has a large temperature sensitivity in late-type stars, while the sensitivity to surface gravity and metallicity are small, making $\text{H}\alpha$ and other Balmer lines suitable T_{eff} -indicators. Obviously, the method is still model dependent to a certain extent, especially on the convection parameters of the model atmosphere (see Chapter 1), but also on the LTE assumption for the hydrogen level populations (see e.g. Barklem 2007b; Pereira et al. submitted). In addition, the hydrogen lines are broad features in these stars, and a reliable flat-fielding (Sect. 5.4.2) of the observed spectrum is critical to recover the true line shape (Korn et al., 2007).

Finally, we have also inferred effective temperatures from the LTE excitation equilibrium of Fe I. This atom has numerous spectral lines in the observed stars, originating from atomic states with a range of different excitation energies (0 – 5 eV). Therefore, if the temperature structure of the model is wrong, the abundances based on individual lines will show a systematic trend with the excitation potential of the lower level involved in the transition. By fine-tuning the effective temperature of the model, the abundances can be reconciled and the trend flattened. This technique may give very precise relative effective temperatures, especially if large number of lines are accessible. Further, it is advantageous that it is not sensitive to either reddening nor the detailed shape of the continuum. However, also this method is highly dependent on the model atmosphere and the LTE assumption. Even if a flat excitation equilibrium can be established, there is no guarantee that the inferred T_{eff} is correct, due to possible systematic errors in the modelling procedure

that have a differential impact on level populations of different excitation energies.

To conclude, all methods have their individual pros and cons and we chose to adopt a photometric T_{eff} -scale for all stars, mainly to make the analysis as homogeneous as possible. Our observations did not cover any Balmer lines for the hottest targets, nor did the spectra collected for these stars contain enough iron lines to establish the excitation equilibrium. In addition, we could minimise the impact of possible patchy reddening over the field-of-view by relying on fiducial colour-magnitude sequences (Sect. 6.2.2).

5.5.2 Surface gravity

Once the effective temperature has been determined, the surface gravity can be found by using the relations $L = 4\pi R^2 F = 4\pi R^2 \sigma T_{\text{eff}}^4$, $g = GM/R^2$ and the definition of absolute bolometric magnitude (Sect. 5.1). After some simplifications, we obtain for g in cgs units [cm/s^2]:

$$\log g = -12.51 + \log M/M_{\odot} + 0.4 \times M_{\text{bol}} + 4 \times \log T_{\text{eff}} \quad (5.1)$$

In addition to T_{eff} , it is thus necessary to have estimates of the stellar mass and the absolute bolometric magnitude. The former is determined from stellar evolution models, assuming a certain age (13.5 Gyr) and chemical composition of the cluster stars. The exact values are not critical, since the mass-dependence is comparably weak. The absolute bolometric magnitude is obtained from the observed (apparent) visual magnitude V , an estimate of the so called distance modulus ($V - M_V = 12.57$), as well as the bolometric correction. The distance modulus can be inferred by comparing the observed colour-magnitude diagram to photometry of field stars with similar properties and distances that are known through parallax measurements⁴. For NGC 6397, this has been done using the upper MS and SGB (12.58 ± 0.08 , Gratton et al. 2003) and dwarfs of spectral type M on the lower MS ($12.13 - 12.24$, Reid & Gizis 1998). Finally, the bolometric correction is obtained from T_{eff} and $[\text{Fe}/\text{H}]$, using the empirical calibration by Alonso et al. (1999).

There are also spectroscopic techniques to infer surface gravity, which we explore in Sect. 7.3.5. The most common method is to make use of the electron density-dependence of the ionisation equilibrium of iron (see Eq. 1.2). An LTE atmosphere of low surface gravity and electron density ($P_e \propto g^k$, where $k \approx 1/3 \dots 2/3$, Gray 2005) has a higher fraction of singly ionised iron compared to neutral. If the surface gravity of the model is incorrect, the iron abundance inferred from FeI will show a systematic offset from those inferred from FeII lines. Again, by reconciling the two species we obtain an estimate of $\log g$, containing a more or less severe bias due to the simplifying assumptions of 1D and LTE. In principal, all species with detectable spectral lines from different ionisation stages, such as Ca, Ti, and Cr, can be used to derive the surface gravity.

⁴The parallax distance is inferred by measuring the apparent movement of the star relative to the fixed positions of very distant objects, as the Earth orbits around the Sun.

Chapter 6

Signatures of intrinsic Li depletion and Li-Na anti-correlation in the metal-poor globular cluster NGC 6397

The following article was published in *Astronomy & Astrophysics* in August 2009 (Lind, Primas, Charbonnel, Grundahl, & Asplund). The work is based on data collected at European Southern Observatory (ESO), Paranal, Chile, under program IDs 077.A-0018(A) and 281.D-5028(A), as well as data collected with the Danish 1.54 m at European Southern Observatory (ESO), La Silla. Tables 6.2, 6.3, and 6.4 are only available in electronic form at the CDS: <http://vizier.u-strasbg.fr/viz-bin/VizieR?-source=J/A+A/503/545>.

6.1 Introduction

The detection of Li in the atmospheres of old and metal-poor Population II stars has opened up an observational link to the primordial Universe. ${}^7\text{Li}$ is indeed one of four isotopes that were synthesised by nuclear reactions shortly after the Big Bang. With the most recent determination of the baryon density from the 5-year release of WMAP data, $\Omega_b h^2 = 0.02273 \pm 0.00062$ (Dunkley et al., 2009), an initial abundance of $N({}^7\text{Li})/N(\text{H}) = 5.24^{+0.71}_{-0.67} \times 10^{-10}$ or $A(\text{Li}) = 2.72 \pm 0.06^1$ is obtained from standard Big Bang nucleosynthesis (BBNS) (Cyburt et al., 2008). This is significantly higher than what is found for the “Spite plateau” (Spite & Spite, 1982) in the Galactic halo, a well-defined Li abundance plateau consisting of metal-poor halo dwarfs and early SGB stars.

The plateau abundance in the field has been determined in a number of recent studies to span the range $A(\text{Li}) \approx 2.0 - 2.4$ for stellar metallicities $[\text{Fe}/\text{H}] = (-3.5) - (-1.0)$, with a possible tendency toward increasing lithium abundance with increasing metallicity

¹ $A(\text{Li}) = \log \left(\frac{N(\text{Li})}{N(\text{H})} \right) + 12$

(Ryan et al., 2001; Meléndez & Ramírez, 2004; Charbonnel & Primas, 2005; Asplund et al., 2006; Bonifacio et al., 2007a; Hosford et al., 2009; Aoki et al., 2009). Differences between the various analyses may arise from the choice of effective temperature scale and corrections for non-LTE effects. It is nevertheless clear that a discrepancy by a factor of 2 – 4 with the cosmological prediction is unavoidable, suggesting that the stars have undergone the corresponding surface depletion of Li. An important fact is that in all the recent observational analysis (i.e., 21st century) of halo field stars, no evidence of significant dispersion has been found along the plateau, except for a few stars with strong Li abnormalities (Ryan et al., 1999; Asplund et al., 2006).

Soon after the discovery of the Spite plateau, Michaud et al. (1984) predicted Li depletion under the combined action of gravitational settling and weak turbulence in the radiative zones of Population II stars. Using sophisticated stellar models that treat atomic diffusion and radiative acceleration from first principles, Richard et al. (2005) illustrate how the comparably low Li value found in old, metal-poor stars could be naturally explained, assuming rather strict limits to the turbulent transport extent and efficiency. However, as of today the nature of the underlying physical mechanism responsible for turbulence has not been definitively identified, the main difficulty for the conjectured processes (mass loss, rotation-induced mixing, ...) being to account for the negligible Li dispersion along the plateau.

Charbonnel & Primas (2005) revisited the literature Li data for halo field stars with particular focus on the evolutionary status of the sample stars. This study discovered for the first time that the mean Li value appear to be higher for the TO and SGB stars than for the dwarfs. This result, together with the finding that all halo stars with Li abnormalities (i.e., strong deficiency or high content) lie on, or originate from, the hot side of the plateau, lead the authors to suggest that the most massive (i.e., post-MS) of the halo stars still observable today have had a different Li history than their less massive dwarf counterparts. Charbonnel & Primas (2005) suggested that such a behaviour may be the signature of a transport process of chemical elements and angular momentum whose efficiency changes on the blue edge of the plateau. This behaviour corresponds to that of the generation and filtering of internal gravity waves in both Population II and I stars (Talon & Charbonnel, 2003; Charbonnel & Talon, 2008). Talon & Charbonnel (2004) describe how internal gravity waves coupled with rotation-induced mixing are expected to lead to higher Li homogeneity among the plateau dwarf stars than among the more massive, slightly evolved stars, a scenario which may explain the observational findings by Charbonnel & Primas (2005). Speaking in favour of this model is its ability to simultaneously explain the internal solar rotation profile and the time evolution of the Li abundance at the surface of solar- and F-type stars as seen in Galactic open clusters (Charbonnel & Talon, 2005).

By turning to stars in metal-poor Galactic globular clusters, the intrinsic stellar processes involved can be further constrained. This approach presents some obvious advantages. In particular, the evolutionary status of the observed stars can be determined unambiguously and, presumably, all stars in a cluster were born with the same metallicity (although the surface metallicities observed today may vary between stars in different evolutionary phases, due to the effects of atomic diffusion Korn et al. 2007; Lind et al.

2008).

NGC 6397 is one of the most well-studied metal-poor globular clusters and its Li content has been documented down to the magnitude of the cluster TO point in several studies (Pasquini & Molaro, 1996; Castilho et al., 2000; Thévenin et al., 2001; Bonifacio et al., 2002; Korn et al., 2006, 2007), however, with rather poor number statistics. Bonifacio et al. (2002) found $A(\text{Li}) = 2.34 \pm 0.06$ for the mean abundance of twelve TO stars, whereas Korn et al. (2007) found 2.24 ± 0.05 for five TO stars and 2.36 ± 0.05 for two SGB stars. By comparing this observed abundance difference of Li (as well as Fe, Ca, Mg, and Ti) to predictions from the stellar-structure models by Richard et al. (2005) and references therein, Korn et al. (2007) empirically constrain the efficiency of slow macroscopic motions counteracting atomic diffusion below the convective envelope, which should ultimately provide clues on the origin of turbulence. Note that some slow macroscopic process is also required to reproduce the observed morphologies of globular cluster colour-magnitude diagrams (VandenBerg et al., 2002).

Interpreting abundance trends in globular clusters must however be done with great caution. Indeed, it is well-known that globular-cluster stars present striking anomalies in their light element content that are not seen among their field counterparts (for reviews see e.g. Gratton et al. 2004; Charbonnel 2005). More precisely, C, N, O, Na, Mg, and Al abundances show large star-to-star variations within individual clusters. C and N, O and Na, and Mg and Al are respectively anti-correlated, the abundances of C, O, and Mg being depleted in some stars while those of N, Na, and Al are enhanced. Importantly, the abundance of Li was found anti-correlated with that of Na and correlated with that of O in turnoff stars in the more metal-rich globular clusters NGC 6752 and 47 Tuc (Pasquini et al., 2005; Bonifacio et al., 2007b). These abundance patterns are explained by contamination of the star-forming gas by hydrogen-processed material ejected by a first generation of short-lived massive globular-cluster stars. This increases the Na abundances while lowering the O and Li abundances with respect to the pristine cluster composition in a second generation long-lived low-mass stars. In the framework of the self-enrichment scenario the Li content of globular-cluster stars is actually an important tool to quantify the dilution factor between the ejecta of the massive stars responsible for pollution and the pristine intra-cluster matter (Prantzos & Charbonnel, 2006; Decressin et al., 2007b,a). Gratton et al. (2001) and Carretta et al. (2005) uncovered rather large variations in both O and Na, anti-correlated with each other, in SGB and dwarf stars in NGC 6397 (see also Norris & Da Costa 1995; Castilho et al. 2000 for bright giants). This cluster has thus suffered from internal pollution in its infancy.

In the present study we analyse Li and Na abundances for a large sample of stars in NGC 6397, in an attempt to disentangle the primordial value of Li, with effects of atomic diffusion and intrinsic stellar depletion on the one hand, and early cluster pollution on the other hand. Sect. 6.2 describes the observations and data reduction, Sect. 6.3 describes the determination of stellar parameters and the abundance analysis. In Sect. 6.4 we present the Li and Na abundances found, and in Sect. 6.5 we discuss signatures of Li depletion in the cluster. Sect. 6.6 summarises our conclusions.

6.2 Observations

The observations include spectroscopic data, described in Sect. 6.2.1, and photometric data, described in Sect. 6.2.2. All targets, coordinates, and photometry are listed in Table 6.2. The locations of the targets in the observed colour-magnitude diagram ($V - (v - y)$) of the cluster are shown in the right-hand panel of Fig. 6.5.

6.2.1 High and medium-high resolution spectroscopy

All our targets have been selected from the Strömgen *uvby* photometric survey carried out by F. Grundahl, matching the $(b - y)$ and c_1 ranges spanned by the field stars analysed by Charbonnel & Primas (2005). In total, 349 stars were observed across the colour-magnitude diagram of NGC 6397, from just below the cluster TO point ($V \approx 17$) to the end of the RGB ($V \approx 11.5$). Each evolutionary phase is well sampled with around 180 stars at the TO, 80 on the SGB, and 90 stars on the RGB. Here we present data from two observing runs with FLAMES on the VLT-UT2 (Pasquini et al., 2002), one that collected the Li data for the whole sample in June 2006 and a second run that completed the data set with Na abundance indicators for a subset of the targets in Aug. 2008. The dates, set-ups, exposure times, and atmospheric conditions are summarised in Table 6.1.

Both sets of observations have used the GIRAFFE+UVES combined mode of FLAMES, with Medusa fibres allocated to the faintest targets and UVES fibres allocated to the brightest end of the RGB. During the first observing campaign (2006), we selected the high-resolution GIRAFFE set-ups H679.7 (also known as HR15) and H627.3 (HR13), which yield respectively $R = 19\,000$ and $22\,300$, and spectral ranges of $660.7 - 696.5$ nm and $612.0 - 640.5$ nm. Both settings were observed in combination with the UVES Red 580 setting ($R = 47\,000$, spectral range: $480 - 680$ nm, with a small gap in the middle). The first GIRAFFE set-up covers the ${}^7\text{Li}$ resonance line at 670.7 nm, whereas the second setting covers the NaI doublet at $615.4/616.0$ nm.

Unfortunately, the detection of the NaI doublet at $615.4/616.0$ nm proved to be realistic only for the brightest targets of our sample, therefore preventing conclusions on the existence of a Li-Na anti-correlation. To overcome this problem, we proposed to observe a stronger NaI doublet (at 818.3 nm and 819.4 nm,) and were granted 3 hours through the Director General Discretionary Time channel in Aug. 2008. Because of the limited time request we carefully selected a sub-set of our initial sample, mainly including the brightest TO and SGB stars (in total, 117 stars), with both high and low Li. For these observations, we used the high-resolution GIRAFFE set-up H805.3A (also known as HR19A, characterised by $R = 14\,000$ and spectral range $774.5 - 833.5$ nm,) in combination with the UVES Red 860 set-up ($R = 47\,000$, spectral range $760 - 1000$ nm).

Standard data reduction of the 2006 GIRAFFE observations was performed with the Geneva Base Line Data Reduction Software (girBLDRS), version 1.13.1. To correct for the highly elevated dark current in the upper corner of the old CCD a carefully scaled and smoothed 2D dark-frame was subtracted from each science frame. The 2008 data were obtained after the GIRAFFE CCD upgrade that took place in Apr. /May 2008 and contain

negligible dark current. These data were reduced with the ESO GIRAFFE pipeline, version 2.5.3. UVES data reductions were performed with the FLAMES UVES pipeline, version 2.9.7.

After initial reduction followed sky-subtraction and radial-velocity correction. Through radial-velocity measurements we identified six non-members. Furthermore, we disregarded one star that appeared to be too metal-rich to be a cluster member, three stars that clearly fall off the cluster sequence, and yet three more stars for which the observed spectra are of too poor quality. All stars that were rejected are listed with comments in Table 6.2. The remaining sample consists of 32 stars with spectra obtained with the UVES Red 580 set-up (we hereafter refer to this set as the 'UVES sample') and 284 stars with spectra obtained with the GIRAFFE H679.7 and H627.3 set-ups. The UVES sample and the GIRAFFE sample have 11 stars in common. A sub-sample of eight stars were observed in the UVES Red 860 set-up and 117 with the GIRAFFE H805.3A set-up. The UVES sample and GIRAFFE sample have two stars in common.

The mean barycentric radial velocity obtained for all cluster members is $18.5 \pm 0.2 \text{ km s}^{-1}$, in good agreement with Lind et al. (2008) ($18.1 \pm 0.3 \text{ km s}^{-1}$) and Milone et al. (2006) ($18.36 \pm 0.09 (\pm 0.10) \text{ km s}^{-1}$).

6.2.2 Strömgren photometry

The Strömgren *uvby* photometry employed for this investigation was obtained at the Danish 1.54m telescope on La Silla, Chile, and is identical to the data set used by Korn et al. (2007); Lind et al. (2008). We reiterate the main points here. All *uvby* observations were collected during a two week run in May 1997, with a large number of observations of standard stars observed on the photometric nights. The field covered is roughly $9'$ in diameter and slightly west of the cluster centre. For the photometric reductions we used the same programs and procedures as described in Grundahl et al. (1998, 1999, 2000, 2002b). The photometric zero points in *vby* have errors of approximately 0^m01 .

The observed $(b - y)$, $(v - y)$, and c_1 colours were corrected for the reddening of NGC 6397, using the relations $E_{b-y} = 0.74 \times E_{B-V}$, $E_{v-y} = 1.70 \times E_{b-y}$, and $E_{c_1} = 0.20 \times E_{b-y}$ (Crawford, 1975). We adopted a value of 0.179 for E_{B-V} , following Anthony-Twarog & Twarog (2000), and 12.57 for the cluster distance modulus. The observed colours of our targets show a spread around the cluster sequence, of the order of 2.2% for $(v - y)$ and larger, 3.7%, for $(b - y)$. To reduce the uncertainty in the photometric colours we constructed colour-magnitude fiducials for the cluster, as described in Korn et al. (2007); Lind et al. (2008). The observed colour is interpolated at constant V -magnitude onto the fiducial sequence. The main advantage of using this method is that relative effective temperatures are more precisely determined, which in turn lowers the spread in chemical abundances.

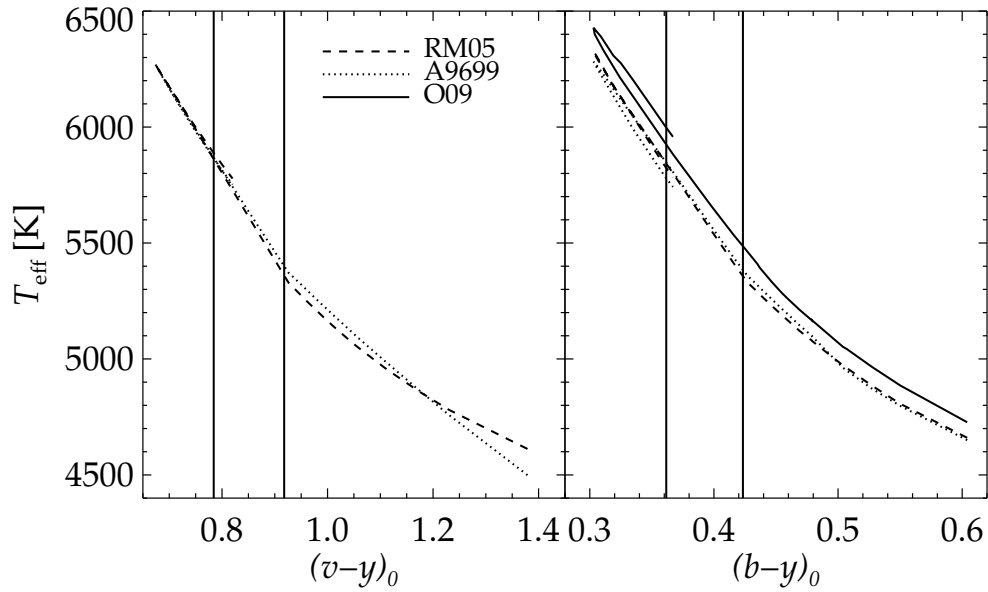


Figure 6.1: The $(b - y) - T_{\text{eff}}$ and $(v - y) - T_{\text{eff}}$ relations considered in the analysis. The vertical lines mark the area that is linearly interpolated (see text). The scale by Önehag et al. (2009, O09) for pre-TO stars fall above the one for post-TO stars and vice versa for the scale by Alonso et al. (1996, 1999, A9699). The scale by Ramírez & Meléndez (2005, RM05) is the same for pre- and post-TO stars.

Table 6.1: FLAMES observations.

Date	UVES setting	GIRAFFE setting	Exposure time [s]	Average seeing ["]
2006 Jun 19	Red 580	H627.3	2×2775	1.08
2006 Jun 19	Red 580	H679.7	1×2775	1.08
2006 Jun 20	Red 580	H679.7	2×2775	1.08
2006 Jun 20	Red 580	H627.3	2×2775	1.01
2006 Jun 21	Red 580	H627.3	2×2775	0.75
2006 Jun 21	Red 580	H679.7	3×2775	0.78
2006 Jun 26	Red 580	H627.3	3×2775	1.16
2006 Jun 26	Red 580	H679.7	2×2775	0.76
2006 Jun 27	Red 580	H679.7	1×2775	0.56
2006 Jun 27	Red 580	H627.3	3×2775	0.46
2006 Jun 28	Red 580	H679.7	3×2775	0.69
2008 Aug 3	Red 860	H805.3A	2×2775	0.94
2008 Aug 28	Red 860	H805.3A	1×2775	1.17

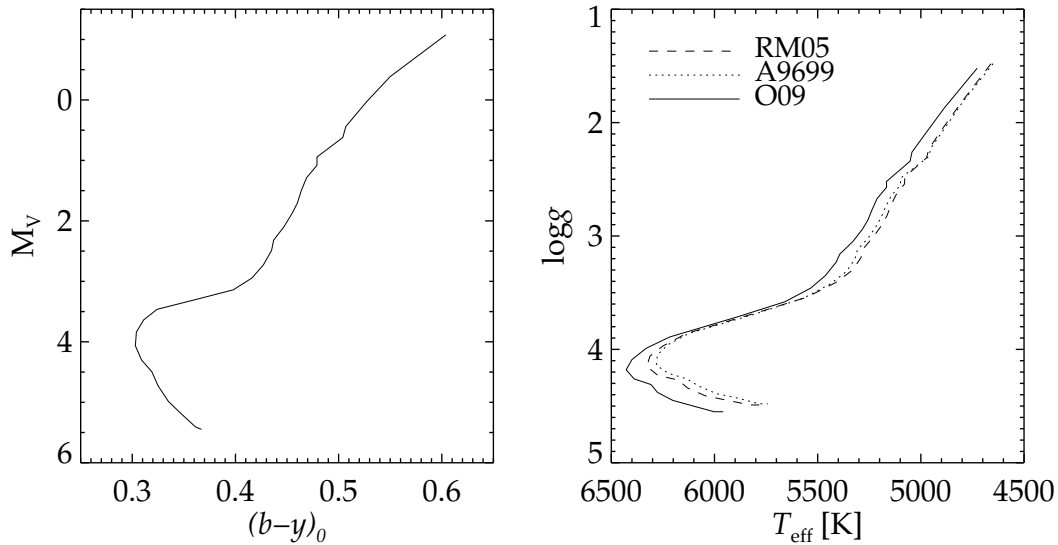


Figure 6.2: *Left:* The $(b-y)_0 - M_V$ fiducial used to derive stellar parameters. *Right:* The three $(b-y)$ -based stellar-parameter sets.

Table 6.3. Iron lines measured in the UVES spectrum of the RGB star #17691. The full table can be retrieved from CDS/Vizier.

Ion	λ [nm]	$\log gf$	Ref.	W_λ [pm]	A(Fe)
FeI	491.9	-0.34	1	9.43 ± 0.12	5.38 ± 0.03
FeI	498.6	-1.33	1	4.76 ± 0.05	5.38 ± 0.01
FeI	499.4	-2.97	1	8.24 ± 0.10	5.55 ± 0.03
FeI	501.5	-0.30	1	4.00 ± 0.07	5.41 ± 0.01
FeI	502.8	-1.12	1	1.97 ± 0.05	5.36 ± 0.01
FeI	504.4	-2.02	1	1.82 ± 0.08	5.39 ± 0.02
FeI	506.0	-5.43	1	2.22 ± 0.09	5.64 ± 0.02
FeI	508.3	-2.84	1	8.52 ± 0.09	5.53 ± 0.02
FeI	512.7	-3.25	1	7.19 ± 0.05	5.56 ± 0.01
FeI	514.2	-2.24	1	3.35 ± 0.06	5.49 ± 0.01
FeI	519.9	-2.09	1	5.19 ± 0.11	5.47 ± 0.02
FeI	521.7	-1.16	1	3.95 ± 0.08	5.42 ± 0.02
FeI	522.6	-4.76	1	4.71 ± 0.09	5.60 ± 0.02
FeI	523.3	-0.06	1	10.25 ± 0.10	5.30 ± 0.02
FeI	524.2	-0.97	1	2.54 ± 0.05	5.41 ± 0.01
FeI	524.7	-4.97	1	4.03 ± 0.09	5.66 ± 0.02
FeI	530.7	-2.91	1	4.46 ± 0.10	5.44 ± 0.02
FeI	534.0	-0.72	1	5.98 ± 0.09	5.43 ± 0.02
FeI	536.5	0.23	1	3.48 ± 0.05	5.32 ± 0.01
FeI	536.5	-1.02	1	1.95 ± 0.09	5.23 ± 0.03
FeI	538.3	0.64	1	5.55 ± 0.04	5.16 ± 0.01
FeI	539.7	-1.98	1	12.90 ± 0.09	5.58 ± 0.02
FeI	540.6	-1.85	1	12.87 ± 0.07	5.53 ± 0.01
FeI	541.5	0.64	1	4.91 ± 0.08	5.12 ± 0.02
FeI	550.1	-3.05	1	8.64 ± 0.08	5.70 ± 0.02
FeI	550.7	-2.79	1	9.46 ± 0.08	5.68 ± 0.02
FeI	556.7	-2.67	1	0.91 ± 0.03	5.39 ± 0.02
FeI	570.2	-2.14	1	2.79 ± 0.07	5.40 ± 0.02
FeI	595.7	-4.50	1	1.66 ± 0.06	5.49 ± 0.02
FeI	606.5	-1.41	1	5.94 ± 0.11	5.32 ± 0.02
FeI	613.7	-1.41	1	7.90 ± 0.12	5.55 ± 0.03
FeI	615.2	-3.37	1	0.84 ± 0.07	5.53 ± 0.04
FeI	621.3	-2.48	1	3.24 ± 0.07	5.42 ± 0.01
FeI	621.9	-2.45	1	4.08 ± 0.09	5.52 ± 0.02
FeI	624.1	-3.17	1	0.94 ± 0.03	5.43 ± 0.02
FeI	625.3	-1.77	1	6.90 ± 0.07	5.63 ± 0.01
FeI	626.5	-2.54	1	3.66 ± 0.08	5.51 ± 0.02
FeI	634.4	-2.88	1	1.03 ± 0.10	5.42 ± 0.05

Table 6.3. Continued.

Ion	λ [nm]	$\log gf$	Ref.	W_λ [pm]	A(Fe)
FeI	639.4	-1.58	1	7.47 ± 0.08	5.58 ± 0.02
FeI	641.2	-0.72	1	4.02 ± 0.06	5.43 ± 0.01
FeI	643.1	-1.95	1	6.75 ± 0.07	5.49 ± 0.01
FeI	648.2	-3.01	1	1.42 ± 0.12	5.53 ± 0.04
FeI	649.5	-1.24	1	8.87 ± 0.08	5.50 ± 0.02
FeI	649.9	-4.69	1	1.28 ± 0.06	5.63 ± 0.02
FeI	660.9	-2.66	1	1.34 ± 0.08	5.46 ± 0.03
FeI	666.3	-2.46	1	2.72 ± 0.09	5.50 ± 0.02
FeI	667.8	-1.42	1	6.65 ± 0.15	5.53 ± 0.03
FeI	675.0	-2.58	1	2.12 ± 0.11	5.47 ± 0.03
$\langle A(\text{Fe})_{\text{I}} \rangle = 5.45 \pm 0.02$					
FeII	492.4	-1.32	4	10.30 ± 0.13	5.37 ± 0.03
FeII	510.1	-4.14	2	0.34 ± 0.07	5.38 ± 0.09
FeII	519.8	-2.23	2	4.87 ± 0.10	5.45 ± 0.02
FeII	523.5	-2.15	2	5.13 ± 0.13	5.40 ± 0.03
FeII	526.5	-3.13	3	1.25 ± 0.15	5.46 ± 0.06
FeII	528.4	-3.19	3	2.48 ± 0.10	5.52 ± 0.02
FeII	532.6	-3.22	2	1.21 ± 0.10	5.52 ± 0.04
FeII	541.4	-3.64	3	0.54 ± 0.08	5.55 ± 0.07
FeII	542.5	-3.37	2	1.02 ± 0.10	5.55 ± 0.05
FeII	553.5	-2.87	3	2.35 ± 0.03	5.54 ± 0.01
FeII	614.9	-2.72	2	0.74 ± 0.08	5.49 ± 0.05
FeII	624.8	-2.33	2	1.64 ± 0.10	5.49 ± 0.03
FeII	636.9	-4.25	2	0.46 ± 0.07	5.68 ± 0.07
FeII	645.6	-2.08	2	2.37 ± 0.09	5.45 ± 0.02
$\langle A(\text{Fe})_{\text{II}} \rangle = 5.49 \pm 0.02$					
(1) O'Brian et al. (1991)				(2) Biemont et al. (1991)	
(3) Raassen & Uylings (1998)				(4) Fuhr et al. (1988)	

6.3 Analysis

For the abundance analysis we used a grid of 1D, LTE, plane-parallel and spherical, MARCS model atmospheres (Gustafsson et al., 2008). LTE abundances of Li and Na were derived from spectrum synthesis, using the Uppsala code BSYN. Non-LTE abundance corrections were thereafter applied. LTE abundances of Fe and Ca were derived from equivalent width measurements, using the corresponding Uppsala code EQWIDTH.

6.3.1 Effective temperatures and surface gravities

The cluster *uvby*-photometry was used to calculate effective temperatures for the whole sample. We implemented a number of different calibrations based on the colour indices $(v - y)$ and $(b - y)$ and c_1 . Table 6.2 lists effective temperatures calculated using the relations published in Alonso et al. (1996, 1999); Ramírez & Meléndez (2005); Önehag et al. (2009). The first three are calibrated on the infra-red flux method (IRFM), whereas the last is based on theoretical colours from MARCS model atmospheres (Gustafsson et al., 2008). For all stars we assumed $[\text{Fe}/\text{H}] = -2.0$. The IRFM colour- T_{eff} relations constructed for MS stars were calibrated on stars with $\log g \gtrsim 3.8$. We accordingly set a limit in absolute visual magnitude, $M_V > 3.3$, for which the MS calibrations are trusted. Analogously, the giant calibrations were calibrated on stars with $\log g \lesssim 3.5$ and we trust them for $M_V < 2.8$. This leaves a gap on the SGB where no calibration is suitable. In this range we interpolated linearly between each dwarf- and giant-calibration pair (see vertical lines in Fig. 6.1). To each of the obtained effective-temperature scales we calculated surface gravities from the relation between surface gravity, effective temperature, stellar mass, and luminosity. The details of the calculations are given in Lind et al. (2008).

Önehag et al. (2009) have calculated synthetic $(b - y)$ -colours for a grid of effective temperatures, surface gravities, and metallicities. We interpolated in the grid constructed for $[\text{Fe}/\text{H}] = -2.0$, which spans the parameter-space of the sample (see Fig. 4 in Önehag et al. 2009). The interpolation was done iteratively until the parameters found for each star were fully consistent, i.e. the $T_{\text{eff}} - \log g$ pairs found based on the observed colour are also constrained by relation to mass and luminosity.

For the 32 RGB stars observed with UVES, we could also derive $\text{H}\alpha$ -based effective temperatures, using BSYN. Stark broadening is based on the tabulations by Stehlé & Hutcheon (1999) and self-broadening of hydrogen follow Barklem et al. (2000). The fitting method is automated and based on metal line-free regions extending up to ± 5 nm from the line centre (Lind et al., 2008), avoiding the line core. The wings of the $\text{H}\alpha$ -line become very narrow high up on the RGB, but some sensitivity to effective temperature remains also for these stars. With a high S/N -ratio it is possible to constrain T_{eff} also for the coolest stars in our sample.

Figure 6.2 shows a comparison between all $(b - y) - T_{\text{eff}}$ and $(v - y) - T_{\text{eff}}$ relations. The $(b - y)$ -calibration by Önehag et al. (2009) matches the slope of the corresponding IRFM-based calibrations well, but is offset to higher effective temperatures by approximately 100 K. However, a recent updated calibration based on the IRFM finds effective temperatures that are higher than the existing IRFM calibrations, by similar order of magnitude, at these metallicities (Casagrande et al., 2010). Interestingly, Önehag et al. (2009) predicts slightly higher effective temperatures for dwarfs compared to SGB stars of the same colour, whereas the IRFM scale of Alonso et al. (1996, 1999) has the opposite behaviour (through the sensitivity to the c_1 -index). The interpolation between dwarf and giant calibrations appears more suitable for the $(b - y)$ -relations. The two $(v - y)$ MS scales are too flat to match the slope of the corresponding giant relations well. For this reason we regard the $(b - y)$ -relations as more trustworthy and place greater weight on those. The $\text{H}\alpha$ -based

values are generally cooler than all photometric calibrations, but the relative agreement is satisfactory.

The right panel of Fig. 6.2 shows all $(b - y)$ -based effective-temperature scales with corresponding surface gravity values. Apparently, the two IRFM scales agree well for all but the hottest stars, where the scale by Alonso et al. (1996, 1999) predicts cooler effective temperatures. Again it is seen that the theoretical MARCS scale is offset to higher effective temperatures. The left panel of Fig 6.2 shows the cluster fiducial for $(b - y)_0 - M_V$.

6.3.2 Metallicity

To constrain the cluster metallicity and microturbulence values, we calculated iron abundances from Fe I and Fe II lines for the UVES sample. The ionisation and excitation equilibrium of Fe also provide an additional check of the derived stellar parameters. We selected 48 unblended Fe I lines that have oscillator strengths determined by O'Brian et al. (1991) and 14 Fe II lines that have oscillator strengths determined by Biemont et al. (1991); Raassen & Uylings (1998); Fuhr et al. (1988). Equivalent widths were measured by fitting Gaussian line profiles to the observed, fixing the FWHM of lines weaker than 5 pm to the average value for each individual star. In the GIRAFFE spectra only very few Fe I and Fe II lines are available and it is not possible to obtain reliable measurements for the fainter half of the sample. Table 6.3 lists all Fe I and Fe II lines with references to the adopted $\log gf$ values, as well as the equivalent widths and abundances derived for one RGB star. The full table, including all UVES targets, can be retrieved from the CDS. The table lists also the average abundance derived from Fe I and Fe II lines, respectively, with the error bar representing the standard deviation of the mean abundance.

Microturbulence (χ_t) values were determined by requiring that Fe abundances show no trend with reduced equivalent width ($\log(W_\lambda/\lambda)$) of Fe I lines. We empirically constructed a linear parametrisation of microturbulence with surface gravity, using the UVES targets only, and adopted it for the whole sample. This involved extrapolation to the SGB stars and dwarfs, since our observations do not cover enough strong lines that are sensitive to microturbulence in these stars. The impact on the inferred Li abundances is however negligible. The largest equivalent width measured for the Li line is 6.18 pm, for the SGB star #13160. Varying the microturbulence between 1 km s^{-1} and 2 km s^{-1} lowers the Li abundance inferred for this star by only 0.01 dex.

The excitation equilibrium of Fe is commonly used to constrain effective temperatures. However, 3D modelling of stellar atmospheres show that especially low excitation lines may give strongly overestimated abundances in 1D models of metal-poor stars (Asplund et al., 1999; Collet et al., 2007). In addition, non-LTE effects are likely to have different impact on lines of different excitation potential (Asplund, 2005). The extent to which this could bias the excitation equilibrium is presently not clear. The left-hand histogram in Fig. 6.3 shows the slope of Fe abundances with excitation potential of Fe I lines, derived with the stellar parameter scales by Alonso et al. (1996, 1999) and Önehag et al. (2009). Apparently, both scales are too hot to satisfy the equilibrium. The necessary corrections are of order $(-100) - (-200) \text{ K}$.

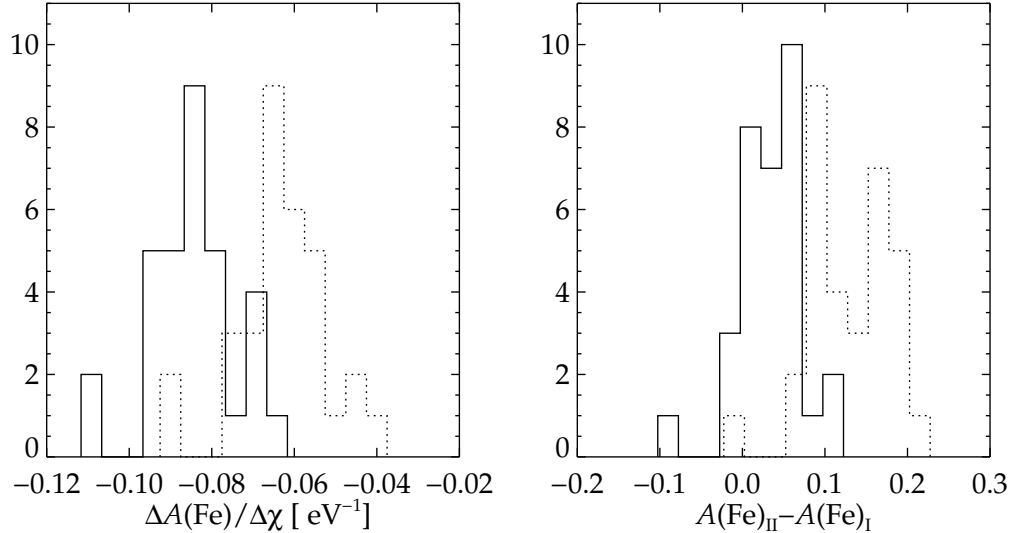


Figure 6.3: *Left:* Histogram of the slope of Fe abundance with excitation potential of neutral and singly ionised Fe lines. Only the UVES sample is shown. Solid lines represent the effective temperature scale by Önehag et al. (2009) and dotted lines the scale by Alonso et al. (1996, 1999). *Right:* Histogram of Fe abundance derived from Fe II lines minus the Fe abundance derived from Fe I lines.

The right-hand histogram in Fig 6.3 shows the Fe abundance derived for singly ionised Fe lines minus the Fe abundance derived from neutral Fe lines. The scale by Alonso et al. (1996, 1999) shows an offset from zero of approximately -0.14 dex, whereas the scale by Önehag et al. (2009) has a smaller offset, -0.05 dex. The mean Fe abundance, as determined from Fe II lines, is 5.41 ± 0.01 , using both scales, with a 1σ dispersion of 0.04 dex. Adopting a solar abundance $A(\text{Fe})_{\odot} = 7.51$ (Asplund et al., 2009), we obtain $[\text{Fe}/\text{H}] = -2.10$. This is in good agreement with most recent estimates made for RGB stars in this cluster; Korn et al. (2007) find -2.12 ± 0.03 for their RGB sample, Gratton et al. (2001) $[\text{Fe}/\text{H}] = -2.03 \pm 0.02 \pm 0.04$, and Castilho et al. (2000) $[\text{Fe}/\text{H}] = -2.0 \pm 0.05$. Lind et al. (2008) report a lower value, $[\text{Fe}/\text{H}] \approx -2.3$, for stars at the base of RGB. The last study implements a cooler effective temperature-scale and base the abundances mainly on Fe I lines, which explains the offset.

The investigation is not indicating that one of the stellar-parameter sets is clearly preferable to the other, but we used the scale by Önehag et al. (2009) to derive abundances of all other elements, because this is the most homogeneous. The changes in Li abundances when implementing the IRFM stellar-parameter scales are discussed in Sect. 6.5.2.

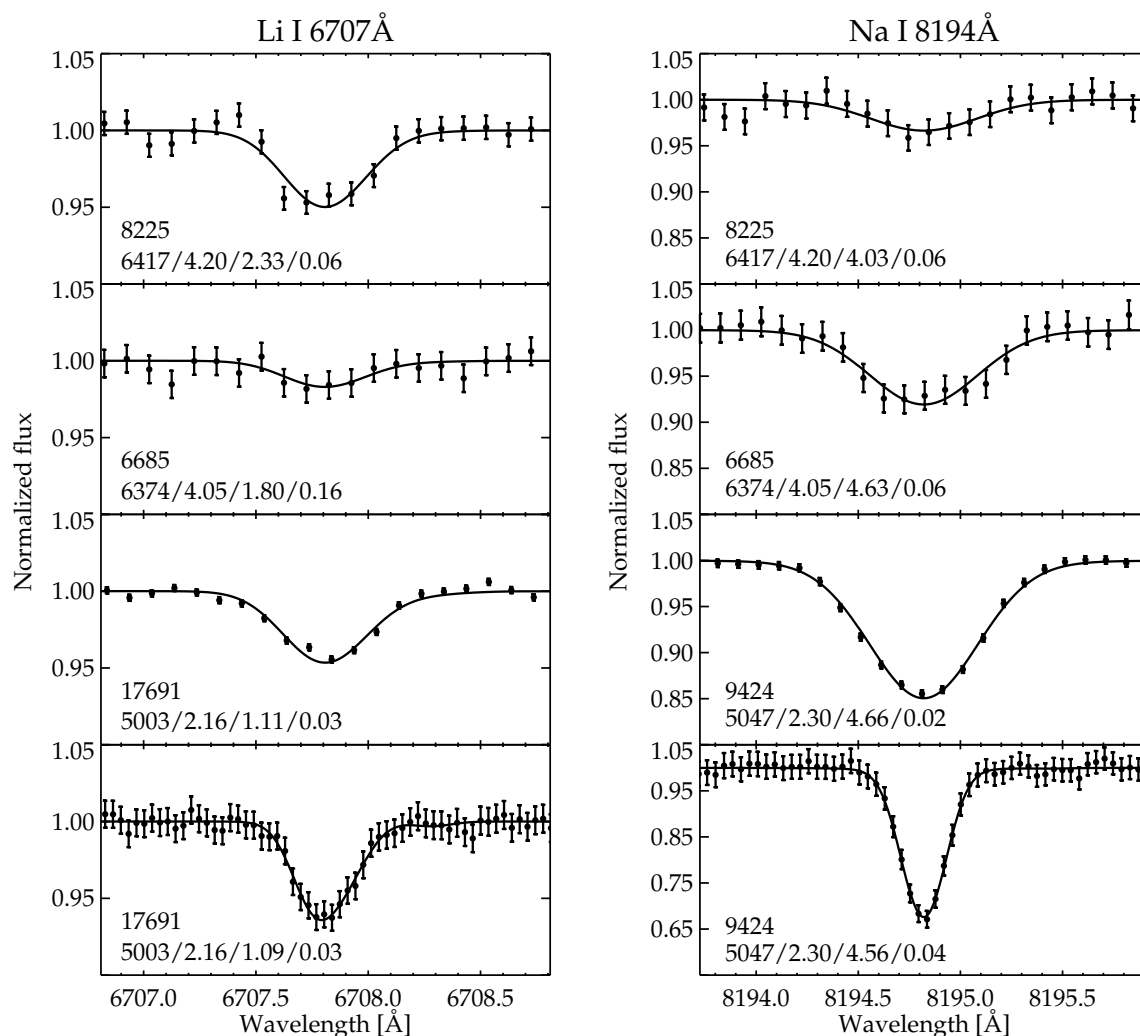


Figure 6.4: Example fits of the Li I 670.7 nm line and the Na I 819.4 nm line. In each panel is indicated the identification number of the star, stellar parameters, and LTE abundance inferred from the given line, according to the syntax $T_{\text{eff}}/\log g/A(x)/e(x)$, where x is the corresponding element and $e(x)$ the error in abundance. *Top:* A Li and Na-normal TO star. *Second from the top:* A Li-poor and Na-rich TO star. *Second from the bottom:* GIRAFFE giant spectrum. *Bottom:* UVES spectrum of same giant.

6.3.3 Lithium

The ${}^7\text{Li}$ resonance line at 670.7 nm has two fine-structure components, separated only by 0.015 nm. At the resolution of GIRAFFE ($R = 19300$) they are indistinguishable, but a small line-asymmetry can be seen in the higher-resolution UVES spectra ($R = 47000$). Accurate measurements of the line require spectrum synthesis (see example fits of the line in Fig.6.4). We adopted $\log gf = -0.009$ and -0.309 for the two components respectively, according to Lindgård & Nielson (1977).

To derive Li LTE abundances for the stars we first normalised each spectrum by iterative fitting of a first order polynomial, taking into consideration a wavelength region extending ± 0.2 nm from the line centre. Synthetic line profiles were convolved with a Gaussian profile to account for the instrumental broadening and broadening due to rotation and macroturbulence. The width of the convolving profile was fixed for each star by measurements of single lines of other species. The Li abundance was then varied to find the best fitting synthetic profile for each star through χ^2 -minimisation. In total, Li abundances or upper abundance limits could be obtained for 305 stars. Following Norris et al. (2001) and Barklem et al. (2005), errors due to observational uncertainties were estimated with the expression: $\sigma_{W_\lambda} = \lambda\sqrt{(n)/(R \times S/N)}$, where n denotes the number of pixels spanning the full-width at half maximum for the line, R the spectral resolution, and S/N the signal-to-noise ratio per pixel.

Non-LTE abundance corrections for Li were calculated according to Lind et al. (2009a), a study that is based on calculations on the same MARCS model atmospheres as here (Gustafsson et al., 2008). In contrast to earlier non-LTE analyses (e.g. Carlsson et al. 1994; Takeda & Kawonomoto 2005) the study makes use of rigorous quantum mechanical calculations (as opposed to the debated but common classical recipes) of cross-sections for collisions with neutral hydrogen, which have influence over the statistical equilibrium of Li. Lind et al. (2009b) show that including the charge transfer reactions between Li and hydrogen in the non-LTE calculations gives abundance corrections that are lower by almost -0.1 dex for dwarfs at $[\text{Fe}/\text{H}] = -2.0$, as compared to neglecting them. For our sample, the MS, TO, and early SGB stars all have non-LTE corrections that are very similar, around -0.06 dex. With decreasing effective temperature and surface gravity the corrections change sign and reach a maximum of $+0.13$ dex for the coolest RGB star.

6.3.4 Sodium

Sodium abundances or upper abundance limits were derived from the 2008 observations for a subset of 117 stars, mainly TO stars and early SGB stars. The abundances were based on the Na I 818.3 nm and 819.4 nm doublet (when the former was too weak to be detected, only the latter was used). This doublet is second in strength after the resonance doublet at 588.5 nm and 589.0 nm, which is strongly affected by interstellar extinction for the cluster stars and is therefore not useful as abundance indicator. As mentioned above, the 568.2/568.8 nm and 615.4/616.0 nm doublets are too weak to be suitable for abundance analysis in the TO region at this metallicity. Despite its unfortunate location in the middle

of a strong telluric band, the 818.3/819.4 nm NaI doublet does not suffer strongly from atmospheric blends that would bias the abundance analysis.

The line-fitting method is the same as described for Li and oscillator strengths by Kurucz & Peytremann (1975) were adopted. We apply non-LTE abundance corrections to the 818.3/819.4 nm NaI lines according to Mashonkina et al. (2000)². The size of the corrections at this metallicity ranges from -0.14 dex for the hottest, highest surface gravity stars, to approximately -0.31 dex for the coolest giants.

6.3.5 Calcium

For the complete sample of 305 stars, only the equivalent widths of Ca lines 612.2 nm and 616.2 nm could be reliably measured. We based the Ca abundance on these two lines for 305 stars, adopting oscillator strengths from Smith & O’Neill (1975)

6.4 Results

6.4.1 Li abundances

Table 6.4 lists the adopted stellar parameters, equivalent widths, and abundances. Fig. 6.5 shows the Li abundances inferred side-by-side with a colour-magnitude diagram where the spectroscopic targets are marked. In agreement with the expectations (see Sect. 6.1), there is a rather well defined abundance plateau among the least evolved stars, followed by a drastic drop in Li abundance in the middle of the SGB ($M_V \approx 3.3$). This pattern is caused by the so-called first dredge-up, i.e., the dilution of the external convective stellar layers with deeper hydrogen-processed material. A second steep drop occurs at $M_V \approx 0.0$, which corresponds to the luminosity of the RGB bump. A similar decrease in Li abundance has been identified in stars located around the RGB bump in NGC 6752 (Grundahl et al., 2002a) as well as in stars in the halo field (Gratton et al., 2000). Charbonnel & Zahn (2007) describe how this second Li abundance drop can be explained by a mixing process called thermohaline convection, which becomes efficient when the hydrogen-burning shell crosses the chemical discontinuity left behind by the first dredge-up, and which rapidly transports surface Li down to internal hotter regions where this fragile element burns.

The average Li abundance on the plateau, i.e. only including stars that have not undergone dilution due to the first dredge-up ($M_V > 3.3$), is 2.25 ± 0.01 , where the error is the standard deviation of the mean. The 1σ dispersion is 0.09 dex.

²The non-LTE calculations presented in Chapter 2 had not been computed at the time of this analysis. We have verified that the non-LTE corrections by Mashonkina et al. (2000) are very similar to our work for the specific lines and stellar parameter space

Table 6.4: Adopted stellar parameters, equivalent widths, and Li, Na, and Ca abundances. The full table can be retrieved from CDS/Vizier.

ID	M_V	T_{eff} [K]	$\log g$	ξ [km/s]	$\log L/L_{\odot}$	$W_{\lambda} 670.7$ [pm]	$A(\text{Li})$	$W_{\lambda} 818.3$ [pm]	$W_{\lambda} 819.5$ [pm]	$A(\text{Na})$	$W_{\lambda} 612.2$ [pm]	$W_{\lambda} 616.2$ [pm]	$A(\text{Ca})$
12138	-1.077	4727	1.52	1.61	2.49	< 0.44	< 0.08	8.85	11.49	4.29	10.91	12.19	4.70
16405	-0.799	4790	1.66	1.58	2.37	< 0.42	< 0.17	± 0.31	± 0.17	± 0.03	± 0.08	± 0.06	± 0.01
14565	-0.709	4811	1.71	1.58	2.33	< 0.43	< 0.19	± 0.06	± 0.02	± 0.01
5644	-0.646	4826	1.74	1.57	2.30	< 0.55	< 0.25	10.30	11.39	4.62
17163	-0.439	4873	1.84	1.56	2.21	0.43	0.19	± 0.02	± 0.07	± 0.01
20820	-0.288	4905	1.92	1.54	2.15	0.70	0.50	10.25	11.40	4.62
8952	-0.029	4955	2.04	1.52	2.04	1.18	0.82	± 0.08	± 0.09	± 0.01
16303	0.024	4965	2.07	1.52	2.02	2.25	1.10	9.97	11.07	4.62
10447	0.077	4975	2.09	1.52	1.99	1.87	1.04	± 0.07	± 1.2	± 0.01
10737	0.090	4977	2.10	1.51	1.99	2.22	1.10	9.78	0.84	4.64
13006	0.220	5002	2.16	1.50	1.93	2.18	1.16	± 0.03	± 0.06	± 0.01
17691	0.229	5003	2.16	1.50	1.93	2.28	1.16	4.00	6.52	3.90	9.40	0.67	4.74
21284	0.463	5044	2.27	1.49	1.83	1.83	1.08	± 0.27	± 0.16	± 0.02	± 0.07	± 0.04	± 0.01
9424	0.528	5047	2.30	1.48	1.81	2.03	1.12	8.62	9.57	4.56
16248	0.563	5049	2.31	1.48	1.79	1.85	1.10	6.77	10.13	4.28	± 0.09	± 0.12	± 0.01
13791	0.650	5062	2.36	1.47	1.76	1.64	1.03	± 0.08	± 0.09	± 0.01	8.43	9.62	4.55
11363	0.882	5144	2.49	1.45	1.66	1.36	1.04	± 0.10	± 0.11	± 0.01
...	6.78	10.34	4.33	8.31	9.54	4.53
...	± 0.20	± 0.09	± 0.02	± 0.13	± 0.14	± 0.02
...	8.15	9.18	4.56
...	± 0.12	± 0.13	± 0.02

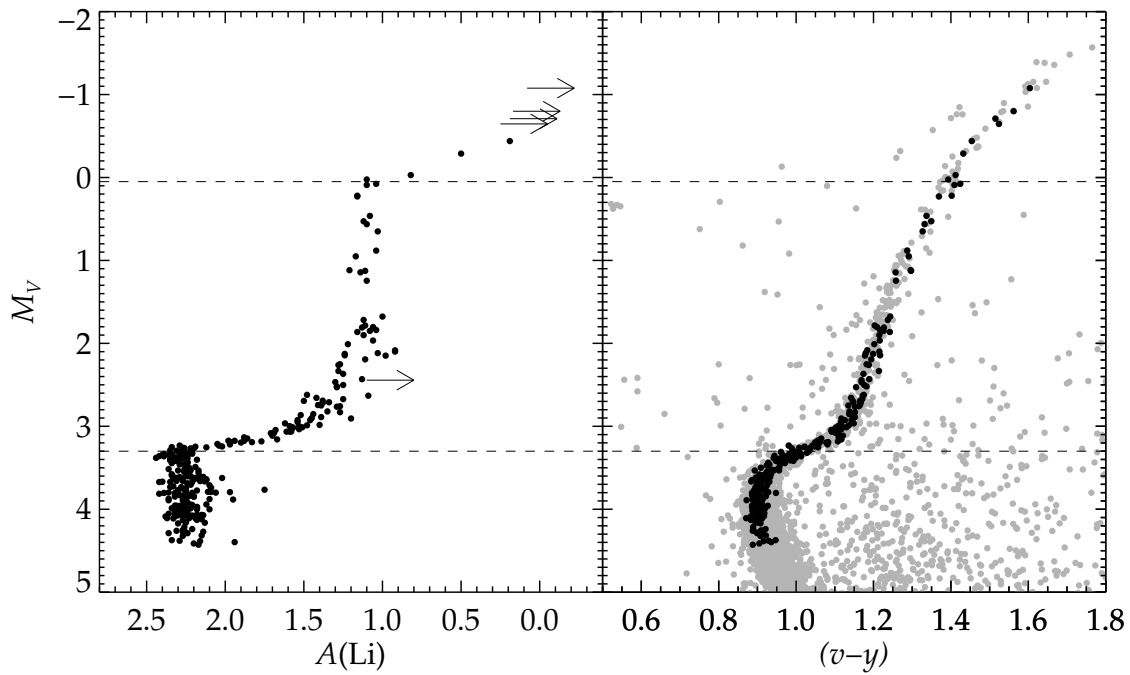


Figure 6.5: *Left:* The abscissa shows non-LTE Li abundances inferred for our sample (the archival data are not included) and the ordinate absolute visual magnitude ($M_V = V - 12.57$). Arrows mark Li upper limits. *Right:* The spectroscopic targets marked with black filled circles in the colour-magnitude diagram of NGC 6397. The two horizontal dashed lines mark the locations of rapid decrease in Li abundance caused by stellar evolution (see text).

6.4.2 Lithium data from the ESO archive

To establish a view of the Li content in NGC 6397 that is as complete as possible, we have searched the ESO archive for observations of more MS, TO, and SGB stars. Especially, to put constraints on the size and significance of a small increase in $A(\text{Li})$ located just before the onset of the first dredge-up (see Sect. 6.5.1 and Fig. 6.6) we would benefit from having more stars. In previous analyses, Bonifacio et al. (2002) analyse Li in twelve TO stars (of which seven stars were previously analysed by Thévenin et al. 2001 and three stars by Pasquini & Molaro 1996) and Korn et al. (2007) analyse five TO stars and two SGB stars. We did not incorporate those stars in our analysis since it would only slightly have increased the number statistics. However, we have retrieved and analysed a set of FLAMES archival data from 2007 (079.D-0399(A), P.I. Gonzalez-Hernandez). These include observations in the GIRAFFE high-resolution set-up H665.0 (HR15N, $R = 17000$), covering the LiI 670.7 nm line for a sample of 80 dwarfs ($M_V \approx 4.9$) and 88 SGB stars ($M_V \approx 3.4$) in NGC 6397. The reduction of the data was performed with the girBLDRS pipeline. In total, 38 MS stars and 55 SGB stars were identified in our *wby* photometric catalogue. For the remaining stars, we add a zero-point correction of 0.09 magnitudes to the visual magnitude scale listed in the archival data, estimated from the targets that were cross-matched between the catalogues. Applying the correction, the two magnitude scales match to typically within 0.02 magnitudes for individual targets. After establishing the visual magnitudes, colours are assigned to each target by interpolating V onto the fiducial cluster sequences, as was done for the main sample (see Sect. 6.2.2).

The results of the analysis of the archival data are shown together with our own data set in Fig. 6.6. One more very Li-poor star, marked with an arrow, was identified in the archive sample, for which only an upper limit to Li could be derived. Especially, the region around $M_V = 3.2 - 3.5$ is now much better sampled, with the archival data confirming the presence of the small abundance increase just before the steep drop. In addition, the plateau is extended to fainter magnitudes, $M_V \approx 5$. Including this archive sample we have Li abundances for 454 stars in the cluster, of which 346 have $M_V > 3.3$. Overall the qualities of the data sets are similar and the abundances agree very well between the samples. In total, 14 SGB stars overlap and thus have observations of the Li line in the H665.0 as well as in the H679.7 setting. The mean difference in Li abundance between these 14 stars is -0.02 ± 0.02 dex, i.e. there is no systematic bias between the data sets.

The average Li abundance on the plateau (i.e., excluding stars with $M_V < 3.3$), including both our data and the archival data, is 2.270 ± 0.005 . Unfortunately Na information is not available for the archive targets.

6.4.3 The Li-Na anti-correlation

As discussed in Sect. 6.1, globular-cluster samples may suffer from bias due to early pollution of the intra-cluster gas by a first generation of more massive, faster evolving stars. It is thus important to discriminate between first-generation stars that formed out of pure pristine material and second-generation stars that formed out of polluted material. The former

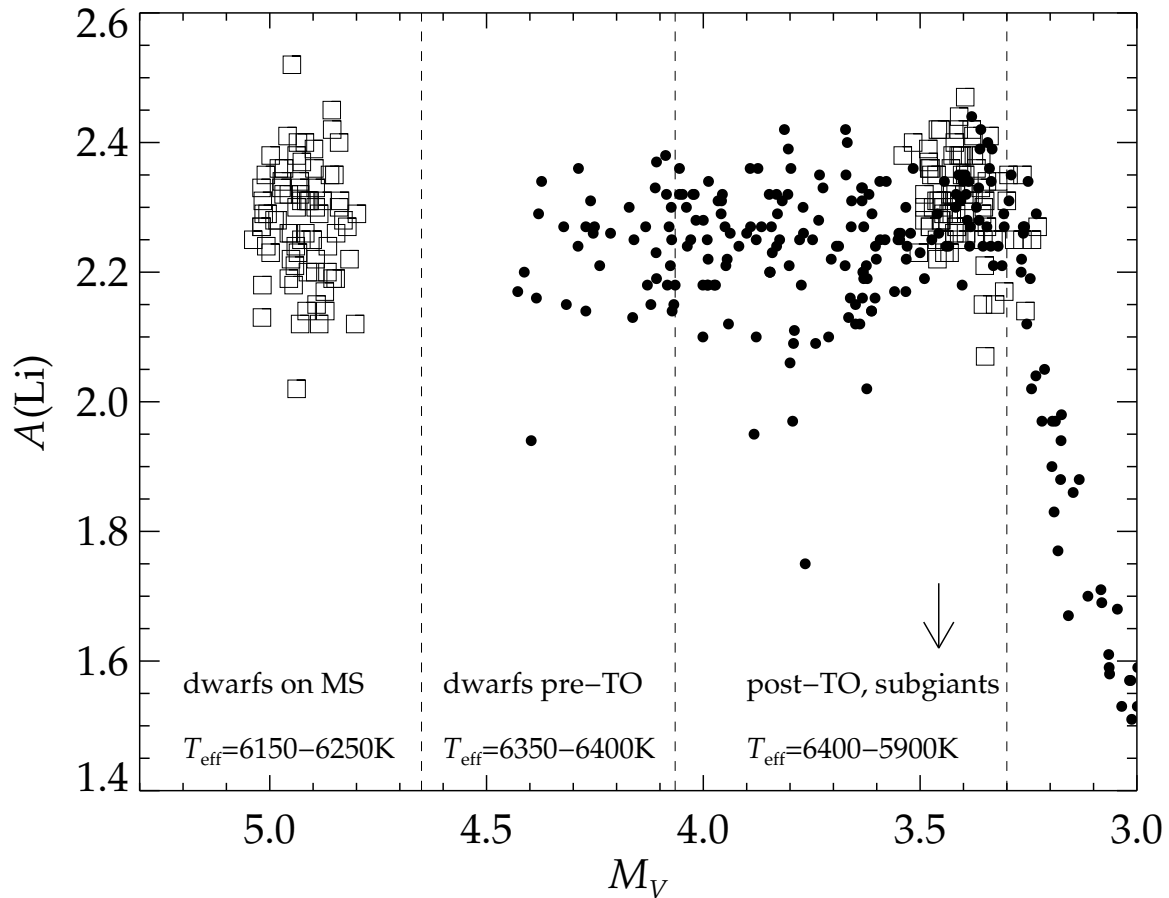


Figure 6.6: Lithium abundance against visual magnitude. The targets of our observations are plotted with filled circles and the archival data are plotted with open squares. Information about evolutionary status and effective temperature for various M_V intervals is also given.

should have been born with the cosmological Li abundance and a low Na-abundance, similar to that of field stars of comparable overall metallicity. The latter may have inherited a lower Li abundance at birth and will also exhibit other signatures of H-burning at high temperature, in particular enhanced Na abundances resulting from the NeNa chain in the polluter stars.

In Fig. 6.7 we report the Li and Na abundances for 100 stars in our sample with $M_V > 3.3$, i.e., those that have not yet undergone Li dilution via the first dredge-up. Note that it is the first time that these quantities are determined simultaneously for such a large sample of TO and SGB stars in a globular cluster. This diagram clearly emphasises the extent of the star-to-star Na abundance variations (by up to 1 dex) within NGC 6397. This is in agreement with the findings by Carretta et al. (2005), which were based on six dwarfs and nine SGB stars. From the appearance of Fig. 6.7, we deduce that the most Li-poor targets indeed show the most elevated Na levels, implying an anti-correlation between the abundances of Na and Li. The spectrum of the most Li-poor and second most Na-rich star in the sample, #6685, is shown in Fig. 6.4. The abundance pattern displayed by this star and by at least three more stars, agrees well with the globular cluster self-enrichment scenario and we conclude that they have likely been formed from polluted gas. Field stars with similar metallicity to NGC 6397 have typical Na abundances in the range $A(\text{Na}) = 3.6 - 3.9$ (Andrievsky et al., 2007). It is thus reasonable to regard stars with $A(\text{Na}) < 3.9$ as belonging to a first generation of non-polluted objects.

To find the statistical significance of the indicated Li-Na anti-correlation we performed linear regression between $N(\text{Li})/N(\text{H})$ and $N(\text{Na})/N(\text{H})$, taking into account measurement errors in both quantities as well as upper limits on Na (IDL-routine `linmix_err`, see Kelly 2007). The analysis gave a correlation coefficient of -0.6 between the Na and Li abundances, which for a sample of this size is highly significant. The probability of two uncorrelated variables producing such a correlation coefficient is less than 0.05%. However, as can be realised from Fig. 6.7, the significance of the anti-correlation is dependent on the most Na-enhanced stars. In fact, performing the same linear regression for stars with $A(\text{Na}) < 4.1$ no significant anti-correlation was found. The Li abundances among the plateau stars are thus not much affected by high degrees of pollution.

In Fig. 6.7 it is also indicated with a tilted arrow approximately how the location of a star would be affected by an erroneous effective temperature. An error of $\Delta T_{\text{eff}} = \pm 100$ K corresponds to $\Delta A(\text{Li}) = \pm 0.07$ and $\Delta A(\text{Na}) = \pm 0.04$. Errors in effective temperature therefore weakly correlate the abundances with each other, rather than anti-correlate them. Hence, it is clear that the anti-correlation itself is not an artifact from uncertainties in the stellar-parameter determination. Possibly even a tighter anti-correlation exists for all targets, but is being distorted by the tendency of effective-temperature errors to align the abundances. As the Li abundance as well as the Na abundance are based on lines from neutral atoms, the effective temperature is the stellar parameter with by far the greatest influence over the results. The uncertainties stemming from surface gravity, microturbulence, and metallicity are all negligible in the context.

The extent of the Li and Na variations found in the present study is similar to that found in NGC 6752 (Pasquini et al., 2005) and 47 Tuc (Bonifacio et al., 2007b), and thus appears

to be independent of the metallicity. However, the Li-Na anti-correlations in NGC 6752 and 47 Tuc are based respectively on nine and four stars only, limiting the comparison. A more detailed discussion of the implications for the self-enrichment of NGC 6397 will be performed in a separate paper where O, Na, Mg, and Al abundance determinations will also be presented for a subset of RGB stars in our sample Chapter 7. In Sect. 6.5 we use the information about Na to constrain intrinsic stellar Li depletion processes.

6.5 Discussion

6.5.1 Signatures of intrinsic lithium depletion

A proposed explanation for the difference between the Li abundance found in the metal-poor halo and the BBNS prediction is intrinsic Li depletion due to the combined effect of gravitational settling and weak turbulence, the nature of which is still a matter of debate. In the case of NGC 6397, the stars on the Spite plateau would have to have been depleted by typically $\Delta A(\text{Li}) = 2.72 - 2.27 = 0.45$ dex, corresponding to almost a factor of three. To constrain the physics involved in producing such depletion, it is important to accurately establish trends of Li abundance with evolutionary phase and effective temperature. In the following, we carry out our analysis based on sub-samples of data defined according to Na content. As discussed in Sect. 6.4.3, it is reasonable to consider that the stars born out of pristine material are those with $A(\text{Na}) < 3.9$.

Fig. 6.8 shows Li abundance vs visual magnitude on the plateau, with abundances binned in groups of targets for clarity. In the lower panel of each plot, the 1σ dispersions in the corresponding bins are shown. The full lines are drawn for the whole sample including both our data and the archival data, i.e., it does not discriminate between first-generation Na-poor stars and second-generation Na-rich objects. The single plateau-star for which only an upper limit could be inferred is not included in the binning. The dashed lines correspond to first-generation stars with $A(\text{Na}) < 3.9$ and dotted lines to second-generation stars with $A(\text{Na}) > 3.9$. Mean error bars for each line are also indicated in the figure. Fig. 6.9 shows the same plot, but using effective temperature as the reference scale instead of visual magnitude. To separate pre- and post-TO stars with the same effective temperature, the dwarfs are represented by open square symbols and the SGB stars with filled circles. The approximate evolutionary status of the stars can be recovered from Fig. 6.6. Stars with $M_V \geq 4$ are dwarf stars below the TO, having effective temperatures reaching from the maximum 6400 K to 6200 K at $M_V \approx 5$. Stars with $M_V < 4$ are slightly more massive objects that have passed the TO, i.e., SGB stars with $T_{\text{eff}} \approx 6400 - 5900$ K. At $M_V \approx 3.3$ the Li dilution process through the first dredge-up sets in.

As can be seen in Figs 6.8 and 6.9, trends of Li abundance with evolutionary phase and effective temperature are not significantly different between first- and second-generation objects. The mean value of $A(\text{Li})$ appears generally to be slightly higher for the first-generation stars (dashed lines) than for the second generation (dotted lines), in agreement with what is expected in the globular cluster self-enrichment framework, but the trends are

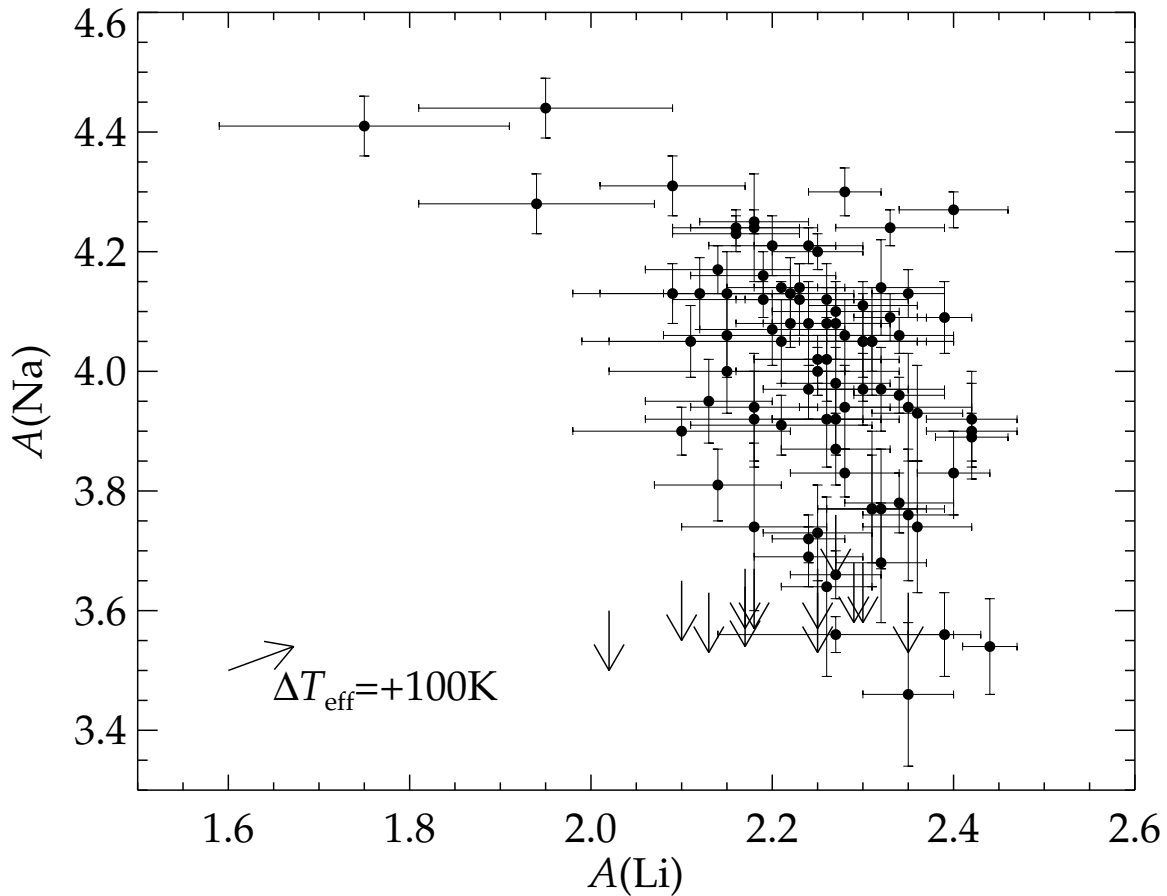


Figure 6.7: Non-LTE Li and Na abundances for the sub-sample of 100 dwarfs and SGB stars with observations in the H805.3A setting and $M_V > 3.3$. The arrows mark upper limits to the Na abundance. If the effective temperature of a target has been underestimated by 100 K, the corresponding point in this diagram should be shifted approximately in the direction of the tilted arrow and in its inverse direction for overestimated effective temperatures.

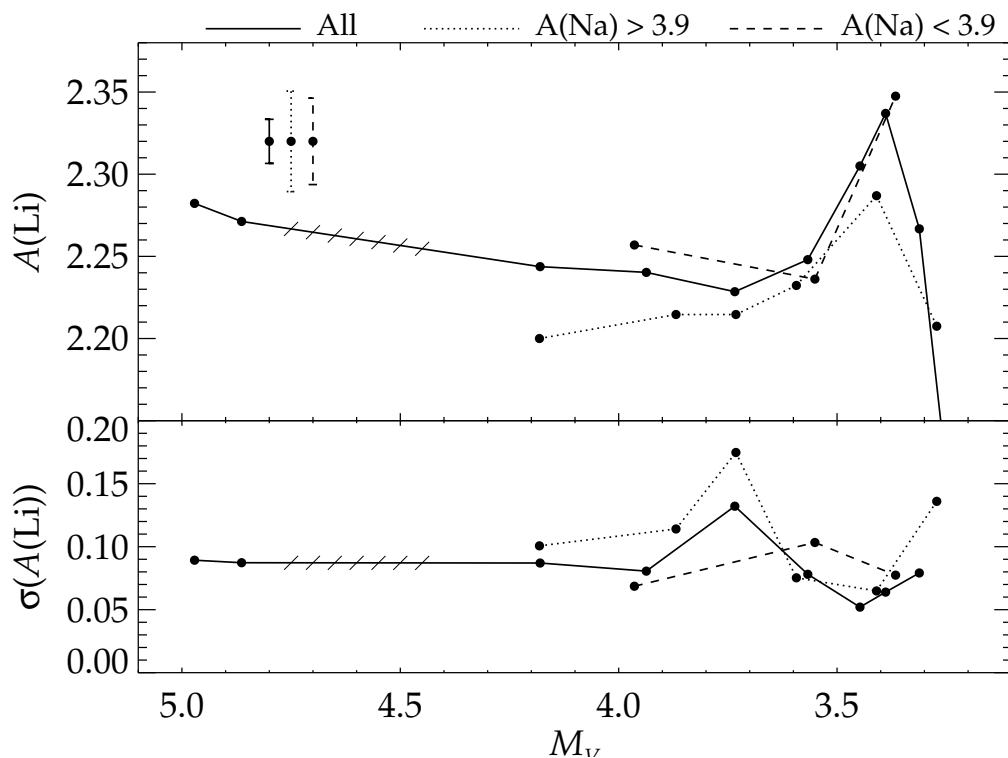


Figure 6.8: Group-averaged Li abundances against visual magnitude. The full line is drawn for the whole sample (including the archival data), i.e., for both first-generation Na-poor stars and second-generation Na-rich stars. Each bin contains 40 stars. The dashed and dotted lines correspond to different sub-sets of our own sample, selected according to their corresponding Na abundances. Each bin contains 13 stars. In the upper left corner mean error bars are shown for each line. Note that the range between $M_V \approx 4.4 - 4.8$ is not sampled by the data.

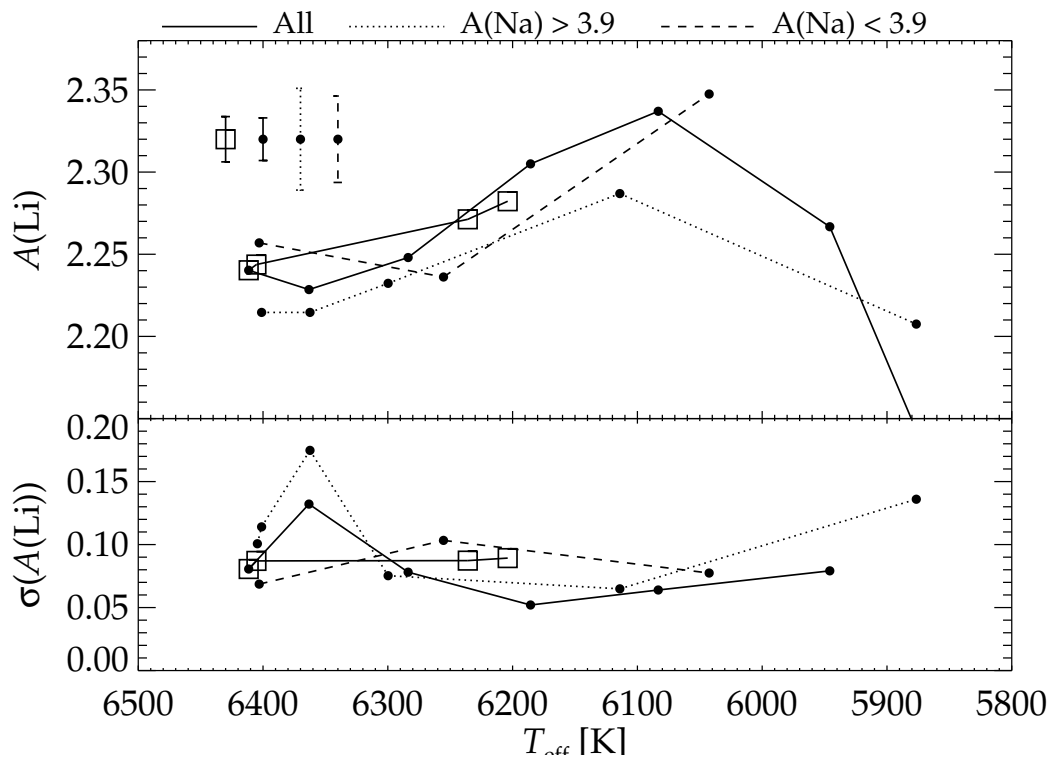


Figure 6.9: Group-averaged Li abundances against effective temperature. The lines correspond to the same sub-samples as in Fig. 6.8. Filled circles represent post-TO stars and open squares pre-TO stars. In the upper left corner mean error bars are shown for each line.

fully compatible within the error bars. We conclude that the mean Li abundance trends of the full sample are not significantly biased by intra-cluster pollution in NGC 6397. On examination of Fig 6.8, we especially note the presence of an upturn in $A(\text{Li})$ just before the steep abundance drop at $M_V \approx 3.3$, which appears rather robust against varying $A(\text{Na})$ in the sample. In a very limited magnitude-range the mean Li abundance increases by around 0.1 dex up to $A(\text{Li}) = 2.35$. As mentioned previously, a difference of this size between TO and SGB stars in NGC 6397 was identified by Korn et al. (2007).

The behaviour of Li abundance with T_{eff} is illustrated in Fig. 6.9. There is an overall increase with decreasing effective temperature in the range 6400 – 6100 K, where a maximum is reached, followed by a decrease again until $T_{\text{eff}} \approx 5900$ K, where the first dredge-up sets in. The initial increase appears to be present both for pre- and post-TO stars. Speculatively, the lower value found for hotter dwarfs compared to cooler dwarfs, could be interpreted as the counterpart of the very right-shoulder of the so-called Li-dip observed in Population I stars (see references in Talon & Charbonnel 1998, 2003). This feature appears in the present data at exactly the same effective temperature as in open clusters: In the Hyades, the mean Li abundance decreases by approximately 0.10 – 0.15 dex in the effective temperature range between 6200 and 6400 K. As discussed by Talon & Charbonnel (1998, 2004), a similarity between Pop I and Pop II dwarfs is theoretically expected, since the depth of the stellar convective envelope, and thus the nature and the efficiency of the Li depletion mechanism, are expected to depend only on the stellar effective temperature³. If this feature is real (see Sect. 6.5.2), it seems that we may have discovered for the first time in Population II stars the very beginning (in terms of effective temperature) of the Li-dip, which may be more shallow at this low metallicity. Note that one should be cautious with interpretations of Li trends for dwarfs in our sample. As mentioned in Sect. 6.2.1, due to observational limitations the majority of our sample stars with Na determination are SGB stars, only a handful being relatively warm dwarfs. No Na abundance determination has thus been carried out for the coolest dwarfs below the TO. However, we have seen that the bias in Li abundance trends among SGB stars due to pollution is weak, which is likely true also for dwarfs.

In Sect. 6.4 we concluded that the most Li-deficient stars in our sample likely belong to a second generation of stars, having experienced intra-cluster pollution. Among the first-generation stars with low Na levels, there are no stars with Li abundances lower than $A(\text{Li}) = 2.0$. The lower panels of Figs. 6.8 and 6.9 show that the abundance dispersion of the full sample is always rather low, below 0.1 dex, except for the bin at $M_V \approx 3.7$ and $T_{\text{eff}} \approx 6350$ K, which contains the most Li-poor star with an abundance detection (see Fig. 6.6) and therefore has a higher dispersion. Focusing on the first generation of Na-poor stars only, the typical abundance scatter is 0.09 dex, not following any obvious trends with effective temperature or visual magnitude. Not shown in the figures is the typical measurement error in abundance, stemming from photon noise, which ranges from

³At a given effective temperature, Pop II stars along the plateau have lower masses than Pop I stars on the cool side of the Li dip. Regarding the depth of the convective envelope however, their lower metallicity compensates for the mass effect. See Talon & Charbonnel (2004) for more details.

0.08 dex for the hottest stars to 0.05 dex for the coolest plateau stars. To this measurement error should be added the propagated uncertainty in stellar parameters. Assuming that the typical star-to-star error in effective temperature, which is the most influential parameter, lies in the range 50 – 100 K, a corresponding additional spread of 0.04 – 0.07 dex in Li abundance is expected. Given these basic estimates, we conclude that the observations are compatible with zero scatter in Li abundance among the first-generation stars.

6.5.2 Effects of stellar parameters and non-LTE

We now briefly discuss the influence on the abundance trends presented in Sect. 6.5.1 from the choice of effective-temperature scale and from the non-LTE treatment. Basically, both effects have a systematic influence over the Li data. If we were to adopt the IRFM-based effective-temperature scale by Ramírez & Meléndez (2005) (see Sect. 6.3.1) the Li abundances of post-TO stars would be systematically lowered by -0.06 dex, thus aggravating further the overall discrepancy to the primordial value. The scale by Alonso et al. (1996, 1999) would act in the same direction, but also have a minor differential impact on the Li abundances since this effective-temperature scale is steeper in the range from the TO to further up the SGB. The TO star abundances would therefore be lowered by a greater amount (-0.1 dex) than the cooler SGB star abundances, which in turn would enhance the abundance upturn seen in Fig. 6.8 and the corresponding maximum abundance seen in Fig. 6.9 at $T_{\text{eff}} = 6100$ K. Nothing would thus qualitatively change in the discussion of abundance trends for post-TO stars. However, implementing either of the two IRFM-based scales would lower the abundances found for cool dwarfs more than hot dwarfs. The difference between these two groups discussed in Sect. 6.5.1, which we speculated could be a signature of the Li-dip, would hence be erased.

As mentioned in Sect. 6.3.3, the non-LTE abundance corrections are similar, approximately -0.06 dex, for all plateau stars. The LTE abundances therefore have the same relative behaviour but are offset to a slightly higher values.

6.5.3 Comparison to other studies

Comparing the found Li abundances to other determinations made for NGC 6397, we find good agreement with Korn et al. (2007), who place their five TO stars with $M_V \approx 3.6$ at $A(\text{Li}) = 2.25$ and two SGB stars with $M_V \approx 3.3$ at $A(\text{Li}) = 2.36$. The similarity between the abundances for TO and SGB stars is partly due to the cancellation between the effects from the cooler effective-temperature scale of Korn et al. (2007) and the fact that they do not correct for non-LTE. For RGB stars the two effects do not cancel (non-LTE corrections are positive for RGB stars) and Korn et al. (2007) thus find abundances that are approximately 0.1 dex lower than ours. The Li abundances reported by Bonifacio et al. (2002) for TO stars lie on average 0.1 dex higher than ours. This difference can be fully traced to their effective-temperature scale, which is hotter by approximately 50 K than the one adopted in this study, and to their use of different non-LTE corrections (Carlsson et al., 1994). For these stars, the corrections by Carlsson et al. (1994) are smaller in absolute

value than the ones found by Lind et al. (2009a). The Li abundances and abundance upper limits reported by Castilho et al. (2000) for 16 RGB stars are in good agreement with ours, except for the Li detections made for giants cooler than 4900 K, which are significantly higher than what we find.

In the extensive literature study of field stars carried out by Charbonnel & Primas (2005), the authors concluded that the stars in their TO and SGB samples generally are more Li-rich than their dwarf sample. Especially, dwarfs that are cooler than 6000 K show a distinct decrease in Li abundance with decreasing effective temperature. As the dwarfs in our sample are all hotter than 6000 K we cannot verify this result. However, with hindsight one may trace a tendency of increasing Li abundance with decreasing effective temperature in the range $T_{\text{eff}} = 6050 - 6400$ K among the MS, TO, and post-TO stars observed by Charbonnel & Primas (2005) (see their online tables 5-9), similar to the one we find.

6.5.4 Comparison to diffusion-turbulence models

Fig. 6.10 and Fig. 6.11 show comparisons of our obtained Li abundances with the predictions from stellar-structure models including atomic diffusion from first principles and an ad-hoc recipe for turbulent mixing (Richard et al. 2005 and references therein). For clarity we show the same group-averaged Li abundances as in Fig. 6.8 and Fig. 6.9, including the whole sample, irrespectively of Na abundance. Only post-TO stars appear in Fig. 6.11. For comparison, the bottom panels of both figures show corresponding trends for binned Ca abundances. Visual magnitudes are converted to stellar luminosities using the bolometric corrections of Alonso et al. (1999). The same three models, T5.80, T6.00, and T6.09, with different efficiencies of turbulent transport, as displayed in Korn et al. (2007); Lind et al. (2008) are shown. To ensure that the model $T_{\text{eff}} - \log(L/L_{\odot})$ -plane is in agreement with our study regarding the location of the TO-point, we add +80 K to the effective-temperature scale of Richard et al. (2005) and +0.05 dex to the logarithmic luminosity-scale. The absolute abundance scale of the models is shifted to agree with the observations for stars evolved beyond the onset of the first dredge-up.

The efficiency of turbulent mixing determines how much Li that is transported between the external convection zone to the region in the stellar interior where Li is destroyed, which in turn has influences over the appearance of the Li abundance plateau. In the T6.09 model, with highest efficiency, the plateau is flat, whereas the surface abundances predicted by the T5.80 model show a clear dependence on stellar luminosity and effective temperature. As seen in Fig. 6.10, the Li abundances of NGC 6397 strictly limit the efficiency of turbulent mixing, although no model perfectly reproduces the observed abundances. In terms of the size of the Li variations on the plateau, the T6.00 model appears to be the best choice, supporting the findings by Korn et al. (2007); Lind et al. (2008). The observed Ca abundance trend is in good agreement with both higher-efficiency models (T6.00 and T6.09), and especially the location of the upturn at $\log(L/L_{\odot}) \approx 0.65$ is matched. However, Fig. 6.11 shows clearly that the behaviour of the post-TO Li abundance with effective temperature is not reproduced by any of the models. Especially the location of the maximum $A(\text{Li})$

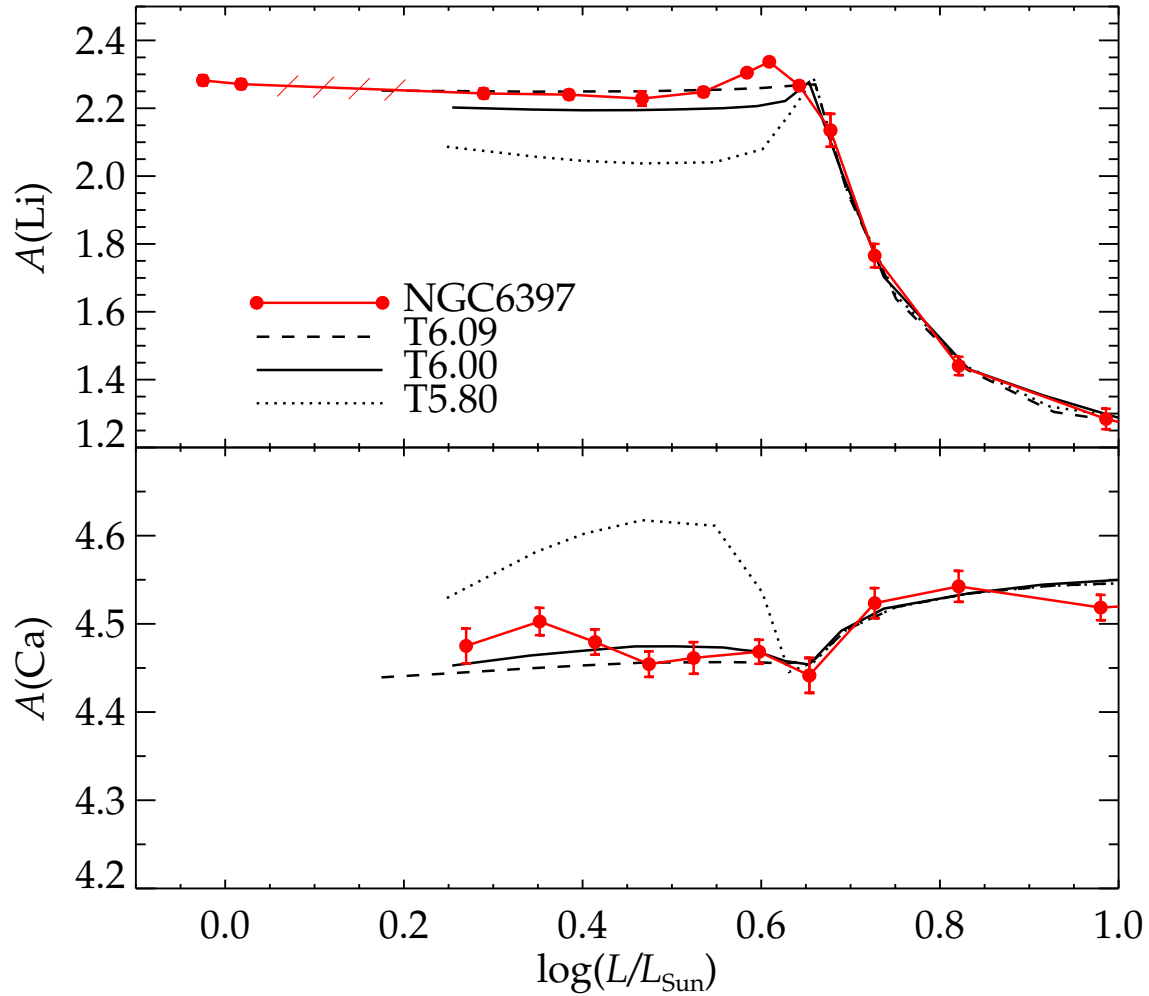


Figure 6.10: *Top*: Comparison between bin-averaged Li abundances (red filled circles connected with solid lines) and the predictions from the stellar-structure models of Richard et al. (2005). T5.80 represents the model with lowest efficiency of turbulent transport, T6.00 intermediate efficiency, and T6.09 highest efficiency. The reference scale is logarithmic luminosities in units of solar luminosities. *Bottom*: The same plot for Ca abundances. A colour version of this figure is available in the online edition of the journal.

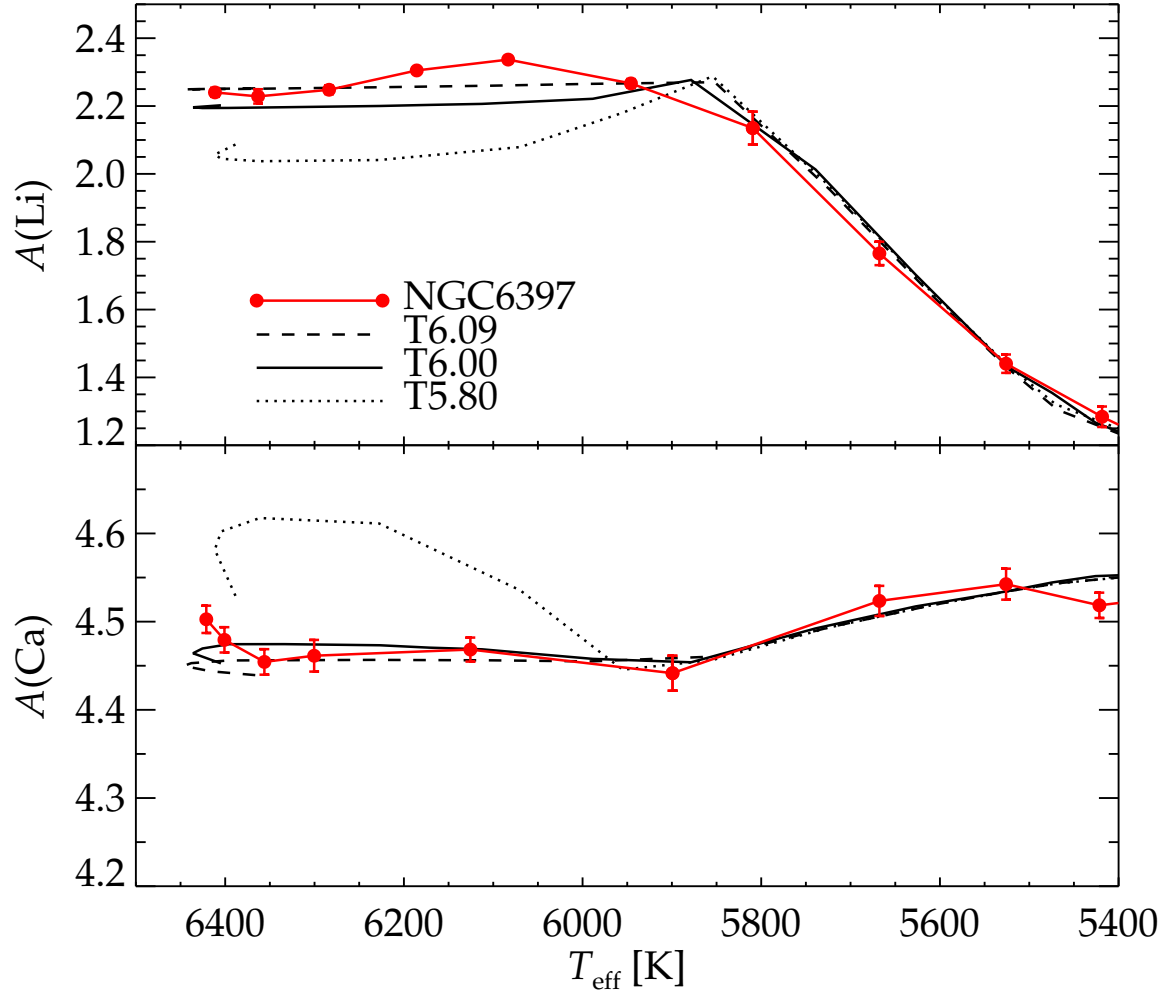


Figure 6.11: *Top:* Same as in in Fig 6.10 but with effective temperature as the reference scale. Here, only post-TO stars are included. *Bottom:* The same plot for Ca abundances. A colour version of this figure is available in the online edition of the journal.

occurs at higher effective temperature than the models predict.

The initial Li abundance predicted by the models, accounting for the adjustment we make in the vertical direction, is $A(\text{Li}) = 2.46$, which is significantly closer, but still not in full agreement with the latest predictions from BBNS of 2.72 ± 0.06 (Cyburt et al., 2008).

6.6 Conclusions

We have presented a comprehensive study of the Li content in a large sample, 454 stars in total, of MS, TO, SGB, and RGB stars in the metal-poor globular cluster NGC 6397. The cluster dwarfs and early SGB stars form a thin Li abundance plateau on the same level as the Spite plateau for field stars, whereas more evolved stars have undergone drastic Li depletion due to physical processes connected to low-mass stellar evolution. Two remarkably well-defined locations in absolute visual magnitudes, $M_V \approx 3.3$ and $M_V \approx 0.0$ respectively, are identified as the locations of corresponding steep Li abundance drops. They correspond respectively to the occurrence of the first dredge-up on the SGB and to the onset of thermohaline mixing at the RGB bump (Charbonnel & Zahn, 2007).

Using information of Li and Na abundance for a sub-sample of 100 dwarfs and early SGB, we have for the first time identified a significant anti-correlation between the two elements in this cluster. This is interpreted as the signature of intra-cluster pollution from a previous generation of more massive stars. The spread in Na and Li abundances of stars not having undergone Li depletion due to dredge-up, is very large, about one order-of-magnitude. However, only a handful of stars show significantly depleted Li levels and the identified anti-correlation depends critically on these objects. For Na-enhancements up to 0.7 dex, no corresponding Li-deficiency can be detected. The average Li abundance is thus not much affected by internal pollution. These abundance patterns have consequences for the self-enrichment scenario in NGC 6397, which will be discussed in a forth-coming paper.

By dividing our sub-sample with Na determinations into two groups, consisting of first and second generation of stars according to the degree of pollution, we illustrate how especially trends of Li abundance with effective temperature and evolutionary phase are in reasonable agreement between the two generations. The average Li abundance is typically $A(\text{Li}) = 2.25$ for stars located below and above the TO, and show a slight upturn of $\Delta A(\text{Li}) \approx 0.1$ dex for stars in the middle of the SGB. This difference agrees with previous findings for the cluster as well as for field stars. We find no support for a significant Li dispersion among the first generation of stars.

The identification of a minor Li deficiency of the hottest dwarfs in our sample compared to slightly cooler dwarfs leads us to suggest that the very right-hand wing of the Li-dip may be visible also among Pop II stars. However, the signature is erased if a different effective temperature scale is adopted.

The detailed picture we have formed of the Li abundance trends in this globular cluster can be used to constrain the physics involved in depleting Li from the photospheres of low-mass metal-poor stars, as well as the extent of the depletion. To illustrate this, we

compare our observational findings to predictions from stellar-structure models including atomic diffusion, with additional turbulence below the convection zone. We find that some turbulence, in a very limited efficiency-range, is indeed required to explain observations. However, these models fail to reproduce the behaviour of Li abundance with effective temperature along the plateau, suggesting that a detailed understanding of the physics responsible for depletion is still lacking.

Chapter 7

Tracing the evolution of NGC 6397 through the chemical composition of its stellar populations

The following article has been recommended for publication in *Astronomy & Astrophysics* in August 2010 (Lind, Charbonnel, Decressin, Primas, Grundahl, & Asplund). The work has been based on data collected at European Southern Observatory (ESO), Paranal, Chile, under program IDs 077.A-0018(A) and 281.D-5028(A), as well as data collected with the Danish 1.54 m telescope at European Southern Observatory (ESO), La Silla.

7.1 Introduction

The abundance patterns of light elements (up to Al) in globular clusters are being carefully investigated. Especially, the origin of the larger spread in C, N, O, Na, Mg, and Al abundances compared to field stars of similar metallicity is being traced. The present status of the observed light element (O, Na, Mg, and Al) abundances in globular clusters and possible consequences for the formation and enrichment history of these stellar populations, have been mapped in a recent series of publications by (e.g. Carretta et al. 2009a, 2010), see also reviews by Gratton et al. (2004) and Charbonnel (2005). The main findings, as inferred from high-resolution spectroscopy of individual globular cluster stars, are apparent enhancements of N, Na, and Al abundances and deficiencies in Li, O, and Mg. Such patterns can be naturally explained by enrichment of the nucleosynthesis rest-products of H-burning at high temperatures (Denisenkov & Denisenkova, 1989; Langer et al., 1993). Since the resulting anti-correlations between particularly O–Na abundances have not only been seen in evolved RGB stars, but also in TO and SGB stars (Gratton et al., 2001), an intrinsic stellar evolutionary cause is very unlikely, i.e. the stars can not have established these abundance patterns themselves. Rather, it is believed that the gas that formed second generation stars in globular clusters underwent early pollution by slow ejecta from intermediate mass or massive stars.

Important in this context is also photometric evidence of multiplicity in some clusters, like ω Cen and NGC 2808, in which several parallel main sequences can be identified. These observations seemingly necessitate that a difference in the He content is present (e.g. Norris 2004), in qualitative agreement with the self-enrichment process responsible for the other light element variations. He enrichment is also commonly invoked to explain the extended horizontal branch observed in many clusters (D’Antona & Caloi, 2008). We are, however, far from building a fully consistent picture of the chemical evolution of globular clusters that can explain all the various observations simultaneously.

A key issue that remains to be settled is the properties of the polluting objects. One possibility is that so called hot bottom burning occurs at the base of the convective envelope in intermediate-mass stars during the asymptotic giant branch (AGB) phase, which would leave nucleosynthesis products in the envelope that is subsequently expelled (Ventura & D’Antona, 2008, 2010). Also, super-AGB stars have been suggested to be responsible for the most extreme anomalies (Pumo et al., 2008). The main alternative scenario is a slow mechanical wind from rapidly rotating massive stars (e.g. Decressin et al. 2007a), whose envelopes have been enriched in H-burning products by deep internal mixing (see Sect. 7.4). Yet another option is mass loss from massive binary systems, as suggested by de Mink et al. (2009).

By accurate abundance analysis of many elements (and isotopic ratios) in large stellar samples, we may pin-point the nature of the progenitors (e.g. Charbonnel 2005, and references therein). A common property of the competing scenarios is that the pollution would alter mainly the light element abundances of second generation stars in globular clusters, thus leaving α and iron-peak elements unaffected. This is necessary to explain the homogeneous composition of these elements seen in most clusters. Elements created in the s-process may be affected by AGB pollution, suggesting the presence of correlations between s-process and light element anomalies. In NGC 6752, an unexplained correlation was indeed identified between Al abundances and Y, Zr, and Ba (Yong et al., 2005), but the systematic heavy elements variations are small (0.1 dex) and comparable to the statistical scatter. One must also bear in mind that the yields of AGB stars are uncertain (e.g. Charbonnel 2007; Decressin et al. 2009; Ventura & D’Antona 2010).

In addition to mapping the presence of abundance trends and correlations it is also essential to investigate, preferably with sound number statistics, the fraction of stars with normal chemical composition, similar to the field, and the fraction of second and possibly third generation stars in globular clusters. Linking this information to other cluster observables one may construct a schematic model for the episodes of star formation and evolution. Carretta et al. (2010) describe a possible general formation scenario in which a precursor population, forming from the gas assembled at a very early epoch inside a CDM halo, efficiently raises the metal content of the gas cloud via core-collapse supernova explosions. Those trigger a second, large episode of star formation, the so called primordial population (first generation). The slow winds of massive or intermediate-mass stars of the primordial population feed a cooling flow, and the intermediate (second) generation of stars are formed in the central parts of the cluster, out of material enriched in H-burning products. The remaining gas is dispersed by core-collapse supernovae of the second gen-

eration and star formation ceases. The present-day cluster is dominated by the second generation, with a smaller fraction, approximately 30%, left of the primordial population. Critical factors that determine the outcome of such a scenario is the initial mass function (IMF) of the polluting stars, the initial total mass of the cluster, and the amount of mixing between processed gas in the slow stellar ejecta and pristine cluster gas. We will discuss these issues further in Sect. 7.4.

HST photometry of NGC 6397 produces a remarkably clean HR-diagram, with a very tight MS (Richer et al., 2008) and a very compact blue horizontal branch, i.e. there are no obvious photometric signs of multiple populations. The cluster is well-studied in terms of number of stars for which high-resolution spectra have been obtained, but only a handful of elements have previously been analysed even on the RGB (most recently by Gratton et al. 2000; Castilho et al. 2000; Thévenin et al. 2001; Korn et al. 2007; Carretta et al. 2009a), as summarised in Table 7.1.

Early studies of the strengths of the G and CN band in RGB stars in NGC 6397 (and other clusters) suggested anomalies in C and N abundance (Bell et al., 1979; Briley et al., 1990). Eventually, Gratton et al. (2001) also detected a significant spread in Na abundance for a sample of ten TO stars and RGB stars, findings that clearly pointed to an intrinsic, rather than evolutionary, origin. Later, Carretta et al. (2005) corroborated these findings for a larger sample of stars and also found a significant O–Na anti-correlation, as well as a large spread in C and N abundance (see also Pasquini et al. 2004). In the latest analysis by Carretta et al. (2009b,a) the O–Na anti-correlation is present, although the number statistics are still rather small, especially oxygen measurements are few. A Mg–Al anti-correlation has not been identified in NGC 6397, but Mg also seems to show a certain scatter (Korn et al., 2007). Lind et al. (2009b) presented Na abundances for > 100 TO, SGB, and RGB stars, and found that the most heavily Na-enriched stars also are significantly depleted in Li. It is thus clear that NGC 6397, like other globular clusters, should no longer be regarded as a single stellar population despite the tightness of its colour-magnitude diagram. However, even if pollution indeed seems to have taken place in the cluster, it is unclear to which extent, and which elements are affected by it. With this study, targeting red giants, we will cover as many elements as possible, for a large sample of stars and give a more decisive answer to this question.

7.2 Observations and analysis

We have obtained high-resolution ($R = 47000$) spectra with the multi-object fibre spectrograph FLAMES/UVES on the VLT, covering the wavelength range 480–680 nm (UVES Red 580 standard setting). For a subset of six stars, we also have spectra covering the wavelength range 760–1000 nm (UVES Red 860 standard setting). Our targets are all RGB stars, whose surface abundances should reflect the initial composition of cluster gas, with the notable exceptions of Li and Be, which are not studied here (Li abundances were published in Lind et al. 2009b). In particular, any internal abundance gradients created by atomic diffusion (Korn et al., 2007; Lind et al., 2008) during the time on the MS have

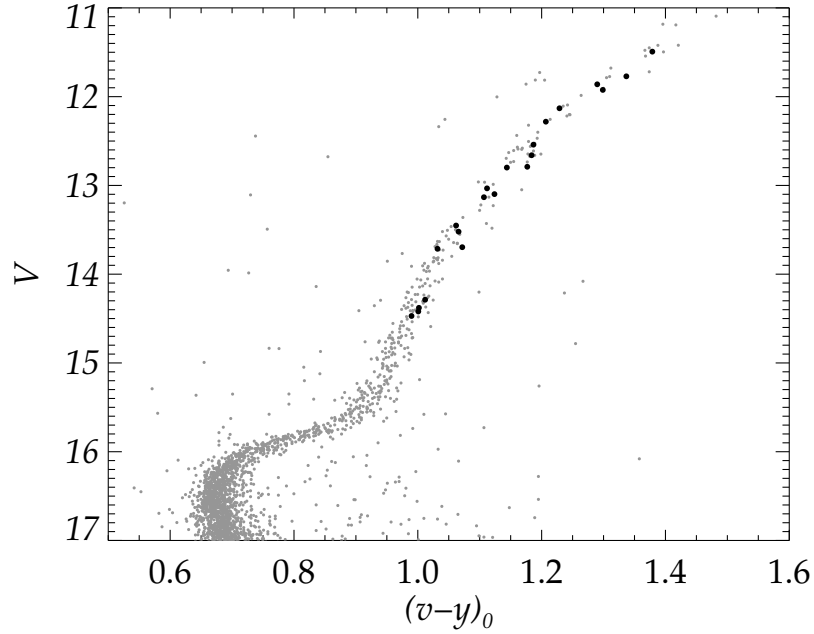


Figure 7.1: The targeted RGB stars are marked with black bullets in the $V - (v - y)$ diagram of NGC 6397. The RGB bump is located at $V \approx 12.6$.

been erased by the growth of the convective envelope.

Presented here is a subset of the targets analysed by Lind et al. (2009b, see Chapter 6), and we refer to this paper for a detailed description of the observations, the data reduction, and the stellar parameter determination. In short, we determined effective temperatures from the $(b - y)$ photometric index, interpolating in the grid of synthetic Strömgren colours computed by Önehag et al. (2009) using MARCS model atmospheres (Gustafsson et al., 2008). Surface gravities were derived from the standard relation to mass and luminosity. In total, we present abundances for 21 red giants distributed along the upper RGB of NGC 6397 (see Fig. 7.1), above and below the bump. The targets span a total range of approximately 500 K in effective temperature and 1.5 dex in surface gravity.

The full list of lines used in the analysis is given in Appendix A (except for all iron lines, which are listed in Lind et al. 2009b), with references to the oscillator strengths that were adopted. The wavelengths and the majority of f -values were taken from the Vienna Atomic Line Database (VALD). In all abundance analysis we used 1D, LTE, hydrostatic model atmospheres computed with the MARCS code (Gustafsson et al., 2008). All models are spherically symmetric models of M_{\odot} . For O, Na, Mg, and Al lines we applied spectrum synthesis with the Uppsala code BSYN, whereas all other elemental abundances were determined from equivalent width measurements of single lines, translated to abundances with the corresponding code EQWIDTH.

Abundance ratios with respect to the Sun were calculated using the solar abundances of Asplund et al. (2009). We stress that our main concern is the relative abundance scale within the cluster, rather than absolute abundances. With our fully homogeneous analysis we constrain relative stellar parameters and abundances very well. The listed abundance errors reflect only on the measurement uncertainty, as estimated from the signal-to-noise ratio of the spectra (Norris et al., 2001), and do not consider uncertainties in the adopted stellar parameters. Upper limits to the equivalent width, and hence the abundance, are calculated by adding twice the estimated measurement uncertainty to the best fitting synthetic spectra.

Fig. 7.2 shows the observed and best-fit model spectra of O, Na, Mg, and Al lines in two RGB stars, #17691 and #12138. The abundances of these four elements are all based on weak lines, whose line formation do not depart substantially from LTE. For Na only, we compute and adopt non-LTE abundances for all targets, whereas LTE is assumed to hold for the other species. The oxygen abundance is determined from the forbidden line at 630 nm, which is believed to have negligible non-LTE corrections, but may be sensitive to granulation effects (Kiselman, 2001; Nissen et al., 2002). For the four targets for which this was possible, we have also determined the oxygen abundance based on the near infra-red triplet lines at 777.1 nm and 777.4 nm, with very good agreement with the 630 nm line in LTE. Fabbian et al. (2009) predict non-LTE corrections for the triplet lines to be of order $(-0.05) - (-0.08)$ dex for our targets, adopting hydrogen collisions with $S_H = 1.0$ (Pereira et al., 2009a). Applying this correction would slightly lessen the agreement with the forbidden line.

The Na abundances are based on the 568.2 nm and 568.8 nm lines, which have non-LTE corrections ≈ -0.07 dex for stars with these stellar parameters (Lind et al. submitted, see Chapter 2). For five targets we have compared the abundances inferred from the 568.2/568.8 nm lines with those inferred from the 818.3/819.4 nm lines by Lind et al. (2009b). As seen in Fig. 7.4, the non-LTE corrected abundances agree well within the uncertainties. The Mg abundance is determined from the Mg line at 571.1 nm, for which Shimanskaya et al. (2000) report non-LTE corrections that are smaller than 0.02 dex for the relevant stellar parameters. The doublet lines of neutral Al at 669.6/669.8 nm are used to infer the Al abundance. We have not found any non-LTE calculations in the literature for these lines in metal-poor giant stars, but since they are weak, high-excitation lines, they should at least be more reliable abundance indicators in LTE than the stronger ultra-violet resonance lines at 396.1/394.4 nm (e.g. Asplund 2005). Furthermore, since our targets all have quite similar stellar parameters the differential non-LTE effects should be small.

7.3 Abundance analysis

Fig. 7.3 shows $[\text{Fe}/\text{H}]$ and abundance ratios relative to Fe¹ for all stars. Table 7.1 lists the mean abundance and dispersion of all elements, compared to values found in the

¹ $[X/Y] = \log \left(\frac{N(X)}{N(Y)} \right)_* - \log \left(\frac{N(X)}{N(Y)} \right)_\odot$

7. Tracing the evolution of NGC 6397 through the chemical composition of its stellar populations

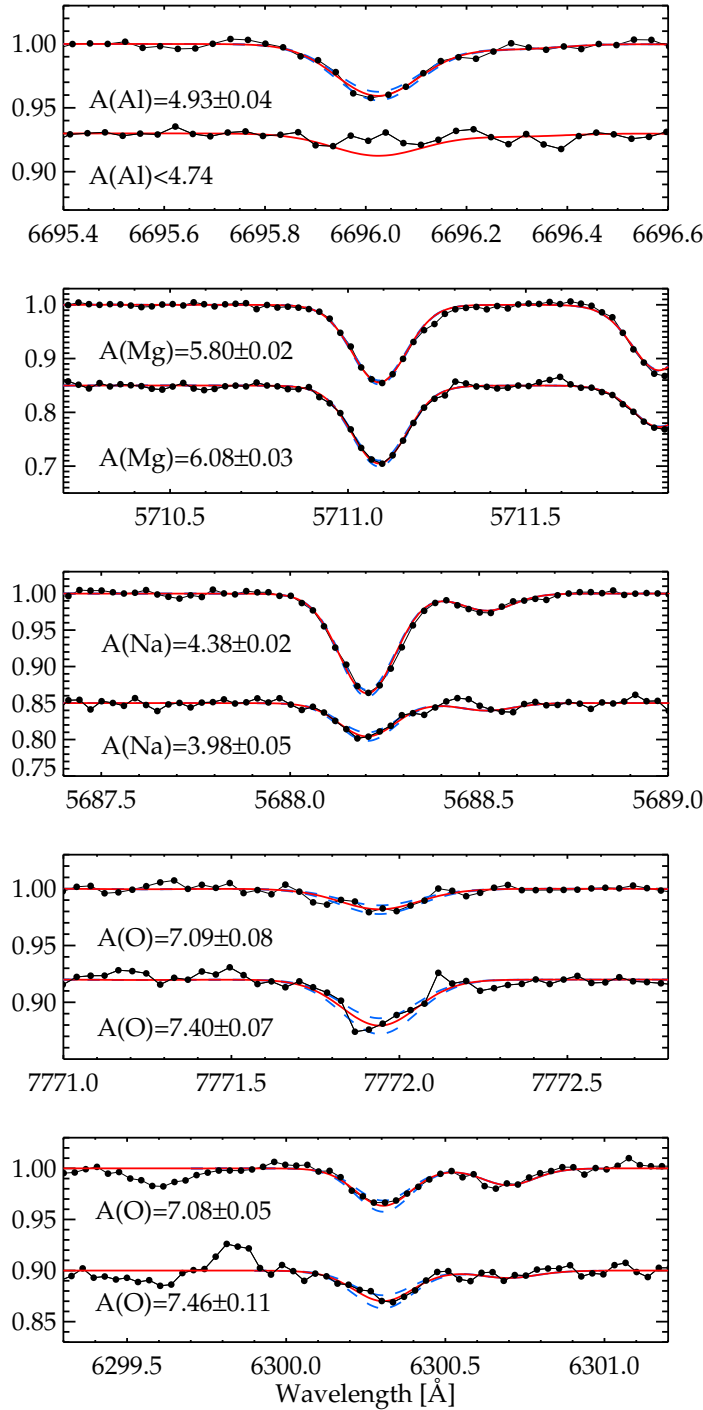


Figure 7.2: The figure shows some sample UVES spectra and the best fitting synthetic models and $\pm 1\sigma$ profiles. The top spectrum in each panel represents a second generation star (12138) and the bottom a first generation star (17691).

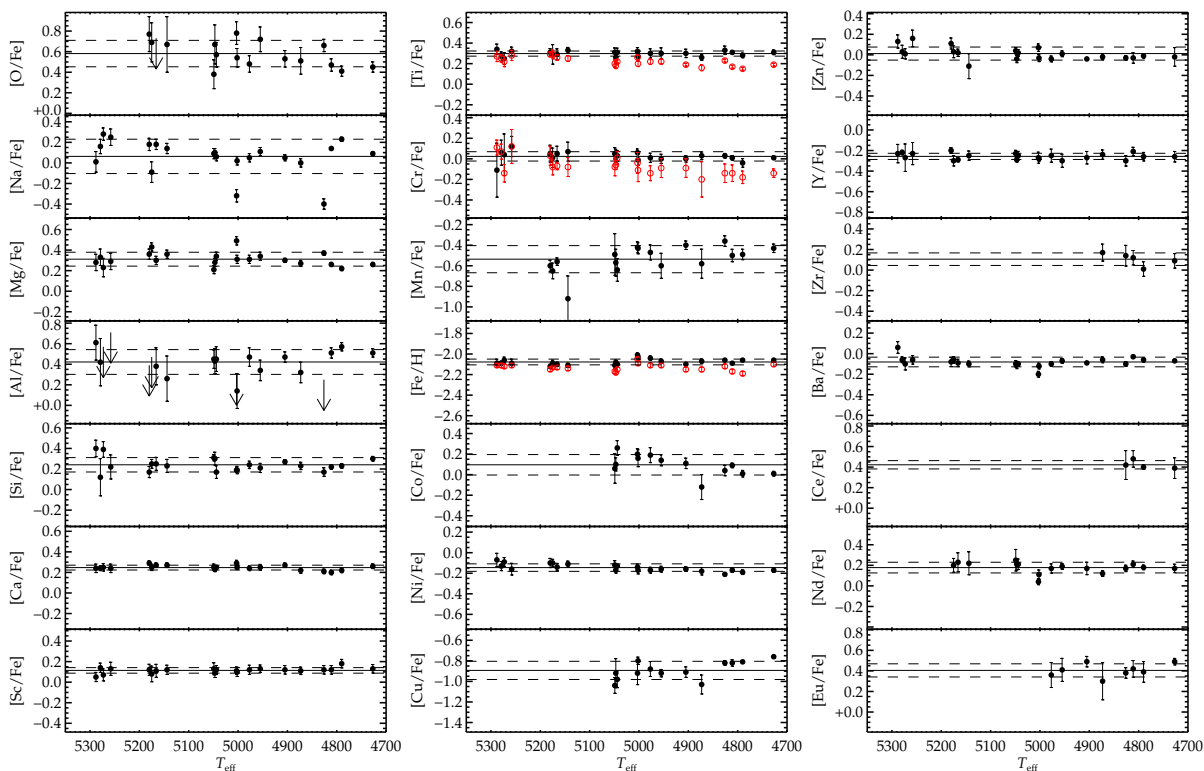


Figure 7.3: Elemental abundances of all targets. Each panel spans 1 dex in abundance and marks the average abundance (solid line) and the 1σ dispersion limits (dashed lines). Two different symbols are used for $[\text{Ti}/\text{Fe}]$, $[\text{Cr}/\text{Fe}]$, and $[\text{Fe}/\text{H}]$: the red open bullets and the black filled bullets in these panels represent abundances inferred from neutral and singly ionised lines, respectively. The hottest star in each panel mark the completeness limit, i.e. all sample stars cooler than this limit are shown.

Table 7.1: Mean abundances and abundance dispersions compared to literature values for NGC 6397. Listed are also the mean abundances of the RGB stars characterised as belonging to the first generation ($< A(X) >_I$, 3 stars) and second generation ($< A(X) >_{II}$, 18 stars), as well as the difference between the two mean quantities.

	n_{stars}	n_{lines}	$< A(X) >$	σ	C09 ^{a,f}	K07 ^{b,f}	G01 ^c	C00 ^d	$< A(X) >_I$	$< A(X) >_{II}$	$\Delta A(X)_{II-I}$
[Fe/H]	21	11-13	-2.08	0.02	-1.95	-2.12	-2.05	-2.0	-2.05 ± 0.02	-2.08 ± 0.01	-0.03 ± 0.02
[O/Fe] ^e	17	1-3	0.58	0.13	0.35	...	0.37	0.15	0.71 ± 0.04	0.56 ± 0.03	-0.15 ± 0.05
[Na/Fe]	21	1-2	0.14	0.17	0.11	...	0.31	0.19	-0.27 ± 0.09	0.12 ± 0.02	0.39 ± 0.09
[Mg/Fe]	21	1	0.31	0.07	0.25	0.37	0.20	...	0.43 ± 0.03	0.29 ± 0.01	-0.14 ± 0.04
[Al/Fe] ^e	21	1-2	0.42	0.12	0.35	...	< 0.34	0.44 ± 0.03	0.10 ± 0.07
[Si/Fe]	21	2-4	0.24	0.07	0.28	0.27	0.20 ± 0.02	0.25 ± 0.02	0.04 ± 0.03
[Ca/Fe]	21	16	0.25	0.02	...	0.37	...	0.20	0.25 ± 0.02	0.25 ± 0.01	-0.00 ± 0.02
[Sc/Fe]	21	5-6	0.11	0.03	0.10 ± 0.01	0.12 ± 0.01	0.01 ± 0.01
[Ti/Fe]	21	3-5	0.30	0.03	...	0.22	...	0.36	0.31 ± 0.01	0.30 ± 0.01	-0.02 ± 0.01
[Cr/Fe]	21	1-2	0.02	0.05	0.03 ± 0.01	0.02 ± 0.01	-0.01 ± 0.02
[Mn/Fe]	17	1	-0.54	0.13	-0.48 ± 0.09	-0.55 ± 0.03	-0.07 ± 0.09
[Co/Fe]	13	1	0.10	0.10	0.12 ± 0.08	0.09 ± 0.03	-0.03 ± 0.09
[Ni/Fe]	21	8-13	-0.14	0.04	-0.15 ± 0.03	-0.14 ± 0.01	0.01 ± 0.03
[Cu/Fe]	13	1	-0.89	0.09	-0.87 ± 0.05	-0.90 ± 0.03	-0.03 ± 0.06
[Zn/Fe]	21	1	0.01	0.06	0.02 ± 0.03	0.01 ± 0.02	-0.01 ± 0.03
[Y/Fe]	21	2	-0.26	0.03	-0.29 ± 0.01	-0.25 ± 0.01	0.04 ± 0.01
[Zr/Fe]	5	1	0.11	0.06	0.14 ± 0.10	0.10 ± 0.03	-0.04 ± 0.11
[Ba/Fe]	21	1-2	-0.08	0.05	...	-0.18	...	-0.16	-0.12 ± 0.04	-0.07 ± 0.01	0.05 ± 0.04
[Ce/Fe]	4	1	0.42	0.04	0.42 ± 0.14	0.42 ± 0.03	0.00 ± 0.14
[Nd/Fe]	16	3-5	0.18	0.05	0.14 ± 0.05	0.19 ± 0.01	0.05 ± 0.05
[Eu/Fe]	8	1	0.40	0.06	0.38 ± 0.05	0.41 ± 0.03	0.03 ± 0.06

^a Carretta et al. (2009a), mean of 13 targets. [Fe/H] based

^d Castolho et al. (2000), mean of ten brightest targets.

on FeI lines.

^b Korn et al. (2007), mean of six brightest targets.

^e Upper limits treated as detections.

^c Gratton et al. (2001), mean of three brightest targets.

^f solar abundances by Asplund et al. (2009) adopted.

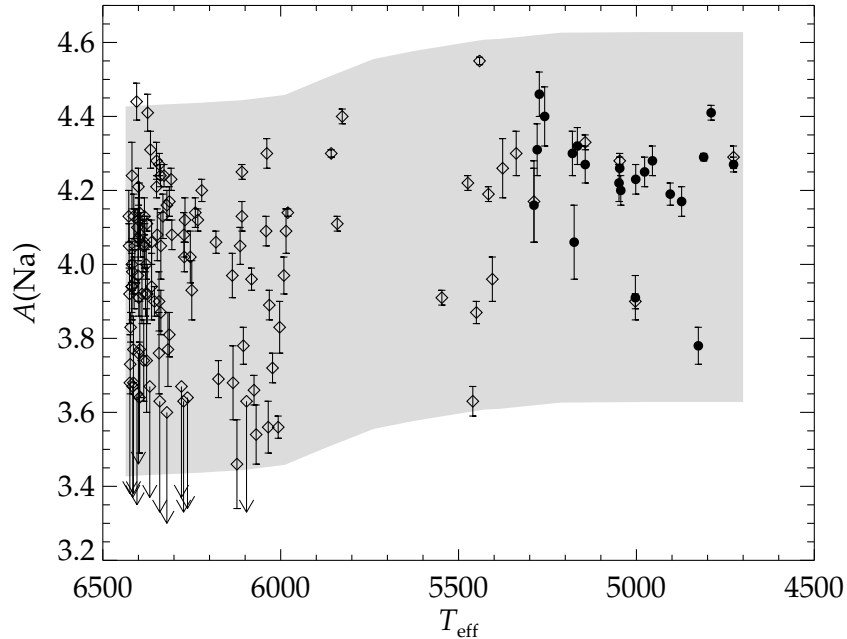


Figure 7.4: Non-LTE Na abundance variation with effective temperature in NGC 6397. Filled bullets represent the RGB stars that are analysed in this study (abundance based on 568.2/568.8 nm lines) and open diamonds the abundances inferred by Lind et al. (2009b) (abundance based on 818.3/819.4 nm lines). The studies have five targets in common. The grey shaded area illustrates, given a range of different initial Na abundances, the predicted evolution of the surface abundance based on a model with atomic diffusion and turbulence below the outer convective zone (Richard et al. 2005, model T6.0).

literature. Only recent studies that analysed stars on the upper RGB, in approximately the same magnitude range as our targets, are included in the comparison.

7.3.1 O, Na, Mg, and Al

In agreement with previous findings for the cluster (e.g. Carretta et al. 2005, 2009a; Lind et al. 2009b), we find a large spread in Na abundance. Fig. 7.4 shows how Na abundances vary with effective temperature for post-TO stars in the cluster, including the RGB star abundances determined in this study, as well as those determined by Lind et al. (2009b) for TO, SGB, and RGB stars. It is apparent that the mean Na abundance is higher by approximately 0.2 dex in the RGB stars ($T_{\text{eff}} < 5600$ K), compared to the TO and SGB group ($T_{\text{eff}} > 5950$ K). For such low-mass stars classical models do not predict any dredge-up of fresh Na produced in situ by proton-capture on pristine ^{22}Ne (see e.g. Charbonnel & Lagarde 2010), so the reason for the apparent Na enhancement must lie elsewhere. A

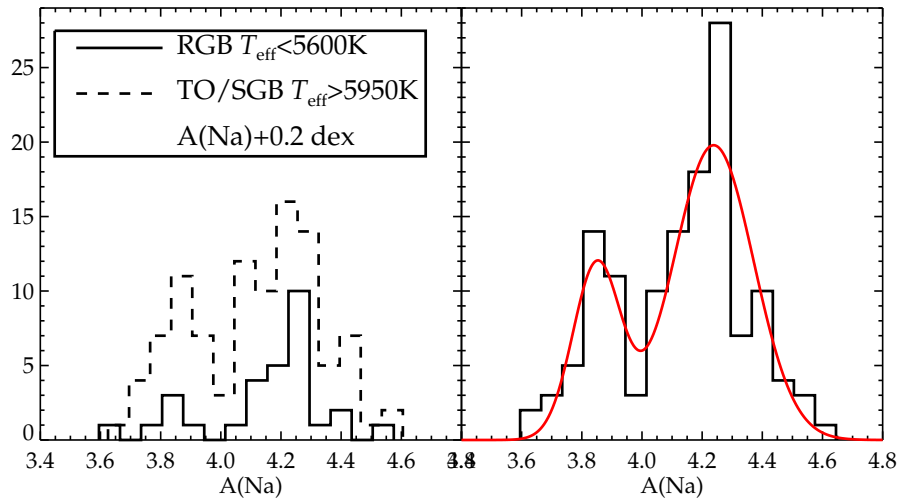


Figure 7.5: The left hand panel shows two histograms of the abundances displayed in Fig. 7.4, separating RGB stars (solid line) from TO and SGB stars (dashed line). A shift of +0.2dex has been added to the TO/SGB group to correct for the presumed effects of atomic diffusion (see text). The right hand panel shows a histogram of the whole sample and a double-Gaussian fit to the distribution.

similar difference was recently identified by D’Orazi et al. (2010), between dwarfs and giants in 47 Tuc, which they propose to be an artificial result, stemming from the assumption of Gaussian line profiles when determining the equivalent widths of the 818.3/819.4 nm lines. This is not an issue for our study, since we are using full spectrum synthesis. Instead, considering the good agreement between the 818.3/819.4 nm lines and the 568.2/568.8 nm lines for the five RGB stars for which both are observed (the mean difference is 0.06 ± 0.02), we propose that the 0.2 dex difference is real. In fact, this is the amount expected from stellar structure models including atomic diffusion, moderated by a certain degree of turbulence below the outer convection zone, as illustrated in Fig. 7.4 (see Richard et al. 2005, and references therein). Korn et al. (2007); Lind et al. (2008) found differences of similar size between dwarf and giant star abundances of Fe and Mg in NGC 6397, well matched by the T6.0 model of Richard et al. (2005). We therefore propose that the TO and SGB stars show lower Na levels because of gravitational settling from the envelope, whereas the initial abundance has been reinstated in the photospheres of RGB stars, due to the dredge-up of segregated pristine material when the convection zone deepened. We note that even if atomic diffusion well accounts for the abundance differences between dwarfs and giants in NGC 6397, the situation may be different for 47 Tuc. This cluster has a higher metallicity ($[\text{Fe}/\text{H}] = -0.76$, Koch & McWilliam 2008), thus hosting TO stars with cooler effective temperatures and larger convective envelopes, which likely makes settling less efficient.

Accounting for the presumed effect of atomic diffusion and adjusting the Na abundances

of TO and SGB stars by +0.2 dex, the abundance histograms shown in Fig. 7.5 reveal an interesting pattern. The Na abundance distribution of both groups appears clearly bimodal, having two peaks separated by ≈ 0.4 dex and the one at higher abundance being larger than the other. The right hand panel of Fig. 7.5 shows the histogram of the merged sample, where the two peaks have become more distinguished. A two-population fit, assuming Gaussian distributions, is also shown with a red solid line. The best fit places the first population around $A(\text{Na}) = 3.85 \pm 0.08$ (mean and standard deviation) or correspondingly $[\text{Na}/\text{Fe}] \approx -0.30$, and the second around $A(\text{Na}) = 4.24 \pm 0.13$ or $[\text{Na}/\text{Fe}] \approx 0.09$. The number ratio is approximately 1:3, with 26% of the stars in the first group and 74% in the second group. We interpret this abundance distribution as a result of intra-cluster pollution, raising the Na abundances of a second generation of stars compared to the first. Such discretization between the present populations has not been possible before for NGC 6397, probably due to small number statistics.

Two of the RGB stars analysed in this study have Na abundances that clearly place them in the first generation ($A(\text{Na}) < 4.0$, #5644 and #17691). Yet one more star can be regarded as a limiting case ($A(\text{Na}) = 4.13 \pm 0.09$, #14592), but considering also its comparably high Mg and O levels we assign this star to the first generation as well. The remaining 18 RGB stars are assigned to the second generation. We ascribe to low number statistics the fact that only three out of 21 RGB stars are found to belong to the first generation (since the number ratio found for the full sample is approximately 1 : 3, we would rather have expected five stars). As can be seen from Fig. 7.6, showing O, Na, Mg, and Al abundances, the populations are most clearly distinguished in a Na–Mg diagram, which likely is due to the more precise determination of these abundance ratios compared to O and Al. The Al lines are not detectable in the first generation stars and we can only infer upper limits to their Al abundance. Nevertheless, the abundances of O, Al, and Mg support the view that the Na-rich stars have been polluted by gas enriched in H-burning products. Table 7.1 lists the mean abundance ratios relative to iron of the stars that we characterise as belonging to the first and second generation. Also the difference in mean abundance ratio is listed.

Carretta et al. (2009b,a) have measured Na abundances in a large number of RGB stars in NGC 6397 and also report O abundances or upper limits for a subset of 13 stars. Table 7.1 lists the mean $[\text{O}/\text{Fe}]$, $[\text{Na}/\text{Fe}]$, and $[\text{Mg}/\text{Fe}]$ ratios for this subset, using the same solar abundances as in this study (Asplund et al., 2009). Accounting for the ~ 0.14 dex difference in mean $[\text{Fe}/\text{H}]$ between the studies, the mean O, Na, and Mg abundances agree rather well (± 0.1 dex). However, the full set of Na abundances published by Carretta et al. (2009b,a) (including the lower resolution measurements with VLT/GIRAFFE) shows a systematic offset towards higher values by typically 0.2 dex. The reason for this offset can be traced to differences in the adopted oscillator strengths (~ 0.05 dex), as well as differences in the non-LTE corrections that have been applied (~ 0.15 dex, see Chapter 2).

According to the distinction by Carretta et al. (2009b,a) the primordial (first) generation is made up of stars with $[\text{Na}/\text{Fe}] \leq [\text{Na}/\text{Fe}]_{\text{min}} + 0.3$ dex, with $[\text{Na}/\text{Fe}]_{\text{min}}$ being the minimum value observed in the cluster and 0.3 dex corresponding to $\sim 4\sigma([\text{Na}/\text{Fe}])$ (where $\sigma[\text{Na}/\text{Fe}]$ is the star-to-star error on $[\text{Na}/\text{Fe}]$). Adopting this definition for our RGB

7. Tracing the evolution of NGC 6397 through the chemical composition of its stellar populations

108

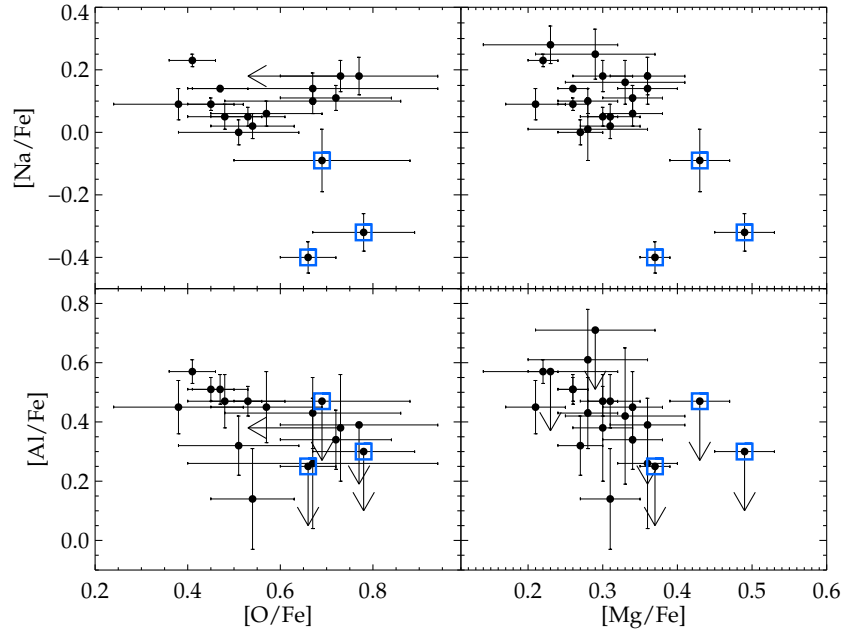


Figure 7.6: Na, Mg, and Al abundances for 21 stars and O abundances for 17 stars. The three Na-poor stars that we assign to the first generation are marked with blue squares.

sample, the first generation would consist of the same three stars, ($[\text{Na}/\text{Fe}]_{\text{min}} = -0.34$). All the other sample stars are then considered as second-generation stars. Further, the authors define an extreme component among second generation stars, if present, as stars having $[\text{O}/\text{Na}] < -0.9$ (or $[\text{O}/\text{Na}] < -1.03$, adopting the solar abundances of Asplund et al. (2009)). For NGC 6397, none of the 13 targets analysed by Carretta et al. (2009a) fall in the extreme component according to this definition and the same is true for our sample. In numbers, Carretta et al. (2009a) find that $25 \pm 13\%$ and $75 \pm 22\%$ of their full sample of stars in NGC 6397 belong to the primordial and intermediate components, respectively, which agrees very well with our results (26% and 74%). Finally, we have also inspected the Na abundance histogram of the full Carretta et al. (2009b) sample, to see if the same double-peaked distribution as in Fig. 7.5 can be distinguished. This is not the case however, which we believe is likely due to the larger measurement errors (typically ~ 0.1 dex, according to their estimate, compared to ~ 0.05 dex in our study), stemming from their lower spectral quality. Obviously, the possibility that the bimodality seen in our abundance data is artificial and not representative of the true distribution cannot be completely ruled out. This is unlikely though, especially considering that the two samples (TO+SGB and RGB) show a very similar pattern.

Fig. 7.7 compares the abundance ratios of our cluster targets to halo field data. As expected, we see that the $[\text{Na}/\text{Fe}]$ ratio of the first generation is in good agreement with

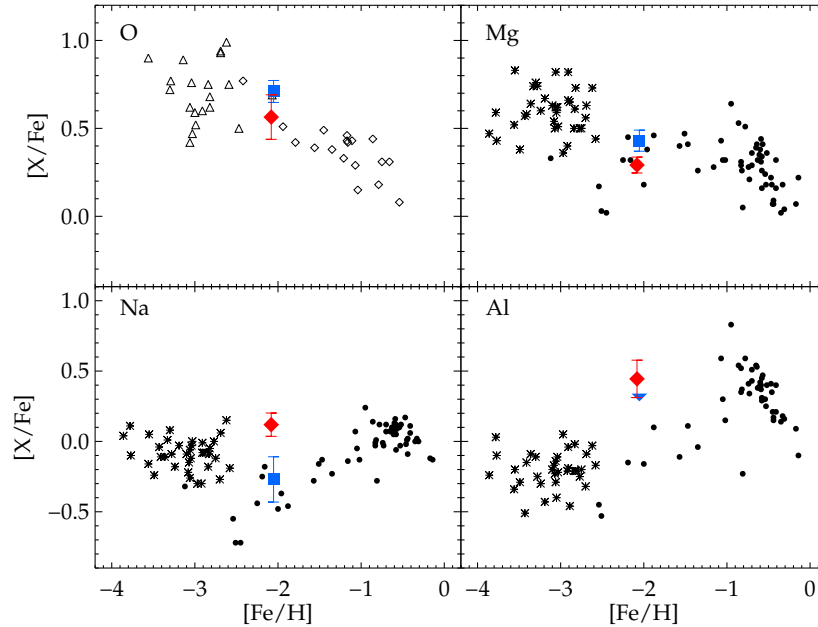


Figure 7.7: Comparison between abundances of RGB stars in NGC 6397 and halo field stars. The blue filled squares represent the mean abundances of the NGC 6397 stars assigned to the first generation and the red diamonds the mean of the second generation. The error bars mark the 1σ dispersion. Upper limits are treated as detections for the second generation averages for Al (two stars) and O (one star) when computing the mean and standard deviation. The literature data for halo field stars are assembled as follows; filled bullets (Gehren et al., 2006), star symbols (Andrievsky et al., 2007, 2008, 2010), open triangles (Cayrel et al., 2004), and open diamonds (Nissen et al., 2002).

the field at this metallicity, whereas the Na abundances of the second generation are clearly enhanced. The $[Al/Fe]$ ratios of the second generation also appear enhanced compared to the field, but only upper limits can be inferred for the first generation, limiting the comparison to field stars. The $[Mg/Fe]$ and $[O/Fe]$ ratios show a smaller total range in the cluster compared to $[Na/Fe]$ and $[Al/Fe]$, which can be understood since the abundances of Mg and O are higher than those of Al and Na by almost three orders of magnitude. Both first and second generation stars may be compatible with the field for O and Mg.

7.3.2 Nitrogen

As mentioned in the introduction, NGC 6397 photometric data appear very homogeneous. However, colour indices designed specifically to trace elemental abundances may provide further support for the presence of multiple populations. As realised by Grundahl et al.

(2002a), the strength of the Strömgren c_1 -index can be used as a tracer of the N abundance, since the u -filter involved in constructing this index covers the 336 nm NH features. Later, Yong et al. (2008a) empirically defined a more suitable index for the purpose, $c_y = c_1 - (b - y)$, which removes much of the temperature sensitivity of c_1 . The top panel of Fig. 7.8 shows a $V - c_y$ diagram, in which we have marked the first and second generation targets in this study with different symbols. We also add the RGB targets analysed by Lind et al. (2009b), assigning stars with $A(\text{Na}) < 4.0$ to the first generation and $A(\text{Na}) > 4.0$ to the second. The clear separation between the generations visible in Fig. 7.8 indicates that also their N abundances are affected. Such a correlation between c_y -index and light element abundances was recently illustrated also by Milone et al. (2010) for the more metal-rich globular cluster NGC 6752. In both clusters the first generation of stars seem to populate a tight, blue RGB sequence in this colour index, and the second generation a more dispersed, red sequence.

In the bottom panel of Fig. 7.8 we have extracted a box centred on the middle RGB and produced a histogram of the c_y index. The magnitude cuts are applied to reduce remaining bias due to temperature effects. Again, we see a two-peaked histogram, very similar to the one obtained for Na abundance. The best fit returns the peak positions at $c_y = -0.341$ and $c_y = -0.306$, with a size relationship of 25% and 75% for the left and right peak, in excellent agreement with previously inferred number fractions for the first and second stellar generation (see Sect. 7.3.1).

We may estimate the corresponding difference in $[\text{N}/\text{Fe}]$ abundance with the theoretical calculations (using synthetic colours) by Önehag et al. (2009), giving an approximate sensitivity of $\delta c_y / \delta [\text{N}/\text{Fe}] = 0.04$ for stars in the same T_{eff} and $\log g$ -ranges in NGC 6752. A somewhat stronger sensitivity, 0.06, was found by Yong et al. (2008a) who empirically correlated spectroscopic N abundances with c_y -colour for the same stars. This cluster has slightly higher metallicity, but it still serves as an order of magnitude estimate. The typical $\Delta[\text{N}/\text{Fe}]$ between stars of the first and second generation thus lies in the range 1–1.5 dex. This is consistent with spectroscopic N measurements by Carretta et al. (2005), who found that six out of nine SGB stars are strongly enhanced in $[\text{N}/\text{Fe}]$ compared to the remaining sample, by as much as 1.5 dex. Pasquini et al. (2008) found all three stars in their sample to be highly N-enriched compared to the field. Spectroscopic N measurements for a large sample of stars in NGC 6397 is obviously desirable.

7.3.3 α and iron-peak elements

Globular clusters are generally very homogeneous in α and iron-peak elements, with the exceptions of peculiar clusters such as ω Cen. In NGC 6397, the star-to-star scatter in $[\text{Fe}/\text{H}]$ in our RGB sample is extremely small, only 0.03 dex, when basing the iron abundance on singly ionised lines. FeI line abundances show a slight decreasing trend with decreasing effective temperature, which is not seen in FeII line abundances. The same pattern is seen for $[\text{Ti}/\text{Fe}]$ and $[\text{Cr}/\text{Fe}]$ ratios, and may indicate that the temperature scale contains a small systematic bias (~ 50 K over a total range of 500 K) or that non-LTE and/or 3D effects have minor differential effects. In Table 7.1, the reported Fe, Ti, and Cr

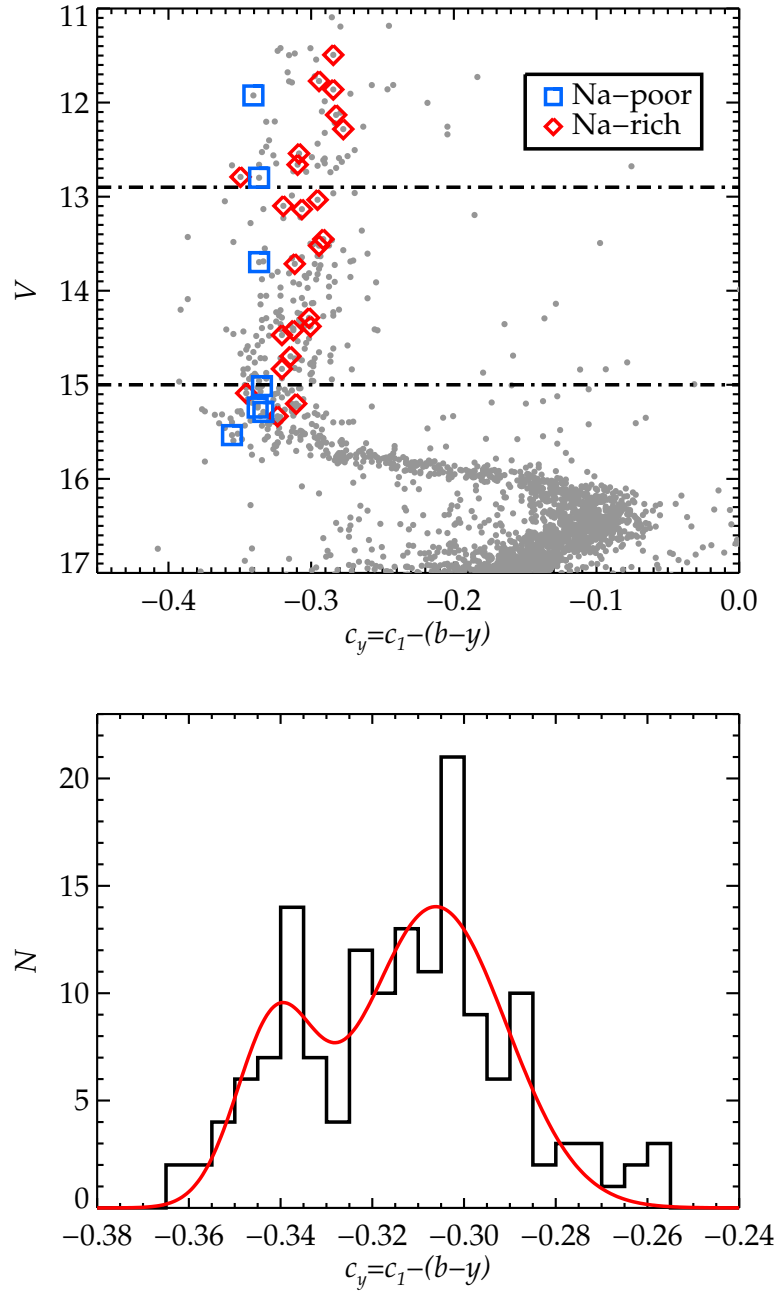


Figure 7.8: The top panel shows the $V - c_y$ diagram of NGC 6397. Na-poor and Na-rich stars are marked with blue squares and red diamonds respectively (abundance data from this study and Lind et al. 2009b). The bottom panel shows a histogram of the c_y index for red giants in the magnitude range $12.9 < V < 15$. For details, see text.

abundances are all based only on singly ionised lines. The abundances of Mn, Co, Cu, and Zn are based on one rather weak neutral line, which likely explains the larger star-to-star scatter in these abundances.

In general, the α and iron-peak elements show the expected pattern, in agreement with the halo field at this metallicity. Ca, Si, Ti, and Sc are overabundant by 0.1 – 0.3 dex, whereas the iron-peak elements Cr, Co, Ni, and Zn are approximately solar. The odd- z elements Mn and Cu are strongly under-abundant compared to the Sun, and the low value we have inferred for Cu ($\langle [\text{Cu}/\text{Fe}] \rangle = -0.89$) is slightly below the values recently inferred for field dwarfs at this metallicity by Primas & Sobeck (2008). The mean Mn abundance ($\langle [\text{Mn}/\text{Fe}] \rangle = -0.54$) is very similar to the LTE abundances inferred by Bergemann & Gehren (2008), but as shown in that study, non-LTE corrections for Mn are positive and rather substantial.

As can also be seen in Table 7.1, there is no significant difference (i.e. $> 2\sigma$) between the mean abundances of intermediate mass (heavier than Al) and iron-peak elements between the stars that we characterise as belonging to the first and second generation.

7.3.4 Neutron capture elements

Metal-poor halo field stars are known to display a large scatter in some of the neutron capture elements, which cannot be explained by observational uncertainties (see e.g. Barklem et al. 2005; Burris et al. 2000). Stars within a globular cluster are generally much more homogeneous in their heavy element abundances, as shown by for example (James et al., 2004) for NGC 6397, NGC 6752, and 47 Tuc and by Yong et al. (2008b) for M4 and M5. This is confirmed by our study, with low abundance dispersions found for Y, Zr, Ba, Ce, Nd, and Eu. The mean abundance ratios we derive for $[\text{Y}/\text{Fe}] = -0.26$ and $[\text{Ba}/\text{Fe}] = -0.08$ are in reasonable agreement with previous estimates for the cluster (in addition to the values listed in Table 7.1, James et al. 2004 determined $[\text{Y}/\text{Fe}] = -0.2$ and $[\text{Ba}/\text{Fe}] = -0.17$ for stars at the base of the RGB). The other elements have not been previously analysed in NGC 6397. Comparing to the values determined for the higher metallicity cluster NGC 6752 by Yong et al. (2005), we see good agreement between Zr, Ba, Ce, Nd, and Eu abundances. However, for Zr this is partly coincidental; accounting for differences in the adopted oscillator strength for the Zr II line at 511.2 nm, our abundance ratio would be 0.3 dex lower. A similar difference is seen when comparing the estimates for $[\text{Y}/\text{Fe}]$. It thus seems that the two clusters are very similar in heavy neutron capture elements having $Z > 56$, whereas the lighter $Z = 39 - 40$ elements are 0.3 dex less abundant in NGC 6397.

According to Burris et al. (2000), Y, Zr, Ba, and Ce are all mainly s-process elements (72-85% s-process contribution), whereas Nd is approximately half r-process, half s-process. Eu is almost a pure (97%) r-process element. For the first time we determine the $[\text{Ba}/\text{Eu}]$ ratio in this cluster, and the value we infer (-0.49), fall rather close to the scaled solar r-process of -0.81 (the scaled s-process value is 1.45). The same is true for the $[\text{Zr}/\text{Eu}]$, $[\text{Ce}/\text{Eu}]$, and $[\text{Nd}/\text{Eu}]$ ratios, whereas $[\text{Y}/\text{Fe}]$ even is slightly below the expectation from pure r-process contribution. It thus seems that chemical enrichment by core-collapse supernovae may be sufficient to explain the observed heavy element abundances, and that

contribution from AGB stars has been limited.

The two stellar generations are very similar in the measured neutron-capture elements (see Table 7.1). Only the [Y/Fe] ratio is higher by $\sim 3\sigma$ in the second generation. The difference (0.04 dex) is, however, too small to be convincing. A comparison to halo field stars does not provide much information, since the stars in the field are highly scattered. The abundances we find for NGC 6397 are well within the ranges found e.g. by François et al. (2007) for a sample of metal-poor field giants.

7.3.5 Helium

If the second generation stars in globular clusters indeed have been enriched in nucleosynthesis products connected to hydrogen-burning, they should also have a higher He content than their first generation counterparts, although we may only speculate on the exact amount.

Recently, di Criscienzo et al. (2010) used the accurate, proper-motion cleaned HST photometry of Richer et al. (2008) to measure the width of the MS in NGC 6397 and constrain the possible helium spread in the cluster. Under the assumption that 70% of the stars belong to the second generation and have a C+N+O enhancement as suggested by spectroscopic observations ($\Delta[(C+N+O)/Fe] \sim 0.25$ according to Carretta et al. 2005), they conclude that the cluster must be very uniform in He abundance, implying only $\Delta Y = 0.02$ between first and second generation. When allowing for higher [(C+N+O)/Fe] over-abundances, a broader spread in helium (ΔY up to 0.04) is compatible with the tightness of the MS. Here we will attempt to constrain this difference by spectroscopic arguments instead.

The He abundance cannot be measured directly in late-type stars, but it nevertheless influences the emerging stellar spectrum. The effects of helium-enrichment in a cool stellar atmosphere have been investigated by Strömgren et al. (1982), who found that changes in the helium-to-hydrogen ratio in F type dwarfs affect the mean molecular weight of the gas and have impact on the gas pressure. However, helium contributes only negligible to line and continuous opacity in a cool atmosphere and does not provide free electrons. Therefore, Strömgren et al. (1982) concluded and demonstrated that a helium-enrichment can be mapped merely as a shift in surface gravity, i.e. a helium-enriched atmosphere is similar to a helium-normal atmosphere with a higher surface gravity, in terms of temperature structure and electron pressure structure. Stars with identical T and P_e structures and the same ratio of metals-to-hydrogen also have identical spectra. The calculation of the necessary shift in surface gravity is given by the relation (see equivalent Eq. 12 in Strömgren et al. 1982).

$$\log g'' = \log g' + \log \left(\frac{(1 + 4 \times y')(1 + y'')}{(1 + 4 \times y'')(1 + y')} \right) \quad (7.1)$$

Here $\log g'$ is the surface gravity of the model with helium-to-hydrogen ratio $y' = N_{\text{He}}/N_{\text{H}}$ and analogously for the double-primed variables. We have tested whether the

7. Tracing the evolution of NGC 6397 through the chemical composition of its stellar populations

Table 7.2: Stellar parameters for #5644 and #14565 derived assuming a normal-star hydrogen and helium composition.

ID	T_{eff} $b - y$	T_{eff} H α	T_{eff} Ex. eq.	$\log g$ Photo.	$\log g$ Ion. eq.
5644	4826	4740	4597	1.74	1.50
14565	4811	4730	4598	1.71	1.52
Δ	15	10	-1	0.03	-0.02

relation holds also for our RGB targets by computing two metal-poor MARCS atmospheric models (Asplund et al., 1997) with $T_{\text{eff}} = 4700$ K. One model has extreme helium-enrichment, $\log g = 1.65$, and $y = 1.0$ (corresponding to helium mass-fraction of $Y = 0.8$). The second model is helium-normal, but with a higher surface gravity, $\log g = 1.95$, and $y = 0.085$ ($Y = 0.25$). All metal abundances relative to hydrogen are the same in both models ($[\text{Fe}/\text{H}] = -2.0$), which means that the helium-rich model has a lower mass fraction of metals. The temperature structure and electron density structure of the two model atmospheres are very similar, as expected, and derived elemental abundances based on the models are the same to within ~ 0.005 dex. We thus consider it safe to use the scaling with surface gravity of normal composition models to mimic helium-enhancement.

We selected one star from each generation to test the hypothesis of a difference in He-content. The stars have essentially identical stellar parameters, which allows a differential comparison. Table 7.2 lists the derived stellar parameters for these two targets. The absolute T_{eff} -values inferred from fitting the wings of the H α line and from the excitation equilibrium of neutral iron are both somewhat lower than the photometric, but the difference between the two selected stars is small for all methods. Since the true difference in He abundance between the stars, if any, is unknown, the effective temperatures have been computed assuming normal helium-to-hydrogen ratio in both objects. None of the methods should be severely biased by this assumption, however. The Strömgen colours have only a weak sensitivity to surface gravity ($\sim \pm 15$ K per ± 0.1 dex in $\log g$), which is also true for neutral iron lines (the differential impact on the iron abundance inferred from low- and high-excitation lines is 0.001 dex per 0.1 dex in $\log g$. This translates to < 0.5 K in effective temperature.). The influence of a higher helium-to-hydrogen ratio on the H α profile has been investigated and found to be negligible as well, if the number density of metals is kept constant. Based on the information in Table 7.2, we conclude that the difference in effective temperature between the stars is likely to be small. We assume that they have the same effective temperature and adopt 10 K as a representative error of the relative difference.

The photometric surface gravities were determined in Lind et al. (2009b), from the common relation between mass, surface gravity, luminosity, and temperature. Assuming $M = 0.8 M_{\odot}$ and bolometric correction $BC = -0.390$, the resulting values are different by 0.03 dex only. However, as the evolution of a helium-enhanced star certainly is different

Table 7.3: Iron mass fractions derived for #5644 and #14565, assuming different mass fractions of helium

ID	5644	14565	14565	14565
y	0.085	0.085	0.170	1.000
Y	0.253	0.253	0.405	0.800
X	0.747	0.747	0.595	0.200
$\log g$	1.50	1.52	1.45	1.21
$A(\text{Fe})$	5.316	5.323	5.323	5.323
$Z(\text{Fe}) * 10^6$	8.662	8.803	7.007	2.353

from a helium-normal, the assumption of equal mass for the two stars may be wrong. If #14565 is helium-enriched compared to #5644 it should, from stellar-evolution arguments, have a lower mass and consequently a lower surface gravity. We have also calculated surface gravities based on the ionisation equilibrium of FeI and FeII. With a normal-star composition for both objects the surface gravity values are different by 0.02 dex. If a higher helium mass fraction is assumed for 14565, the surface gravity value that establishes the equilibrium will shift to lower values in accordance with Eq. 1. However, the iron abundance found relative to hydrogen will be the same in the two cases. We thus conclude that if both stars have the same helium mass fraction, they also have almost the same surface gravity. If not, the difference in $\log g$ cannot be determined independently from the difference in helium content. However, if $\log g$ is calculated by ionisation equilibrium, the effect of the helium enhancement will effectively cancel and $[\text{Fe}/\text{H}]$ will be found the same.

We calculate the iron abundances, $A(\text{Fe})$, and iron mass fractions, $Z(\text{Fe})$, of 5644 and 14565, using $T_{\text{eff}} = 4750 \text{ K}$, microturbulence $\xi_t = 1.7 \text{ kms}^{-1}$ and the surface gravities that satisfy the ionisation equilibrium of iron, which is different for different values of y . The results are given in Table 7.3. When assuming a normal He composition, the iron abundances of the stars agree to within 0.007 dex. A higher mass fraction of helium in 14565 will not affect the iron abundances derived relative to hydrogen, but the mass fraction of iron will be lower. Assuming that the mass fractions of iron are exactly the same for the stars, we can calculate the corresponding difference in helium mass fraction. The errors in $\Delta A(\text{Fe})$ and $\Delta Z(\text{Fe})$ are estimated by the standard deviation of the mean difference for each individual line, to cancel contributions from uncertainties in oscillator strengths. The resulting error is 0.003 dex for FeI and 0.009 dex for FeII. Adopting a relative uncertainty in effective temperature of 10 K corresponds to an additional 0.016 dex. The total error budget is thus 0.028 dex, or 6.7% in iron mass fraction. Assuming that #14565 has the same $Z(\text{Fe})$ as #5644, ΔY between the stars then becomes 0.01 ± 0.06 . We caution that this is far from a stringent constraint on the true difference in Y , especially considering the possibility of a real (small) difference in iron mass fraction. However, it is safe to say that our simple arithmetic exercise clearly dis-favours extreme He-enhancement, in agreement with the photometric tightness of the MS.

In the cluster formation scenario described by Decressin et al. (2007a), with slow winds from rotating massive stars pollute the star forming gas, one expects an anti-correlation between helium and $[O/Na]$ for second generation stars born out of a mixture of stellar ejecta and pristine material. As can be seen in Fig. 13 of Decressin et al. (2007a), the small value implied for ΔY is fully compatible with the corresponding $\Delta [O/Na]$ of 0.75 dex between #5644 and #14565. This good agreement persists over the whole mass range considered by Decressin et al. (2007a), i.e., for polluter stars with masses between 20 and 120 M_{\odot} .

7.4 Consequences for the evolutionary scenario

We will now investigate if the abundance patterns we derived for NGC 6397 can be accounted for in the framework of the so-called “wind of fast rotating massive stars” (WFRMS) scenario (e.g. Prantzos & Charbonnel 2006; Decressin et al. 2007a,b). In this scenario, second generation stars are formed from matter ejected through slow winds of individual massive stars ($M \geq 20 M_{\odot}$), mixed locally with pristine interstellar gas. These massive stars supposedly reach the critical rotational velocity early on the MS phase, and lose significant mass and angular momentum by ejecting material in an equatorial disk. Due to deep rotational mixing, this material is enhanced in H-burning products produced in the stellar core. When the stars explode as supernovae the previously ejected slow material can still be retained in the cluster and united with the inter-stellar medium that form the second generation stars.

7.4.1 Method

We follow the same procedure as described in Decressin et al. (2007a), using the stellar models by Decressin et al. (2007b) that were computed for the metallicity of NGC 6752 ($[Fe/H] \sim -1.56$), i.e. slightly higher than that of NGC 6397 ($[Fe/H] \sim -2.08$). A difference of this size should have no impact on our conclusions (Ekström et al., 2008). However, the enrichment history of the two clusters certainly differ to some extent, which must be considered in the analysis. Especially, the full range in O abundance is twice as large in NGC 6752 (0.8 dex, Yong et al. 2003) compared to NGC 6397 (0.4 dex, see Fig. 7.6). Also, NGC 6752 has a broadened main sequence (Milone et al., 2010) and an extended horizontal branch, indicating a larger variation in the He content.

When establishing the recycling process of NGC 6752, Decressin et al. (2007a) took into account all the material ejected by massive stars rotating at critical velocity, both on the main sequence and during the first part of the central He-burning phase². This allowed the build up of extreme abundance anomalies in both O and Na, and also lead to high He-enrichment for the “extreme component” of second generation stars. As discussed in

²Due to strong mechanical mass loss fast rotating stars actually evolve away from the critical limit during the central He-burning phase, before the He-burning products contaminate the slow wind component (Decressin et al., 2007b; Ekström et al., 2008).

Sect. 7.3.1 and 7.3.5, such extreme anomalies appear to be lacking in NGC 6397, and the second generation stars are probably only mildly overabundant in He. Consequently, we assume that only the slow winds ejected on the main sequence by fast rotating massive stars are recycled into the second generation and we neglect the material that is lost during the luminous blue variable phase. As discussed in Sect. 7.4.5 this may have some impact on the total mass budget, although most of the mass loss through the slow mechanical winds occurs while the fast rotating stars are on the main sequence (in the case of a $60 M_{\odot}$ rotating at critical velocity, 20 and $7 M_{\odot}$ are lost through the mechanical wind on and slightly after the main sequence, respectively). We will not venture to discuss in detail the underlying reason for the different observed abundance patterns in NGC 6752 and NGC 6397, but one may speculate that different initial masses of these clusters have played a role.

7.4.2 Amount of dilution between massive star ejecta and pristine gas

The star-to-star spread in light element abundances observed in globular clusters today implies that all the material ejected by the first generation massive stars was not fully mixed before being recycled into the second stellar generation. Additionally the observed behaviours of both O and Li pinpoints the formation of second generation stars in the vicinity of individual massive stars from their slow winds mixed with pristine interstellar matter.

As explained in Decressin et al. (2007a) we may use the observed Li-Na anti-correlation to estimate the amount of dilution between the massive star ejecta that are totally void of Li and the pristine intra-cluster gas left after the formation of first generation stars, whose Li abundance is assumed to be equal to the primordial (Big Bang) value. We further assume that the slow wind of each individual massive star undergoes locally a variable dilution with time. In the early main sequence phase, the stellar ejecta encounter more pristine gas and are hence more diluted than the matter ejected later. As the stellar winds become more Na-rich later in the course of the evolution of a massive polluter, the Li-Na anti-correlation builds up naturally: second generation low-mass stars with a relatively high Li content and a relatively low Na abundance are created first, while stars formed from matter ejected later have less Li and more Na.

In Fig. 7.9 we present theoretical predictions for the Li and Na abundance variations in the resulting material out of which second generation low-mass stars are assumed to form. The tracks shown correspond to the cases of the ejecta of the 20 and $120 M_{\odot}$ models by Decressin et al. (2007b) for different values (0.2, 0.4, 0.6, and 0.8) of the minimum dilution (along individual tracks dilution decreases from 1 down to this minimum value as the polluter star evolves). Predictions for polluters with different initial masses would fill the whole space between 20 and $120 M_{\odot}$ tracks. The initial (pristine) $[\text{Na}/\text{Fe}]$ value is assumed to be the average that we find for first generation stars (i.e., -0.3 ; see Sect. 7.3.1). For Li we consider the value from WMAP and Big Bang nucleosynthesis ($A(\text{Li}) = 2.72$

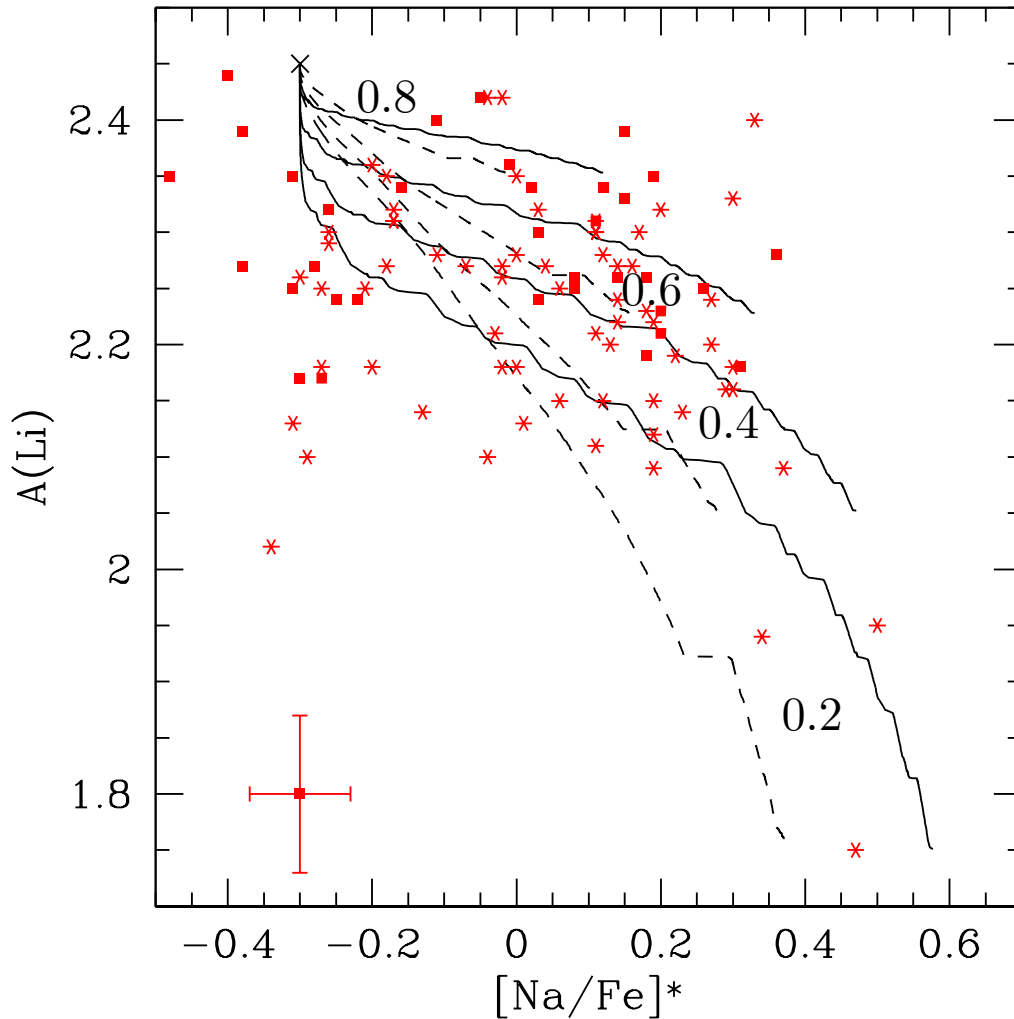


Figure 7.9: Li and Na abundances for TO and SGB stars in NGC 6397 (data from Lind et al. 2009b). The initial $[Na/Fe]$ has been estimated by correcting $A(Na)$ for atomic diffusion by $+0.2$ dex and assuming $[Fe/H] = -2.1$ for all stars. The red asterisks represent TO stars and the red squares subgiants, with the typical size of the error bar indicated. Superimposed are the theoretical predictions for the chemical composition of the matter out of which second generation low-mass stars are expected to form in the WFRMS scenario. The tracks shown correspond to the cases of 20 and $120 M_{\odot}$ polluter stars (dashed and full lines respectively) assuming different values ($0.2, 0.4, 0.6, 0.8$) for the minimum dilution coefficient. See text for more details.

according to Cyburt et al. 2008) and take into account Li depletion of 0.2 dex at the surface of both first and second generation low-mass stars during the main sequence (Charbonnel & Primas, 2005; Lind et al., 2009b). In Fig. 7.9 the theoretical tracks are superimposed on the Li and Na observational data by Lind et al. (2009b) for NGC 6397 TO and SGB stars that have not yet undergone the first dredge-up. TO and SGB stars (defined here as stars fainter and brighter than $V = 16.2$ respectively) are marked with different symbols to also consider the 0.1 dex difference in $A(\text{Li})$ found between these two groups by Lind et al. (2009b), interpreted as a sign of dredge-up of settled Li. Various degrees of dilution explain very well the observed spread, and the bulk of the sample can be reproduced assuming a minimum dilution factor of 0.5 (i.e., at least 50% of the material that formed the corresponding stars is pristine gas). Stars with low-Li and high-Na stars require a lower minimum dilution factor of ~ 0.2 . Within the observational errors the overall agreement between the observational and theoretical trends and dispersions is satisfactory.

7.4.3 Expected anti-correlations

Armed with this calibration for the dilution between massive star ejecta and pristine gas we can now make similar predictions for the (anti-)correlations between O, Na, and Al. For the composition of the pristine cluster gas we use the average values we derived for first generation stars for O and Na ($[\text{O}/\text{Fe}] = 0.77$, $[\text{Na}/\text{Fe}] = -0.3$). Since we could only derive upper limits on the Al abundance of the first generation, we assume a value that is approximately compatible with the field at this metallicity, $[\text{Al}/\text{Fe}] = 0.0$ (see Fig. 7.7).

The theoretical tracks for the chemical composition of material out of which second generation stars can form are shown in Fig. 7.10. They correspond to the case of a minimum dilution equal to 0.2 (for these elements the tracks for other minimal dilution values are superimposed on one another although with different extents) for polluters of various initial masses. As can be seen the tracks do not vary much with polluter mass since the central temperature in massive stars is always high enough to burn protons through CNO-cycles and Ne-Na and Mg-Al chains. However the efficiency of the rotationally-induced mixing increases with stellar mass, implying more extreme abundance variations in the case of the most massive stars. In particular only the most massive stars can be held responsible for the highest Al and Na enrichment observed in NGC 6397. Again, very good agreement is achieved between data and predictions.

Decressin et al. (2007b) described the sensitivity of the model predictions to the nuclear reaction rates adopted in the computations. The stellar models used here were computed with their “set C” for the nuclear reaction rates (see Table 2 of Decressin et al. 2007b). In this case the total magnesium abundance decreases by ~ 0.1 dex only. Assuming an enhancement of the $^{24}\text{Mg}(p,\gamma)$ reaction as done in “set D” of Decressin et al. (2007b) would however lead to a total magnesium abundance decrease by ~ 0.15 dex, in slightly better agreement with our Mg data in NGC 6397.

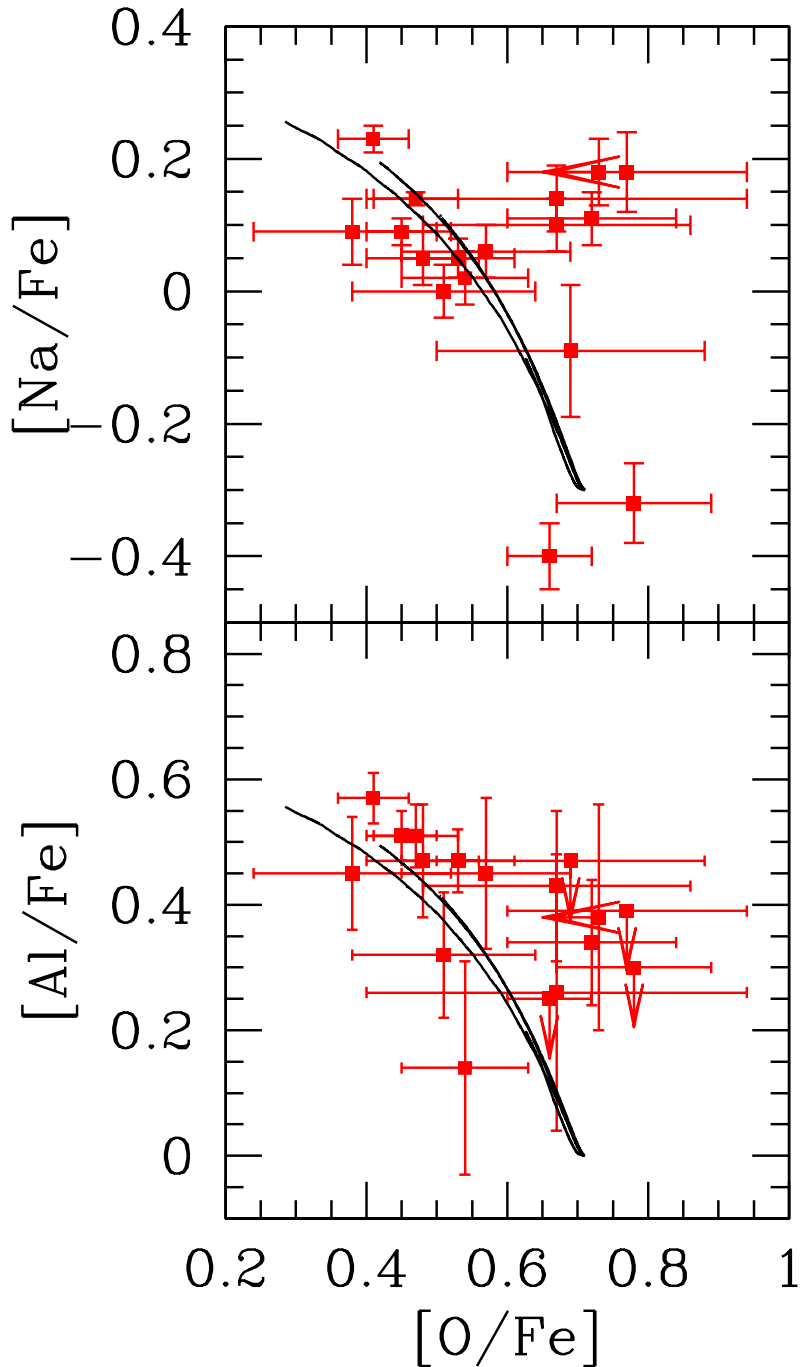


Figure 7.10: O–Na (top) and O–Al (bottom) anti-correlations are shown for the giant stars of NGC 6397. Superimposed are the theoretical predictions for the chemical composition of the matter out of which second generation low-mass stars are expected to form. The tracks correspond to the cases of 20, 40, 60, and 120 M_{\odot} polluter stars for a minimum value of 0.2 for the dilution coefficient.

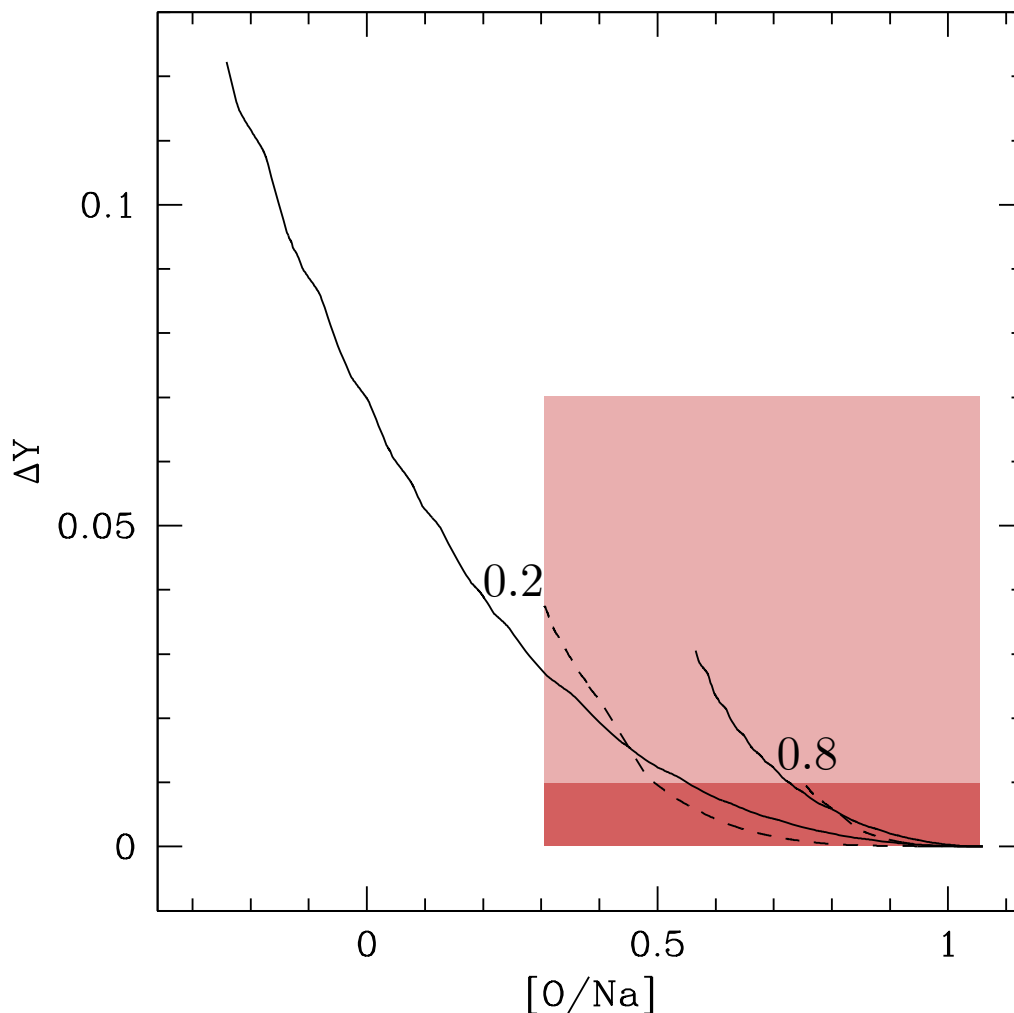


Figure 7.11: r

ratio for second generation stars.] Expected anti-correlation between helium (in mass fraction) and $[O/Na]$ for second generation stars (at birth) born out of material ejected through slow winds of massive stars and diluted with gas of pristine composition. The tracks correspond to the cases of 20 and 120 M_{\odot} polluter stars (dashed and full lines respectively) assuming different values (0.2 and 0.8) for the minimum dilution coefficient. See text for more details. The shaded regions indicate the star-to-star abundance differences derived in Sect. 7.3 for #5644 and #14565 and related uncertainties ($\Delta[O/Na] = 0.75$ and $\Delta Y < 0.07$).

7.4.4 He content

We can now make predictions for the helium spread expected within the WFRMS scenario with the assumptions described above for the specific case of NGC 6397. Fig. 7.11 shows predicted variation in He mass fraction as a function of the [O/Na] ratio. Also shown are the values estimated in Sect. 7.3 for #5644 and #14565. We see that the theoretical helium variation corresponding to a $\Delta[\text{O}/\text{Na}]$ of 0.75 is less than 0.04, fully compatible with the spectroscopic estimate.

When assuming a “standard” IMF (slope of 2.35) for the massive polluter stars and taking into account the variable dilution process described in Sect. 7.4.2, we obtain that $\sim 70\%$ of second generation stars should be born with an helium mass fraction that is 0.02 higher than first generation stars. In addition, about 5-10% of second generation stars are expected to be born within the range $Y = 0.35 - 0.39$. The resulting dispersion in Y is compatible with the constraints obtained from the width of the main sequence ($\Delta Y < 0.04$).

7.4.5 Initial cluster mass

As discussed in Sect. 7.3.1, about 74% of the long-lived low-mass stars still present today in NGC 6397 belong to the so-called second generation, while about 26% were born with the same chemical composition as the massive polluters. Prantzos & Charbonnel (2006) and Decressin et al. (2007a,b) have shown that such high number ratio of second generation stars requires either a very flat IMF for the first generation massive stars, or that a very large number of first generation low-mass stars have escaped the cluster. This second option is favoured by recent finding that the fraction of halo field stars initially formed within globular clusters could be as large as 50% (Martell & Grebel, 2010).

We thus follow here the second scenario, assuming in addition that the first stellar generation consists of stars with initial masses between 0.1 and $120 M_{\odot}$, while the second generation consists only of long-lived low-mass stars ($0.1 - 0.8 M_{\odot}$). The latter assumption obviously minimises the constraints on the mass budget. We use a Salpeter IMF for the massive stars of the first generation, but assume that the present-day log-normal distribution derived by Paresce & De Marchi (2000) reflects the IMF of the long lived low-mass stars of both first and second generation.

We can then derive the amount of first generation long-lived stars that must have been lost in order to fit the high ratio of second to first generation stars (3:1) found in NGC 6397. As we consider pollution by massive star ejecta released on the main sequence only, we have less polluter material to form new stars than in the case of NGC 6752 studied in Decressin et al. (2007a). This effect is partially compensated by the higher dilution needed to reproduce the Li-Na anti-correlation as we form more second generation stars per unit mass released into slow winds. Finally, we find that about 90% of first generation low-mass stars must have been lost by NGC 6397, probably during the early event of gas expulsion by supernovae (see Decressin et al. 2010). The initial mass of NGC 6397 must thus have been ~ 10 times higher than its present day mass.

7.5 Conclusions

In this study of RGB stars in the globular cluster NGC 6397, we have demonstrated the possibility to distinguish between the present stellar generations spectroscopically, by making use of a double-peaked histogram of Na abundances. A two-population fit returns a Na abundance similar to the halo field for 26% of the stars, which we characterise as belonging to a first generation, whereas the remaining 74% (i.e. second generation) show highly elevated Na abundances. This bimodal abundance signature should be verified for an extended sample, and similar histograms may be possible to produce also for N and Al abundance, for which large spreads are present in globular clusters. The abundance spreads are smaller for O and Mg, making the task more challenging. Highly precise abundance analysis, with small statistical error bars will be necessary to distinguish such patterns, if present.

Based on 17 different elements heavier than Al, we conclude that there is no support for α , iron-peak or neutron-capture abundances to be significantly different between the stellar generations. We have also estimated the difference in He abundance between two stars of each generation by enforcing the mass fraction of iron to be same within the error bars of the analysis. Such small (if any) difference in He is expected from models of cluster self-enrichment and also supported by the tightness of the main sequence of NGC 6397. The same exercise should be performed for other globular clusters, especially those showing multiple main sequences, hopefully bringing us closer to identifying the process responsible for early cluster pollution.

Finally we have shown that the abundance patterns observed in NGC 6397 can be well reproduced within the “wind of fast rotating massive stars” scenario. Based on the Li-Na relation we could deduce the dilution factors between the ejecta of massive polluters and interstellar gas of pristine composition. The observed ratio of second to first generation stars was used to estimate the number fraction of first generation long-lived low-mass stars that must have been lost by NGC 6397, and thus the initial mass of this globular cluster. Although we did not make explicit comparisons with the yields of AGB stars, we expect this scenario to be able to account equally well for the observed abundance patterns of this globular cluster.

7. Tracing the evolution of NGC 6397 through the chemical composition of its
124 stellar populations

Table 7.4. Line list with reference to the adopted oscillator strength.

Ion	Wavelength [Å]	χ_l [eV]	$\log(gf)$	Ref.
O I	6300.304	0.000	-9.819	1
O I	7771.941	9.146	0.369	20
O I	7774.161	9.146	0.223	20
Na I	5682.633	2.102	-0.700	2
Na I	5688.194	2.104	-1.400	2
Na I	5688.205	2.104	-0.450	2
Mg I	5528.405	4.346	-0.620	3
Mg I	5711.088	4.346	-1.833	3
Al I	6696.023	3.143	-1.347	4
Al I	6696.185	4.022	-1.576	5
Al I	6698.673	3.143	-1.647	4
Si I	5665.555	4.920	-1.750	5
Si I	5690.425	4.930	-1.769	5
Si I	6155.134	5.619	-0.754	5
Si I	6237.319	5.614	-0.975	5
Ca I	5349.465	2.709	-0.310	6,7
Ca I	5512.980	2.933	-0.464	7
Ca I	5581.965	2.523	-0.555	6,7
Ca I	5588.749	2.526	0.358	6,7
Ca I	5590.114	2.521	-0.571	6,7
Ca I	5601.277	2.526	-0.523	6,7
Ca I	5857.451	2.933	0.240	7
Ca I	6102.723	1.879	-0.793	8
Ca I	6122.217	1.886	-0.316	8
Ca I	6162.173	1.899	-0.090	8
Ca I	6166.439	2.521	-1.142	6,7
Ca I	6439.075	2.526	0.390	6,7
Ca I	6449.808	2.521	-0.502	6,7
Ca I	6471.662	2.526	-0.686	6,7
Ca I	6493.781	2.521	-0.109	6,7
Ca I	6499.650	2.523	-0.818	6,7
Sc II	5239.813	1.455	-0.765	9
Sc II	5526.790	1.768	0.024	9
Sc II	5641.001	1.500	-1.131	9
Sc II	5669.042	1.500	-1.200	9
Sc II	5684.202	1.507	-1.074	9
Sc II	6245.637	1.507	-1.030	5

Table 7.4. Continued.

Ion	Wavelength [Å]	χ_I [eV]	$\log(gf)$	Ref.
Ti I	4981.731	0.848	0.504	10
Ti I	4999.503	0.826	0.250	10
Ti I	5009.645	0.021	-2.259	10
Ti I	5016.161	0.848	-0.574	10
Ti I	5020.026	0.836	-0.414	10
Ti I	5025.570	2.041	0.250	10
Ti I	5147.478	0.000	-2.012	10
Ti I	5210.385	0.048	-0.884	10
Ti I	5866.451	1.067	-0.840	10
Ti I	6258.102	1.443	-0.355	10
Ti I	6258.706	1.460	-0.240	10
Ti II	4779.985	2.048	-1.260	5
Ti II	4805.085	2.061	-0.960	5
Ti II	5005.157	1.566	-2.720	11
Ti II	5013.686	1.582	-2.190	11
Ti II	5418.768	1.582	-2.000	11
Cr I	4922.265	3.104	0.270	10
Cr I	5329.138	2.914	-0.064	10
Cr II	5237.329	4.073	-1.160	10
Cr II	5313.563	4.074	-1.650	10
Mn I	4783.427	2.298	0.042	10
Co I	5369.590	1.740	-1.650	12
Ni I	4904.407	3.542	-0.170	12
Ni I	4935.831	3.941	-0.350	12
Ni I	4953.200	3.740	-0.580	13
Ni I	4980.166	3.606	0.070	13
Ni I	5017.568	3.539	-0.020	13
Ni I	5035.357	3.635	0.290	13
Ni I	5081.107	3.847	0.300	12
Ni I	5082.339	3.658	-0.540	12
Ni I	5084.089	3.679	0.030	12
Ni I	5099.927	3.679	-0.100	12
Ni I	5115.389	3.834	-0.110	12
Ni I	5155.762	3.898	0.011	5
Ni I	6176.807	4.088	-0.260	13
Cu I	5105.537	1.389	-1.516	14
Zn I	4810.528	4.078	-0.137	15
Y II	5087.416	1.084	-0.170	16
Y II	5200.406	0.992	-0.570	16

Table 7.4. Continued.

Ion	Wavelength [Å]	χ_l [eV]	$\log(gf)$	Ref.
Zr II	5112.270	1.665	-0.850	¹⁷
Ba II	5853.668	0.604	-1.000	¹⁸
Ba II	6496.897	0.604	-0.377	¹⁸
Ce II	5274.229	1.044	-0.320	²¹
Nd II	4959.119	0.064	-0.800	¹⁹
Nd II	5092.794	0.380	-0.610	¹⁹
Nd II	5249.576	0.976	0.200	¹⁹
Nd II	5293.163	0.823	0.100	¹⁹
Nd II	5319.815	0.550	-0.140	¹⁹
Eu II	6645.064	1.380	0.200	²²

- ¹ Wiese et al. (1966)
² Kurucz & Peytremann (1975)
³ Lincke & Ziegenbein (1971)
⁴ Wiese et al. (1969)
⁵ Vienna Atomic Line
 Database VALD
⁶ Smith & Raggett (1981)
⁷ Smith (1988)
⁸ Smith & O'Neill (1975)
⁹ Lawler & Dakin (1989)
¹⁰ Martin et al. (1988)
¹¹ Pickering et al. (2001)
¹² Fuhr et al. (1988)
¹³ Wickliffe & Lawler (1997)
¹⁴ Bielski (1975)
¹⁵ Warner (1968)
¹⁶ Hannaford et al. (1982)
¹⁷ Ljung et al. (2006)
¹⁸ Miles & Wiese (1969)
¹⁹ Komarovskii (1991)
²⁰ Biemont & Zeippen (1992)
²¹ See ref. in Yong et al. (2005)
²² Lawler et al. (2001)
-

Table 7.5: Individual star abundances and stellar parameters. The propagated abundance rms error due to uncertainty in equivalent width is written below each table entry. For iron [Fe/H] is given, whereas all other abundances represent [X/Fe].

ID	T_{eff} $\log g$	FeII	FeI	OI	NaI	MgI	AlI	SiI	CaI	ScII	TiI	TiII	CrI	CrII
12138	4727	-2.06	-2.10	0.45	0.09	0.26	0.51	0.30	0.26	0.13	0.19	0.31	-0.14	0.01
	1.52	0.01	0.02	0.05	0.02	0.02	0.04	0.02	0.02	0.04	0.01	0.02	0.04	0.01
16405	4790	-2.06	-2.19	0.41	0.23	0.22	0.57	0.23	0.22	0.18	0.15	0.28	-0.18	-0.04
	1.66	0.01	0.02	0.05	0.02	0.02	0.04	0.02	0.02	0.04	0.01	0.02	0.06	0.04
14565	4811	-2.09	-2.17	0.47	0.14	0.26	0.51	0.22	0.20	0.12	0.17	0.31	-0.14	0.01
	1.71	0.01	0.02	0.06	0.01	0.02	0.05	0.02	0.02	0.04	0.01	0.01	0.08	0.02
5644	4826	-2.06	-2.12	0.66	-0.40	0.37	0.25	0.17	0.21	0.12	0.23	0.33	-0.14	0.03
	1.74	0.01	0.02	0.06	0.05	0.02	9.99	0.04	0.02	0.04	0.01	0.04	0.09	0.02
17163	4873	-2.07	-2.15	0.51	0.00	0.27	0.32	0.23	0.22	0.11	0.16	0.26	-0.20	0.03
	1.84	0.02	0.02	0.13	0.04	0.03	0.10	0.04	0.03	0.04	0.03	0.03	0.17	0.04
20820	4905	-2.10	-2.15	0.53	0.05	0.30	0.47	0.27	0.27	0.12	0.19	0.30	-0.09	0.00
	1.92	0.01	0.02	0.08	0.03	0.02	0.05	0.02	0.02	0.04	0.01	0.04	0.09	0.03
8952	4955	-2.07	-2.11	0.72	0.11	0.34	0.34	0.21	0.25	0.13	0.22	0.30	-0.09	0.00
	2.04	0.02	0.02	0.12	0.04	0.04	0.10	0.04	0.03	0.04	0.02	0.05	0.09	0.04
10737	4977	-2.04	-2.11	0.48	0.05	0.31	0.47	0.24	0.24	0.12	0.22	0.30	-0.14	0.01
	2.10	0.02	0.02	0.08	0.04	0.04	0.09	0.04	0.02	0.04	0.03	0.04	0.07	0.04
13006	5002	-2.03	-2.09	0.54	0.02	0.31	0.14	0.19	0.25	0.10	0.20	0.27	-0.11	-0.01
	2.16	0.02	0.02	0.09	0.04	0.04	0.17	0.04	0.02	0.04	0.03	0.04	0.11	0.05
17691	5003	-2.01	-2.05	0.78	-0.32	0.49	0.30	0.19	0.29	0.11	0.26	0.32	-0.04	0.06
	2.16	0.02	0.02	0.11	0.06	0.04	9.99	0.02	0.03	0.04	0.02	0.04	0.10	0.04
21284	5044	-2.10	-2.15	0.57	0.06	0.34	0.45	0.17	0.25	0.12	0.22	0.31	0.01	0.03
	2.27	0.01	0.02	0.12	0.04	0.04	0.12	0.06	0.01	0.04	0.01	0.04	0.06	0.05
9424	5047	-2.08	-2.18	0.67	0.10	0.28	0.43	0.30	0.23	0.09	0.18	0.26	-0.06	0.03
	2.30	0.02	0.02	0.19	0.04	0.04	0.12	0.06	0.02	0.04	0.03	0.06	0.04	0.06
16248	5049	-2.11	-2.17	0.38	0.09	0.21	0.45	0.31	0.25	0.13	0.20	0.31	-0.08	0.05
	2.31	0.03	0.02	0.14	0.05	0.04	0.09	0.03	0.03	0.06	0.04	0.04	0.09	0.06
11363	5144	-2.11	-2.14	0.67	0.14	0.36	0.26	0.23	0.27	0.12	0.25	0.33	-0.08	0.07
	2.49	0.02	0.02	0.27	0.05	0.04	0.22	0.06	0.02	0.04	0.03	0.03	0.09	0.09
9649	5166	-2.10	-2.13	0.73	0.18	0.30	0.38	0.25	0.27	0.11	0.26	0.29	-0.07	0.05
	2.52	0.02	0.02	9.99	0.05	0.04	0.18	0.06	0.02	0.06	0.03	0.05	0.04	0.07
14592	5175	-2.09	-2.13	0.69	-0.09	0.43	0.47	0.25	0.25	0.08	0.29	0.29	-0.08	0.01
	2.59	0.03	0.02	0.19	0.10	0.04	9.99	0.04	0.03	0.08	0.04	0.09	0.08	0.09
4680	5180	-2.12	-2.15	0.77	0.18	0.36	0.39	0.17	0.29	0.12	0.29	0.31	0.03	0.05
	2.60	0.02	0.02	0.17	0.06	0.05	9.99	0.05	0.02	0.05	0.02	0.04	0.09	0.08
12294	5258	-2.09	-2.11	...	0.25	0.29	0.71	0.22	0.24	0.13	0.28	0.32	0.12	0.12
	2.87	0.04	0.02	...	0.08	0.08	9.99	0.12	0.04	0.06	0.05	0.04	0.16	0.10
7658	5273	-2.06	-2.12	...	0.28	0.23	0.57	0.39	0.25	0.07	0.22	0.25	-0.14	0.04
	2.91	0.03	0.02	...	0.06	0.09	9.99	0.08	0.04	0.06	0.05	0.06	0.09	0.20
11142	5279	-2.09	-2.11	...	0.16	0.33	0.42	0.12	0.24	0.14	0.25	0.27	0.07	0.06
	2.93	0.02	0.02	...	0.07	0.08	0.23	0.18	0.02	0.04	0.04	0.04	0.07	0.12
7728	5288	-2.09	-2.11	...	0.01	0.28	0.61	0.40	0.24	0.05	0.27	0.34	0.11	-0.11
	2.95	0.04	0.02	...	0.10	0.08	0.17	0.08	0.04	0.04	0.05	0.05	0.07	0.26

7. Tracing the evolution of NGC 6397 through the chemical composition of its stellar populations

Table 7.6: Individual star abundances and stellar parameters. The propagated abundance rms error due to uncertainty in equivalent width is written below each table entry. For iron [Fe/H] is given, whereas all other abundances represent [X/Fe].

ID	T_{eff} log g	FeII	MnI	CoI	NiII	CuI	ZnI	YII	ZrII	BaII	CeII	NdII	EuII
12138	4727	-2.06	-0.43	0.01	-0.17	-0.76	-0.02	-0.26	0.09	-0.07	0.39	0.17	0.49
	1.52	0.01	0.04	0.02	0.02	0.01	0.09	0.05	0.07	0.01	0.10	0.04	0.03
16405	4790	-2.06	-0.49	0.01	-0.19	-0.81	-0.01	-0.26	0.01	-0.06	0.40	0.18	0.39
	1.66	0.01	0.05	0.03	0.02	0.01	0.02	0.04	0.07	0.02	0.02	0.02	0.10
14565	4811	-2.09	-0.50	0.09	-0.17	-0.82	-0.03	-0.21	0.12	-0.03	0.48	0.21	0.42
	1.71	0.01	0.06	0.02	0.02	0.03	0.05	0.04	0.07	0.01	0.08	0.03	0.08
5644	4826	-2.06	-0.36	0.04	-0.21	-0.82	-0.03	-0.30	0.14	-0.10	0.42	0.17	0.38
	1.74	0.01	0.05	0.05	0.01	0.02	0.02	0.05	0.10	0.02	0.14	0.03	0.05
17163	4873	-2.07	-0.58	-0.12	-0.18	-1.03	-0.02	-0.24	0.17	-0.06	...	0.12	0.30
	1.84	0.02	0.14	0.12	0.04	0.09	0.03	0.04	0.08	0.03	...	0.03	0.18
20820	4905	-2.10	-0.40	0.11	-0.16	-0.91	-0.04	-0.27	...	-0.09	...	0.17	0.49
	1.92	0.01	0.04	0.05	0.02	0.05	0.01	0.06	...	0.01	...	0.06	0.05
8952	4955	-2.07	-0.60	0.14	-0.16	-0.92	0.01	-0.30	...	-0.07	...	0.19	0.41
	2.04	0.02	0.12	0.05	0.03	0.04	0.03	0.06	...	0.02	...	0.03	0.11
10737	4977	-2.04	-0.47	0.19	-0.17	-0.88	-0.04	-0.25	...	-0.10	...	0.17	0.36
	2.10	0.02	0.07	0.07	0.03	0.07	0.03	0.06	...	0.02	...	0.04	0.12
13006	5002	-2.03	-0.43	0.16	-0.17	-0.80	-0.03	-0.28	...	-0.12	...	0.11	...
	2.16	0.02	0.05	0.08	0.04	0.04	0.04	0.02	...	0.03	...	0.04	...
17691	5003	-2.01	-0.42	0.20	-0.14	-0.92	0.07	-0.27	...	-0.20	...	0.04	...
	2.16	0.02	0.05	0.05	0.03	0.11	0.04	0.05	...	0.03	...	0.03	...
21284	5044	-2.10	-0.64	0.26	-0.13	-0.98	0.02	-0.25	...	-0.10	...	0.21	...
	2.27	0.01	0.11	0.07	0.01	0.08	0.03	0.04	...	0.02	...	0.05	...
9424	5047	-2.08	-0.57	0.10	-0.17	-0.92	-0.04	-0.29	...	-0.11	...	0.21	...
	2.30	0.02	0.13	0.06	0.03	0.14	0.04	0.02	...	0.04	...	0.05	...
16248	5049	-2.11	-0.49	0.06	-0.12	-1.04	0.04	-0.23	...	-0.10	...	0.25	...
	2.31	0.03	0.20	0.14	0.04	0.08	0.03	0.03	...	0.03	...	0.10	...
11363	5144	-2.11	-0.92	...	-0.11	...	-0.11	-0.25	...	-0.10	...	0.22	...
	2.49	0.02	0.22	...	0.03	...	0.12	0.04	...	0.03	...	0.11	...
9649	5166	-2.10	-0.56	...	-0.14	...	0.02	-0.29	...	-0.09	...	0.23	...
	2.52	0.02	0.04	...	0.04	...	0.04	0.02	...	0.04	...	0.09	...
14592	5175	-2.09	-0.65	...	-0.10	...	0.03	-0.30	...	-0.06	...	0.20	...
	2.59	0.03	0.08	...	0.04	...	0.06	0.05	...	0.03	...	0.07	...
4680	5180	-2.12	-0.60	...	-0.10	...	0.11	-0.20	...	-0.08
	2.60	0.02	0.05	...	0.04	...	0.05	0.03	...	0.04
12294	5258	-2.09	-0.16	...	0.16	-0.23	...	-0.06
	2.87	0.04	0.06	...	0.08	0.11	...	0.04
7658	5273	-2.06	-0.09	...	0.01	-0.27	...	-0.10
	2.91	0.03	0.04	...	0.05	0.13	...	0.06
11142	5279	-2.09	-0.13	...	0.03	-0.22	...	-0.06
	2.93	0.02	0.04	...	0.06	0.02	...	0.03
7728	5288	-2.09	-0.07	...	0.13	-0.23	...	0.06
	2.95	0.04	0.06	...	0.06	0.09	...	0.06

Chapter 8

Conclusions and outlook

It is beyond doubt that high-precision abundance analysis is a powerful tool to investigate the origin and cosmic evolution of elements and the nature of the stars in which they are created, destroyed and re-cycled. The work presented in this thesis has shed new light on the processes that affect the evolution of Li abundance in low-mass stars, which in turn can help us form a consistent picture of primordial nucleosynthesis and the birth of the Universe. We have also been able to trace the star formation history that characterise globular clusters, which are fundamental building blocks of the Milky-Way and other galaxies.

8.1 The cosmological Li problem

Our detailed analysis of the Li surface abundances of globular cluster stars certainly supports the hypothesis that some Li has settled below the convection zone in metal-poor main sequence stars and is being dredged up to the surface in the early subgiant phase. As discussed in Chapter 6, this scenario may provide at least part of the solution to the cosmological lithium dilemma. Encouraging in this context is the good consistency found for the abundance trends of other elements, like Ca and Na, as presented in this thesis and additionally Fe, Mg, and Ti, as shown in Lind et al. (2008); Korn et al. (2007).

However, given the subtle effects that atomic diffusion has on the surface evolution of Li and other elements, it will require much effort both on the modelling side and the observational side to convincingly resolve the cosmological Li problem. Future observations must map the metallicity dependence of the depletion physics in order to constrain the elusive source of turbulence in radiative layers. Globular clusters are excellent targets for such investigations due to their uniform ages and metallicities, and the large number statistics that can be obtained. In addition, the poorly investigated relation between Li abundance and stellar rotation and/or binarity could give important insights. Rotating stellar models with a consistent physical treatment of the transport of angular momentum and chemicals (Talon & Charbonnel, 2003, 2004) should be extended to Pop II stars, so that predictions for the surface evolution of elements can be made directly from first principles.

Should we finally reach a consensus between observations of ${}^7\text{Li}$ in metal-poor halo

stars and modelling of the microscopic diffusion of this element, we may simultaneously exacerbate another alarming cosmological problem. The handful of measurements that have been made of the much more fragile isotope ${}^6\text{Li}$ (Asplund et al., 2006; Cayrel et al., 2007; Smith et al., 1998), will namely be exceedingly difficult to explain if ${}^7\text{Li}$ has undergone significant surface depletion, given that ${}^6\text{Li}$ is not synthesised in the standard Big Bang scenario. Clearly, the ${}^6\text{Li}$ abundances deserve further attention, especially considering the challenges involved in its measurements. The lighter isotope, if present, can only be detected through a slight depression in the red wing of Li I 670.7 nm line. To properly disentangle the ${}^6\text{Li}$ feature from asymmetries caused by the convective motions requires precise 3D modelling accounting for departures from LTE, as well as high-quality observational data. The sampling of the necessary extremely high-resolution spectra will certainly become more routinely performed with future large telescope facilities, like the ultra-stable optical spectrograph ESPRESSO planned for the VLT (Pasquini et al., 2009), or CODEX ($R \lesssim 120000$) proposed for the E-ELT (Pasquini et al., 2010).

In addition to the debate on the amount of photospheric depletion of Li in stars, this fundamental discrepancy has many other interesting aspects. Maybe the Spite plateau is indeed representative of the primordial abundance, but the standard model of Big Bang nucleosynthesis is in error, despite its numerous successes. Various flavours of non-standard physics like decaying dark matter particles at the time of BBN, have been suggested to reconcile both or either of the ${}^7\text{Li}$ and ${}^6\text{Li}$ abundances with the predictions (e.g. Jedamzik & Pospelov 2009, and references therein). The Large Hadron Collider may in the coming years bring discoveries of supersymmetry and thereby support or refute the proposed particles.

8.2 Multiple populations in globular clusters

Our work has made a convincing case for the presence of two stellar populations in the globular cluster NGC 6397. With a high-precision, homogeneous analysis of a large stellar sample we could disentangle differences in the original chemical compositions of stars with evolutionary effects, causing elemental abundances differences between stars in different regions of the HR diagram. The robust signs of intrinsic bimodality in spectroscopic Na and photometric N abundances are promising for the ability of future studies to unequivocally separate the different populations and pin-point the differences in the chemical abundances of many more elements to high precision.

The intriguing question of the nature of the early generation of polluting stars in globular cluster has indeed great potential of being resolved within the coming decade or so. Several different observational tests can and should be made in this direction, like examining the C+N+O abundance spectroscopically for a large sample of stars belonging to different generations in a globular cluster, as this sum is predicted to increase with AGB star pollution. Investigations have so far reached different conclusions on this point for different clusters (e.g. Yong et al. 2009; Smith et al. 2005). Also the Li abundances of the extreme populations in clusters like NGC 2808, could give a more decisive answer, since super-AGB stars may under certain circumstances be efficient Li-producers (Ventura &

D’Antona, 2010), whereas massive stars only destroy this element. Additionally, it is definitely worthwhile to extend the work presented in Sect. 7.3.5 to cluster having undergone heavier pollution than NGC 6397, and constrain spectroscopically the helium difference of stellar ‘pairs’ belonging to different generations. It is possible, that ΔY can even be inferred directly by targeting the chromospheric He I line at 1083 nm in red giants, provided that a reliable non-LTE analysis technique can be developed (which is an extremely challenging task). From the stellar modelling point-of-view the credibility of AGB star yields would surely benefit from improvements in the treatment of convection, and mass loss which contain the largest uncertainties (Charbonnel, 2005; Ventura & D’Antona, 2010).

Present day medium-to-high resolution spectrographs on the generation of very large telescopes are operating at the limit of their capabilities when targeting turn-off stars even in nearby globular clusters. However, the next generation of extremely large telescopes will certainly provide much greater feasibility and enable us to probe both farther and deeper. The optical and near infra-red multi-object spectrograph OPTIMUS-EVE proposed for the E-ELT (Hammer et al., 2010) will be able to collect light from 40-70 objects with a resolving power of $R = 18000 - 30000$, but vastly superior in terms of efficiency with its 42 m mirror (target depth for $R = 20000 - 30000$ observations is $I = 23.5$).

8.3 The future of high-precision abundance analysis

The non-LTE analysis presented in Chapter 2 has already contributed to a more accurate derivation of Li abundances in late-type stars for a variety of different applications, such as the modelling of the Spite Plateau of halo stars (Meléndez et al., 2010), the connection between stellar Li abundance and the existence of orbiting exo-planets (Baumann et al., 2010), and the origin of the Li-enrichment that has been detected in some giant stars (Kumar & Reddy, 2009; Gonzalez et al., 2009). Especially in the latter case, the non-LTE corrections can be size-able ($\lesssim +0.35$ dex) due to efficient over-ionisation in low surface-gravity stars (see Sect. 3.3) and thus crucial for correct interpretations.

Surely, future Na abundance analyses can benefit in a similar manner from the results presented in Chapter 3. By establishing the most realistic Na model atom to date, we have been able to clarify the influence from remaining uncertainties in collisional cross-sections, and thereby ensured that the non-LTE modelling is indeed robust in this respect and certainly always a better approach than traditional LTE modelling. Further, our initial attempts to extend the non-LTE analysis for trace elements to 3D hydro-dynamical model atmospheres are indeed encouraging. We have demonstrated that we are able to accurately predict solar line profiles in 3D without the introduction of fudge factors such as micro- and macroturbulence and make a precise derivation of the solar Na abundance. The centre-to-limb variations of the solar Na I lines are not reproduced to a satisfactory degree however, which calls for further improvements of the modelling procedure before combined 3D, non-LTE modelling can be extended to a cover a wider stellar parameter space.

Nevertheless, 3D modelling of late-type stellar atmospheres bears enormous potential

for placing abundance analysis of late-type stars, especially metal-poor ones, on a much firmer footing. Even though the differences with respect to traditional 1D modelling are minor for the specific case of the Sun (Chapter 4), stars with lower metallicity may behave very differently. 1D static models enforce radiative equilibrium and cannot incorporate the important cooling that occurs through the adiabatic expansion of gas in the atmosphere. With few metals in the atmosphere, there is less radiative heating, pushing the energy balance far from radiative equilibrium and bringing down the temperatures of optically thin layers considerably compared to the 1D case (e.g. Asplund 2005). As shown by e.g. Collet et al. (2007) LTE abundances of C, N, O and Fe in metal-poor giants could be affected by as much as a factor of ten. Of equal importance is the development of non-LTE analysis in 3D atmospheres. In fact, non-LTE effects such as over-ionisation of neutral minority species may well be more severe than predicted with 1D models, due to the steeper temperature gradients.

With the continuous development of quantum mechanical calculations of collisional cross-sections and radiative transition probabilities, also the prospects for accurate non-LTE calculations are indeed encouraging. The investigation of charge exchange reactions and bound-bound collisional excitation with hydrogen will in time be extended to more complex elements than Li and Na. Also R-matrix and close-coupling calculations for electron collisions are becoming increasingly common (e.g. for O I by Barklem 2007a, B I by Ballance et al. 2007, Fe II by Ramsbottom et al. 2007, and CH by Baluja & Msezane 2001) and can in certain cases replace general recipes such as the Born approximation or allow for improved scaling relations (see e.g. work by Kim 2001). Clearly, the late-type star community is competing with high-energy astro-physics about the time and labour of atomic physicists. To make progress, we must stress the importance of accurate atomic data for neutral atoms, molecules, and singly ionised ions.

Combined 3D, non-LTE modelling, given the trace element assumption, will certainly gain more ground in the coming years, possibly with profound impact on many areas of astrophysics that are relying on the chemical signatures of stars. With the great light-collecting capability of current and future generation of very large and extremely large telescopes we can measure the electromagnetic spectrum emitted by stars in all Galactic components with extraordinary detail. The progress on that end must be matched by a similar development of the analysis tools at hand, to make full use of the information that is actually provided to us. Indeed, theorists and observers alike should aim not to be the ones setting the limit for what is possible

Bibliography

- Allen, C. W. 1976, *Astrophysical Quantities* (*Astrophysical Quantities*, London: Athlone (3rd edition), 1976)
- Allen, C. W. 2000, *Allen's Astrophysical Quantities*, 4th edn. (Springer, Berlin)
- Allende Prieto, C., Asplund, M., & Fabiani Bendicho, P. 2004, *Astronomy and Astrophysics*, 423, 1109
- Allende Prieto, C., Hubeny, I., & Lambert, D. L. 2003, *Astrophysical Journal*, 591, 1192
- Alonso, A., Arribas, S., & Martínez-Roger, C. 1996, *Astronomy and Astrophysics*, 313, 873
- Alonso, A., Arribas, S., & Martínez-Roger, C. 1999, *Astronomy and Astrophysics, Supplement*, 140, 261
- Andrievsky, S. M., Spite, M., Korotin, S. A., et al. 2010, *Astronomy and Astrophysics*, 509, A88+
- Andrievsky, S. M., Spite, M., Korotin, S. A., et al. 2007, *Astronomy and Astrophysics*, 464, 1081
- Andrievsky, S. M., Spite, M., Korotin, S. A., et al. 2008, *Astronomy and Astrophysics*, 481, 481
- Anstee, S. D. & O'Mara, B. J. 1995, *Monthly Notices of the Royal Astronomical Society*, 276, 859
- Anthony-Twarog, B. J. & Twarog, B. A. 2000, *Astronomical Journal*, 120, 3111
- Aoki, W., Barklem, P. S., Beers, T. C., et al. 2009, *Astrophysical Journal*, 698, 1803
- Asplund, M. 2005, *Annual Review of Astronomy and Astrophysics*, 43, 481
- Asplund, M., Carlsson, M., & Botnen, A. V. 2003, *Astronomy and Astrophysics*, 399, L31
- Asplund, M., Grevesse, N., Sauval, A. J., & Scott, P. 2009, *Annual Review of Astronomy and Astrophysics*, 47, 481

- Asplund, M., Gustafsson, B., Kiselman, D., & Eriksson, K. 1997, *Astronomy and Astrophysics*, 318, 521
- Asplund, M., Lambert, D. L., Nissen, P. E., Primas, F., & Smith, V. V. 2006, *Astrophysical Journal*, 644, 229
- Asplund, M. & Lind, K. 2010, in *IAU Symposium*, Vol. 268, *IAU Symposium*, ed. C. Charbonnel, M. Tosi, F. Primas, & C. Chiappini, 191–200
- Asplund, M., Nordlund, Å., Trampedach, R., Allende Prieto, C., & Stein, R. F. 2000, *Astronomy and Astrophysics*, 359, 729
- Asplund, M., Nordlund, Å., Trampedach, R., & Stein, R. F. 1999, *Astronomy and Astrophysics*, 346, L17
- Ballance, C. P., Griffin, D. C., Berrington, K. A., & Badnell, N. R. 2007, *Journal of Physics B Atomic Molecular Physics*, 40, 1131
- Baluja, K. L. & Msezane, A. Z. 2001, *Journal of Physics B Atomic Molecular Physics*, 34, 3157
- Barklem, P. S. 2007a, *Astronomy and Astrophysics*, 462, 781
- Barklem, P. S. 2007b, *Astronomy and Astrophysics*, 466, 327
- Barklem, P. S., Belyaev, A. K., & Asplund, M. 2003, *Astronomy and Astrophysics*, 409, L1
- Barklem, P. S., Belyaev, A. K., Dickinson, A. S., & Gadéa, F. X. 2010, *Astronomy and Astrophysics*, 519, A20+
- Barklem, P. S., Christlieb, N., Beers, T. C., et al. 2005, *Astronomy and Astrophysics*, 439, 129
- Barklem, P. S. & O'Mara, B. J. 1997, *Monthly Notices of the Royal Astronomical Society*, 290, 102
- Barklem, P. S., Piskunov, N., & O'Mara, B. J. 2000, *Astronomy and Astrophysics*, 363, 1091
- Baumann, P., Ramírez, I., Meléndez, J., Asplund, M., & Lind, K. 2010, *Astronomy and Astrophysics*, 519, A87+
- Bell, R. A., Dickens, R. J., & Gustafsson, B. 1979, *Astrophysical Journal*, 229, 604
- Belyaev, A. K. & Barklem, P. S. 2003, *Physical Review A: General Physics*, 68, 062703
- Bensby, T., Feltzing, S., & Lundström, I. 2003, *Astronomy and Astrophysics*, 410, 527

- Bergemann, M. & Gehren, T. 2008, *Astronomy and Astrophysics*, 492, 823
- Bielski, A. 1975, *Journal of Quantitative Spectroscopy and Radiative Transfer*, 15, 463
- Biemont, E., Baudoux, M., Kurucz, R. L., Ansbacher, W., & Pinnington, E. H. 1991, *Astronomy and Astrophysics*, 249, 539
- Biemont, E. & Zeppen, C. J. 1992, *Astronomy and Astrophysics*, 265, 850
- Bonifacio, P., Molaro, P., Sivarani, T., et al. 2007a, *Astronomy and Astrophysics*, 462, 851
- Bonifacio, P., Pasquini, L., Molaro, P., et al. 2007b, *Astronomy and Astrophysics*, 470, 153
- Bonifacio, P., Pasquini, L., Spite, F., et al. 2002, *Astronomy and Astrophysics*, 390, 91
- Botnen, A. 1997, Master's thesis, Master's thesis, Inst. Theor. Astrophys. Oslo (1997)
- Briley, M. M., Bell, R. A., Hoban, S., & Dickens, R. J. 1990, *Astrophysical Journal*, 359, 307
- Brodie, J. P. & Strader, J. 2006, *Annual Review of Astronomy and Astrophysics*, 44, 193
- Bruls, J. H. M. J., Rutten, R. J., & Shchukina, N. G. 1992, *Astronomy and Astrophysics*, 265, 237
- Burris, D. L., Pilachowski, C. A., Armandroff, T. E., et al. 2000, *Astrophysical Journal*, 544, 302
- Carlson, B. G. 1963, *Methods of Computational Physics*, ed. Alder, B., Fernbach, S., Rottenberg, M (Academic Press, New York)
- Carlsson, M. 1986, *Uppsala Astronomical Observatory Reports*, 33
- Carlsson, M. 1992, in *Astronomical Society of the Pacific Conference Series*, Vol. 26, *Cool Stars, Stellar Systems, and the Sun*, ed. M. S. Giampapa & J. A. Bookbinder, 499–+
- Carlsson, M., Rutten, R. J., Bruls, J. H. M. J., & Shchukina, N. G. 1994, *Astronomy and Astrophysics*, 288, 860
- Carretta, E., Bragaglia, A., Gratton, R., & Lucatello, S. 2009a, *Astronomy and Astrophysics*, 505, 139
- Carretta, E., Bragaglia, A., Gratton, R. G., et al. 2009b, *Astronomy and Astrophysics*, 505, 117
- Carretta, E., Bragaglia, A., Gratton, R. G., et al. 2010, *Astronomy and Astrophysics*, 516, A55+

- Carretta, E., Gratton, R. G., Lucatello, S., Bragaglia, A., & Bonifacio, P. 2005, *Astronomy and Astrophysics*, 433, 597
- Casagrande, L., Ramírez, I., Meléndez, J., Bessell, M., & Asplund, M. 2010, *Astronomy and Astrophysics*, 512, A54+
- Castelli, F. & Kurucz, R. L. 2004, *ArXiv Astrophysics e-prints*
- Castilho, B. V., Pasquini, L., Allen, D. M., Barbuy, B., & Molaro, P. 2000, *Astronomy and Astrophysics*, 361, 92
- Cayrel, R., Depagne, E., Spite, M., et al. 2004, *Astronomy and Astrophysics*, 416, 1117
- Cayrel, R., Steffen, M., Chand, H., et al. 2007, *Astronomy and Astrophysics*, 473, L37
- Charbonnel, C. 2005, in *IAU Symposium, Vol. 228, From Lithium to Uranium: Elemental Tracers of Early Cosmic Evolution*, ed. V. Hill, P. François, & F. Primas, 347–356
- Charbonnel, C. 2007, in *Astronomical Society of the Pacific Conference Series, Vol. 378, Why Galaxies Care About AGB Stars: Their Importance as Actors and Probes*, ed. F. Kerschbaum, C. Charbonnel, & R. F. Wing, 416–+
- Charbonnel, C. & Lagarde, N. 2010, *Astronomy and Astrophysics*, 522, A10+
- Charbonnel, C. & Primas, F. 2005, *Astronomy and Astrophysics*, 442, 961
- Charbonnel, C. & Talon, S. 2005, *Science*, 309, 2189
- Charbonnel, C. & Talon, S. 2008, in *IAU Symposium, Vol. 252, IAU Symposium*, ed. L. Deng & K. L. Chan, 163–174
- Charbonnel, C. & Zahn, J.-P. 2007, *Astronomy and Astrophysics*, 467, L15
- Collet, R., Asplund, M., & Trampedach, R. 2007, *Astronomy and Astrophysics*, 469, 687
- Crawford, D. L. 1975, *Publications of the Astronomical Society of the Pacific*, 87, 481
- Croft, H., Dickinson, A. S., & Gadea, F. X. 1999, *Monthly Notices of the Royal Astronomical Society*, 304, 327
- Cyburt, R. H., Fields, B. D., & Olive, K. A. 2008, *Journal of Cosmology and Astro-Particle Physics*, 11, 12
- D’Antona, F. & Caloi, V. 2008, *Monthly Notices of the Royal Astronomical Society*, 390, 693
- de Mink, S. E., Pols, O. R., Langer, N., & Izzard, R. G. 2009, *Astronomy and Astrophysics*, 507, L1

- Decressin, T., Baumgardt, H., Charbonnel, C., & Kroupa, P. 2010, *Astronomy and Astrophysics*, 516, A73+
- Decressin, T., Charbonnel, C., & Meynet, G. 2007a, *Astronomy and Astrophysics*, 475, 859
- Decressin, T., Charbonnel, C., Siess, L., et al. 2009, *Astronomy and Astrophysics*, 505, 727
- Decressin, T., Meynet, G., Charbonnel, C., Prantzos, N., & Ekström, S. 2007b, *Astronomy and Astrophysics*, 464, 1029
- Dekker, H., D’Odorico, S., Kaufer, A., Delabre, B., & Kotzlowski, H. 2000, in *Society of Photo-Optical Instrumentation Engineers (SPIE) Conference Series*, Vol. 4008, *Society of Photo-Optical Instrumentation Engineers (SPIE) Conference Series*, ed. M. Iye & A. F. Moorwood, 534–545
- Denisenkov, P. A. & Denisenkova, S. N. 1989, *Astronomicheskij Tsirkulyar*, 1538, 11
- Denisenkov, P. A. & Denisenkova, S. N. 1990, *Soviet Astronomy Letters*, 16, 275
- di Criscienzo, M., D’Antona, F., & Ventura, P. 2010, *Astronomy and Astrophysics*, 511, A70+
- Dimitrijević, M. S. & Sahal-Bréchet, S. 1985, *Journal of Quantitative Spectroscopy and Radiative Transfer*, 34, 149
- Dimitrijević, M. S. & Sahal-Bréchet, S. 1990, *Journal of Quantitative Spectroscopy and Radiative Transfer*, 44, 421
- D’Orazi, V., Lucatello, S., Gratton, R., et al. 2010, *Astrophysical Journal, Letters*, 713, L1
- Drawin, H.-W. 1968, *Zeitschrift für Physik*, 211, 404
- Dunkley, J., Komatsu, E., Nolte, M. R., et al. 2009, *Astrophysical Journal, Supplement*, 180, 306
- Edvardsson, B., Andersen, J., Gustafsson, B., et al. 1993, *Astronomy and Astrophysics*, 275, 101
- Ekström, S., Meynet, G., Maeder, A., & Barblan, F. 2008, *Astronomy and Astrophysics*, 478, 467
- Fabbian, D., Asplund, M., Barklem, P. S., Carlsson, M., & Kiselman, D. 2009, *Astronomy and Astrophysics*, 500, 1221
- Feautrier, N., Han, X.-Y., & Lind, K. in preparation, *Astronomy and Astrophysics*
- François, P., Depagne, E., Hill, V., et al. 2007, *Astronomy and Astrophysics*, 476, 935

- Freytag, B., Allard, F., Ludwig, H., Homeier, D., & Steffen, M. 2010, *Astronomy and Astrophysics*, 513, A19+
- Fuhr, J. R., Martin, G. A., & Wiese, W. L. 1988, *Atomic transition probabilities. Scandium through Manganese* (New York: American Institute of Physics (AIP) and American Chemical Society, 1988)
- Fuhrmann, K., Pfeiffer, M., Frank, C., Reetz, J., & Gehren, T. 1997, *Astronomy and Astrophysics*, 323, 909
- Gao, X., Han, X., Vokny, L., Feautrier, N., & Li, J. 2010, *Physical Review A: General Physics*, 81, 022703
- Gehren, T., Shi, J. R., Zhang, H. W., Zhao, G., & Korn, A. J. 2006, *Astronomy and Astrophysics*, 451, 1065
- Gonzalez, O. A., Zoccali, M., Monaco, L., et al. 2009, *Astronomy and Astrophysics*, 508, 289
- Gratton, R., Sneden, C., & Carretta, E. 2004, *Annual Review of Astronomy and Astrophysics*, 42, 385
- Gratton, R. G., Bonifacio, P., Bragaglia, A., et al. 2001, *Astronomy and Astrophysics*, 369, 87
- Gratton, R. G., Carretta, E., Claudi, R., Lucatello, S., & Barbieri, M. 2003, *Astronomy and Astrophysics*, 404, 187
- Gratton, R. G., Sneden, C., Carretta, E., & Bragaglia, A. 2000, *Astronomy and Astrophysics*, 354, 169
- Gray, D. F. 2005, *The Observation and Analysis of Stellar Photospheres* (Cambridge University Press, 3rd ed.)
- Grevesse, N., Asplund, M., & Sauval, A. J. 2007, *Space Science Reviews*, 130, 105
- Grundahl, F., Briley, M., Nissen, P. E., & Feltzing, S. 2002a, *Astronomy and Astrophysics*, 385, L14
- Grundahl, F., Catelan, M., Landsman, W. B., Stetson, P. B., & Andersen, M. I. 1999, *Astrophysical Journal*, 524, 242
- Grundahl, F., Stetson, P. B., & Andersen, M. I. 2002b, *Astronomy and Astrophysics*, 395, 481
- Grundahl, F., Vandenberg, D. A., & Andersen, M. I. 1998, *Astrophysical Journal, Letters*, 500, L179+

- Grundahl, F., VandenBerg, D. A., Bell, R. A., Andersen, M. I., & Stetson, P. B. 2000, *Astronomical Journal*, 120, 1884
- Gustafsson, B., Bell, R. A., Eriksson, K., & Nordlund, A. 1975, *Astronomy and Astrophysics*, 42, 407
- Gustafsson, B., Edvardsson, B., Eriksson, K., et al. 2008, *Astronomy and Astrophysics*, 486, 951
- Hammer, F., Kaper, L., & Dalton, G. 2010, *The Messenger*, 140, 36
- Hannaford, P., Lowe, R. M., Grevesse, N., Biemont, E., & Whaling, W. 1982, *Astrophysical Journal*, 261, 736
- Harris, W. E. 1996, *Astronomical Journal*, 112, 1487
- Hauschildt, P. H., Allard, F., & Baron, E. 1999, *Astrophysical Journal*, 512, 377
- Hayek, W., Asplund, M., Collet, R., & Nordlund, A. submitted, *Astronomy and Astrophysics*
- Hoang Binh, D. & Van Regemorter, H. 1997, *Journal of Physics B Atomic Molecular Physics*, 30, 2403
- Holweger, H. & Mueller, E. A. 1974, *Solar Physics*, 39, 19
- Hosford, A., Ryan, S. G., García Pérez, A. E., Norris, J. E., & Olive, K. A. 2009, *Astronomy and Astrophysics*, 493, 601
- Igenbergs, K., Schweinzer, J., Bray, I., Bridi, D., & Aumayr, F. 2008, *Atomic Data and Nuclear Data Tables*, 94, 981
- James, G., François, P., Bonifacio, P., et al. 2004, *Astronomy and Astrophysics*, 427, 825
- Jedamzik, K. & Pospelov, M. 2009, *New Journal of Physics*, 11, 105028
- Jurić, M., Ivezić, Ž., Brooks, A., et al. 2008, *Astrophysical Journal*, 673, 864
- Kaulakys, B. 1991, *Journal of Physics B Atomic Molecular Physics*, 24, L127
- Kelly, B. C. 2007, *Astrophysical Journal*, 665, 1489
- Kim, Y. 2001, *Physical Review A: General Physics*, 64, 032713
- Kiselman, D. 1997, *Astrophysical Journal, Letters*, 489, L107+
- Kiselman, D. 2001, *New Astronomy Review*, 45, 559
- Koch, A. & McWilliam, A. 2008, *Astronomical Journal*, 135, 1551

- Komarovskii, V. A. 1991, *Optics and Spectroscopy*, 71, 322
- Korn, A. J., Grundahl, F., Richard, O., et al. 2006, *Nature*, 442, 657
- Korn, A. J., Grundahl, F., Richard, O., et al. 2007, *Astrophysical Journal*, 671, 402
- Krstić, P. S. & Schultz, D. R. 2009, *Journal of Physics B Atomic Molecular Physics*, 42, 065207
- Kumar, Y. B. & Reddy, B. E. 2009, *Astrophysical Journal, Letters*, 703, L46
- Kurucz, R. L. 1970, *SAO Special Report*, 309
- Kurucz, R. L. 1993, *SYNTHE spectrum synthesis programs and line data (Kurucz CD-ROM, Cambridge, MA: Smithsonian Astrophysical Observatory, —c1993, December 4, 1993)*
- Kurucz, R. L. & Peytremann, E. 1975, *SAO Special Report*, 362
- Lambert, D. L. 1993, *Physica Scripta Volume T*, 47, 186
- Langer, G. E., Hoffman, R., & Sneden, C. 1993, *Publications of the Astronomical Society of the Pacific*, 105, 301
- Lawler, J. E. & Dakin, J. T. 1989, *Journal of the Optical Society of America B Optical Physics*, 6, 1457
- Lawler, J. E., Wickliffe, M. E., den Hartog, E. A., & Sneden, C. 2001, *Astrophysical Journal*, 563, 1075
- Leenaarts, J. & Carlsson, M. 2009, in *Astronomical Society of the Pacific Conference Series*, Vol. 415, *Astronomical Society of the Pacific Conference Series*, ed. B. Lites, M. Cheung, T. Magara, J. Mariska, & K. Reeves, 87–+
- Lincke, R. & Ziegenbein, B. 1971, *Zeitschrift fur Physik*, 241, 369
- Lind, K., Asplund, M., & Barklem, P. S. 2009a, *Astronomy and Astrophysics*, 503, 541
- Lind, K., Asplund, M., Barklem, P. S., & Belyaev, A. K. submitteda, *Astronomy and Astrophysics*
- Lind, K., Asplund, M., Barklem, P. S., Leenaarts, J., & Pereira, T. M. D. in preparation, *Astronomy and Astrophysics*
- Lind, K., Charbonnel, C., Decressin, T., et al. submittedb, *Astronomy and Astrophysics*
- Lind, K., Korn, A. J., Barklem, P. S., & Grundahl, F. 2008, *Astronomy and Astrophysics*, 490, 777

- Lind, K., Primas, F., Charbonnel, C., Grundahl, F., & Asplund, M. 2009b, *Astronomy and Astrophysics*, 503, 545
- Lindgård, A. & Nielson, S. E. 1977, *Atomic Data and Nuclear Data Tables*, 19, 533
- Ljung, G., Nilsson, H., Asplund, M., & Johansson, S. 2006, *Astronomy and Astrophysics*, 456, 1181
- Ludwig, H., Caffau, E., Steffen, M., et al. 2009, *Memorie della Societietá Astronomica Italia*, 80, 711
- Martell, S. L. & Grebel, E. K. 2010, *Astronomy and Astrophysics*, 519, A14+
- Martin, G. A., Fuhr, J. R., & Wiese, W. L. 1988, *Phys. Chem. Ref. Data*, 17, 3
- Mashonkina, L. I., Shimanskii, V. V., & Sakhbullin, N. A. 2000, *Astronomy Reports*, 44, 790
- Meléndez, J., Casagrande, L., Ramírez, I., Asplund, M., & Schuster, W. J. 2010, *Astronomy and Astrophysics*, 515, L3+
- Meléndez, J. & Ramírez, I. 2004, *Astrophysical Journal, Letters*, 615, L33
- Meylan, G. & Heggie, D. C. 1997, *Astronomy and Astrophysics Reviews*, 8, 1
- Michaud, G., Fontaine, G., & Beaudet, G. 1984, *Astrophysical Journal*, 282, 206
- Mihalas, D. 1978, *Stellar atmospheres* (San Francisco, W. H. Freeman and Co. 2nd ed.)
- Miles, B. M. & Wiese, W. L. 1969, *Atomic Data*, 1, 1
- Milone, A. P., Piotto, G., King, I. R., et al. 2010, *Astrophysical Journal*, 709, 1183
- Milone, A. P., Villanova, S., Bedin, L. R., et al. 2006, *Astronomy and Astrophysics*, 456, 517
- Muthsam, H. J., Kupka, F., Löw-Baselli, B., et al. 2010, *New Astronomy*, 15, 460
- Nieva, M. F. & Przybilla, N. 2007, *Astronomy and Astrophysics*, 467, 295
- Nissen, P. E., Primas, F., Asplund, M., & Lambert, D. L. 2002, *Astronomy and Astrophysics*, 390, 235
- Nissen, P. E. & Schuster, W. J. 2010, *Astronomy and Astrophysics*, 511, L10+
- Nordlund, Å., Stein, R. F., & Asplund, M. 2009, *Living Reviews in Solar Physics*, 6, 2
- Norris, J. E. 2004, *Astrophysical Journal, Letters*, 612, L25
- Norris, J. E. & Da Costa, G. S. 1995, *Astrophysical Journal, Letters*, 441, L81

- Norris, J. E., Ryan, S. G., & Beers, T. C. 2001, *Astrophysical Journal*, 561, 1034
- O'Brian, T. R., Wickliffe, M. E., Lawler, J. E., Whaling, J. W., & Brault, W. 1991, *Journal of the Optical Society of America B Optical Physics*, 8, 1185
- Önehag, A., Gustafsson, B., Eriksson, K., & Edvardsson, B. 2009, *Astronomy and Astrophysics*, 498, 527
- Paresce, F. & De Marchi, G. 2000, *Astrophysical Journal*, 534, 870
- Park, C. 1971, *Journal of Quantitative Spectroscopy and Radiative Transfer*, 11, 7
- Pasquini, L., Avila, G., Blecha, A., et al. 2002, *The Messenger*, 110, 1
- Pasquini, L., Bonifacio, P., Molaro, P., et al. 2005, *Astronomy and Astrophysics*, 441, 549
- Pasquini, L., Bonifacio, P., Randich, S., Galli, D., & Gratton, R. G. 2004, *Astronomy and Astrophysics*, 426, 651
- Pasquini, L., Cristiani, S., Garcia-Lopez, R., Haehnelt, M., & Mayor, M. 2010, *The Messenger*, 140, 20
- Pasquini, L., Ecuivillon, A., Bonifacio, P., & Wolff, B. 2008, *Astronomy and Astrophysics*, 489, 315
- Pasquini, L., Manescau, A., Avila, G., et al. 2009, in *Science with the VLT in the ELT Era*, ed. A. Moorwood, 395–+
- Pasquini, L. & Molaro, P. 1996, *Astronomy and Astrophysics*, 307, 761
- Pavlenko, Y. V. & Magazzu, A. 1996, *Astronomy and Astrophysics*, 311, 961
- Peach, G., Saraph, H. E., & Seaton, M. J. 1988, *Journal of Physics B Atomic Molecular Physics*, 21, 3669
- Pereira, T. M. D., Asplund, M., & Kiselman, D. 2009a, *Astronomy and Astrophysics*, 508, 1403
- Pereira, T. M. D., Asplund, M., Trampedach, R., Collet, R., & Leenaarts, J. submitted, *Astronomy and Astrophysics*
- Pereira, T. M. D., Kiselman, D., & Asplund, M. 2009b, *Astronomy and Astrophysics*, 507, 417
- Phelps, J. O. & Lin, C. C. 1981, *Physical Review A: General Physics*, 24, 1299
- Pickering, J. C., Thorne, A. P., & Perez, R. 2001, *Astrophysical Journal, Supplement*, 132, 403

- Prantzos, N. & Charbonnel, C. 2006, *Astronomy and Astrophysics*, 458, 135
- Prialnik, D. 2000, *An Introduction to the Theory of Stellar Structure and Evolution*, ed. Prialnik, D. (Cambridge University Press, 2000)
- Primas, F. & Sobeck, J. 2008, in *American Institute of Physics Conference Series*, Vol. 1001, *Evolution and Nucleosynthesis in AGB Stars*, ed. R. Guandalini, S. Palmerini, & M. Busso, 230–234
- Pumo, M. L., D'Antona, F., & Ventura, P. 2008, *Astrophysical Journal, Letters*, 672, L25
- Raassen, A. J. J. & Uylings, P. H. M. 1998, *VizieR Online Data Catalog*, 334, 300
- Ramírez, I. & Meléndez, J. 2005, *Astrophysical Journal*, 626, 465
- Ramsbottom, C. A., Hudson, C. E., Norrington, P. H., & Scott, M. P. 2007, *Astronomy and Astrophysics*, 475, 765
- Reddy, B. E., Tomkin, J., Lambert, D. L., & Allende Prieto, C. 2003, *Monthly Notices of the Royal Astronomical Society*, 340, 304
- Reid, I. N. & Gizis, J. E. 1998, *Astronomical Journal*, 116, 2929
- Richard, O., Michaud, G., & Richer, J. 2005, *Astrophysical Journal*, 619, 538
- Richer, H. B., Dotter, A., Hurley, J., et al. 2008, *Astronomical Journal*, 135, 2141
- Rutten, R. J. 2003, *Radiative Transfer in Stellar Atmospheres* (Utrecht University lecture notes, 8th edition)
- Ryan, S. G., Kajino, T., Beers, T. C., et al. 2001, *Astrophysical Journal*, 549, 55
- Ryan, S. G., Norris, J. E., & Beers, T. C. 1999, *Astrophysical Journal*, 523, 654
- Rybicki, G. B. & Hummer, D. G. 1991, *Astronomy and Astrophysics*, 245, 171
- Sansonetti, C. J., Richou, B., Engleman, R. J., & Radziemski, L. J. 1995, *Physical Review A: General Physics*, 52, 2682
- Sansonetti, J. E. 2008, *Journal of Physical and Chemical Reference Data*, 37, 1659
- Scharmer, G. B., Bjelksjo, K., Korhonen, T. K., Lindberg, B., & Petterson, B. 2003, in *Society of Photo-Optical Instrumentation Engineers (SPIE) Conference Series*, Vol. 4853, *Society of Photo-Optical Instrumentation Engineers (SPIE) Conference Series*, ed. S. L. Keil & S. V. Avakyan, 341–350
- Scharmer, G. B. & Carlsson, M. 1985, *Journal of Computational Physics*, 59, 56
- Seaton, M. J. 1962, *Proceedings of the Physical Society*, 79, 1105

- Shi, J. R., Gehren, T., & Zhao, G. 2004, *Astronomy and Astrophysics*, 423, 683
- Shimanskaya, N. N., Mashonkina, L. I., & Sakhbullin, N. A. 2000, *Astronomy Reports*, 44, 530
- Short, C. I. & Hauschildt, P. H. 2003, *Astrophysical Journal*, 596, 501
- Short, C. I. & Hauschildt, P. H. 2005, *Astrophysical Journal*, 618, 926
- Smith, G. 1988, *Journal of Physics B Atomic Molecular Physics*, 21, 2827
- Smith, G. & O'Neill, J. A. 1975, *Astronomy and Astrophysics*, 38, 1
- Smith, G. & Raggett, D. S. J. 1981, *Journal of Physics B Atomic Molecular Physics*, 14, 4015
- Smith, V. V., Cunha, K., Ivans, I. I., et al. 2005, *Astrophysical Journal*, 633, 392
- Smith, V. V., Lambert, D. L., & Nissen, P. E. 1998, *Astrophysical Journal*, 506, 405
- Spite, M. & Spite, F. 1982, *Nature*, 297, 483
- Stehlé, C. & Hutcheon, R. 1999, *Astronomy and Astrophysics, Supplement*, 140, 93
- Stein, R. F. & Nordlund, A. 1998, *Astrophysical Journal*, 499, 914
- Strömgren, B., Gustafsson, B., & Olsen, E. H. 1982, *Publications of the Astronomical Society of the Pacific*, 94, 5
- Sydoryk, I., Bezuglov, N. N., Beterov, I. I., et al. 2008, *Physical Review A: General Physics*, 77, 042511
- Takeda, Y. & Kawanomoto, S. 2005, *Publications of the Astronomical Society of Japan*, 57, 45
- Takeda, Y., Zhao, G., Takada-Hidai, M., et al. 2003, *Chinese Journal of Astronomy and Astrophysics*, 3, 316
- Talon, S. & Charbonnel, C. 1998, *Astronomy and Astrophysics*, 335, 959
- Talon, S. & Charbonnel, C. 2003, *Astronomy and Astrophysics*, 405, 1025
- Talon, S. & Charbonnel, C. 2004, *Astronomy and Astrophysics*, 418, 1051
- Thévenin, F., Charbonnel, C., de Freitas Pacheco, J. A., et al. 2001, *Astronomy and Astrophysics*, 373, 905
- Unsöld, A. 1955, *Physik der Sternatmosphären, MIT besonderer Berücksichtigung der Sonne*. (Berlin, Springer, 1955. 2. Aufl.)

- van den Bergh, S. 1993, in *Astronomical Society of the Pacific Conference Series*, Vol. 50, *Structure and Dynamics of Globular Clusters*, ed. S. G. Djorgovski & G. Meylan, 1–+
- van den Bergh, S. 2008, *Monthly Notices of the Royal Astronomical Society*, 385, L20
- van Regemorter, H. 1962, *Astrophysical Journal*, 136, 906
- VandenBerg, D. A., Richard, O., Michaud, G., & Richer, J. 2002, *Astrophysical Journal*, 571, 487
- Ventura, P. & D’Antona, F. 2008, *Astronomy and Astrophysics*, 479, 805
- Ventura, P. & D’Antona, F. 2010, *Monthly Notices of the Royal Astronomical Society*, 402, L72
- Vögler, A., Shelyag, S., Schüssler, M., et al. 2005, *Astronomy and Astrophysics*, 429, 335
- Warner, B. 1968, *Monthly Notices of the Royal Astronomical Society*, 140, 53
- Wickliffe, M. E. & Lawler, J. E. 1997, *Astrophysical Journal*, Supplement, 110, 163
- Wiese, W. L., Smith, M. W., & Glennon, B. M. 1966, *Atomic transition probabilities. Vol. 1: Hydrogen through Neon. A critical data compilation*, ed. Wiese, W. L., Smith, M. W., & Glennon, B. M. (NSRDS-NBS 4, Washington, D.C.: US Department of Commerce, National Bureau of Standards, 1966)
- Wiese, W. L., Smith, M. W., & Miles, B. M. 1969, *Atomic transition probabilities. Vol. 2: Sodium through Calcium. A critical data compilation*, ed. Wiese, W. L., Smith, M. W., & Miles, B. M. (NSRDS-NBS, Washington, D.C.: US Department of Commerce, National Bureau of Standards, —c 1969)
- Woosley, S. E. & Weaver, T. A. 1995, *Astrophysical Journal*, Supplement, 101, 181
- Yan, Z.-C., Tambasco, M., & Drake, G. W. F. 1998, *Physical Review A: General Physics*, 57, 1652
- Yong, D., Grundahl, F., D’Antona, F., et al. 2009, *Astrophysical Journal*, Letters, 695, L62
- Yong, D., Grundahl, F., Johnson, J. A., & Asplund, M. 2008a, *Astrophysical Journal*, 684, 1159
- Yong, D., Grundahl, F., Lambert, D. L., Nissen, P. E., & Shetrone, M. D. 2003, *Astronomy and Astrophysics*, 402, 985
- Yong, D., Grundahl, F., Nissen, P. E., Jensen, H. R., & Lambert, D. L. 2005, *Astronomy and Astrophysics*, 438, 875
- Yong, D., Karakas, A. I., Lambert, D. L., Chieffi, A., & Limongi, M. 2008b, *Astrophysical Journal*, 689, 1031

Acknowledgments

There have been times when conducting my PhD research has felt like riding alone on a never-ending roller coaster, with the daily frustration of non-detectable spectral lines and non-cooperative codes that iterate to divergence, mixed with the satisfaction of an accepted paper or the reward of seeing my work acknowledged by the community. Fortunately, the times have indeed been more numerous when I have felt truly blessed to be in the prosperous scientific environment of Garching, surrounded by fellow students facing the same fears, as well as experienced researchers to guide me forward. I sincerely hope that I will have the privilege of pursuing my continued scientific career in their company.

My warmest thank you is directed to my two thesis supervisors for their time and support. I am much grateful to Francesca Primas for always being positive and encouraging about my work and her invaluable advice in research and sometimes research politics. I sincerely wish to thank Martin Asplund for his unfailing ability to inspire, his most useful habit to keep asking until I give a satisfying answer, and all back up otherwise.

Second, my deepest gratitude is extended to Corinne Charbonnel, Frank Grundahl, and Paul Barklem, without whom this thesis would not have been possible. I thank them for giving me the opportunity to learn from their expertise, for always being patient, and for all rounds of electronic champagne shared after a successful submission.

During my time at the European Southern Observatory and Stellar Astrophysics and Galactic Archeology group at the neighboring Max-Planck Institute for Astrophysics, I have had the pleasure of meeting a large number of excellent scientists; students and professors, observers and theoreticians, in-house and elsewhere. I would like to mention, in random order, some people in particular, who contributed to the progress of my work by interaction and discussions; Patrick Baumann, Camilla Juul Hansen, Jennifer Sobeck, Luca Pasquini, Maria Bergemann, Mats Carlsson, Tiago Pereira, Jorritt Leenarts, Luca Sbordone, Andrey Belyaev, Nicole Feautrier, Remo Collet, Wolfgang Hayek, Olivier Richard, Luca Casagrande, Thibaut Decressin, and Achim Weiss. Surely, the list should be extended.

Before arriving to ESO in 2007, I my scientific career started at the Department of Physics and Astronomy at Uppsala University in Sweden. I could never have wished for a better preparation for the life of astronomy, and my warmest gratitude is directed to all who made my time there memorable and for their continuing support and interaction. In particular, I would like to mention Andreas Korn, who early on taught me the importance of a careful analysis, Bengt Gustafsson, Bengt Edvardsson, Kjell Eriksson and Anna Önehag.

The IMPRS programme has offered ample opportunity for scientific as well as social interaction between the astronomical institutes of Munich and I thank my fellow IMPRS students for making my stay here truly enjoyable. Finally, my family and close friends have always offered me support and comfort when the road ahead has seemed very long. I thank you all for listening and always believing in my endeavors. Especially, I would like to thank my sister Anna for giving me her permission to pursue a career abroad, and my friend Sara, who unknowingly made me fall in love with the cold, dark, star-lit sky of a Swedish December midnight.

Last but not least, I am forever indebted to Jon Sundqvist, who has contributed to every thought outlined in this thesis by infinite number of discussions, iteration of drafts and ideas. I thank him for always reminding me to keep a critical attitude and to see the big picture behind the details. Most importantly, I thank him for making the journey with me.

Munich, September 2010

Karin Lind

Curriculum Vitae

KARIN LIND

02.05.1984 Born in Motala, Sweden

EDUCATION

01.09.1999 – High School Degree in natural sciences, Platengymnasiet, Motala,
01.06.2002 Sweden.

01.09.2003 – Degree in Master of Science in physics and astrophysics, Uppsala Uni-
31.08.2007 versity, Uppsala, Sweden. Master thesis project conducted at the De-
partment of Physics and Astronomy.
Master thesis supervisors:
Dr. Andreas Korn
Prof. Bengt Gustafsson

01.09.2007 – International Max Planck Research School (IMPRS) PhD student po-
31.08.2010 sitioned at the European Southern Observatory (ESO), Garching bei
München, Germany.
PhD thesis supervisors:
Dr. Francesca Primas (Head of User Support Department, ESO)
Prof. Martin Asplund (Director at the Max Planck Institute for As-
trophysics, MPA, Garching)

REFEREED PUBLICATIONS

2008 **K. Lind**, A. J. Korn, P. S. Barklem, F. Grundahl
*Atomic diffusion and mixing in old stars II. Observations of stars in
the globular cluster NGC 6397 with VLT/FLAMES-GIRAFFE*
Astronomy & Astrophysics, 2008, 490, 777-786

2009 **K. Lind**, F. Primas, C. Charbonnel, F. Grundahl, M. Asplund
*Signatures of intrinsic Li depletion and Li-Na anti-correlation in the
metal-poor globular cluster NGC 6397*
Astronomy & Astrophysics, 2009, 503, 545-557

2009 **K. Lind**, M. Asplund, P. S. Barklem
Departures from LTE for neutral Li in late-type stars
Astronomy & Astrophysics, 2009, 503, 541-544

-
- 2010 **K. Lind**, M. Asplund, P. S. Barklem
Departures from LTE for neutral Na in late-type stars
Astronomy & Astrophysics, 2010, submitted
- 2010 **K. Lind**, C. Charbonnel, T. Decressin, F. Primas, F. Grundahl,
M. Asplund
*Tracing the chemical evolution of NGC6397 through the chemical com-
position of its stellar populations*
Astronomy & Astrophysics, 2010, recommended for publication
- 2010 P. Baumann, I. Ramirez, J. Meléndez, M. Asplund, **K. Lind**
Lithium depletion in solar-like stars: no planet connection
Astronomy & Astrophysics, to be published

NON-REFEREED PUBLICATIONS

- 2009 **K. Lind**, F. Primas, C. Charbonnel, F. Grundahl, M. Asplund
*Observational signatures of lithium depletion in the metal-poor globu-
lar cluster NGC6397*
Proceedings for the IAU symposium 268, Geneva 2009, Cambridge
University Press
- 2009 M. Asplund & **K. Lind**
*LiBeB in the light of 3D hydrodynamical models and non-LTE line
formation*
Proceedings for the IAU symposium 268, Geneva 2009, Cambridge
University Press
- 2009 F. Primas, **K. Lind**, C. Charbonnel, F. Grundahl, M. Asplund
The lithium history of NGC6397
Proceedings for the IAU General Assembly, Rio 2009, Cambridge Uni-
versity Press

CONFERENCE TALKS AND SEMINARS

- 05.2010 Contributed conference talk, The chemical evolution of the Milky Way
Galaxy, Ringberg Castle, Tegernsee, Germany. *The chemical evolution
of NGC 6397*

- 05.2010 Contributed talk, workshop on Excellence Cluster, Research Area G, ESO, Garching, Germany. *The chemical composition of the two stellar generations in NGC 6397.*
- 02.2010 Institute seminar, Lund University, Sweden. *Observational signatures of lithium depletion in Galactic halo stars.*
- 01.2010 Institute seminar, Max-Planck Institute for Astrophysics, Garching. *Observational signatures of lithium depletion in Galactic halo stars.*
- 12.2009 Institute seminar, Uppsala University, Sweden. *Observational signatures of lithium depletion in Galactic halo stars.*
- 11.2009 Contributed talk, IAU symposium 268: Light elements in the Universe, Geneva, Switzerland. *Observational signatures of lithium depletion in the globular cluster NGC 6397.*
- 09.2009 Contributed talk, Stellar Astrophysics and Galactic Archeology workshop I, Eibsee, Germany. *Non-LTE line formation of Li and Na in late-type stars.*
- 09.2008 Contributed talk, Stellar Astrophysics and Galactic Archeology workshop II, Kreuth, Germany. *Lithium observations in globular clusters with VLT/FLAMES.*
08. 2008 Contributed talk, Chemical Evolution of Dwarf Galaxies and Stellar Clusters, Garching, Germany. *Lithium abundances of 300 stars in the metal-poor globular cluster NGC6397.*
- 05.2008 Institute seminar, ESO, Garching, Germany. *Stellar abundances in globular clusters.*
- 03.2008 Insitutue seminar, ESO, Garching, Germany. *Li in globular clusters - diluted, depleted and polluted?*
- 08.2007 Institute seminar, Uppsala University, Sweden. *Abundance patterns on the subgiant branch of the globular cluster NGC6397.*

SCHOLARSHIPS

09.2007– IMPRS/Marie-Curie Early Training Site Project. Garching, Germany
04.2008

06.2007 Anna och Allan Löfbergs stiftelse. Uppsala, Sweden.

